Self-similar Infall Models for Cold Dark Matter Haloes

by

Morgan Le Delliou

A Thesis
submitted to the Department of Physics
in conformity with the requirements for
the Degree of

Doctor of Philosophy

Queen's University
Kingston, Ontario, Canada

September, 2001

ABSTRACT

How can we understand the mechanisms for relaxation and the constitution of the density profile in CDM halo formation? Can the old Self-Similar Infall Model (SSIM) be made to contain all the elements essential for this understanding?

In this work, we have explored and improved the SSIM, showing it can at once explain large N-body simulations and indirect observations of real haloes alike. With the use of a carefully-crafted simple shell code, we have followed the accretion of secondary infalls in different settings, ranging from a model for mergers to a distribution of angular momentum for the shells, through the modeling of a central black hole. We did not assume self-similar accretion from initial conditions but allowed for it to develop and used coordinates that make it evident.

We found self-similar accretion to appear very prominently in CDM halo formation as an intermediate stable (quasi-equilibrium) stage of Large Scale Structure formation. Dark Matter haloes density profiles are shown to be primarily influenced by non-radial motion. The merger paradigm reveals itself through the SSIM to be a secondary but non-trivial factor in those density profiles: it drives the halo profile towards a unique attractor, but the main factor for universality is still the self-similarity. The innermost density cusp flattening observed in some dwarf and Low Surface Brightness galaxies finds a natural and simple explanation in the SSIM embedding a central black hole.

Relaxation in cold collisionless collapse is clarified by the SSIM. It is a continuous process involving only the newly-accreted particles for just a few dynamical times. All memory of initial energy is not lost so relaxation is only moderately violent. A sharp cut off, or population inversion, originates in initial conditions and is maintained through relaxation. It characterises moderately violent relaxation in the system's Distribution Function. Finally, the SSIM has shown this relaxation to arise from phase space instability once the halo has been stirred enough through phase mixing.

Extensions of these explorations are possible and expected to refine our understanding of the formation of dark halo density profiles. A link should be sought, for instance, between the present results on relaxation and the entropy of the system.

Keywords: dark matter, galaxy formation, self-similar infall, density profile, density cusps, distribution function, angular momentum, mergers, black holes

UNIVERSITÉ LOUIS PASTEUR-STRASBOURG I
RÉSUMÉ DE LA THÈSE DE DOCTORAT

Discipline :	Sciences de la Terre et de l'Univers
Spécialité (facultative) :	Cosmologie (Astrophysique)
Présentée par :	Le Delliou Morgan
Titre :	**Self-Similar Infall Models for Cold Dark Matter Haloes (Des modèles autosimilaires d'accrétion secondaire dans leurs applications aux halos de matière sombre froide, dite CDM)**
Unité de Recherche :	UMR No 7550 Observatoire de Strasbourg
Directeur de Thèse :	Henriksen, Richard N. Professeur Queen's University at Kingston, Ontario, Canada
Co-Directeur de Thèse :	Blanchard, Alain Professeur

Condensé:

Comment pouvons-nous comprendre les mécanismes de relaxation et de constitution des profils de densité induits par la formation des halos CDM? Peut-on faire figurer dans le vieux modèle autosimilaire d'accrétion secondaire (SSIM) tous les éléments nécessaire à cette compréhension?

Dans ce travail, nous avons exploré et amélioré le SSIM, et montré qu'il est capable d'expliquer autant les grandes simulations à N corps que les observation indirecte de halos véritables. En utilisant un simple programme dit 'à coquilles sphériques', conçut avec précautions, nous avons suivis l'accrétion secondaire de systèmes dans différentes conditions, allant d'un modèle d'agrégation jusqu' à une distribution de moment angulaire, en passant par la modélisation d'un trou noir central. Nous n'avons pas posé l'autosimilarité de l'accrétion dès les conditions initiales, mais au contraire laissé libre son développement et utilisé un système de coordonnées qui la met en évidence.

Nous avons trouvés que l'accrétion autosimilaire apparat de façon commune dans la formation de halo CDM comme un état intermédiaire stable de quasi-équilibre dans la formation des grandes structures. Nous avons montrés que les profils de densité des halos de matière sombre sont principalement déterminés par les vitesses transverses. Le paradigme de l'agrégation se révèle, à travers le SSIM, tre un facteur secondaire mais non trivial de la formation de ces profils de densité: il conduit le profil du halo vers un attracteur unique, mais le facteur principal de l'universalité du profil reste l'autosimilarité. L'aplatissement du profil de densité en son centre observé, dans quelques galaxies naines et à faible intensité de surface, trouve une explication simple et naturelle avec le SSIM incluant un trou noir central.

Par ailleur, la relaxation dans les effondrements gravitationnels à basses températures et sans collisions s'explicite dans le SSIM. C'est un processus continu impliquant principalement les particules nouvellement accrétées, pendant un petit nombre de temps dynamiques. Toute mémoire contenue dans les états d'énergie initiale n'est pas complétement détruite, et donc la relaxation est seulement modèrément violente. Une coupure franche à basse énergie dans la fonction de distribution, aussi appelée inversion de population, qui prend sa source dans les conditions initiales mais est entretenue par la relaxation, caractérise cette dernière dans la fonction de distribution de système. En fin de compte, le SSIM a montré que la relaxation modérément violente résulte de l'instabilité de l'espace de phase après que le halo ait été assez brouillé par le mélange des phases.

Des extensions à ces explorations sont possibles et devraient affiner notre compréhension de la formation des profils de densité des halos de matière sombre. Par exemple, l'on devrait explorer le lien entre les résultats actuels sur la relaxation et l'entropie du système.

Mots-clefs: matière sombre, formation des galaxies, accrétion autosimilaire, profil de densité, densité centrale, fonction de distribution, moment angulaire, agrégation, trous noirs

Résumé:

La compréhension des principes sous-jacent à la formation des grandes structures de l'univers est l'un des problèmes fondamentaux de la cosmologie moderne. Tel qu'il nous apparaît, en cette fin de siècle, l'univers semble dessiner une mousse de galaxies dont les bulles contiennent de grand vides. Cette hiérarchie complexe de regroupements en gigogne laisse présager d'une explication moins naïve que celle, par exemple de la fragmentation simultanée d'un nuage de gaz primordial uniforme.

La mesure de la masse des galaxies et amas de galaxies par différentes méthodes indépendantes conduit à poser l'hypothèse, dominante, de l'existence d'une masse non détectée: la matière sombre. Deux type de modèles se dégagent de ce paradigme: les modèles de matiére sombre chaude (HDM), dont les scénarios d'évolution privilégient l'importance du champ de vitesses primordial et l'émergence des structures par fragmentation sur des échelles de plus en plus petites à partir de la coalescence de "crêpes, ou caustiques, de Zel'Dovich" (dues au flot primordial), et ceux dit de matière sombre froide (CDM), privilégiant l'importance du champ des fluctuations de densité et la construction des structures par coalescence de surdensités sur des échelles de plus en plus grandes.

Le type de modèle qui semble le plus à même de reproduire toutes les échelles de structures observées reste du côté des modèles CDM, malgré les problèmes qui leur sont inhérents. Dans ce cadre, les germes des grandes structures se trouvent dans les rides à la surface du champ de densité cosmologique uniforme, et c'est la croissance et le regroupement de ces germes évolués qui conduisent aux structures observées. La constitution de ces nuages de matière sombre, dits halos, permet également de comprendre les prémisses de la formation des galaxies puisque leur matiére baryonique, minoritaire, n'a plus qu'à descendre au fond du puits de potentiel créé par la matière sombre, liant ainsi la cosmologie à l'étude de la dynamique des galaxies. Le développement de ces germes peut être considéré séparément dans l'hypothèse que les agrégations (mergers) ne jouent pas un rôle primordial dans la formation des halos CDM. C'est ce que nous nous sommes efforcé de démontrer dans cette thèse.

Les travaux actuels dans le domaine tendent à insister sur l'importance du profil de densité (distribution de la densité de masse en fonction de la distance au barycentre du halo) à la virialisation dans la compréhension de la formation des halos CDM. Certains groupes proposent même l'existence d'un profil universel, dit NFW, ne dépendant que de l'échelle de masse du halo (c.f. Navarro, Frenk & White, 1996, [32] ApJ 462, 563), détecté dans leurs simulations à N corps. Relayée par plusieurs autres études, cette proposition se heurte à plusieurs obstacles: d'autres groupes trouvent un profil universel différent (Moore et al.,1999, [71], appelé ici Moore99 MNRAS, 310, 1147) ou même réfutent l'universalité d'un tel profil (Jing & Suto, 2000, [70] ApJL,529, L69). De récentes observations des galaxies à faible densité lumineuse de surface (LSB) et des galaxies naines à dominante de matière sombre (Kravtsov et al., 1998, [31]ApJ, 502, 48, et Stil, 1999, [75] thse de doctorat, observatoire de Leiden, Pays bas) tendent également à jeter le doute sur ces profils issus de simulation de pure CDM et à ouvrir la porte aux modèles alternatifs et aux aménagement de la matière CDM classique. Par ailleurs, la possibilité d'existence d'un

profil universel à entraîné certains groupes à tenter de comprendre les mécanismes pouvant être responsable d'un tel résultat. Par exemple, Syer & White (1998, [33] MNRAS, 293, 337) font appel au processus d'agrégation répétée qui entraîne l'évolution dynamique du profil de densité par rétroaction entre l'émiettement des satellites absorbés par effet de marée et leur chute vers le centre du halo par la friction dynamique. Enfin, l'application de la théorie cinétique à la dynamique stellaire fournit des outils statistiques d'étude des équilibres gravitationnels (la fonction de distribution, notée PDF, mesurant la densité de masse de l'espace des phases du système; par ex. Bertin & Stiavelli, 1984, [58] A&A, 137, 26, ou Merritt et al., 1989, [60] MNRAS, 236, 829) qui ont été repris dans le cadre des halos de matière sombre et qui pourraient permettre d'expliquer de manière plus fondamentale l'émergence d'un état d'équilibre et du profil de densité.

Dans ce contexte les modèles d'accrétion secondaire autosimilaires (SSIM) semblent prometteurs, malgré leurs restrictions. Dérivant des travaux originaux de Gunn & Gott (1972, [30] ApJ, 176, 1) et de Bertschinger (1985, [36] ApJS, 58, 39) qui mirent en évidence la solution stationnaire du problème d'accrétion secondaire en symétrie sphérique, le modèle donne une origine dynamique au profil universel qui émerge de l'autosimilarité (Fillmore & Goldreich, 1984, [35] ApJ, 281, 1). Il contient également le mécanisme de constitution de l'équilibre gravitationnel, mis en évidence par Henriksen & Widrow (1999, [42] , MNRAS, 302, 321) á travers l'étude de l'espace des phases, de la PDF et d'une version modifiée du théorème du viriel. D'autres groupes se sont attachés à étendre le champ de validité du modéle SSIM en y injectant des conditions initiales non-autosimilaires et plus complexes, calculant par exemple le profil initial de densité à partir de modèles cosmologiques contemporains (Hoffman & Shaham,, 1985, [37] ApJ, 297, 16, Ryden & Gunn, 1987, [47] ApJ,318, 15 ou Avila-Reese et al., 1999, [49] MNRAS, 310, 527) ou de fonds de densité primordiale différents du traditionnel univers d'Einstein-de Sitter(Subramanian et al., 1999, [45] soumis ApJ, astro-ph/9909279), ou même ajoutant les effets, ignorés en symétrie sphérique, de vitesses non radiales au niveau de l'accélération centrifuge (White & Zaritski, 1992, [52] ApJ, 394, 1, Ryden, 1993, [53] ApJ, 418, 4 ou Sikivie et al., [51] PhysRevD, 56, 1863) ou encore d'une dispersion transverse des vitesses (Subramanian, 1999, [46] soumis ApJ, astro-ph/9909280).

Les travaux effectués au cours de cette thèse font suite à ceux du modèle de Henriksen & Widrow qui avaient étudié la structure de l'espace des phases et l'établissement d'une phase autosimilaire de quasi-équilibre pour le SSIM en symétrie sphérique. Ces études font l'usage du formalisme de Carter & Henriksen (1991, [43] JMPS, 32, 2580) qui permet d'exprimer les équations d'un système sous une forme qui se simplifie lorsque ce dernier évolue de manière autosimilaire (le système devient alors stationnaire dans ces variables). Plusieurs tentatives ont été faites pour expliquer en termes plus simples les liens entre ce formalisme et les autosimilarités qu'il unifie. Cette thèse en a tenté une nouvelle.

Dans un premier temps, nous avons élargi le SSIM à la présence de moment angulaire en utilisant le cadre autosimilaire précédent. Ensuite, des modèles semi-analytiques ont été établis: un premier, pour tenter de mettre en parallèle les arguments de Syer & White sur les effets des agrégations (mergers) avec un modèle les reproduisant par l'absorption

d'une coquille sphérique de surdensité déposée aux limites d'un coeur de halo ayant déjà évolué jusqu'en phase d'accrétion autosimilaire. Un second pour introduire des moments angulaires respectant l'autosimilarité pour les coquilles sphériques du modèle simple. Enfin, avec le développement de mesures de la PDF, la modélisation de la présence d'un trou noir central au coeur du halo a été introduite (Henriksen & Le Delliou, [86] en prparation pour MNRAS) pour permettre d'expliquer, avec la CDM, les faibles densités centrales récemment observées.

Cette thèse décrit les difficultés techniques rencontrées lors de la création des différent codes dits à pellicules, ou coquilles, en passant par la longueur de lissage nécessaire au passage du centre (singularité de la symétrie sphérique), l'importance de l'auto-interaction des pellicules qui doit respecter la répartition du volume de la pellicule (modélisée par une coquille infiniment mince) par rapport à sa position nominale et le jeu entre le pas de temps d'intégration et la longueur de lissage résolu par une exploration par simulation de Monte Carlo du plan de paramètres. Le choix de l'intégrateur s'est avéré crucial car la longueur de lissage fixe une échelle minimum pour le pas d'intégration et force donc d'éviter les intégrateurs trop sophistiqués. Le choix s'est porté sur un simple Runge-Kutta du deuxième ordre. La manière de mesurer l'énergie potentielle gravitationnelle a aussi nécessité des ajustements indispensables: comme le système étudié n'est ni infini, ni fermé, la définition simpliste de l'énergie potentielle comme proportionnelle au potentiel gravitationnel ne peut être employée. Il faut revenir aux définitions fondamentales à base de gradients du potentiel comme celle issue du tenseur de Chandrasekhar (voir Binney & Tremaine, 1987, [87] Galactic Dynamics, Princeton, Princeton University Press) ce qui entraîne que l'énergie, contrairement au potentiel, ne dépend pas des pellicules extérieures au système (à cause de la symétrie sphérique).

Ensuite, le choix s'est porté sur les conditions initiales des simulations: d'une part, entre conditions cosmologiques (perturbation centrale d'un modèle d'Einstein-de Sitter avec un flot initial de Hubble) ou non, d'autre part, sur l'établissement des pellicules avec une masse constante, un espacement constant sur l'échelle des rayons, ou bien par perturbation des positions de pellicules modélisant initialement une densité constante afin de refléter le statut physique de la perturbation centrale.

Pour l'exploration des possibilités de modélisation d'agrégations, une autre simulation a été nécessaire pour déterminer les gammes pertinentes de masses et de densités moyenne relative au coeur du halo.

La symétrie sphérique entraînant la conservation du moment angulaire, la distribution radiale de moment angulaire respectant l'autosimilarité doit être établie aux condition initiales. Il est à noter que sa forme diffère d'une loi de puissance, et par conséquent l'autosimilarité ne peut être qu'inexacte en présence de moment angulaire.

La problématique principale de la modélisation d'un trou noir central provient de la définition de la masse entrant dans le trou noir. En effet, en l'absence de moment angulaire, comme modélisé ici, toutes les pellicules traversent le centre. La structure de l'espace des phases permet cependant une évaluation algorithmique du rayon de Schwarzschild et de la masse du trou noir central au cours du temps, et ce malgré le fait que la vitesse de

la lumière dans l'espace des variables autosimilaires n'est en général pas conservée.

Les mesures de PDF dans l'espace des phases ont été testées, pour les PDFs avec distribution de vitesses isotropes, par génération puis application de la mesure sur une sphère de Plummer, et pour les PDFs avec vitesses radiales, sur le modèle de PDF de Henriksen & Widrow.

Les résultats obtenus furent conformes aux attentes et même parfois surprenants: la modélisation des agrégations de satellites a montré que le coeur est capable d'assimiler de grosses perturbations tout en retrouvant son régime autosimilaire initial. L'observation de l'évolution des particules de surdensité assimilées dans l'espace des phases du système révéle que les grandes lignes de l'argument de Syer & White se retrouvent dans un contexte d'accrétion secondaire, accréditant la thèse que l'agrégation ne serait pas essentielle à la formation des halos. En revanche le profil de densité réserve des surprises: l'attracteur semi-universel mis en évidence par Fillmore & Goldreich devient entièrement universel (valable aussi pour les perturbations cosmologiques initiales plus concentrées que lui) lors de l'assimilation d'une seule surdensité par le coeur.

Les mesures de PDF sur les systèmes à espaces des phases purement radials ont confirmé les résultats de Henriksen & Widrow quant à la dépendance à l'énergie, ainsi que leurs conjectures, suivant celles de Merritt et al., quant à la coupure asymptotique aux énergies négatives.

L'addition d'une distribution radiale de moment angulaire confirme les soupons selon lesquels l'effet du moment angulaire serait d'aplanir relativement le profil de densité au centre et de le creuser aux limites. Cet effet est tel que, d'une distribution initiale du moment angulaire justifiée par des arguments Dimensionnels, il est possible d'obtenir avec le SSIM des profils de densité similaires à ceux fournis par les simulations tridimensionnelles à N corps et un profil NFW peut même être optimisé pour décrire nos resultats.

L'addition d'un trou noir renforce le comportement du modèle SSIM classique, puisqu'il ne s'agit que de rajouter au centre du halo une pellicule massive immobile, variable ou non. L'essentiel réside dans le fait que la PDF garde, comme pour le SSIM exploré par Henriksen & Widrow, la même dépendance par rapport à l'énergie et la même coupure asymptotique (cut off) aux énergies les plus négatives. Cela renforce la thèses de Henriksen & Le Delliou permettant une compatibilité des observations avec des halos CDM simple entourant un trou noir. En vérité, les simulations ont confirmés l'effet d'aplanissement de la densité centrale prédit par Henriksen & Le Delliou. Des indications de croissance autosimilaire du trou noir central sont même obtenues dans une version modifiée d'évaluation du rayon de Schwarzschild.

La conclusion de ces travaux est la suivante: les modéles autosimilaires d'accrétion secondaire se sont révélés capables de fournir le pouvoir explicatif qui manque aux grandes simulations à N corps tout en sortant de leurs limitations traditionnelles (symétrie sphérique empêchant les agrégations de deux halos de centres différents, accrétion purement radiale, d'où la difficulté d'exploration des conséquences de la présence d'un trou noir central) et en fournissant des pistes aux observations (profil de densité, évaluation d'une phase de quasi-équilibre viriel très stable aux perturbations massiques et radi-

ales). Nous avons donc confirmé les conjectures de Syer & White sur la dynamique des agrégations tout en les élargissant au contexte de l'accrétion. Nous avons mis à jour l'extrême robustesse du quasi-équilibre de la phase d'accrétion autosimilaire. Nous avons montré que le comportement du profil de densité des halos de matière sombre froide peut se comprendre entièrement par l'influence de la composant non-radiale des vitesses des particules, en ajoutant l'effet d'un trou noir central pour rendre compte de l'aplanissement central observé, et que les agrégations répétées ne tiennent pas cette place centrale dans l'effondrement sans collisions des halos de matière sombre.

De plus, notre modèle nous a permis l'étude approfondie du phénomène de relaxation violente qui caracterise les effondrement gravitationnels: Il ressort de notre modèle qu'il subsiste des corrélations entre les énergies initiales et finales du système, conduisant à une relaxation violente modérée. De plus cette relaxation ne concerne que les particules les plus récemment accrétées, détectées par leur étalement en énergies finales, et qui se regroupent en bordure du système dans l'espace des phase et dans la PDF.

Les mesures de PDF ont validé les conjectures émises par Henriksen & Widrow quant à la dépendance dans l'énergie et à la coupure asymptotique.

D'autre part, ces travaux ouvrent la porte à de nombreuses précisions sur leurs résultats (par exemple, l'implantation d'un trou noir central au sein d'un halo avec moment angulaire, la mesure de PDF dépendant aussi du moment angulaire pour les systèmes non-isotropes et mme suggèrent la valeur d'une étude future sur des modèles de halos de matière sombre aux symétries moins contraignante en utilisant les variables autosimilaires de Carter & Henriksen (modèle à symétrie axiale, réévaluation de résultats de simulations à N corps à l'aide de variables autosimilaires).

ACKNOWLEDGEMENTS

I would like to thank Dick (Richard N.) Henriksen for supervising this thesis and supporting (bearing?) me along the way with his sense of humour, his deep understanding and curiosity for physics and his much used sense of composure.
Thanks are also due to Sir Thibaut de Lery, Grand Knight of the Order of Tetrapilectomy, for his many encouragements, enlightenning discussions on physics, politics, life, and the pursuit of happiness. I would also like to thank Minhhuy Ho, for his strong moral support and scientific maieutics. He truly was the wise old man on top of the mountain of the many silly dangers, with scarce words of wisdom.
Mustapha Ishak was of great help and support.
The much regretted Mahmoud Aburihan should not have defected so soon. He will be missed, and his memory honored.
Discussions and help were also very precious for the scientific achievement presented here (see the velocity dispersion measurements of the black hole halo) when offered by Jeroen Stil.
Recognition must be granted to the Queen's Astrophysics Research Group, its Professors, the Physics department support staff and its graduate students George, JJ, Tom, Rupinder, Doug, the three Steves, Ghisia, Myron and Aphra, Jason, Ian, Luke, Dave and Kathy, Nicos and Nick, Joe and Tara... for accomodating my quirks and providing the help and scientific environment without which no thesis can bloom and prosper.
I would like to thank Ella for her support, granola and linguistic rectitude. Now I speaky Englishy good.
My parents deserve a big percentage of the zero royalties that this thesis will yield, since they are one of the main sponsors and also the affectionate and efficient cause of my being... able to write it.
Une personne marque de son empreinte indélébile l'ensemble du concentré de temps et d'idées qu'est cette thèse: Céline Ai Treu Am Nguyen ou Nina, elle continuera à marquer ces pages par sa présence en creux.

ABSENCE

J'aurai à soulever la vie immense
Qui maintenant encore est ton miroir:
Pierre à pierre j'aurai à la reconstruire.
Combien de paysages sont devenus dérisoires
Et dépourvus de sens, pareils
A des luminaires que l'aube écarte,
Combien de sentiers ont perdu leur parfum.
Après-midi qui furent asile de ton image,
Musiques où toujours tu m'attendais,
Paroles de ce temps-là,
Vous devez être brisées
Et par mes mains,
Rebelles et avec douleur.
Le ciel vif, immense, Clame et clame sans cesse
ton abandon.
Dans quel creux enfouir mon âme
Où je ne puisse pas surveiller ton absence
Qui comme un soleil terrible sans crepuscule
Brille, définitive et implacable ?
Ton absence me tient
Comme corde enserrant une gorge.

Fervor de Buenos Aires, 1923
Traduction de Gonzalo Estrada et Yves Peneau.
JORGE LUIS BORGES

Contents

List of Figures

List of Tables

Chapter 1

Yellow and Black General Introduction

"C'était à Mégara, faubourg de Cathage, dans les jardin d'Hamilcar..."

Salammbô
GUSTAVE FLAUBERT

"A beginning is a time of extreme delicacy."

Dune
FRANK HERBERT

1.1 Problems in cosmology

Understanding the principles involved in the establishment of quasi-stable large scale structures in the universe is one of the main goals of modern physical cosmology.

The universe as we know it today is radically different than that in which people at the beginning of the century believed they were living: instead of being a sea of suns, more or less evenly spaced, or an island of sand grains — suns — floating in a vast emptiness, we are now embedded in a foam of galaxies, replicas of the island of sand picture, with huge voids between the bubble walls. This complex hierarchy of nested groupings testifies for a less naive explanation than, say, a collective and simultaneous fragmentation of a uniform primordial gas.

Measurements of dynamical masses have shown large discrepancies with the observed luminous mass. The theoretically conservative answer to that inconsistency is based on the search for this electromagnetically discrete mass, dubbed for that reason "dark matter" (DM). Considering that it may constitute, together with some form of Dark Energy that would have the effects of Einstein's cosmological constant, the vast majority (80 to 99%) of the mass-energy of the universe, understanding the formation of Large Scale Structures (LSS) within the frame of Hot Big Bang Cosmology leads to the exploration of the behaviour of DM. Setting aside the search for its nature, it is still of interest for LSS formation to know the kind of kinematics that dominates the DM in order to predict the type of scenario for LSS formation. One active paradigm of DM studied in this present work is collisionless cold dark matter (CDM).

Cosmological LSS formation theory has been approached in two distinct fashions: due to the progresses in computing power, large N-body simulations have been performed and studied in the scope of inputting physics judged relevant and retrieving its products in terms of LSS. But this leaves us with just another layer of phenomenological descriptions. To go beyond that and really understand the physics of LSS, another type of approach involving analytical and semi-analytical models is needed.

In contrast with what can be inferred from the trend in numerical cosmology to favour large N-body simulations with as many degrees of freedom and as much physics as possible, modeling means simplifying. Too much simplification will not be able to reproduce the aspects of reality deemed relevant for the studied problem. That is why modeling is funambulist art. It also yields the classical understanding of phenomena (in terms of simplest elements, if possible related to intuition). In this work we used the model for single collapsed objects that has been referred to as the Self-Similar Secondary Infall Model (SSIM) and we attempted to study its predictions in terms of dynamics as well as extend its validity beyond some of its oversimplistic assumptions.

1.2 The Dark Matter

> There are more things in the Heavens
> and on the Earth than in all the
> dreams of philosophy
>
> *Hamlet* I, V 166 (1602) WILLIAM SHAKESPEARE

The paradigm of dark matter comes from the various ways available to astrophysicists so as to measure the mass of galaxies and clusters: a simple minded way would be to look at the average mass per unit of light intensity given out by stars, then multiply that

by the amount of light given out by a galaxy or cluster. That would weigh the amount of luminous mass. Of course, there are other more sophisticated ways of measuring the luminous mass but this one is indicative enough to realise the problems involved.

Another possible way of measuring the mass of galaxies and clusters is by its dynamical effects on its surrounding masses: if some masses are orbiting around, say, a galaxy, and they are small enough compared to the galaxy, they will have a rotational velocity characteristic of the mass of the galaxy. In turn their velocities can be used to characterise the mass encompassed within their orbits. Underlying these results lies the Virial Theorem. It states that any self-gravitating cloud of mass will find its kinetic energy twice canceled by its gravitational potential energy when at equilibrium. Therefore the total energy of the system will be equal to minus the kinetic energy at its equilibrium state. This is still true for the specific forms of the energies (energies per unit mass) so one can get at the total potential energy of an equilibrium system by measuring its velocities only, and then get the total gravitating mass. This principle can be applied in various more or less complex ways, using statistical averaging or not, but these methods are all based on the principle of the dynamical signature of mass.

When confronted, it appears that there is discrepancy between the luminous mass and the gravitating mass, more pronounced for larger and larger structures. This is at the origin of the postulate of the existence of some non-luminous "dark matter" present in a more diffuse fashion than the luminous one, but in large amounts.

1.3 Motivations for the present study

> In science, we try to speak to people,
> so as everyone understands,
> of things that no one knew before.
> In poetry, it is exactly the opposite.
>
> PAUL DIRAC (1902-1984)

Modern Large Scale Structure formation theories are dealing with the question of how to grow ripples on a universe almost uniformly populated with mass into the mass aggregations we can observe nowadays, from galaxies to superclusters of galaxies. Given the Dark Matter paradigm, the question becomes how to grow dark matter structures. From the structure formation's point of view, the important question about the nature of dark matter comes down to the difference in time-scales for clustering via gravitational collapse versus free streaming from initial velocities into caustics — that is to say between cold and hot DM.

The present picture, based on observations, favours the CDM pole. In this picture,

LSS are formed by the collapse of the uniform background mass around those seed-ripples, which at the same time can merge with each other. These seeds can then be considered separately for their growth into haloes if mergers[1] are not considered to play a determining role in the properties of the final halo produced. The role of mergers is one of the questions we will explore in the present work.

Since regular matter is then thought to form galaxies by falling in the middle of haloes, once we can understand the properties of the final haloes, we can understand the premises of galaxy formation and Cosmology can yield inputs for Galactic Astrophysics.

Current research is focusing on understanding the radial mass density distribution, or density profile, of DM haloes. Some groups are finding what could be a universal — or unique, once haloes are scaled appropriately — profile for every halo in numerical simulations, whereas others are finding a different innermost density cusp for the universal profile, or even disagreeing with the universality of those profiles. New observations are even casting doubt by disagreeing with all the results on the innermost density cusp in the centre of haloes.

Understanding the density profile, then, lies at the centre of current questions on LSS formation. In particular, separating the various paradigms involved in the formation of pure CDM haloes is an important theoretical task, whether it is testing the repeated merger paradigm, or the importance of non-radial motion. Proposing extensions of the pure CDM model to explain the newest observations is also of great interest. But using a model to reproduce the profile and perhaps explain its universality does not provide as deep an insight as studying the dynamics involved with such a successful model. Gravitational collapse of collisionless systems is believed to involve an incomplete and rapid mode of energetic relaxation called 'violent relaxation'. Analysis of the processes involved in such relaxation, therefore, is crucial. This is precisely what this work proposes to tackle.

In chapter 2, we will review the background of LSS formation in the general terms of the DM paradigm and the main models that are spawned by it. We will also give a general overview of the SSIM and its main results. Chapter 3 will discuss the formalism and results of the semi-analytical model on which the present work is based. Chapter 4 will document technical details that were solved in the shell codes that have been written in order to perform the numerical calculations. Chapter 5 will explore the SSIM's equilibrium by measuring its Probability Distribution Function and energy correlation in detail, as well as perturb the model to represent the effects of Merger events on a CDM halo. Chapter 6 will then extend the SSIM to model the introduction of angular momentum and its effects. It will also extend the SSIM to model the establishment of a central growing mass representing the possibility of galactic supermassive black holes in

[1] In the context of LSS formation, mergers designate the process of merging with each other already evolved haloes which masses are not widely different.

dark haloes. Finally, chapter 7 will give the general conclusions on the work as well as suggest possible extensions.

Chapter 2

Large Scale Structures and Models

> If the facts don't fit the theory, change the facts.
>
> ALBERT EINSTEIN

2.1 Cosmology and Large Scale Structure Formation

2.1.1 Observational motivation of the Dark Matter Paradigm

Since the fate of the universe is sealed in part by its mass content, cosmology has driven observations to weigh the amount of mass existing. A simple way to do this in a universe populated by galaxies and clusters as main structures is to count the mass in each structure, get an average and multiply it by the number of such structures (or number density if you want to get at the density of the universe). When observers tried to measure masses of LSS like galaxies they looked at simple dynamics: Kepler's 3rd law relates the mass inside a certain radius to the rotational velocity of a test particle at that radius as

$$GM(r) = v_r^2 r. \tag{2.1}$$

Now if all the mass is detected, i.e. by its emissions of light (visible or other wavebands), when we get to the edge of a galaxy we should see the mass becoming constant and therefore the outermost particles (stars, then HI gas) rotating at keplerian characteristic decreasing velocity: $v_r \propto r^{-\frac{1}{2}}$.

Instead, flat or rising rotation curves are observed (e.g. Sancisi & van Albada [1] for spiral galaxies, but similar statistical studies have been performed on elliptical galaxies,

e.g. in Bertola & Capaccioli [2]), implying that $M(r) \propto r$, hence that $\rho \propto r^{-2}$and that $v_r^2 = cst$. This latter property of what is in fact the spherically-averaged tangential velocity distribution leads to the identification of such a system in literature as an isothermal sphere, in reference to a Maxwell-Boltzmann statistic with constant temperature.

Similar dynamical arguments are used on clusters of galaxies (e.g. Carlberg *et al.* [3]). Other mass estimates for clusters can be used: Virial-type arguments can be used to estimate the mass those clusters should have to retain the high energy X-ray emitting gas they contain (e.g. Songaila *et al.* [4]). Densities of electrons/protons can be obtained by measuring the distortion those clusters induce on the Cosmic Microwave Background Radiation by Compton scattering of this Cosmic Microwave Background Radiation's photon by their electrons (Sunyayev-Zel'Dovich effect, e.g. Holder & Carlstrom [5]). At last gravitational lensing of light from far sources, like quasars, by the mass distribution in clusters (e.g. van Waerbeke *et al.* [6]) can be used to yield mass estimates for LSS. All these estimates can be combined to obtain a complete picture of LSS mass distribution.Those and several other routes to the mass content of the universe allow one to estimate the average density of mass. There is an obvious discrepancy between these estimates and the mass of the observed luminous matter, which leads to the postulate of non-luminous gravitating mass, or Dark Matter (DM). Some attempts have been made to explain away those dynamical behaviours by modifying the laws of gravity (e.g. Modified Newtonian Dynamics, called MoND gravity, higher order derivative terms in the geometric tensor, modifying Einstein's gravity) but the wealth of independent means of getting at the presence of dark gravitating structures strongly favours the existence of DM. All in all,the mass of all DM exceeds that of Baryonic matter by about a factor of 10 (e.g. Faber & Gallagher [7] or Peebles 80a [8])

The nature of dark matter may be varied. From Big Bang (BB) Nucleosynthesis (BBN), calculating the relative abundance of primordial elements, it appears that we are only seeing part of the normal matter (baryonic matter; e.g. Schramm & Turner [9]) so some of it may be hidden in dark form, as MAssive Compact Halo Objects (MACHOs) (sub-solar mass objects first detected through gravitational microlensing by the EROS collaboration [10]) or as discrete cold, neutral molecular gas clouds. Some hypotheses even rely on primordial black holes (masses gravitationally collapsed at very early times after the Big Bang, e.g. Ivanov *et al.* [11]), which could avoid limitations from Big Bang Nucleosynthesis, but lack of observational indications make these hypotheses unlikely.

Current results place the density of matter to be $\Omega_m \in [0.2, 0.5]$ with a most likely value at $\Omega_m \approx 0.3$ whereas Big Bang Nucleosynthesis places the limit for baryonic matter at $\Omega_B h^2 \leq 0.019$ (with $h \sim 0.65$ with errors, current favoured estimates place $\Omega_B \sim 0.05$). All in all, the mass content of the universe is likely to be dominated by non-baryonic DM. Particle physics proposes a wealth of candidates for non-baryonic DM , labeled

WIMPs (for Weakly Interacting Massive Particles).Those range from massive neutrinos to axions, and to various supersymmetric particles. Massive neutrinos are now likely since the confirmation by the Super-Kamiokande detector of results from its ancestor experiment Kamiokande's mixing angle between different types of neutrinos [12] :$\Delta m^2 \sim a$ few times $10^{-3} eV^2$, but with expected masses insufficient for accounting for the observed Ω_m. Axions are Goldstone bosons (particles produced by a symmetry breaking and allowing for the acquisition of mass by the originally symmetric particles) prescribed by Peccei and Quinn to dynamically break the CP symmetry in Quantum ChromoDynamics [13]. Supersymmetric particles are particles that would be prescribed by the existence of a symmetry between bosons and fermions, a symmetry much favoured by particle physicists, and at the root of the most advanced attempts at quantum gravity with Superstring Theories and their background M-theory. As far as LSS formation is concerned, it suffices to distinguish among DM particles on the basis of their dynamical behaviour in gravity. The two main types of behaviour are related to the relativistic or non-relativistic nature of the rms velocity field for the DM particles: if the particles are light (like neutrinos) and likely to be fast, to the point of being relativistic when decoupled, then they are designated Hot DM. If they are slow or very heavy so that their mass energy is much larger than their kinetic energy, they fall into the category of Cold DM. Any intermediate case will just behave as a mix of the HDM and CDM main features (like Warm DM, when the particles are of comparable masses and rms kinetic energies, or even in the scenarii of mixed CHDM).

Current results, spawning from the combination of the Supernova Cosmology Project [14] and of the analysis of the Cosmic Microwave Background Radiation ([15], [16] and [17]), are pointing towards the presence of a cosmological constant or "dark energy," as some have modeled its cause, to the amount of $\Omega_\Lambda \approx 0.7$. As far as LSS formation is concerned, this only plays the role of cosmological background. (For a good review on DMs see Bergström [18].)

2.1.2 Hot Dark Matter

HDM is thus constituted of very relativistic WIMPs. This implies that at early stages of the collapse of primordial structures, the fluctuations of the velocity field dominate over density perturbations. This is the realm of the Zel'Dovich approximation, the analytical attempt at understanding the period of linear, free streaming HDM (e.g. neutrinos). These scenarii lead to the formation of density caustics called pancakes because of their flattened shape. This shape results from the three-dimensional streaming having an unstable nature which would favour the strongest streaming direction, leading to a faster collapse along that line. This picture applied to a random velocity field displays, because

of the topology of a vector field in three dimensions, the emergence of void nodes separated by membranes of connected pancakes, the intersections of which form filaments of overdensities, which in turn build up haloes at their nodes. This web-like picture of very largest scale structures has been characterised by Shandarin and Zel'Dovich [19] to be exactly analogous to the kind of patterns one can observe from geometrical optics through a rippled interface between two different refraction index media (e.g. images seen under a bridge or at the bottom of a swimming-pool). From those initial LSS, the density field then takes over to fragment them into smaller and smaller scale structures. This is the famous top-down hierarchical picture characteristic of HDM scenarios.

The major flaw for LSS formation of these types of scenarios is that they do not produce enough smaller scale structures like galaxies, and therefore are ruled out by observation: the power spectrum of such a model is too small at large radial wavevector k.

The power spectrum is defined as the Fourier transform of the autocorrelation function of the density field: P(k)=FT($< \delta\rho_{\underline{x_0}} \delta\rho_{\underline{x_0}+\underline{x}} >_{x_0}$) where

$$\delta\rho_x = (\rho - \rho_{bkg})/\rho_{bkg} \tag{2.2}$$

is the density contrast at point x and the average is noted $\overline{f} \equiv < f(x) >_x$. It is a widely used statistical measurement of LSS, which describes well the nature of clustering that will take place in a model where it is given as the initial condition.

For HDM models, P(k) is too small at large k when confronted with the power spectrum of observed LSS (Sugiyama [20]). This led further investigations to concentrate on the opposite kind of scenario: CDM.

2.1.3 Cold Dark Matter

Contrary to HDM, CDM behaves like non-relativistic, self gravitating dust. In the study of its evolution, the density field is assumed to be primordial: the seeds of LSS are then the density perturbations, or density contrast $\delta\rho$, that will grow through gravitational instability and collapse into primordial haloes. These will then merge with their gravitationally bound neighbours to form larger and larger scale structures. This picture, characteristic of CDM, is referred to as a bottom-up type hierarchical clustering scenario.

Because of the fundamental importance in these scenarii of primordial haloes, they can be studied from different perspectives: one can either try to understand the global picture that CDM collapse induces, or concentrate on understanding the formation of one idealised generic CDM halo. The first approach has yielded various phenomenological explorations through N-body simulations of idealised CDM patches of universe, sometimes completed with hydrodynamical treatments of the baryonic part of their mass content.

In these simulations, certain features or statistics are singled out as significant for confrontation with observations. Global phenomenological statistics can be derived from cosmological N-body simulations and compared with their observational counterparts: n-point correlation functions constitute a set of standard descriptive statistics which can be used to confront simulated LSS with existing ones. They also allow for some dynamical modeling of the universe as a statistical realisation of a random process (see the adaptation of the Bogoliubov-Born-Green-Kirkwood-Yvon —BBGKY— hierarchy equations from plasma physics in Peebles 1980 [21]).

Various other statistics can be used, like the mass function which gives the number of haloes in a given realisation at a determined mass scale and can be related to the statistics of halo masses. But understanding of these statistics requires the emergence of a vocabulary that has to be built from simpler, more refined models of the physics directly responsible for each of these aspects of LSS formation. Two main streams of semi-analytical approach aim at getting these statistics from initial structure of the density field: one is based on the density or mass excursion set, following the heuristic formula derived by Press and Schechter (PS, 1974 [27]), singling out successively regions whose average density is higher than a time-dependent threshold. The other focuses on density peaks of a gauβian random field after the approach of Bardeen *et al.*[1] (BBKS, 1986 [22]), who were using a single scale for peak identification and assigning them the same mass. Bond *et al.* (BCEK, 1991 [25]) used the random walk or excursion set formalism, smoothing the linear density peaks on various mass scales and then identifying collapsed regions by their average density being above a certain threshold. Unfortunately, neither of these approaches succeeds in overcoming the cloud-in-cloud problem[2] as identified e.g. in Bardeen *et al.*(BBKS, 1986 [22])or in Bond *et al.* (BCEK, 1991 [25]). That is why, along this line, generalised approaches were pursued, like that of Lacey & Cole (1993 [28]), or like the Peak Patch picture of Bond & Myers (1996 [26]). The Peak Patch picture is a mixture of PS's excursion set formalism and Bond, *et al.* 91 (BCEK) which first identify Patches of halo using the density average threshold method of Bond, *et al.* 91 (BCEK), then solves the cloud-in-cloud problem by trimming the patches identified so that they don't overlap and allows for Peak displacement through the Zel'Dovich approximation. This model still uses the spherical top hat and homogeneous spheroid approximation, a singular and very untypical self-gravitating collapse model, to determine the characteristics of the virialised region identified as bound. A recent example of refinement of this latter homogeneous

[1]First elaborated by Doroshkevich (1970 [23]) and Doroshkevich & Shandarin (1978 [24]) for HDM.

[2]Identification of small objects already included in larger objects so that they would be multiply counted, i.e. at two mass scales, the identification of clouds does not take into account that some of the smaller mass scale can be already counted in the larger scale cloud, when a smaller mass scale cloud is a sub-cloud of the larger mass scale one.

density approximation can be found in Shapiro *et al.* (1999 [29]) which uses truncated isothermal spheres[3].

Other properties are attached to one halo and can therefore be used also in the second approach. The density profile gives the radial dependence of mass for a given halo that can be related to observed density profiles. But single halo properties are just a refined way of assessing LSS in the CDM paradigm. The constitution of those properties is imprinted by significant physics that is not made obvious by their mere measurement. Again for these characteristics, some more refined modeling is needed in order to understand the importance of the various aspects of the physics used in large N-body simulations. Some aspects are already addressed by the general picture models previously cited , but more specialised and singular approaches are fruitful. Among these are e.g. the repeated merger picture of Syer & White (1998 [33]), and the Secondary Infall Model (SIM) started by Gunn & Gott (1972 [30]).

But the standard CDM model (often referred as SCDM) also has its problems: it creates too many small scale structures compared with observation (its power spectrum is too high at small wavelength). Several avenues are taken to remedy that: Warm DM (WDM, where the initial velocity dispersion is not neglected), mixed DM, with some H and CDM, and self interacting CDM, to remedy also the apparently singular density profile produced by CDM simulations compared with some observed flatness of cores of DM haloes (Kravtsov *et al.* 1998 [31]).

2.2 Self-Similar Infall Models

The more specific frame in which this present work is placed is that of the SSIM of a generic CDM halo. In this frame, the study of CDM halo formation focuses on the smooth accretion of mass on one generic halo in the hope that it will yield some insight on any particular halo's characteristics.

It is affiliated with the original work of Gunn & Gott (1972 [30]), which placed infall in the context of accretion of normal matter onto clusters of galaxies. They found that infall would become self-similar and produce a density profile $\rho \propto r^{-\frac{9}{4}}$ in spherical symmetry, similar to Bertschinger (85 [36]). Their work was pursued further by Fillmore and Goldreich (Fillmore & Goldreich,84 [35])with spherical, cylindrical and planar symmetries. Fillmore & Goldreich found that there was a one-sided attractor power law $\rho \propto r^{-2}$ for the SSIM density profile when the initial density is flatter than the attractor.

Both they and Bertschinger modeled the phase space behaviour of their models as one single winding, eternal, steady, self-similar stream of particles. More recently, an N-

[3]As previously stated, isothermal refers here to the density profile leading to a flat rotation velocity curve.

body three-dimensional simulation by Moutarde *et al.* (95 [39]) showed that CDM haloes whatever their initial conditions develop a self-similar infall determined at the turnaround radius of each bound particle[4], which is not a mean behaviour but more a generic pattern for collisionless collapse of smooth initial density profiles. This is not so surprising as it is a defining feature of self-similarity to arise as an intermediate asymptotic state, in flows and collapses where the system is far from its initial condition and boundary constraints that could force a preferred scale of any kind on the evolution (for a discussion of self-similarity, see Henriksen [40]). In their SSIM, Henriksen & Widrow (HW97 [41], HW99 [42]) confirmed the tendency to self-similarity by monitoring a collapse from Hubble flow using revealing self-similar sets of variables following the method developed by Carter & Henriksen (91 [43]).

On the front of cosmology meanwhile, the formalism of the autocorrelation function (ξ) and the power spectrum was being developed. Hoffman & Shaham (Hoffman & Shaham,85 [37]) made an attempt at linking the SSIM initial conditions to the power spectrum by postulating $\rho \propto \xi$ (taking the spherically averaged ξ)(see also Hoffman 88 [38]). More recently, another scheme for generation of initial density from the power spectrum was used (HW95 [44], HW97 [41], HW99 [42], Subramanian *et al.* 99a [45], Subramanian 99b [46]). From the definition

$$FT^{-1}(P(k)) = \xi(x) = \langle \delta\rho.\delta\rho_{+x} \rangle \cong \langle \delta\rho^2 \rangle \propto \sqrt{\delta\rho^2}^2, \tag{2.3}$$

coming from variance of the gauβian distribution of the fractional density contrast averaged over a comoving sphere of radius x (c.f. Peebles 1980 [21]), the initial profile is taken to be $\delta\rho \propto \sqrt{\xi}$. Others have taken more complex routes from P to ρ like the Bardeen *et al*, 86 correspondence between ρ and ξ (Ryden & Gunn 87 [47] , del Popolo *et al.* 2000 [48]), the use of the PS excursion set formalism in order to get the mass spectrum of initial perturbations (e.g. Avila-Reese *et al.* 99 [49]), generalisations of the Hoffman & Shaham,85 method (see Lokas 2000 [50]) or even the use of a more complex P(k) than just $P(k) \propto k^n$ (as in Sikivie *et al.* 97 [51] where a full CDM power spectrum is used). Some authors (Subramanian *et al.* 99a [45], Subramanian 99b [46]) even examined other background cosmological settings than the Einstein-de Sitter, $\Omega = 1$, which usually embeds the SSIM.We will use the HW99 conventions with an Einstein-de Sitter background for the course of this work.

The evolution of the halo is then usually carried out by a semi-analytic Lagrangian N-body treatment (Hoffman & Shaham,85 [37], Hoffman 88 [38], White & Zaritsky 92 [52], Ryden 93 [53], HW97 [41], Avila-Reese *et al.*. 99 [49], HW99 [42], del Popolo *et al.* 2000 [48] and in the present work). Some works (e.g. Fillmore & Goldreich,84 [35],

[4]The turnaround radius of a mass particle is the distance to the centre of its final englobing halo at the moment it is breaking away from cosmological expansion and starting to fall towards the halo.

Bertschinger 85 [36]) assume self-similarity and iterate the solutions to the equations of motion until convergence. Others use adiabatic invariants in iterative methods (Ryden & Gunn 87[47], Sikivie *et al.* 97[51], Lokas 2000 [50]). Alternately, some treat the SSIM as a statistical fluid from its phase space density and through the Collisionless Boltzmann's Equations (CBE), also termed Vlasov equations (HW95 [44], HW97 [41], Teyssier *et al.* 97 [54], HW99 [42], and Subramanian *et al.* 99a [45] and 99b [46]).

Early versions of the SSIM were criticised for assuming that the infall would be self-similar, as was the case in Fillmore & Goldreich,(84) or Bertschinger , or for imposing a spherical symmetry, which is highly unrealistic in regards of the commonly accepted repeated merger formation paradigm.

As an answer to these criticisms, some authors allowed for the evolution to start from non-self-similar conditions (White & Zaritsky 92 [52], Ryden 93 [53], HW95 [44], HW97 [41], Avila-Reese *et al.* 99 [49], HW99 [42], del Popolo *et al.* 2000 [48]) and even attempted to include the effects of non-radial velocities (rotation) which are excluded at first by the spherical symmetry. Some responded by just allowing for transverse velocity dispersions (Subramanian *et al.* 99a[45] and 99b [46]), others by including angular momentum in the dynamics and/or energetics of the problem (Ryden & Gunn 87 [47], White & Zaritsky 92 [52], Ryden 93 [53], Sikivie *et al.* 97 [51], Avila-Reese *et al.* 99 [49]) or hinting at its effects as a modification of the Phase-Space dimensionality of the system ([54] with the clarification of the effect of transverse velocity dispersion from Tormen *et al.* 97 [55]).

This overview of the current status of the SSIM does not pretend to be exhaustive, but to touch on the most burning issues addressed by the model.

Chapter 3

The Self-Similar Infall Model

3.1 The SSIM theoretical background:

> You never understand the
> mathematics
> You just get used to it.
>
> JOHANN VON NEUMANN
> (1903-1957)

This section will be devoted to the development of the formalism engaged in the description of the SSIM. The value of using the Carter & Henriksen,(91) formalism is threefold: we expect self-similarity to arise as an intermediate asymptote. The physics of systems which are not strongly constrained by initial or boundary conditions has displayed an asymptotic approach to self-similar behaviour for restricted regions of space and time far from the influence of those boundaries and set ups. The Carter & Henriksen frame allows us to describe any system in terms which are stationary (in the case of a time dependent system) when the evolution is self-similar without presuming in advance its self-similarity. Lastly, this description allows for an accurate numerical treatment of the system over several orders of magnitude during the self-similar phase of evolution.

The spherical system will be described as a hierarchy of cocentered spherical shells. The equations of motion will be shown in their simplicity before shell-crossing but a statistical approach is needed to follow the system beyond that point. This more fundamental approach will yield again the equations of motion, density and mass conservation equations, and a Virial-type theorem will be derived in this spherical symmetric case with angular momentum. Because of the self-similarity involved in the model, a set of special variables following the Carter & Henriksen,(91) formalism will be derived and

the statistical moment hierarchy of equations will follow up to a self-similar form of the virial theorem. Because of the obscurity of the meaning of some terms in the self-similar virial equation, a Cartesian, 3-dimensional version of this self-similar hierarchy will be displayed from some notes by Henriksen [96].

3.1.1 Presentation of the problem

Classical mechanics

The SSIM starts with the assumption of self-gravitating dust. Then spherical symmetry is imposed on the system. In terms of Newton's law, spherical symmetry allows the Gauβ theorem to simplify the dynamics as a one-dimensional system of encased spherical, infinitely thin shells taken as dynamical units, interacting with all the mass underneath them

$$a_{shell} = -\frac{GM_{under\ shell}}{r^2_{shell}}. \tag{3.1}$$

Before shell-crossing (that is as long as the dynamics of neighbouring spherical shells do not lead them to cross radial positions), the inside mass is constant and the linear regime is just free fall under the influence of that mass. This simple picture gets much more complex after shell-crossing, since the inside mass varies, sometimes drastically, which is where the relaxation takes place, as we will see. The origin of Eq.(3.1) can be taken from the more fundamental concept of gravitational potential, introducing Poisson's equation in the dynamics of the system:

$$\left\{ \begin{array}{c} a_{shell} = -\nabla\Phi = -\frac{\partial\Phi}{\partial r} \\ \Delta\Phi = \frac{1}{r^2}\frac{\partial}{\partial r}\left(r^2\frac{\partial\Phi}{\partial r}\right) = 4\pi G\rho \end{array} \right\}, \tag{3.2}$$

where ρ is the mass volume-density at the shell, being constant on one shell. Eqs.(3.2) can be recognised merely as the Lagrange equations for such a system with the angular momentum j^2 set to 0 (see appendix B). Another approach is to consider the more fundamental statistical mechanics of the system, developing the work started by Henriksen [95].

Statistical treatment

This section will be dedicated to the extension of the Collisionless Boltzmann's Equation and its moments hierarchy to spherical symmetry with angular momentum.

In this context, the new fundamentals are the Probability Distribution Function (PDF: phase space mass density), f (which in general depends on time t and phase space position), and the gravitational potential, Φ, and the governing equations are the Collisionless

Boltzmann's Equation (CBE), also referred to as the Vlasov Equation, and the Poisson field equation:

$$\begin{array}{c} \frac{df(\vec{x},\vec{v},t)}{dt} = 0 \Leftrightarrow \partial_t f + \partial_{\vec{v}} H.\partial_{\vec{x}} f - \partial_{\vec{x}} H.\partial_{\vec{v}} f = 0 \\ \Delta\Phi = 4\pi G\rho = 4\pi G \int f d\vec{v} \end{array} \tag{3.3}$$

where H is the specific Hamiltonian (i.e. per unit mass) of the system.

In spherical symmetry, the specific Hamiltonian becomes (see appendix B)

$$H = \frac{1}{2}\left(v_r^2 + \frac{j^2}{r^2}\right) + \Phi$$

(recall that the norm squared $j^2$is constant because of the symmetry). Then Eqs.(3.3) can be rewritten using the definitions of the canonical distribution function $f \equiv \frac{F}{8\pi^2 r^2}\delta(\vec{j}^2 - j^2)$ (in the case of non-pure-radial-motion, one can replace $F(r,v_r)\delta(\vec{j}^2 - j^2)$ by $F(r,v_r,j^2)$) and the linear radial density $\nu \equiv 4\pi r^2 \int f d\vec{v} = \int F dv_r (dj^2)$ (with these definitions,

$$\rho = \frac{1}{4\pi r^2}\nu \tag{3.4}$$

is the relation between the usual volume density and the linear radial density):

$$\partial_t F + v_r \partial_r F + \left(\frac{j^2}{r^3} - \partial_r \Phi\right)\partial_{v_r} F = 0 \tag{3.5}$$

$$\partial_r\left(r^2 \partial_r \Phi\right) = G \int F dv_r dj^2 \tag{3.6}$$

(For the absence of j derivatives coming from the conservation of j^2, see Fujiwara 83 [91]). These last equations are given in the non-zero angular momentum case but setting $j^2 = 0$ and using the alternate definition of F yields the pure radial case.

Continuity Integrating Eq.(3.5) over the radial velocity, that is taking its zeroth moment, allows one to derive the equation of continuity for that system:

$$\partial_t \nu + \partial_r\left(\nu \overline{v_r}\right) = 0, \tag{3.7}$$

using the definition of the first order from the general expression

$$\nu \overline{v_r^n} = \int v_r^n F dv_r. \tag{3.8}$$

The surface terms in Eq.(3.7) vanish since the integration of Eq.(3.5) runs from $-\infty$ to ∞ and F vanishes at infinity.

Euler's equation The first moment of Eq.(3.5) ($\int v_r CBE dv_r$), with the help of the second order of Eq.(3.8) and some Integration By Parts (on the last term), is the dynamical equation of the fluid of massive shells characterised by the probability given by the PDF:

$$\partial_t \left(\nu \overline{v_r}\right) + \partial_r \left(\nu \overline{v_r^2}\right) - \nu \left(\frac{j^2}{r^3} - \partial_r \Phi\right) = 0, \tag{3.9}$$

where again the surface terms vanish.

Mass conservation Examining the definition of mass inside a given radius, we can relate that mass to the PDF:

$$M(r) = \int_0^r dr 4\pi r^2 \rho(r) = \int_0^r dr \nu(r) = \int_0^r dr \int_{\Re} dv_r F. \tag{3.10}$$

So the integral of (3.7) over the radius range should yield the mass conservation:

$$\frac{dM(r)}{dt} = \left[\nu \overline{v_r}|_0 - \nu \overline{v_r}|_r\right] = -\nu \overline{v_r}|_r ,$$

hence the flux through radius r determines the mass conservation: at the edge of isolated systems, the mass is conserved.

Virial Theorem The Same operation performed on Eq.(3.9) leads to a form of the Virial Theorem in these symmetry conditions.

First, the definitions of several terms are needed: from the integration of Eq.(3.6) and the definitions (3.10) and (3.4) the *gravitational energy* can be extracted, using the Chandrasekhar definition (e.g. in Binney & Tremaine [87] Eq.(2-123) and, for spherical symmetry, Eq.(2-128)):

$$r^2 \partial_r \Phi = GM(r)$$

$$-W = \int dr \nu r \partial_r \Phi = \int dr r 4\pi \rho G M \tag{3.11}$$

The radial Kinetic energy follows:

$$K = \frac{1}{2} \int dr \nu \overline{v_r^2} = T + \frac{1}{2}\Pi \tag{3.12}$$

with

$$T = \frac{1}{2} \int dr \nu \overline{v_r}^2, \tag{3.13}$$

$$\sigma_{v_r^2} = \overline{v_r^2} - \overline{v_r}^2$$

and

$$\Pi = \int dr \nu \sigma^2_{v_r^2}. \tag{3.14}$$

Here we have to define the angular Kinetic energy:

$$L_{kin} = \int dr \nu \frac{j^2}{r^2} = \int dr 4\pi\rho j^2 = 4\pi \overline{j^2} M(r) \tag{3.15}$$

where

$$M\overline{j^2} = \int dr \rho j^2.$$

Finally the moment of inertia of the system is defined according to

$$I = \int \rho r^2 d^3x = 4\pi \int \rho r^4 dr = \int \nu r^2 dr. \tag{3.16}$$

Then one can rewrite the evolution of the moment of inertia using Eq.(3.7) and Integration By Parts and retaining the surface terms:

$$\frac{1}{2}\frac{dI}{dt} = \int dr . r \nu \overline{v_r} - \frac{1}{2} r^2 \nu \overline{v_r}|_r .$$

The Virial equation follows from I's second time derivative, as may be identified in the radial first moment of Eq.(3.9): identifications of terms from Eqs. (3.11), (3.15) and (3.12) can be made directly or after an Integration By Parts, for the kinetic energy, yielding some more surface terms:

$$\frac{1}{2}\frac{d^2 I}{dt^2} = 2T + \Pi + L_{kin} + W - \frac{1}{2}\frac{d}{dt}\left(r^2 \nu \overline{v_r}|_r\right) - r \nu \overline{v_r^2}\Big|_r . \tag{3.17}$$

For a self-gravitating, isolated system at equilibrium, a form of the Virial Theorem emerges: the isolation condition cancels the surface terms, the equilibrium statement cancels the derivatives of time and a new definition of total kinetic energy

$$K_{tot} = T + \frac{1}{2}\Pi + \frac{1}{2}L_{kin}$$

yields the Virial ratio:

$$\frac{2K_{tot}}{W} = -1.$$

This shows that an equilibrium system can be detected by measuring its Virial ratio. This remark will prove to be important later.

3.1.2 The Self-Similar Scaling Variables

Self-Similarity is a property exhibited by many systems, when no preferred scale is imposed on them by initial conditions or boundary conditions. It therefore arises often as an intermediate stage of evolution, and in intermediate regions: far from the influence

of initial conditions, and remote from the scale imposition by the boundaries of the system. Hence, we expect the SSIM to undergo an intermediate self-similar phase. In order to simplify the treatment of the system, self-similar rescaling variables, which make the description stationary, are used. They are generated using the formalism of Carter & Henriksen,(91)[43], more simply stated in [40]. In order to expose the extent of the power of such formalism, and to give insight into self-similar conservation equations, we will consider the full 3-dimensional description of a self-gravitating system. But first we will use that formalism on the restriction of the problem to the spherically-symmetric-with-angular-momentum case and describe the procedure in detail.

Spherical symmetry with angular momentum

We start with the Collisionless Boltzmann's Equation and Poisson's equations (Eqs. (3.5) and (3.6)).

The self-similar variables The following subsection is an attempt at stating simply the non-trivial roots for the self-similar variables and can be mostly ignored on a first reading.

The system's phase space can be broken down into four components

$$\left(t,\ r,\ v_r,\ j^2 \right).$$

The corresponding Dimensions Lie Algebra is then

$$\left(\textit{time},\ \textit{radius},\ \textit{radial velocity},\ \textit{angular momentum},\ \textit{mass} \right) \equiv \left(t,\ r,\ v_r,\ j^2,\ m \right)$$

and the element of this rescaling Lie Algebra, which also can be viewed as the element of the generated additive (logarithmic) rescaling Abelian group, can be written as

$$a = \left(\alpha\ \ \delta\ \ \nu\ \ \lambda\ \ \mu \right).$$

Of course, this Dimensional[1] manifold is not necessarily made of independent components: radial velocity and angular momentum are fundamentally functions of length and time, so are related to t and r, and physical constants of the problem may impose some additional relationships between components of a (e.g. Newton's constant G brings about a relation between at least time and length). Keeping dependent quantities in the

[1] **We will use the notations from Carter & Henriksen,(91) [43] to distinguish between geometrical dimensions and Physical measurement units, also called Dimensions, by the use of a lower case d for anything related to the geometrical dimensions and an upper case D for the unit related Dimensions.**

dimensionality of the Dimensions Algebra can be convenient for dealing with the extra dependent types of quantities.

In this context, rescaling corresponds just to moving about in the Dimensional manifold. Imposing self-similarity corresponds to fixing the direction of displacement a. Each physical quantity F is represented in the Lie Algebra by a 'Lie Dimensionality covector' $d_F = \begin{pmatrix} d_{F1} & d_{F2} & d_{F3} & d_{F4} & d_{F5} \end{pmatrix}$ corresponding to the traditional Dimensional analysis of F. It is a measure of the sensitivity of F to rescaling in each of the Lie Algebra components. The progression of the system along a translates into the rescaling of F by incrementing additively its logarithm by an amount given by the scalar product

$$a.d_F \equiv \alpha d_{F1} + \delta d_{F2} + \nu d_{F3} + \lambda d_{F4} + \mu d_{F5}$$

which means that the Lie derivative of F satisfies

$$kLF = (a.d_F)F \tag{3.18}$$

with the multiplicative version of kL instead of the logarithmic one so that

$$kL \equiv \alpha t\partial_t + \delta r\partial_r + \nu v_r\partial_{v_r} + \lambda j^2\partial_{j^2} + \mu m\partial_m \tag{3.19}$$

or in other words

$$k \equiv e^a.$$

From Dimensional analysis of the gravitational potential and the constancy of G, one can indeed find several relations between the Lie Dimensions

$$d_G + d_m - d_r = d_{v^2} = 2d_{v_r} = d_{E_{specific}} = d_{r^2/t^2} = 2d_r - 2d_t \tag{3.20}$$

so the covector d_G can be expressed as

$$d_G = \begin{pmatrix} 0, & 1, & 2, & 0, & -1 \end{pmatrix}$$

but also as

$$d_G = \begin{pmatrix} -2, & 3, & 0, & 0, & -1 \end{pmatrix}$$

since we can find from Eqs.(3.20) that

$$d_{v_r} = d_r - d_t \Leftrightarrow \nu = \delta - \alpha. \tag{3.21}$$

Likewise, the analysis of the definition for angular momentum yields the equation

$$d_{j^2} = d_{r^2v^2} = 2d_r + 2d_{v_r} = 4d_r - 2d_t \Leftrightarrow \lambda = 4\delta - 2\alpha. \tag{3.22}$$

Then, if G is a constant of Nature, it cannot be affected by any change, least of which would be the rescaling of measurement units:

$$kLG = 0 \Rightarrow \mu = 2\nu + \delta = 3\delta - 2\alpha$$

Keeping in mind these relations, we can then reduce the dimensionality of the Dimension Algebra to four:

$$a = \begin{pmatrix} \alpha & \delta & \nu & \lambda \end{pmatrix} \in Lie_{Dim}.$$

Searching for a complete set of coordinates for the system in the Lie Algebra, one can always simplify things by choosing one of the coordinates to be measured along the direction k of self-similar motion and the rest of them to be orthogonal to this direction. By normalising the former, and taking into account that since we have a time dependent system, it is convenient to choose an oblique time to measure the self-similar displacement, one can then write:

$$kLT = 1 \tag{3.23}$$

for the self-similar time, and

$$kLX^i = 0,\ i \in [1; dim(Lie_{Dim}) - 1] \tag{3.24}$$

(with $\dim(\mathrm{Lie}_{Dim}) = 4$ here) for the other coordinates. It is remarkable that these other coordinates then are invariant under rescaling by construction and therefore a scale invariant system described by them would be "time"-independent (using the self-similar time).

Now using the definition of Eq.(3.19) and our choice of measuring the self-similar direction with an oblique time (T=T(t)), we can get from Eq.(3.23)

$$\alpha t \partial_t T = 1 \Rightarrow e^{\alpha T} = |\alpha' t| \Leftrightarrow T = \frac{1}{\alpha} \ln |\alpha' t|, \tag{3.25}$$

and from Eqs.(3.24) comes the general form that each self-similar variable follows,

$$\alpha t \partial_t X^i + \delta r \partial_r X^i + \nu v_r \partial_{v_r} X^i + \lambda j^2 \partial_{j^2} X^i = 0,$$

which can be solved by the method of characteristics[2]:

$$\frac{dt}{\alpha t} = \frac{dr}{\delta r} = \frac{dt}{\nu v_r} = \frac{dj^2}{\lambda j^2}$$

[2]This method transform the P.D.E. into O.D.E.s by postulating underlying characteristic curves along which separate parameters can be held constants (or evolving according to the O.D.E.):

$$\alpha t \partial_t + \delta r \partial_r + \nu v_r \partial_{v_r} + \lambda j^2 \partial_{j^2} = \frac{\partial t}{\partial \xi^i}\partial_t + \frac{\partial r}{\partial \xi^i}\partial_r + \frac{\partial v_r}{\partial \xi^i}\partial_{v_r} + \frac{\partial j^2}{\partial \xi^i}\partial_{j^2} = d_{\xi^i}.$$

Each of these allow to write the strings of equations

$$d\xi^i = \frac{dt}{\frac{\partial t}{\partial \xi^i}} = \frac{dr}{\frac{\partial r}{\partial \xi^i}} = \cdots$$

yields 3 independent equations.

The first can be chosen to involve the time and radius terms, the second, time and radial velocity and the third, time and angular momentum:

$$\frac{|\alpha' t|^{\frac{\delta}{\alpha}}}{r} = cst\ along\ characteristic\ curve = \varsigma$$

$$\frac{|\alpha' t|^{\frac{\nu}{\alpha}}}{v_r} = cst\ along\ characteristic\ curve = \xi$$

$$\frac{|\alpha' t|^{\frac{\lambda}{\alpha}}}{j^2} = cst\ along\ characteristic\ curve = \eta$$

so each value of the three parameters fixes the one-dimensional characteristic curve along which each solution lives:

$$X^i = X^i(\varsigma, \xi, \eta)$$

the functions X^i being a priori arbitrary. We can then choose their dependences, and name the self-similar variables, in this case:

$$\begin{aligned}(X^1)^{-1} = X^{-1} = \varsigma &= \frac{|\alpha' t|^{\frac{\delta}{\alpha}}}{r} \\ (X^2)^{-1} = Y^{-1} = \xi &= \frac{|\alpha' t|^{\frac{\nu}{\alpha}}}{v_r} \\ (X^3)^{-1} = Z^{-1} = \eta &= \frac{|\alpha' t|^{\frac{\lambda}{\alpha}}}{j^2}\end{aligned}$$

which can be rewritten using Eq.(3.25) as

$$\begin{aligned} r &= Xe^{\delta T} \\ v_r &= Ye^{\nu T} \\ j^2 &= Ze^{\lambda T} \end{aligned} \tag{3.26}$$

to complete the set of self-similar phase-space variables.

Self-similar form for the equations The choice we made of a self-similar time (Eq.(3.23)) simplifies any further form for physical quantities: because

$$kLT = 1 \Leftrightarrow kL \equiv \frac{\partial}{\partial T}, \tag{3.27}$$

any quantity g which satisfies Eq.(3.18) and therefore, from Eq.(3.27), admits solutions in the form

$$g = e^{(a.d_g)T}\overline{g}(X, Y, Z), \tag{3.28}$$

is said to have a self-similar behaviour (in Eq. (3.28), $\overline{g}$ only depends on variables which are invariant under the rescaling a). In general, a non-self-similar system depends on all

variables ($\overline{g}(T,X,Y,Z)$) but choosing this set will allow demonstrating the occurrence of self-similarity in the form of stationarity.

To obtain Eqs. (3.5) and (3.6) in self-similar form, all the physical quantities must be re-expressed according to Eq.(3.28), for instance the distribution function and the gravitational potential read, from their Dimensions covectors

$$d_F = \begin{pmatrix} 0, & -1, & -1, & -1, & 1 \end{pmatrix} \equiv \begin{pmatrix} 0, & 0, & 1, & -1 \end{pmatrix} \equiv \begin{pmatrix} 1, & -3, & 0, & 0 \end{pmatrix}$$
$$d_\Phi = \begin{pmatrix} 0, & 0, & 2, & 0 \end{pmatrix} = \begin{pmatrix} -2, & 2, & 0, & 0 \end{pmatrix}$$

as follows:

$$F = e^{(\nu-\lambda)T}\overline{F} = e^{-(3\delta-\alpha)T}\overline{F}$$
$$\Phi = e^{2\nu T}\overline{\Phi} = e^{2(\delta-\alpha)T}\overline{\Phi}$$

In addition, the derivatives of the problem must be re-expressed in the new coordinate system using the chain rule:

$$\partial_{x^i} = \frac{\partial T}{\partial x^i}\partial_T + \frac{\partial X}{\partial x^i}\partial_X + \frac{\partial Y}{\partial x^i}\partial_Y + \frac{\partial Z}{\partial x^i}\partial_Z$$

with

$$e^{-T} = |\alpha' t|^{-\frac{1}{\alpha}} \Leftrightarrow T = \frac{1}{\alpha}\ln|\alpha' t|$$

so

$$\begin{aligned} X &= re^{-\delta T} = r\,|\alpha' t|^{-\frac{\delta}{\alpha}} & T &= \tfrac{1}{\delta}\ln\tfrac{r}{X} \\ Y &= v_r e^{-\nu T} = v_r\,|\alpha' t|^{-\frac{\nu}{\alpha}} \ \textit{but also} & &= \tfrac{1}{\nu}\ln\tfrac{v_r}{Y} \\ Z &= j^2 e^{-\lambda T} = j^2\,|\alpha' t|^{-\frac{\lambda}{\alpha}} & &= \tfrac{1}{\lambda}\ln\tfrac{j^2}{Z} \end{aligned}$$

The derivatives then read

$$\begin{aligned} \partial_t|_{r,v_r,j^2} &= \tfrac{1}{\alpha|t|}\partial_T - \tfrac{\delta}{\alpha|t|}X\partial_X - \tfrac{\nu}{\alpha|t|}Y\partial_Y - \tfrac{\lambda}{\alpha|t|}Z\partial_Z \\ &= \tfrac{|\alpha'|}{\alpha}e^{-\alpha T}\left(\partial_T - \delta X\partial_X - \nu Y\partial_Y - \lambda Z\partial_Z\right) \\ \partial_r|_{t,v_r,j^2} &= e^{-\delta T}\partial_X \\ \partial_{v_r}|_{t,r,j^2} &= e^{-\nu T}\partial_Y \\ \partial_{j^2}|_{t,r,v_r} &= e^{-\lambda T}\partial_Z \end{aligned}$$

The last three derivatives are justified in the previous equations by the fact that at t maintained constant, Eq.(3.25) impiies that T is also maintained constant.

Using these new coordinates and physical quantities, the Collisionless Boltzmann's Equation then reads:

$$\frac{|\alpha'|}{\alpha}e^{-\alpha T}\left(\partial_T - \delta X\partial_X - \nu Y\partial_Y - \lambda Z\partial_Z\right)\left(e^{(\nu-\lambda)T}\overline{F}\right) + Ye^{\nu T}e^{-\delta T}\partial_X\left(e^{(\nu-\lambda)T}\overline{F}\right) +$$
$$\left(\frac{Ze^{\lambda T}}{X^3e^{3\delta T}} - e^{-\delta T}\partial_X\left(e^{2\nu T}\overline{\Phi}\right)\right)e^{-\nu T}\partial_Y\left(e^{(\nu-\lambda)T}\overline{F}\right) = 0$$

$$\Leftrightarrow \frac{|\alpha'|}{\alpha}\left(\partial_T + (\nu-\lambda) - \delta X\partial_X - \nu Y\partial_Y - \lambda Z\partial_Z\right)\overline{F} + Y\partial_X\overline{F} + \left(\frac{Z}{X^3} - \partial_X\overline{\Phi}\right)\partial_Y\overline{F} = 0$$

the exponentials being simplified using the correspondences of Eqs. (3.21) and (3.22).The constant of integration α' is then set to $\alpha' = \alpha > 0$ so that the equations can display their almost self-similar form (this convention will hold for the rest of this work).

$$\Leftrightarrow (\nu-\lambda)\overline{F} + \partial_T\overline{F} + (Y-\delta X)\partial_X\overline{F} +$$

$$\left(\frac{Z}{X^3} - \partial_X\overline{\Phi} - \nu Y\right)\partial_Y\overline{F} - \lambda Z\partial_Z\overline{F} = 0. \tag{3.29}$$

[3] And the Poisson's equation is rewritten as

$$e^{-\delta T}\partial_X\left(X^2 e^{2\delta T}e^{-\delta T}\partial_X(e^{2\nu T}\overline{\Phi})\right) = G\int_{\Re_Y\Re_Z^+} e^{(\nu-\lambda)T}\overline{F}e^{\nu T}dY e^{\lambda T}dZ$$

the exponentials simplify naturally to yield

$$\Longleftrightarrow \partial_X\left(X^2\partial_X\overline{\Phi}\right) = G\int_{\Re_Y\Re_Z^+}\overline{F}dY dZ. \tag{3.30}$$

Moments *For this next section, the overbars on self-similar functions can be dropped, keeping in mind that we are dealing with rescaled functions, so that we can use the overbar to mean the usual average over velocities.*

In parallel to Eq.(3.8), the nth self-similar moments of the self-similar velocity Y or angular momentum Z, weighted with the self-similar PDF define the radial self-similar density and velocity moments:

$$\Gamma = \int dY dZ F = 4\pi r^2\rho e^{-(\nu-\lambda)T}e^{-\nu T}e^{-\lambda T} = 4\pi r^2\rho e^{-2\nu T}, \tag{3.31}$$

$$\Gamma\overline{Y^n} = \int dY dZ Y^n F = 4\pi r^2\rho e^{-(n+2)\nu T} \tag{3.32}$$

[3]Note that the characteristic curves of the CBE without angular momentum and during the self-similar infall phase ($\partial_T\overline{F} = 0$) are close to the energy contours:

$$\begin{cases} \frac{dX}{d\epsilon} = Y - \delta X \equiv p \\ \frac{dY}{d\epsilon} = -\left(\nu Y + \frac{d\overline{\Phi}}{dX}\right) \end{cases} \Rightarrow$$

$$\frac{d}{dX}\left(\frac{p^2}{2}\right) + (2\delta-1)p + \frac{d}{dX}\left(\overline{\Phi} + \frac{\delta(\delta-1)}{2}X^2\right) = 0 = \frac{d\epsilon}{dX}$$

and this is close to the derivative of form

$$E = \frac{Y^2}{2} + W_\bullet(X).$$

and

$$\Gamma\overline{Z^n} = \int dY dZ.Z^n F = 4\pi r^2 \rho e^{-(n\lambda+2\nu)T} = 4\pi r^2 \rho e^{-(n\delta+[n+2]\nu)T}. \tag{3.33}$$

Using these definitions, the integrations of the moments of Y weighted by the self-similar Collisionless Boltzmann's Equation are yielding the usual equations in self-similar form.

The zeroth moment gives the self-similar continuity equation:

$$(\partial_T \Gamma + 2\nu\Gamma - \delta X \partial_X \Gamma) + \partial_X(\Gamma\overline{Y}) = 0. \tag{3.34}$$

The first Y moment yields the self-similar Euler equation:

$$\left(\partial_T(\Gamma\overline{Y}) + 3\nu\Gamma\overline{Y} - \delta X \partial_X(\Gamma\overline{Y})\right) + \partial_X(\Gamma\overline{Y^2}) - \Gamma\frac{\overline{Z}}{X^3} + \Gamma\partial_X\Phi = 0. \tag{3.35}$$

Integrating of Eq.(3.34) with X gives the self-similar mass conservation equation:

$$\frac{dM}{dT} + (3\delta - 2\alpha)M - \left(\delta - \overline{Y(1)}\right)\Gamma(1) = 0, \tag{3.36}$$

where we have defined the self-similar mass naturally as

$$M = \int_0^1 dX.\Gamma, \tag{3.37}$$

and we have chosen arbitrarily the boundary of the system to be at X=1.

With the Energy definitions parallel to Eqs. (3.12), (3.15) and (3.11),

$$K = \frac{1}{2}\int_{0,\Re_Y\Re_Z^+}^1 dX dY dZ.F(Y^2 + \frac{Z}{X^2}) = \frac{1}{2}\int_{0,\Re_Y\Re_Z^+}^1 dX\Gamma\left(\overline{Y^2} + \frac{\overline{Z}}{X^2}\right) \tag{3.38}$$

and

$$W = -\int_0^1 dX.X\int_{\Re_Y\Re_Z^+} dY dZ.F\partial_X\Phi = -\int_0^1 dX.X\Gamma\partial_X\Phi$$

$$= -\int_0^1 dX\int_{\Re_Y\Re_Z^+} dY dZ\int_0^X dX'\int_{\Re_{Y'}\Re_{Z'}^+} dY' dZ'.G\frac{F(X,Y,Z)F(X',Y',Z')}{X}, \tag{3.39}$$

the last step using an integrated version of self-similar Poisson's equation to write W in terms of the fundamental functions of the problem, and the moment of inertia definition

$$I = \int dX dY dZ.X^2 F = \int dX.X^2\Gamma, \tag{3.40}$$

one can write the self-similar Virial equation from the integration $\int_0^1 dX.X^*$Eq.(3.35)

$$\frac{1}{2}\left[\frac{d^2I}{dT^2} + 5(2\delta - \alpha)\frac{dI}{dT} + (5\delta - 3\alpha)(5\delta - 2\alpha)I\right] - \delta\Gamma(1)\overline{Y}(1) =$$

$$2K + W + \frac{1}{2}\left[\frac{d^2M}{dT^2} - (2\delta - \alpha)\frac{dM}{dT} + (5\delta - 3\alpha)(3\delta - 2\alpha)M\right]. \tag{3.41}$$

When the system is in self-similar phase, our set of variable translating it into having no T dependence for any physical quantity, the derivatives vanish and we are left with a Virial ratio $-\frac{2K}{W}$ which is not 1 but higher. The surface terms are not of simple interpretation, but they translate the fact, pointed out in the self-similar limit of Eq.(3.36), that the self-similar phase requires a non-zero flux of mass at the boundary of the system. In other words, the self-similar phase is driven by the infall of mass into the core. To reach a more clear picture of the nature of those surface terms it is necessary to get back to the full-blown 3-dimensional expression of the problem.

General non-spherically symmetric case

Using the same method as in section 3.1.2, we can derive the forms of the self-similar variables as well as the self-similar PDF and the self-similar potential:

$$\begin{aligned} \alpha' t &= e^{\alpha T} \\ \underline{r} &= \underline{X} e^{\delta T} \\ \underline{v} &= \underline{Y} e^{\nu T} \end{aligned},$$

where, as in 3.1.2, $\nu = \delta - \alpha$ and $\mu = 3\delta - 2\alpha$, and

$$\begin{aligned} f = \overline{f} e^{-(3\delta-\alpha)T} \quad &, \overline{f} = \overline{f}(T, \underline{X}, \underline{Y}) \\ \Phi = \overline{\Phi} e^{2\nu T} \quad &, \overline{\Phi} = \overline{\Phi}(T, \underline{X}) \end{aligned}.$$

Using these we can write the self-similar Collisionless Boltzmann's Equation and the self-similar Poisson's equation (again, we take $\alpha' = \alpha > 0$):

$$\partial_T \overline{f} - (3\delta - \alpha)\overline{f} + (\underline{Y} - \delta \underline{X}).\partial_{\underline{X}} \overline{f} - \left[(\delta - \alpha)\underline{Y} + \partial_{\underline{X}} \overline{\Phi}\right].\partial_{\underline{Y}} \overline{f} = 0 \tag{3.42}$$

$$\nabla^2_{\underline{X}} \overline{\Phi} = 4\pi G \int \overline{f} d^3 \underline{Y}. \tag{3.43}$$

Thus, with the definitions of self-similar density and mass and of the moments of the velocity weighted with the PDF,

$$\overline{\rho} = \int \overline{f} d^3 \underline{Y}, \tag{3.44}$$

$$\overline{M} = \int \overline{\rho} d^3 \underline{X} \tag{3.45}$$

and

$$\overline{\rho \underline{Y}^n} = \int \overline{f} \underline{Y}^n d^3 \underline{Y}, \tag{3.46}$$

(the overbar form Y signifying here averaging over the velocity space), the integration over velocities of Eq.(3.42) yields the self-similar continuity equation:

$$\partial_T \overline{\rho} + (3\delta - 2\alpha)\overline{\rho} + \partial_{\underline{X}}.\left(\overline{\rho}(\underline{\overline{Y}} - \delta\underline{X})\right) = 0. \tag{3.47}$$

Likewise, the integration of that equation over space is the mass conservation equation:

$$d_T\overline{M} + (3\delta - 2\alpha)\overline{M} + \oint \overline{\rho}(\underline{\overline{Y}} - \delta\underline{X}).d\underline{\underline{S}}_{\underline{X}} = 0. \tag{3.48}$$

It is to be noted that the two first terms of Eq.(3.48) are equivalent to writing the real mass conservation without sources ($\partial_t M = 0$). This points out the primordial role of the last term, a modified self-similar flux of mass across the boundaries of the system, in maintaining the self-similarity (when $d_T\overline{M} = 0$).

From now on we can drop the overbars as a sign of scaled quantities, since we are working only in that frame.

Now the first moment of the Y_j component of velocity over velocity space weighted by the self-similar PDF yields the firsts of Jean's equations, Euler's equations:

$$\partial_T\left(\rho\overline{Y}_j\right) + (\delta - 3\alpha)\rho\overline{Y}_j - \delta\underline{X}.\partial_{\underline{X}}\left(\rho\overline{Y}_j\right) + \partial_{\underline{X}}.\int d^3\underline{Y}f\underline{Y}Y_j + \rho\partial_{X_j}\Phi = 0. \tag{3.49}$$

Then the integration of Eqs.(3.49) times $X_k$over space leads to the Virial tensor equations: using the definitions

$$K_{jk} = \frac{1}{2}\int \rho\overline{Y_jY_k}d^3\underline{X}, \tag{3.50}$$

for the kinetic energy tensor,

$$W_{jk} = -\int \rho X_k\partial_{X_j}\Phi\, d^3\underline{X}, \tag{3.51}$$

for the gravitational potential energy tensor, and

$$I_{jk} = \int \rho X_jX_k d^3\underline{X}, \tag{3.52}$$

for the moment of inertia tensor, one can get

$$\frac{1}{2}\left(\frac{d^2I_{jk}}{dT^2} + 5(2\delta - \alpha)\frac{dI_{jk}}{dT} + (5\delta - 3\alpha)(5\delta - 2\alpha)I_{jk} + \frac{dA_{jk}}{dT} + (5\delta - 3\alpha)A_{jk}\right) = 2K_{jk} + W_{jk} \tag{3.53}$$

where the surface term

$$A_{jk} = \oint X_jX_k\overline{\rho}(\underline{\overline{Y}} - \delta\underline{X}).d\underline{\underline{S}}_{\underline{X}},$$

which trace is just the radius squared of the system times the mass flux across its boundaries seen in Eq.(3.48).

3.1.3 Summary

We have then seen that before shell-crossing (in section 3.1.1), the equations of motion look like the free fall of mass shells on all the shells contained inside their radius. After shell-crossing, we have followed the evolution of the system from the Collisionless Boltzmann's Equation (CBE) which led to the equation of motion in the Eulerian form, the continuity equation, the mass conservation equation and the virial equation. The latter will prove important for the interpretation of the dynamics of the SSIM gravitational collapse: when the system reaches a self-similar state, the self-similar-time derivatives vanish, displaying as in [42] a state of quasi-equilibrium characterised by a modified virial ratio springing out of the self-similar virial equation. The Cartesian representation of the equations points out that the surface terms involved in this self-similar-virial ratio probably correspond to some representation of the mass flux through the boundaries of the system, which then appears as an essential element in maintaining the system self-similar [42].

3.2 Motivations for and Results from the model

Using this frame of self-similar variables and self-similar equations to study the SSIM, we can start, from the previous section's analytical results, to answer some questions of importance that arise from the field of LSS formation: the density profile of Dark Matter haloes and the dynamics of their gravitational collapse. After reviewing the state of the field on density profiles, we will first express the self-similar equations of motion. Then we will relate the other assumptions of the SSIM to its final conditions. Particularly we will relate those initial conditions to the determination of the type of self-similarity that will be used in the self-similar variables in order to approach dynamically the self-similar state. We will first do so, recalling the results from [42] in radial spherical symmetry, then extend them to the presence of angular momentum. In a second section, we will sum up the current approach to the dynamics of the DM gravitational collapse, in terms of PDF.Then we will present the way this work will handle PDFs, as well as the additional tool given by the virial ratio in the understanding of the SSIM's dynamics.

3.2.1 Density profiles

The density profiles of CDM haloes have a direct link with observations of spiral galaxies: their velocity rotation curve (see equation (2.1)) is a direct consequence of the mass density profile that characterises them. It is possible that they contain some information about the dynamics that formed them as well as the cosmological background in which they arose. On one hand they are therefore good constructs for observational falsifications

of both dynamical LSS formation paradigms and global Cosmological geometries. On the other hand, the predictions of any given model should be constrained into explaining the observed shape(s) of density profile(s).

Observations and predictions of the density profile:

The first direction comes from observations and fits that are produced to express them into simple functional forms. One of the first of such efforts was made by de Vaucouleurs (1948 [56]) for the surface density of elliptical galaxies

$$\Sigma \propto e^{-a.r^{\frac{1}{4}}} \Leftrightarrow \rho \propto \frac{e^{-a.r^{\frac{1}{4}}}}{r}. \tag{3.54}$$

It is reproduced in simulations by numerous authors (van Albada 1982 [57], Bertin & Stiavelli 1984 [58], Stiavelli & Bertin 1985 [59], Merritt *et al.* 1989 [60], hereafter MTJ, Aguilar & Merritt 1990 [61]) but most of them are not dealing with collisionless DM.

Most of the fits proposed subsequently, from astronomical observations or from N-body simulations followed the generic form (we will use here the parameter α_p to replace the use of α from the literature for the central logarithmic slope in order to avoid confusion with the time self-similar index previously named α)

$$\rho \propto r^{-\alpha_p} \left(1 + \left(\frac{r}{r_s}\right)^{\gamma}\right)^{-\frac{\beta-\alpha_p}{\gamma}}, \tag{3.55}$$

some of the principal proponents being Jaffe (1983 [62] with $\alpha_p = 2$, $\gamma = 1$ and $\beta = 4$) and Hernquist (1990 [63] with $\alpha_p = 1$, $\gamma = 1$ and $\beta = 4$):

$$\rho \propto r^{-1} \left(1 + \left(\frac{r}{r_s}\right)\right)^{-3}. \tag{3.56}$$

Both fit astronomical observations of galaxies (including their baryonic component)reasonably well. In essence Eq. (3.55) is just a smooth way of joining two power laws: an inner core power law and an outer profile, that can be bluntly characterised by the 'knee' shaped, non-smoothly varying form:

$$\frac{\rho}{\rho_c} = \begin{cases} \delta \left(\frac{r}{r_s}\right)^{-\alpha_p}, & r < r_s \\ \delta \left(\frac{r}{r_s}\right)^{-\beta}, & r > r_s \end{cases} \tag{3.57}$$

More recently, N-body simulations have served as basis for such fitting and one group of collaborators has argued for universal profiles of DM haloes: Navarro *et al.* (hereafter NFW, 1996 [32]) found that the profile

$$\rho \propto r^{-1} \left(1 + \left(\frac{r}{r_s}\right)\right)^{-2}, \tag{3.58}$$

with $\alpha_p = 1$, $\gamma = 1$ and $\beta = 3$, fitted CDM haloes with only one free parameter corresponding to the mass scale of the halo. Although its universality was confirmed by many authors (Moore *et al.* 98a [64], 98b [65], Huss *et al.* 99a [66], 99b [67], Kull 99 [68], using a [Bond, *et al.* (91)]-type approach to the intermediate and far profile, Jing 2000 [69]), its full validity has been questioned from various angles until some serious discrepancies were unavoidable: Jing [69] found it to apply mostly for equilibrium haloes, a scatter ensuing from inclusion of non-equilibrium ones. Moore *et al.* 98a [64] and 98b [65] found that α_p was rising up to 1.4 without converging when N-body resolution was increased. Eventually, Moore *et al.* (1999 [71] hereafter Moore99), followed by Ghigna *et al.* (1999 [72]), prescribed a new form from the convergence they found of N-body simulations with resolution:

$$\rho \propto r^{-1.5}\left(1+\left(\frac{r}{r_s}\right)\right)^{-1.5}, \tag{3.59}$$

with $\alpha_p = 1.5$, $\beta = 3$. Jing & Suto (2000 [70]) reconciled NFW and Moore99 by dividing their mass range validity, finding that clusters were better fitted by the NFW profile, while the Moore99 profile was more adapted to galaxy-mass haloes. Other N-body simulations found strong discrepancies in the inner slope and even in the outer one: Tittley & Couchman (2000 [73]), using Eq. (3.57), find $\alpha_p = 1.8$ and β ranging from 2.4 to 2.7. Voglis (94 [74]) finds $\alpha_p = 2.7$ and $\beta \approx 5$ from Probability Distribution Functions (PDFs). Moutarde *et al.* (95 [39]) find $\alpha_p = 1.8$ and that β steepens from 2 on larger scales. Kravtsov *et al.* 98 [31] found on Low Surface Brightness (LSB) Galaxies and DM dominated Dwarf galaxies that they where fitted well by NFW profile but with a central logarithmic slope much shallower (α_p ranging from 0.2 to 0.4 instead of 1). Their results hold weight because they agree with a few others (e.g. Stil, 1999 [75], and the discussion of these results by Moore, 1994 [76]). This central cusp behaviour opened the door for alternate models as non-collisionless CDM in such studies as Sellwood 2000 [77] and Walker 99 [78]. Moreover some WIMP models' DM annihilations are found to produce too much gamma radiation in the case of steep central cusps compared to observations (Flores & Primack 94 [79]). A few others find a flatter slope than 1 for the inner core, like del Popolo *et al.* [48] and their Bardeen *et al*, 86 initial conditions of the SSIM, which reproduce the outer and intermediate features of NFW. However, it seems that the observational difficulty of extracting inner rotation curves or gravitational lensing information on very small scales might explain these discrepancies: van den Bosch *et al.* (2000 [80]) found that taking into account beam smearing, the density profiles of Low Surface Brightness galaxies are consistent with steep central cusps, in contrast to previous claims. Clearly more observation is needed to decide this issue.

The second direction comes from semi-analytic models like the PS excursion set or the SIM. The aim is then to construct density profiles from first principles and then confront

them with observations (astronomical or N-body). In fact they all derive from the SSIM: as stated in the previous section, the pure SSIM yields power law profiles with a one-sided attractor at $\alpha_{pa} = 2$ for initial profiles shallower than 2 and a continuum of attractors $\alpha_{pa} = \frac{3\alpha_{pi}}{1+\alpha_{pi}}$ for initial power law α_{pi} (FG84 [35], Bertschinger 85 [36], HW95 [44], HW99 [42], with Gunn & Gott [30], Hoffman & Shaham [37], Hoffman 88 [38] as peculiar cases with $\alpha_{pi} = 3$). With the constraints of radial infall and spherical symmetry, the SSIM with its power law initial profile displays signs of oversimplification, when confronted with observed halo formation in N-body simulations. That fact led to the introduction, in order to obtain more realistic density profiles, of angular momentum, more complex initial conditions, and explorations of the SSIM for gas.

Simple addition of angular momentum yields $2 \leq \beta < 3$ for the outer slope (Ryden & Gunn [47], White & Zaritsky [52], Sikivie [51] with $\beta = 2$ for $\alpha_{pi} < 2$).

For the inner slope, the addition of angular momentum modifies the results of the SSIM such that $\alpha_p = 1.5$ (Ryden & Gunn [47] for purely circular orbits only, Ryden 93 [53]) or allows $\alpha_p = \overline{\alpha_p} \in [\alpha_{pa}; 2]$ for $\alpha_{pi} < 2$.

The case $\alpha_p = \alpha_{pa}$ can be found in Sikivie [51]. In Subramanian *et al.* 99a [45], $\alpha_p = 2$ for insufficient transverse velocity dispersion $\sigma_t^2 < \frac{\Phi}{2}$, and $\alpha_p = \alpha_{pa}$ otherwise, with the additional condition of sufficient transverse over radial velocity $\sigma_t^2 > \sigma_r^2$ allowing $\alpha_p = \alpha_{pa}$ to hold even for $\alpha_{pa} < 1$. Similarly, Subramanian *et al.* 99b [46] find $\alpha_p = \alpha_{pa}$ for $\sigma_t \lesssim \sigma_r$ and $\alpha_p = \overline{\alpha_p}$ for $\sigma_t \sim \sigma_r$.

The study of the SSIM for gas led Teyssier *et al.* 97 [54] to find the same attractor continuum but with a limit of $\alpha_{pi} > \frac{1}{2}$ and one-sided limit at $\alpha_p = 1$. This new limit was caused by the change in Phase-Space dimensionality introduced by the isotropisation of the velocity distribution by pressure. Comparing their results with those from isotropic velocity dispersions of Tormen *et al.* 97 [55], they concluded that this flattening with respect to the CDM one-sided attractor could parallel the effect of angular momentum.

More complex initial conditions involve initial density profiles produced by PS excursion set formalism (Nusser & Sheth 99 [81], Avila-Reese *et al.* [49]), by the density from the Bardeen *et al*, 86 version of this formalism (Del Popolo [48]) or density profiles embedded in non Einstein-de Sitter Background cosmologies (Subramanian *et al.* 99a [45]).

Nusser & Sheth (99 [81]) found a central slope between the two extended attractors obtained from the two simpler links given previously between the power spectrum and its autocorrelation function on one hand, and the initial density profile ($\alpha_p \in \left[\frac{3(n+3)}{n+5}; \frac{3(n+3)}{n+4}\right]$), surrounded by the NFW profile. Avila-Reese *et al.* (99 [49]) left aside the inner profile but found that the outer profile depended on mass scale and environment: $\beta \in \left[\ 2\ ;\ 4\ \right]$, with β shallower (≈ 2) for satellites and groups of haloes, the NFW β ($= 3$) applying for isolated haloes and β steeper (≈ 4) for richer clusters of haloes. Del Popolo (00 [48])

managed to reproduce NFW β using a [Bardeen *et al*, (86)]-type spectrum as initial conditions and even finding an α slightly flatter than NFW. Finally, using a fluid approach to the SSIM, Subramanian *et al.* (99a[45]) found $\beta = 4$ in an open CDM model, and even $\beta \to \infty$ ($\rho \propto \sqrt{1 - \left(\frac{r}{r_\lambda}\right)^{\alpha_{pi}}}$ with r_λ the maximum turnaround radius depending on the cosmological constant) in a ΛCDM model.

Interpretation of the formation of the density profile

Understanding the formation of the density profile comes after measuring or producing it in a simulation. This understanding is all the more important in the context of the possibility of a controversial universal profile (the claim for the NFW profile [32], or for the Moore 99 one [71]).

Syer & White (1998 [33]) gave an argument for the NFW universality involving the balance between tidal stripping[4] of absorbed satellite haloes by a larger one while they sink towards its centre under the influence of the second force in balance: dynamical friction[5]. The feedback mechanism between tidal stripping and dynamical friction drives the profile of the halo towards the universal one. This is done under the thrust of repeated mergers by either disseminating the satellite's material by tidal stripping to soften a steeper density than the universal profile, or sinking the satellite's core to the centre of the halo by dynamical friction to steepen a shallower density than that of NFW. Subramanian *et al.* (99a[45]) independently gave a similar argument to come up with a power law profile on a Dimensional analysis basis. In their version of the argument, a nested sequence of undigested cores forms locally $\rho \propto r^{-\frac{3(n+3)}{n+5}}$, even for $n < 1$, where the form of the power law comes from scaling arguments.

The Syer&White argument emphasises the importance of repeated mergers in the process of hierarchical CDM halo formation. Nevertheless, all studies that attempted to assess that claim found that repeated mergers were not necessary: in their model from PDF, Aguilar & Merritt (90 [61]) already found that there was no need for clumpy initial conditions. Later on several N-body simulations showed that the NFW profile did not need repeated mergers to arise, or even that the flow in full 3-dimensional conditions was smooth from more general principles: Moutarde *et al.* (95 [39]) found that self-similar evolution arose naturally from collisionless collapse, implying through the SSIM

[4]Tidal stripping is the phenomenon that occurs when a halo is stripped of its outer layers under the influence of the differential gravity, or tidal force, of another halo.

[5]Dynamical friction occurs on a massive object traveling through a gravitating medium. It is called a friction because the force resulting from the ensemble of gravitating masses in the medium on the object is approximately proportional to its velocity and pointing in the opposite direction, like a fluid dragging force

that the infall was smooth. After the publication of [33], several groups assessed their assumption: Huss *et al.* 99a [66] found that the NFW profile was not affected by the change of cosmological symmetries imposed on the infall, except if the infall was not only forced to be spherically symmetric but disallowed non-radial forces. Huss *et al.* 99b [67] completed this picture with the examination of various cosmological backgrounds, confirming the unaffected NFW profile. Moore *et al.* 99 [71] found that suppressing the smaller scale substructures by the means of a WDM cut-off in the power spectrum left their results unchanged. Lastly Tittley & Couchman (2000 [73]) did the same kind of tampering with subclumping structures by the means of a top hat convolution to truncate the power spectrum.

Meanwhile, indications could be found in several works of the importance of non-radial motion at the core of haloes: Huss *et al.* 99b [67] clearly found a correlation in their figure 17 between the flattening of the density from isothermal to NFW behaviour and the isotropisation of the velocity dispersion[6]. Moreover this flattening doesn't appear, in [66], for the case of pure radial force. A similar flattening was obtained by Tormen *et al.* [55] with similar anisotropy-flattening correlation. Teyssier *et al.* [54] have also found that isothermal profiles are linked with radial infall and isotropic velocity dispersions from gas are associated with flatter profiles. This puts into perspective the role of the dimensionality of the Phase-Space representing the infall emerges as a signature necessary for shallower cusps. It also echoes the results of Moutarde *et al.* [39] where a model 3-dimensional infall, made out of a combination of cylindrical-symmetric and spherical-symmetric components, yields a cusp intermediate between the cusps produced from a cylindrical-symmetric model and that from a spherical-symmetric one. Moutarde *et al.* explain that intermediate cusp with the dimensionality of the available phase space for the infall. In addition, their central logarithmic slope is similar to that found by Ryden & Gunn [47] for isotropic velocities, as opposed to radial or purely circular. Their central velocity being also isotropic, they parallel those correlations as an explanation scheme for the cusp profile.

The inclusion of some kind of "rotation" (angular momentum) in the SSIM by several authors ([47], [52], [53], [45], [46], [51]) has shown some promises of shallow inner density cusps.

Nevertheless, another effect is needed if indications of inner cusps even shallower than NFW ([31], [75]) are to be taken seriously, since according to Subramanian (99b [46]) it is very difficult to obtain such flattening only from angular momentum without tangential velocities so dominant that the core would become essentially static. Some work has been done by Peebles (1972 [82]), Young (1980 [83]) and Quinlan *et al.* (1995 [84]) showing that

[6]Occurrence of the NFW type of flattening in the center of the halo from the isothermal density profile happens in the very region where the velocity dispersion turns from dominantly radial to isotropic.

adiabatic growth of a black hole can form inner cusps shallower than isothermal depending on the galaxy model, but they only achieved cusps as shallow as $\alpha_p = \frac{3}{2}$ (to be compared with Eq.(3.59)). Only in Nakano & Makino (1999 [85]) can a flatter core ($\alpha_p = \frac{1}{2}$) be formed through a markedly non-adiabatic, merger-triggered appearance of a black hole and the ensuing population inversion. However Henriksen has shown (Henriksen & Le Delliou 2001 [86]) that self-similar infall on a black hole with angular momentum yields a core as flat as $\alpha_p = \frac{1}{2}$, the population inversion resulting from the self-similar relaxation process.

All these interpretations of the formation of CDM halo density profiles conveyed the importance of a theoretical study of mergers, angular momentum and embedding of a black hole in those objects. The simplicity of the SSIM makes it an attractive basis from which to expand the theory. The expansion can test the Syer & White assumptions by the modeling of mergers through the infall of peripheral overdensities on an established self-similar core embedded in a SSIM. The model can also straightforwardly expand to include the effect of rotation by the onset of spherically symmetric, radially dependent angular momentum. Eventually, the radial infall model can be accommodated to present some kind of phase space mechanism for growing a central point mass modeling an embedded black hole.

Due to limits on time, inclusion of an embedded black hole with angular momentum model and monitoring of less restrictive symmetries using the Carter & Henriksen,(91), formalism to emphasise the emergence of self-similarity couldn't be included in the present work.

Self-similar equations of motion

From Eq.(3.29), the equations of motion arise as equations of its characteristics, since particle trajectories are identified with characteristic curves (see [42]):

The time characteristic equation identifies almost the characteristic curvilinear variable with self-similar time (completely up to the definition of origin). The angular momentum equation yields back its part of Eq.(3.26). The radial equation yields the relation between self-similar radius and self-similar velocity

$$\partial_T X = Y - \delta X, \tag{3.60}$$

the velocity characteristic yields the self-similar Newton's equation, namely the Lagrangian (as opposed to Eulerian) equation of motion

$$\partial_T Y = \left(\frac{Z}{X^3} - \partial_X \overline{\Phi} \right) + (1 - \delta) Y. \tag{3.61}$$

Using the integral of Eq.(3.30) over radius, and the definition (3.37), one can rewrite Eq.(3.61) so that together with Eq.(3.60) they form the Lagrangian dynamics equations:

$$\begin{cases} \frac{dY}{dT} = \left(\frac{Z}{X^3} - \frac{M}{X^2}\right) + (1-\delta)Y \\ \frac{dX}{dT} = Y - \delta X \end{cases} . \tag{3.62}$$

Determining the self-similarity index and the final density profile from initial conditions

[7]As it appears in the previous calculations, there are only two free self-similar indices: α and δ. The former sets the scaling for lengths and the latter, for time. Since there is only one Lie self-similar direction of rescaling, those are fixed once this direction is determined. But since only the direction of rescaling is relevant, the scales on the Dimension axes is just a gauge fixed by the attribution of initial scales to the T=0 Dimensional quantities. Therefore, the self-similarity class is fixed by setting a value to the ratio $\frac{\delta}{\alpha}$, for non-zero αs.

Now we add the remaining assumptions of the SSIM: cosmology and density perturbation. Cosmology dictates that for a CDM halo studied in the rest frame of its centre, the velocities will follow a Hubble flow at recombination, which corresponds to the beginning of the infall. The cosmological frame is chosen to be an Einstein-de Sitter model, so the scale factor goes like

$$a_s \propto t^{\frac{2}{3}}$$

(see Misner, Thorne & Wheeler 73 [92] p735, or d'Inverno 92 [93] p333), and the uniform background density reads then:

$$\rho = \frac{1}{6\pi G t^2},$$

and the Hubble parameter, which sets initial velocities can be written

$$H = \frac{v_r}{r} = \frac{2}{3t}. \tag{3.63}$$

Setting for the rest of the work t_0 =1 at beginning of collapse (which incidentally sets $\alpha = 1$), G=1 for the self-similar variables, the initial background density then reads

$$\rho_0 = \frac{1}{6\pi},$$

but for simplification of the Poisson's equation, for instance, we will redefine

$$4\pi\rho_0 \equiv \rho_0$$

[7]The following introduction and two subsections are written after personal notes from R.N. Henriksen [97].

so that the value we will use for the initial background density in the simulations is

$$\rho_0 = \frac{2}{3}. \tag{3.64}$$

In self-similar variable terms, Eq.(3.63) reads

$$Y = \frac{2}{3} X e^{-\alpha T(=0)} = \frac{2}{3} X \tag{3.65}$$

because we consider the expansion from, t=1, T=0, initial conditions. Cosmology also imposes an initial density profile as a perturbation over a constant background. The simplest perturbation is a scale-free perturbation, that is a power-law. This can be derived by Dimensional arguments from a piecewise approximation of the power spectrum by power laws. We will adopt this initial profile in this work without linking it directly to a power spectrum of density fluctuations, since various ways of linking P(k) to the initial power-law index are possible. We will then adopt

$$\rho = \rho_0 \left(1 + \lambda . X^{-\epsilon}\right),$$

where λ is a constant.

The onset of self-similarity in the SSIM may be shown to occur for each shell at the turn-around radius, a, and turn-around time, t_0 by showing $\frac{d \ln a}{d \ln t_0}$ to be a constant asymptotically.

Self-similarity class of the radial SSIM In the SSIMs without angular momentum the self-similar classes are manifest in their relative logarithmic derivatives in the de Sitter cosmological frame. They are obtained using a similar method as in Henriksen 89 [94], hereafter H89, revolving around a generalised Friedman equation for the motion of individual shells before shell-crossing. The equation, coming from the free fall of a shell of mass before shell-crossing, relates a scaling factor S common to all shells with its derivatives in terms of a self-similar time variable ξ and assumes same the form as Friedman's equation for the cosmological Friedman-Lemaître-Robertson-Walker scaling factor:

$$(d_\xi S)^2 - \frac{1}{S} = -1.$$

the turn-around time and radius are then defined by $r = aS$,

$$\frac{dS}{d\xi}(\xi(t_0)) = 0 \Leftrightarrow S = 1$$

(note that here the turn-around radius *is* the Lagrangian label a). So the relative logarithmic derivatives of a and t_0 follows after some calculations:

$$\frac{d\ln a}{d\ln t_0} = \frac{\frac{1+(1+\epsilon)qx^\epsilon}{1+qx^\epsilon}}{\frac{\frac{\epsilon}{2}\left(3\sqrt{q}x^{\frac{\epsilon}{2}}+(1+3qx^\epsilon)\arccos\left(\frac{1}{\sqrt{1+qx^\epsilon}}\right)\right)}{\left(\sqrt{q}x^{\frac{\epsilon}{2}}+(1+qx^\epsilon)\arccos\left(\frac{1}{\sqrt{1+qx^\epsilon}}\right)\right)}}, \tag{3.66}$$

with q defined from the initial mass expression:

$$M(r) = M_f x^3(1+\frac{x^{-\epsilon}}{q}),$$

the scaled radius is defined with a fiducial radius ($r_f = (\lambda)^{\frac{1}{\epsilon}}$) as well as the fiducial mass:

$$x = \frac{r}{r_f},\ M_f = \frac{4\pi}{3}\rho_b r_f^3,$$

and the background density ρ_b is the Dimensional version of the previous ρ_0.

The limit at large radius (far from boundary conditions, in the self-similar regime) of the logarithmic derivatives in Eq.(3.66) yields the similarity class (because it goes to a constant, giving a power law, or scale-free, behaviour):

$$\lim_{x\to\infty}\left(\frac{d\ln a}{d\ln t_0}\right) \equiv \left.\frac{d\ln(X_a e^{\delta T})}{d\ln(\frac{1}{\alpha}e^{\alpha T})}\right|_{T=0} = \left.\frac{d(\delta T)}{d(\alpha T)}\right|_{T=0} = \frac{\delta}{\alpha}$$

and from Eq.(3.66):

$$= \frac{\frac{(1+\epsilon)qx^\epsilon}{qx^\epsilon}}{\frac{\frac{3\epsilon}{2}qx^\epsilon\arccos\left(\frac{1}{\sqrt{1+qx^\epsilon}}\right)}{qx^\epsilon\arccos\left(\frac{1}{\sqrt{1+qx^\epsilon}}\right)}} = \frac{2}{3}\frac{(1+\epsilon)}{\epsilon},$$

so for the purely radial case,

$$\frac{\delta}{\alpha} = \frac{2}{3}\left(1+\frac{1}{\epsilon}\right). \tag{3.67}$$

In that case the self-similar density profile arises from simple Dimensional analysis:

$$d_\rho = \left(\ d_t = 0 \quad d_r = -3 \quad d_{v_r} = 0 \quad d_m = 1\ \right),$$

so using the constancy of G to reduce the dimensionality,

$$d_\rho = \left(\ 0 \quad -3 \quad 0\ \right) + \left(\ -2 \quad 3 \quad 0\ \right) = \left(\ -2 \quad 0 \quad 0\ \right),$$

we find that the density should scale as

$$\rho \propto e^{-2\alpha T},$$

while radius scales as in Eq.(3.26;1), so that

$$e^T \propto r^{\frac{1}{\delta}} \Rightarrow \rho \propto r^{-2\frac{\alpha}{\delta}} = r^{-\frac{3\epsilon}{(1+\epsilon)}}.$$

Self-similarity class in the angular momentum SSIM In the SSIM with angular momentum, matters are a bit more complex: the perturbations to the initial de Sitter energy have now an angular momentum component which imposes another condition to keep the generalised Friedman equation self-similar (see H89 [94]). This in turn imposes a form for angular momentum which deviates from the functional form that comes directly from its self-similar variable Z, and changes the turn-around radius from its Lagrangian label to a smaller radius. Finally, the logarithmic derivatives of the turn-around time and radius don't converge exactly far from the boundaries of the system to a constant (unlike the radial case), leaving the self-similarity only exact for vanishing angular momentum. This points towards an approximate validity of self-similarity in an intermediate region remote enough from the centre and from the outermost turn-around radius to be scale free . Indeed, in the centre, finite size effects (smoothing of initial power law, granular nature of subclumps involved in the infall) impose scales, and on the outer edge, particles are dominated by angular momentum and beyond that outermost radius they never turn-around so that this limit radius becomes a natural scale.

The self-similar generalised Friedman equation derives from the expression of the total energy in terms of its kinetic and potential components:

$$(d_\xi S)^2 - \frac{1}{S} + \frac{J^2}{S^2} = -1, \tag{3.68}$$

where we have defined the former turn-around radius, now self-similar Lagrangian label (recall that for bound shells, E<0, hence the -1 in Eq. (3.68))

$$a = \frac{GM(r)}{|E|}, \tag{3.69}$$

the current radius of a spherical shell being the self-similar

$$r = aS(\xi),$$

with the self-similar variable

$$\xi = \sqrt{\frac{2GM}{a^3}}(t - t_0(a)),$$

$t_0(a)$ is just the turn-around time, so at turn-around, $\xi = 0$. Maintaining the self-similarity of Eq.(3.68) requires a condition on the angular momentum which defines the constant

$$J^2 = \frac{j^2}{2GMa}. \tag{3.70}$$

The expression for the initial perturbed mass remains unchanged

$$M(r) = \frac{4\pi}{3}\rho_b r_f^3 x^3 \left(1 + \frac{x^{-\epsilon}}{q}\right) \tag{3.71}$$

with the same definitions as previously, but the initial energy is added with the angular momentum perturbation to the de Sitter cosmology: since the unperturbed energy is marginally unbound ($E_{de\ Sitter}$=0 for a constant density background and a Hubble flow), it reads

$$E(r) = \frac{H^2 r^2}{2} - \frac{GM(r)}{r} + \frac{j^2}{2r^2} = -\frac{4\pi G\rho_b \lambda}{(3-\epsilon)} r^{(2-\epsilon)} + \frac{j^2}{2r^2}. \tag{3.72}$$

Combining Eqs. (3.71) and (3.72) in the definition (3.69), one can get

$$\frac{x}{a} = \frac{2J^2(1+qx^\epsilon)}{\left[1 - \sqrt{1 - 4J^2(1+qx^\epsilon)^2}\right]},$$

which yields from Eq.(3.70) the expression for the self-similar compatible angular momentum in the SSIM

$$j^2 = \frac{4\pi G\rho_b \lambda r_f^{4-\epsilon}}{(3-\epsilon)} x^{4-\epsilon}\left[1 - \sqrt{1 - 4J^2(1+qx^\epsilon)^2}\right], \tag{3.73}$$

which is different than the self-similar expression obtained by Dimensional analysis and recognising the self-similar density profile $\rho \propto r^{-2\frac{\alpha}{\delta}}$:

$$j^2 = Ze^{\lambda T} \propto r^{\frac{\lambda}{\delta}} = r^{4-2\frac{\alpha}{\delta}} \propto r^4\rho,$$

but Eq.(3.73) can be recognised as a corrected version of the previous expression if one replaces the self-similar final density profile with the initial density perturbation $\delta\rho \propto r^{-\epsilon}$.

The integration of Eq.(3.68) gives a solution up to a constant that can be determined by solving the original equation at turn-around time for S:

$$\xi + C = -\sqrt{S - (S^2 + J^2)} + \arcsin\left[\frac{2S-1}{\sqrt{1-4J^2}}\right],$$

and at turn-around ($d_\xi S = 0$, and $S_{ta} \underset{J\to 0}{\longrightarrow} 1$ from the radial case, the other solution giving the inner turning point)

$$S_{ta} = \frac{1}{2}\left[1 + \sqrt{1 - 4J^2}\right],$$

so the constant C is set to

$$0 + C = \sqrt{0} + \arcsin 1 \Leftrightarrow C = \frac{\pi}{2}.$$

The turn-around time can then be derived from the solution at t=0 as a function of the initial radius, since $S=\frac{r}{a} = \frac{x}{a}$, with the second a taken in units of the fiducial radius.

Then, the logarithmic derivatives are computed thus

$$\frac{d\ln t_0}{d\ln r_{ta}} = \frac{d\ln t_0}{d\ln(aS_{ta})} = \frac{\frac{d\ln t_0}{d\ln x}}{\frac{d\ln a}{d\ln x}},$$

as for the radial case, and it can be obtained that

$$\frac{d\ln a}{d\ln x} = 1 + \epsilon \frac{qx^\epsilon}{(1+qx^\epsilon)\sqrt{1-4J^2(1+qx^\epsilon)^2}}$$

and

$$\frac{d\ln t_0}{d\ln x} = \frac{\epsilon}{2}\left[\frac{1}{(1+qx^\epsilon)} + \frac{3qx^\epsilon}{(1+qx^\epsilon)\sqrt{1-4J^2(1+qx^\epsilon)^2}}\right] +$$

$$+ \frac{4J^2\epsilon(1+qx^\epsilon)\sqrt{2J^2qx^\epsilon}}{\left(1-\sqrt{1-4J^2(1+qx^\epsilon)^2}\right)\sqrt{1-4J^2(1+qx^\epsilon)^2}\sqrt{1-\sqrt{1-4J^2(1+qx^\epsilon)^2}}} \times$$

$$\frac{1}{\sqrt{\frac{8J^2qx^\epsilon}{1-\sqrt{1-4J^2(1+qx^\epsilon)^2}}} + \pi + \arcsin\left(\frac{qx^\epsilon - \sqrt{1-4J^2(1+qx^\epsilon)^2}}{(1+qx^\epsilon)\sqrt{1-4J^2}}\right)}.$$

The recurrence of $\sqrt{1-4J^2(1+qx^\epsilon)^2}$ imposes a maximum radius of validity since its argument has to be positive, so the method of taking the large radius limit used for the purely radial case cannot be extended exactly, so the self-similarity index can only be reached through approximating that J is small. Then the radial case is re-obtained.

$$\frac{d\ln a}{d\ln x} \underset{J\to 0}{\sim} 1 + \epsilon\frac{qx^\epsilon}{(1+qx^\epsilon)} \underset{x\to\infty}{\to} 1+\epsilon,$$

and

$$\frac{d\ln t_0}{d\ln x} \underset{J\to 0}{\sim} \frac{\epsilon}{2}\frac{1+3qx^\epsilon}{1+qx^\epsilon} + \frac{2\epsilon\sqrt{qx^\epsilon}}{(1+qx^\epsilon)\sqrt{1+qx^\epsilon}} /$$

$$\left[\frac{\sqrt{8qx^\epsilon}}{(1+qx^\epsilon)} + \pi + \arcsin\left(1 - \frac{2}{(1+qx^\epsilon)}\right)\right] \underset{x\to\infty}{\sim}$$

$$\frac{3qx^\epsilon\epsilon}{2qx^\epsilon} + \frac{2\epsilon}{(1+qx^\epsilon)\left[\frac{\sqrt{8qx^\epsilon}}{(1+qx^\epsilon)} + \pi + \arcsin(1)\right]} \underset{x\to\infty}{\sim}$$

$$\frac{3\epsilon}{2}+\frac{\epsilon}{\sqrt{2qx^{\epsilon}}}\underset{x\to\infty}{\longrightarrow}\frac{3\epsilon}{2},$$

so, as in the radial case,

$$\left.\frac{d\ln t_0}{d\ln a}\right|_{J\to 0}\underset{x\to\infty}{\longrightarrow}\frac{3\epsilon}{2(1+\epsilon)}\equiv\frac{\alpha}{\delta}.$$

All in all, it appears that self-similarity is only approximately reached in the SSIM when angular momentum is added and we will use the purely radial model as a basis for self-similarity in the angular momentum case, when it is weak enough not to distort the phase space.

3.2.2 Dynamics of gravitational collapse

Review of the approach to the dynamics of gravitational collapse

The possibility that CDM haloes exhibit a universal density profile implies that the dynamics of formation through pure gravitational collapse erases at least some of the memory of the halo's initial conditions so as to move every halo from the range of possible starting conditions towards one unique outcome. This hints towards the idea first put forward by Lynden-Bell (1967 [34]) of violent relaxation[8] in the statistics of mutually exclusive, distinguishable particles: developed in the frame of stellar orbit statistics, this picture of a collisionless self-gravitating gas describes how rapidly varying potentials quickly wash out the traces of initial conditions by phase mixing and equipartition of energy, leaving the system relaxed. This antinomic expression of violent relaxation emphasises the rapidity of the system's memory loss due to violently changing gravitational fields. In violent relaxation, the memory loss of initial conditions not only affects the phase-space by phase mixing, but also arises in the mixing of energies:

$$\frac{dE}{dt}=\frac{1}{2}\frac{dv^2}{dt}+\frac{d\Phi}{dt}=\mathbf{v}.\frac{d\mathbf{v}}{dt}+\frac{\partial\Phi}{\partial t}+\mathbf{v}.\nabla\Phi=\left.\frac{\partial\Phi}{\partial t}\right|_{\mathbf{x}(t)} \tag{3.74}$$

Such a drastic process is therefore likely to appear in the collapse of a CDM halo, it being a system of free-falling self-gravitating many-bodies, and the density profile is

[8]Relaxation refers to the convergence of dynamical processes which erase in phase space the memory of a system's initial conditions. The term violent relaxation was proposed to account for the rapid timescale of relaxation encountered in collisionless, self-gravitating systems that obey a different statistics than the usual ones (refer to Lynden-Bell, 1967 [34], for more precision). Note that the development of the self-similar state studied in this work is also a relaxation towards virialisation.

one of the clues of memory loss if it is really universal when the system virialises[9]. But the question of how violent is the relaxation involved in the dynamics of DM haloes encourages one to go still further and ask if and how the system can retain some of its memory in its energies. In fact, it was found as early as 1982 by van Albada [57] that N-body simulations of elliptical galaxy formation displayed some correlations between initial and final energies. Later on, Spergel & Hernquist (92 [88]) remarked that if violent relaxation were so efficient as to make all final states equiprobable, the mass and energy of such system in its maximum entropy state should be infinite and therefore the spread of energies for violent relaxation should be limited. In his simulations, Voglis (94 [74]) displayed the formation of an isothermal core surrounded by a halo, where again relaxation was only moderately violent (the energy mixing being partial, especially in the halo where initial and final energies of particles are found to be correlated). In a more general context, the simulations by Moutarde *et al.* (95 [39]) showing a self-similar infall hinted that the self-similar relaxation process preserved some memory. Moreover, the different semi-analytical method used by Kull (99 [68], mixing excursion set formalism and integrals of the motion) showed that the virialisation of CDM haloes didn't require energy dissipation. The simulations from Tormen *et al.* (97 [55]) also characterised the process of halo formation as an alternation between merging and relaxation phases. This sheds light on the decoupling found by Natarajan *et al.* (97 [89]) between a fast energy exchange, or relaxation, characteristic time and a slow dynamic time in haloes which produces in their simulations a quasi-equilibrium for CDM collapse. In their reassessment of the SSIM ([44], [41], [42]), Henriksen & Widrow also found that relaxation was only moderately violent: The self-similar phase of the infall can be characterised by a quasi-equilibrium state measure by the modified version of the Virial Theorem ($\frac{2K}{W} = cst \neq 1$) and the final energies still correlate, though with some dispersion, to the initial ones.

The tool that is fundamental to study the statistics of a many-body system appears already in the field of stellar dynamics: the Probability Distribution Function (PDF) represents the Phase-Space mass distribution. In his first exploration of violent relaxation, Lynden-Bell [34] prescribed that the PDF of the relaxed system should be a Fermi-type distribution, as a result of an incomplete violent relaxation. He showed as well that there is no finite self-gravitating system whose stationary[10] state extremises its entropy (indeed extremising the entropy of a self-gravitating system imposes to find an isothermal profile, which implies an infinite mass, so the constitution of the extremum

[9] A virialised system is one that follows the virial theorem ($\frac{d^2 I_{ij}}{dt^2} = 0 \Rightarrow 2K + W = 0$ where $I_{ij} = \int x_i x_j \rho d^3x$ is the moment of inertia tensor, $K = \int \rho \overline{\left(\frac{\vec{v}^2}{2}\right)} d^3x$ is the kinetic energy of the system and $W = \int \rho \mathbf{x}.\nabla\Phi d^3\mathbf{x}$ is Clausius's Virial as well as the gravitational potential energy of the system. See e.g. Binney & Tremaine [87] p213). The terms denote a self-gravitating system at equilibrium.

[10] A system is stationary in the sense that its PDF has no time variation ($\frac{\partial f}{\partial t} = 0$).

entropy profile for a finite amount of mass is always incomplete). He also showed that even if the fine-grained PDF, which obeys the Collisionless Boltzmann's Equation (CBE), allowed for the conservation of the total mass of Phase-Space elements of higher density than a given level f, $M(f)$, to be conserved, this is not the case for the coarse-grained PDF ($M(\overline{f})$ is *not* conserved). In this work and other semi-analytical or numerical explorations of collisionless systems, simulations are solving for fine grained PDF with numerical smoothing. Nevertheless the approximation that the smoothing still represents the fine grained PDF can be questionable.

Since any naïve approach to the steady state of such system seems excluded, there are several types of approach which have proved to be fruitful: one is to prescribe extra macroscopic constraints on the system when extremising the entropy (Stiavelli & Bertin 1987 [90]). Another is to assume a form of the PDF based on dynamical arguments limiting the available phase space: Bertin & Stiavelli 1984 [58] and Stiavelli & Bertin 1985 [59] used a family of Maxwellian forms based on integrals of motion, generalised by MTJ [60] to "negative temperatures" and another form of angular momentum cut-off. Spergel & Hernquist [88] limited the available phase space by approximating violent relaxation dynamical processes as a sequence of 2-body scattering events. Henriksen & Widrow [42] arrived at a form similar to MTJ by mixing their dynamical arguments with self -similar prescriptions on stationary solutions [44]. An alternative approach is to suggest PDF forms from the fit of numerical simulations (e.g. Voglis [74], Aguilar & Merritt [61]), or even simply to measure the PDF of equilibrium outcomes of numerical simulations (like van Albada [57], Natarajan [89], or Henriksen & Le Delliou [86]). In table 3.1 is summarised some of the PDF forms used by various authors.

In this work, we will try to understand the dynamics of the collapse of our system in terms of the degree of violent relaxation occurring during the infall. We will be using measurements of the PDF and of the virial ratio, and looking at energy correlations. We will also confront the measurements of PDF with the static predictions of Henriksen & Widrow [44].

The answers from the SSIM

Self-similar Virial ratio Section 3.1.2 shows that when the system is self-similar, the virial equations denote a quasi-equilibrium solution that can be characterised by the system's virial ratio: in the case of a stationary, self gravitating system, this ratio is -1 (see Binney & Tremaine [87]). For the self-similar stationarity the system exhibits a virial ratio different than -1 but nevertheless constant. This can be seen in the spherically symmetric system with angular momentum in Eq.(3.41) when all T derivatives are 0:

$$\frac{2K}{W} = -1 + \frac{1}{2}(5\delta - 3\alpha)(5\delta - 2\alpha)I/W$$

Stiavelli & Bertin:[58] & [59]	$f = \begin{cases} A(-E)^{3/2} exp\left[-aE - b\left(J_z^2/2\right) - cI_3\right] & E \leq 0 \\ 0 & E > 0 \end{cases}$
Stiavelli & Bertin:[90]	$f = A\, exp\left\{-aE - \delta\left[\frac{J^2}{\lvert E\rvert^{3/2}}\right]^{\alpha_1/2}\right\}$
MTJ_1 [60]	$f(E,J^2) = \begin{cases} A(-E)^{3/2} exp\left[a\left(E - J^2/2r_a^2\right)\right] & E \leq 0 \\ 0 & E > 0 \end{cases}$
MTJ_2 [60]	$f(E,J^2) = \begin{cases} A(-E)^{3/2} e^{\pm aE}\left(1 - J^2/J_0^2\right)^{-1} & E \leq 0 \\ 0 & E > 0 \end{cases}$
Spergel & Hernquist [88]	$f(E) = \begin{cases} Ae^{-\beta E}\left(E - \Phi_0\right)^2 & \Phi_0 < E < \Phi(r_a) \\ Ae^{-\beta E}\{(E - \Phi_0)^2 + & E > \Phi(r_a) \\ C\left(E - \Phi(r_a)\right)^{-1/2}\} & \end{cases}$
Voglis [74]	$f = A(-E)^{3/2} \frac{N_h(E,L^2) + N_0 e^{bE_c}(E/E_c)^p}{exp[\beta(E-E_c)]+1}$
Henriksen & Widrow [42]	$f(E) = \begin{cases} A(-E)^{1/2} exp\left[aE\right]\delta(j^2) & E \leq 0 \\ 0 & E > 0 \end{cases}$

Stiavelli & Bertin:[58] & [59]	$E = \frac{v^2}{2} + \Phi$ and $I_3 = \frac{J^2}{2} + cst$	$a > 0$, "temperature"
Stiavelli & Bertin:[90]	δ and α_1, parameters from	maximum entropy method
MTJ_1 [60]	r_a , characteristic radius	$-a < 0$, "temperature"
MTJ_2 [60]	J_0 , cut-off angular momentum	
Spergel & Hernquist [88]	r_a, characteristic radius	Φ_0, central potential
Voglis [74]	N_h , root of an equation	
Henriksen & Widrow [42]	δ, the Dirac distribution	$-a < 0$, "temperature"

Table 3.1: Some Probability Distribution Functions

$$-\delta\Gamma(1)\overline{Y}(1)/W$$

$$-\frac{1}{2}(5\delta-3\alpha)(3\delta-2\alpha)M/W \tag{3.75}$$

The extra terms from the mass, the moment of inertia and the surface are difficult to interpret in these forms. But the same feature can be seen in the full 3-dimensional case: Eq.(3.53) where the T derivatives vanish reads

$$\frac{1}{2}\left((5\delta-3\alpha)(5\delta-2\alpha)I_{jk}+(5\delta-3\alpha)A_{jk}\right)=2K_{jk}+W_{jk}.$$

Taking the trace, one gets the scalar virial equation

$$\frac{1}{2}\left((5\delta-3\alpha)(5\delta-2\alpha)I+(5\delta-3\alpha)A\right)=2K+W,$$

and the virial ratio then reads:

$$\frac{2K}{W}=-1+\frac{1}{2}\left((5\delta-3\alpha)(5\delta-2\alpha)I/W+(5\delta-3\alpha)A/W\right) \tag{3.76}$$

which is less than -1 since, every other terms being positive and W negative, the extra terms are negative. The interpretation of the extra terms is then strictly the same as in section 2 of [42]: the first comes from the time-dependence of the self-similar system, the second from the system's boundary mass flux. In this light the extra terms of Eqs.(3.75) or (3.76) can be interpreted as such: the first extra term is the analog of the comoving coordinate-type effect, that can be found e.g. in cosmological flows, and the two other terms correspond to the boundary mass flux (related to the self-similar mass M by setting $\frac{dM}{dT}=0$ in Eq.(3.36)).

The scaled quantities like K and W being specific energies, it can be shown that their scaling is the same ($\mathbf{E}$=E$e^{2(\delta-\alpha)T}$) and therefore that the self-similar virial ratio is the same as the real virial ratio. The study of the behaviour of that virial ratio will then teach us about the state of equilibrium or quasi-equilibrium which the system is experiencing.

Distribution function As argued in section 4 of [42] for the radial case, the passage from infall self-similar phase ($\frac{d}{dT}=0$) to stationary phase ($\frac{d}{dt}=0$) is smooth and lead to a self-similar equilibrium. Those have been studied in [44] for several cases: the radial, spherically symmetric case yields a self-similar, and a real, distribution function of the form

$$F(X,Y)=F(E)\propto|E|^{\frac{1}{2}}. \tag{3.77}$$

In the isotropic velocity case of spherical symmetry, the PDF is still only a function of energy but then

$$F(X,Y,Z)=F(E)\propto|E|^{-(\delta'+1/2)}=|E|^{-\frac{3\delta-\alpha}{2(\delta-\alpha)}} \tag{3.78}$$

(the prime denotes the difference in conventions used in the stationary cases compared to the time dependent cases for self-similar indices).

The anisotropic velocity case is more problematic since part of the solution found by Henriksen & Widrow is an arbitrary function F of a composite variable of X, Y and angular momentum squared Z ($\xi = \frac{|\delta' Z + Y^2 + 2\Phi|^{\delta'+1}}{Z} \equiv j^{-2}|E|^{\delta'+1}$), and the Dimensional variable solution reads:

$$f(j^2, E) = j^{-\frac{2\delta'+1}{\delta'+1}} F(\xi) = j^{-\frac{3\delta-\alpha}{2\delta-\alpha}} F\left(j^{-2}|E|^{\frac{2\delta-\alpha}{\delta-\alpha}}\right). \tag{3.79}$$

The axisymmetric cases treated in [44] are not touched in this work.

3.3 Summary of the initial state of the model

> Everything should be made as simple as possible, but not simpler.
>
> JOHANN VON NEUMANN (1903-1957)

From the works of Henriksen and Widrow [44], [41] and [42], the SSIM for radial orbits in spherical symmetry is known to yield the following results:

3.3.1 Density profile

The outcome of the SSIM in terms of density profile can be condensed to the following points: for any power law perturbation of a cosmological background, there exists a one-sided universal attractor for the final density profile [42]. Relating it to a cosmological, initial, scale-free power spectrum using Eq.(2.3), the density profile predicted for CDM haloes reads

$$\frac{\rho}{\rho_c} = \begin{cases} \left(\frac{r}{r_s}\right)^{-2}, & n < 1 \\ \left(\frac{r}{r_s}\right)^{-\frac{3(n+3)}{n+5}}, & n > 1 \end{cases}. \tag{3.80}$$

Moreover, in the range of acceptable initial conditions (for which the mass of the halo converges) the variations on the density logarithmic slope index are small ($2 \leq \frac{3(n+3)}{n+5} \leq \frac{9}{4}$). In addition, it is remarkable that the self-similar scaling of the system during its evolution is holding even for $n < 1$.

This attractor provides a natural explanation for the controversial universality of the density profile debated in the field, since self-similarity is a generic feature of intermediate asymptotes for systems such as CDM haloes.

3.3.2 Self-similar dynamics of gravitational collapse

Phase space instability

The SSIM also allows one to explain the internal dynamics producing the density profile in terms of self-similar gravitational collapse. In [41], it is shown that the phase mixing seen in Fillmore & Goldreich,84 [35] is supplemented by a phase space instability in the time-dependent development of the gravitational collapse which leads to some kind of coarse-graining of the phase space structure and breaks the infinitely winding stream of [35] into a hierarchy of characteristic curves. It is remarkable that this instability, which could be set up by numerical noise in [41] and the present work because of the nature of N-body simulations, is confirmed to be arising from fine grained phase mixing by Rasio *et al.* [99] and by Merrall [102] in their approaches to the spherical collisionless collapse using very accurate phase space methods respecting the Liouville incompressible flow of the PDF.

Moderately violent relaxation

The exhibition of the self-similar virial ratio for the radial SSIM and the study of its evolution with time was performed in [42]. There it was shown that radial spherical infall leads to a quasi-equilibrium self-similar infall phase. This phase is characterised by its constant, non-unity, virial ratio that falls quietly to its usual equilibrium value once the boundary mass flux is interrupted, and by its stationarity in self-similar variable that denotes the self-similar nature of the infall. The moderation in the system's relaxation was shown by exhibiting a remaining correlation between the shells' initial and final specific energies.This allows for the prediction of the radial spherical PDF from the transition to steady state, which matches that of an *a priori* different steady-state self-similarity PDF studied in [44]. Predictions of the PDF for the presence of angular momentum, though only available for steady-state, are also proposed there.

Finally a "negative temperature" exponential cut-off in energy is used in the PDF in [42], by analogy with MTJ [60] and arguing, for the steep initial conditions case ($\epsilon > 2$), that the smoothing of the initial density profile's central cusp (so as to always remain with finite densities) will induce a cut-off in energies. We will argue that such conditions are expected in the primordial universe (no infinite density is physical if it doesn't arise in a black hole or at the big bang; even if a black hole sits in the centre of a halo, it will certainly deplete the central halo region from its density). As for the shallow case, we will show that the cut-off comes from the furthest shells and can be explained in terms of influence of neighbouring haloes (e.g. leading to Zel'Dovich's Voids).

Chapter 4

Shell code generic techniques: the semi-analytical model's implementation

> Une erreur peut devenir exacte
> selon que celui qui l'a commise
> s'est trompé ou non.
>
> PIERRE DAC

This chapter will deal with general technical problems encountered with the implementations of the semi-analytical SSIM. More specific problems related to each peculiar implementation will be addressed in their respective chapters.

Unexpected difficulties encountered will be outlined in the first section, followed by some necessary technical definitions in order to express the terms in which are tackled the smoothing length-timestep relation. This relation will be outlined in this chapter's third section, while the equations of motion and integration schemes will be detailed in the fourth section, and the handling of initial conditions by the model in section 5.

4.1 Difficulties with shell codes: Nobody expects the Spanish Inquisition!

In this work, several difficulties attached to the implementation of shell codes were overcome. These are related to the need for smoothing the singular force law necessary for the integration of shells passing through the centre, which detailed implementation will be given in section 4.2.3; to the extreme sensitivity to the right amount of self-interaction

for shells throughout the halo and, to the trade-off between timestep size and smoothing length in order to obtain a realistic yet fast integration.

4.1.1 Smoothing length

A common feature of all N-body simulations, smoothing lengths are characteristic lengths introduced artificially to be able to handle self-gravitating two-body encounters. Naïvely, this can be understood as the result of the inverse square law between two bodies being singular when they are located at the same place. For the SSIM, the symmetry being spherical, particles are then spherical shells of mass about the centre of symmetry and Gauβ's law teaches us that the force felt by each shell is only the result from all the shells it contains. But the force law is still singular in the centre, if any finite, non-zero, amount of mass is located there, so there is still need for a smoothing of the force law in the centre of the halo.

The smoothing of the force law in the centre leads of course to unrealistic dynamics of shells and non-conservation of energy when they fall inside the range of the smoothing length. That is why there is a delicate balance to find between a smoothing length that is too small and which leads to the computing of too large numbers for the simulation to handle, and one that is too large and alters drastically the dynamics of the system in the delicate regions (e.g. relaxation region, shell-crossing region).

The smoothing length will be noted ϵ_s.

4.1.2 Sensitivity to self-interaction

Since discrete treatment of the system by a simulation requires the representation of the continuous mass distribution over the volume of the halo by a finite number of infinitely thin shells of mass, depending on the location of the shell compared to the corresponding density volume it represents, there is bound to be some self-interaction of shells. Indeed, it is crucial that the fraction of the mass of a shell pertaining, in the continuous mass distribution representation, to the volume located bellow the shell's allotted radius be counted as interacting with the shell. If this effect is not taken into account, the dynamics of the collapse in the simulation can be drastically affected and the energetics of the core can be deeply modified. Such extreme sensitivity was experienced in this work as an obstacle to the comparison with the results from [42], especially those concerning the virial ratio.

4.1.3 Integrator choice

Another aspect of the criticality of the smoothing length comes from its relation to the appropriate timestep of the simulation. If the timestep is too large, the finite difference

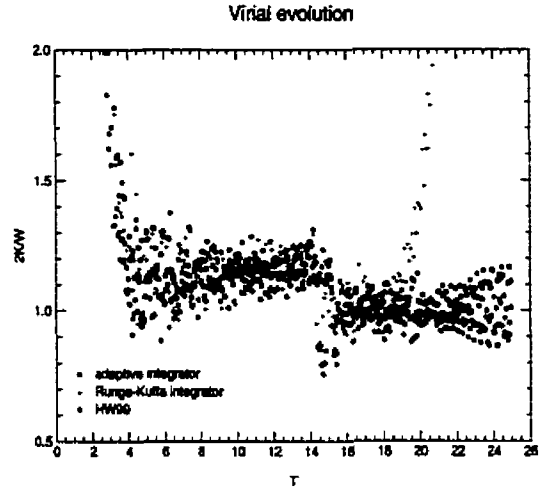

Figure 4.1: Integrator stability comparison between the simple Runge-Kutta, eulsim and previous result from HW99 [42]

approximations made in the integration scheme are no longer valid. The smaller the timestep, the more accurate the integration process is. But this integration scheme is only valid if the resulting radii steps are not too much smaller than the smoothing length, since then the force law, invalid when approaching the centre closer than the smoothing length, is treated strictly by the integrator. It is then better to use a coarse enough integration to ignore scales smaller than the smoothing length.

This brings out the delicate balance between the smoothing length and the timestep that has to be preserved as well as the need for an integrator that is not too sophisticated in the centre.

This work went first along the line of a safer integration routine, using the adaptive, semi-implicit Euler discretisation with h-extrapolation code from the Konrad-Zuse-Zentrum fuer Informationstechnik, Berlin, available in freeware, and called eulsim. But the nature of Lagrangian integration of the system, as an N-body problem, didn't allow for optimum use of the routine: eulsim couldn't handle the integration of the whole system as a unit because of the need for the creation of arrays of order N*N, too heavy for our computing powers. Instead it could only be used as a stepping device for each individual shell at each timestep, which made the simulation very slow. Finally, the need for a coarse treatment in the centre, the alternative being unrealistic integrations, led us to use a simple second order Runge-Kutta integrator, which turned out to be ten times faster than the more sophisticated eulsim.

Nevertheless eulsim was used to check the validity of integration by the Runge-Kutta scheme: being more accurate than the Runge-Kutta integrator, it yields for instance a

more stable integration even after the end of the self-similar phase. That is made obvious in the evolution of the virial ratio (see figure 4.1).

4.1.4 The relation between ϵ_s and the timestep δt

The limit of the balance between timestep and smoothing length should be the optimum relation between the two in order to get a satisfactory integration. The SSIM can be approached from four different avenues in order to obtain and tune the relation between the smoothing length and the timestep of a given simulation. One can obtain analytical expressions for this functional relation in three different ways: the first of which comes from constraining the size of an individual radial step of integration. It also can be deducted from imposing that the Kepler period of a circular orbit at the smoothing radius be much smaller than the timestep. Alternatively, one can verify the conformity of the functional form with a Dimensional analysis using Kepler's law and the self-similar expressions for the system's mass profile and radius. Eventually, the safest route to and real tuning of the needed relation is through Monte Carlo simulation and test of the simulation scheme. A more detailed description of these requires us to accurately define some of the choices of description made in the model's implementation. Therefore, we will proceed first to those definitions in the next section.

4.2 Some Definitions

In the difficulties encountered in the building of the codes necessary for the simulations, some preliminary definitions turned out to be crucial for the understanding and careful handling of the model.

4.2.1 The halo, or core of the infall

In this semi-analytical model, we start with a spherically symmetric model of a patch of the primordial universe after the Recombination epoch, centered on a power law perturbation of the background. After some numerical evolution of the collapse, a core is formed at the centre of the infall (see Fillmore & Goldreich [35] or Bertschinger [36]) which represents the constitution of the halo. The definition taken here for particles belonging to the halo makes use of the Lagrangian treatment of the shells: since we keep track of the original radial ordering of shells, which happens to also be the ordering along the Fillmore & Goldreich stream of particles falling for the first time through the origin of the spherical system, we chose to define the core as the set of particles which have passed at least once through the origin, as illustrated in figure 4.2.

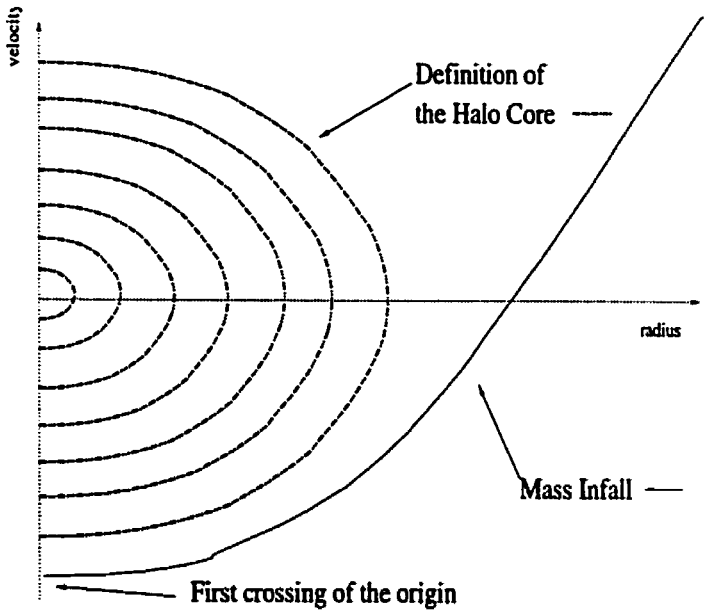

Figure 4.2: Definition of the core. This drawing represents the Fillmore & Goldreich solution in phase space and highlight in thick dash-triple-dot the phase space area selected as core by exclusion of the stream of first infalling particles (solid line).

The simulation handles the passing of shells through the origin by allowing for negative radii during the timestep evolution, and then mirroring into positive radii the particles that have passed through so that the velocities are translated into the positive radius axis:

$$X_{after\ 1\ timestep} < 0 \Rightarrow \begin{cases} X = -X \\ Y = -Y \end{cases} . \tag{4.1}$$

The core boundary can be defined through its Lagrangian index i_{core} (for an explanation of Lagrangian indices, see appendix C) by using the topological property of the most recent shell-crossing the origin for the first time: it is the largest Lagrangian index for which the integration over one timestep has just brought its radial coordinate to a negative value, to be mirrored according to Eq.(4.1),

$$i_{core}(T) = \sup\{i | X_{after\ 1\ timestep}(i)(T) < 0\}. \tag{4.2}$$

This definition reproduces the figure 4.2, since the Lagrangian indices give the ordering along the winding stream of particles as long as it is not destroyed by phase space instability, which happens to shells only after they have been phase mixed by passing a small number of times through the origin. The winding stream is therefore well defined around the boundaries of the core, allowing for the definition (4.2) to hold.

In addition, the radius of the core (called X_{core} in scaled variable, r_{core} otherwise) can be defined as the largest radius of a particle included in the core by its operative definition.

4.2.2 Discretisation of the shells

In order to treat numerically the evolution of the halo, we need to represent the continuous distribution of concentric shells by a discrete hierarchy of shells. In order to simplify the self-interaction problem and the initial boundary shells expressions, each shell was chosen to represent mass from the density distribution volume contained between itself and its immediate lower preceding shell. That way, the initial centre shell contains all the mass within its sphere (the 0^{th}shell radius being 0), and all shells are fully self-interacting.

The mass volume-density then is defined by the discrete distribution in radius x:

$$\rho = \sum_{j=1}^{n} m_j / x^2 \delta(x - x_j), \tag{4.3}$$

where the total number of shells is n and the mass of an individual shell tagged j is m_j, the division factor coming from the conversion to spherical symmetry. We can then define

the mass contained inside the radius of one shell i by

$$iM(x_i) = \int_0^{x_i} \rho(x,t)x^2dx = \sum_{j=1}^{i} \int_{x_{j-1}}^{x_j} \rho(x,t)x^2dx = \sum_{j=1}^{i} m_j, \tag{4.4}$$

where the shells are indexed by their radius.

4.2.3 The Potential and Energies

Kinetic energy, Potential and gravitational energy

The Kinetic energy of a shell i can be defined with its radial velocity and angular momentum:

$$K_i = \int_{r_{i-1}}^{r_i} dr' r'^2 \frac{1}{2}\rho \left(v_r^2 + \frac{j^2}{r'^2} \right) = \frac{1}{2} m_i \left(v_{ri}^2 + \frac{j_i^2}{r_i^2} \right).$$

The kinetic energy of the core is then simply

$$K = \int_0^{r_{core}} dr' r'^2 \frac{1}{2}\rho \left(v_r^2 + \frac{j^2}{r'^2} \right) = \frac{1}{2} \sum_{i=1}^{i_{core}} m_i \left(v_{ri}^2 + \frac{j_i^2}{r_i^2} \right).$$

The definition of the gravitational potential for a spherically symmetric system can be found in Eq.(2-22) from Binney & Tremaine [87]:

$$\Phi(r) = -4\pi G \left[\frac{1}{r} \int_0^r \rho(r') r'^2 dr' + \int_r^\infty \rho(r') r' dr' \right] = \left[-\frac{GiM(r)}{r} - 4\pi G \int_r^\infty \rho(r') r' dr' \right].$$

As stated previously, the potential energy is given by Chandrasekhar's definition, and in spherical symmetry, the potential gravitational energy of the core is following Eq.(3.11):

$$W = -\int_0^{r_{core}} dr' r' \rho(r') GiM(r') = -\sum_{i=1}^{i_{core}} m_i \frac{GiM(r_i)}{r_i},$$

where i_{core} is the last shell in the core. Similarly, for one shell i, the integral has to span the radius of the region collapsed onto the shell, which is defined previously as between the shell itself and its immediate lower preceding one.

$$W_i = -\int_{r_{i-1}}^{r_i} dr' r' \rho(r') GiM(r') = -m_i \frac{GiM(r_i)}{r_i}.$$

Smoothing the force law

Because of the symmetry combined with the numerical treatment of the system, we have to introduce a smoothing of the gravitational force law. Let us smooth it via the inverse radial dependence smoothing: the smoothed radius can be set to

$$r_\epsilon = \sqrt{r^2 + \epsilon_s^2}$$

to avoid too sharp transition between the unaffected scales and the modified region. For consistency we can start with the potential:

$$\Phi(r) = -4\pi G \left[\frac{1}{r_\epsilon}\int_0^r \rho(r')r'^2 dr' + \int_r^\infty \rho(r')f(r')dr'\right] = \left[-\frac{GM(r)}{r_\epsilon} - 4\pi G\int_r^\infty \rho(r')f(r')dr'\right].$$

Here we have introduced a modification of the geometrical factor, i.e. f(r) instead of r, in the second integral to maintain the cancellation of the extra terms in the energy and force calculations:

$$\partial\Phi(r)/\partial r = -\frac{GM(r).r}{r_\epsilon^3} - 4\pi G\left[\frac{1}{r_\epsilon}\rho(r)r^2 - \rho(r)f(r)\right] = -\frac{GM(r).r}{r_\epsilon^3}$$

hence the function f is to be chosen in order to keep the second term null as

$$f(r) = \frac{r^2}{r_\epsilon} \underset{r\gg\epsilon_s}{\simeq} r.$$

The radial gravitational acceleration will then take the modified form

$$a_r = -\frac{GM(r).r}{r_\epsilon^3}. \tag{4.5}$$

The potential energy for shell i turns into

$$W_i = -\int_{r_{i-1}}^{r_i} dr'r'^3\rho(r')\partial_{r'}\Phi(r') = -m_i r_i^2 \frac{GiM(r_i)}{r_{\epsilon i}^3},$$

and the core potential energy reads

$$W = -\int_0^{r_{core}} dr'r'^3\rho(r')\partial_{r'}\Phi(r') = -\sum_{i=1}^{i_{core}} m_i r_i^2 \frac{GiM(r_i)}{r_{\epsilon i}^3}.$$

The angular momentum term also contains a possible singularity, if j^2 is taken constant over the centre. It can be modified similarly to the potential in an ad hoc fashion: the resulting centrifugal acceleration (j being a constant of motion) can then take the form

$$a_{centrifugal} = \nabla\left(\frac{j^2}{2r_\epsilon^2}\right) = -\frac{j^2 r}{r_\epsilon^4}, \tag{4.6}$$

and for one shell i, the form of the kinetic energy becomes

$$K_i = \int_{r_{i-1}}^{r_i} dr' r'^2 \frac{1}{2}\rho \left(v_r^2 + \frac{j^2}{r_\epsilon'^2} \right) = \frac{1}{2} m_i \left(v_{ri}^2 + \frac{j_i^2}{r_{\epsilon i}^2} \right). \tag{4.7}$$

The core kinetic energy then reads

$$K = \int_0^{r_{core}} dr' r'^2 \frac{1}{2}\rho \left(v_r^2 + \frac{j^2}{r_\epsilon'^2} \right) = \frac{1}{2} \sum_{i=1}^{i_{core}} m_i \left(v_{ri}^2 + \frac{j_i^2}{r_{\epsilon i}^2} \right).$$

Chandrasekhar's versus naïve definition of Potential energy

In this work, the system considered is thus the core of the halo, a time dependent non-isolated system of finite size. A naïve definition of the potential energy would be as the sum of the weighted potential

$$W_{naive} = \frac{1}{2} \int d^3x \rho \Phi = 2\pi \int dr r^2 \rho \Phi.$$

Because of the finite size of the system and of the stream of incoming shells during some phases of development of the halo, the transformation between the Chandrasekhar definition and the naive definition involves surface terms which are not taken into account in the naïve definition.

In fact the definition of infinitesimal potential energy coming from the work done on a sphere of mass brought from infinity also involves the gradient of the potential (see Binney & Tremaine [87], Eq.(2-18)). The divergence theorem is needed to get to W_{naive} but it generates again surface terms.

In fact, the SSIM can be used to show that the naïve, or classical, definition of energy for one shell can be represented by Chandrasekhar's (e.g. Eq.(3.11)) for the purpose of the PDF calculation (see section 4.2.4) with the benefit of ignoring the noise and error associated with a finite N-body simulation. We checked this choice by reproducing the PDF slope from a Plummer's sphere phase space realisation, as well as the PDF slope from the radial Henriksen & Widrow model's phase space realisation generated by an independent program; the reproduction of the virial ratio values from the Henriksen & Widrow simulations [42] was also used to validate this choice.

These checks confirm that the Chandrasekhar definition of the energy allows us to reproduce accurately the given sample's PDF (this will be studied in more detail in section 5.1.4). They are presented in figure 4.3. They also justify the choice made for measurements of the PDF of a different implementation of the smoothing length in the energy compared with that presented above for the dynamics of the simulations. This latter point will be discussed in more detail in the section devoted to energy measurement for PDFs (section 5.1.3).

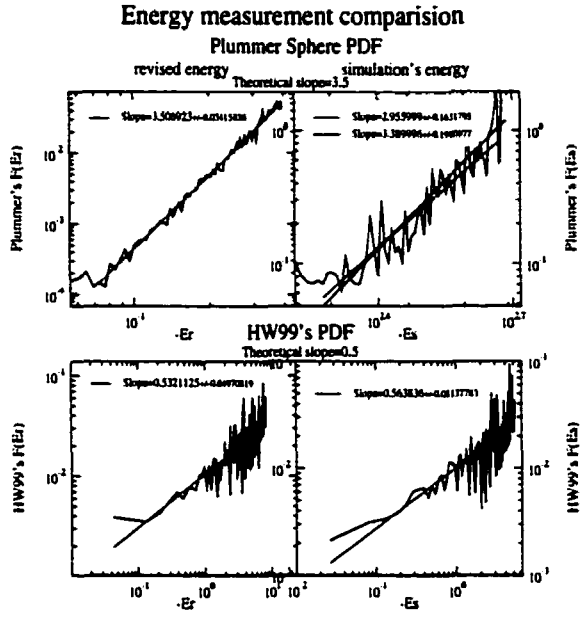

Figure 4.3: PDF from Plummer Sphere and HW99, [42] for the two energy evaluation methods: the left panels corresponds to the use of Chandrasekhar's definition of potential energy in E_r, whereas the right panels refer to the use of the naïve definition of the potential energy in E_s.

By contrast, the classical definition of energy was retained for the energy correlations measurements because of its physical meaningful foundation. In fact, section 4.2.4 demonstrate the use of a modified classical definition, which is strictly equivalent to the naïve one with the appropriate choice of reference value for the potential.

4.2.4 Why using Chandrasekhar's Energy definition

Using Chandrasekhar's definition for gravitational energy measurements displays a non-conservation of the energy for an individual shell. On another hand, using the classical definition of that energy leads to worse resolution of the PDF compared with HW99.

The classical definition includes an extra term which fixes the zero of the potential at infinity, but this is an arbitrary convention. By changing the evaluation reference point for a constant value of the potential at a different location, this freedom allows one to take advantage of the analytical predictions of the SSIM to scrap the numerical noise inherent to N-body simulations with finite Ns. By then showing that the extra term (hereafter called Ext) have a variation for individual shells inside the analytical self-similar system that is exactly proportional to the Chandrasekhar's definition, one can boost the PDF measurement resolution by adopting Chandrasekhar's energy.

The following section will demonstrate how a change of reference point for the energy and an analytical treatment of the system can insure that Ext can effectively be absorbed into Chandrasekhar's energy.

The self-similar density profile

From HW99 and all studies of the SSIM, the density profile in scaled variables during the infall phase is stationary and follow:

$$\overline{\rho} = \lambda X^{-\frac{2}{\delta_0}}, \text{ where } \delta_0 = \begin{cases} \delta & \delta < 1 \\ 1 & \delta \geq 1 \end{cases}, \tag{4.8}$$

and δ is the similarity index from initial conditions leading to a certain turnaround radius/time dependence.

In practice δ_0 is deduced from initial conditions of simulations and λ can be measured on the fully constituted density profile of i.e. the last measurement in the infall phase.

The energy definition

Classical, or naïve, definitions We have seen that Chandrasekhar's definition of the gravitational energy leads for the SSIM to the form

$$W_\Phi = -\frac{GM}{r}.$$

The usual definition brings an extra term which we will generically call Ext:

$$\Phi = -\frac{GM}{r} - \int_r^\infty \rho r' dr' = -\frac{GM}{r} + Ext_0. \tag{4.9}$$

In fact, this term serves to fix the zero of gravitational energy at infinity.

Change in perspective But this comes from the spherically symmetric solution of the Poisson's equation with a peculiar choice of integration constants.

If one makes the choice of reference at an inner cusp radius instead of infinity ($r_c \to 0$), then Poisson's equation can be solved as follows (from [115, Henriksen 01]and other classical texts)

$$\frac{1}{r^2}\frac{d}{dr}\left(r^2\frac{d\Phi(r)}{dr}\right) = 4\pi G\rho(r)$$

$$\Leftrightarrow r^2\frac{d\Phi}{dr} - \left(r^2\frac{d\Phi}{dr}\right)_{r_c} = G\left(M(r) - M(r_c)\right),$$

with

$$M(r) - M(r_c) = 4\pi\int_{r_c}^{r}\rho(r')r'^2dr'.$$

Assuming $r_c \to 0$ so that the mass under r_c is negligible, this definition is compatible with the usual one and we can allow the mass $M(r_c)$ to be 0. Then the mass distribution inside r_c being negligible, we can take $\frac{d\Phi}{dr}\big|_{r_c} = 0$. Any central mass will then have the usual form of the total potential from the linearity of Poisson's equation:

$$\Phi_T = \Phi - \frac{GM_{central}}{r} + \frac{GM_{central}}{r_c}.$$

Thus

$$\frac{d\Phi}{dr} = \frac{GM}{r^2}$$

which can be integrated into

$$\Phi - \Phi(r_c) = -\frac{GM}{r} + 4\pi G\int_{r_c}^{r}\rho(r')r'dr' = -\frac{GM}{r} + Ext,$$

to be compared with Eq.(4.9).

SSIM evaluation Going to self-similar scaled variables compatible with given initial conditions, the self-similar potential reads

$$\overline{\Phi} - \overline{\Phi_c} = -\frac{G\overline{M}(X)}{X} + 4\pi G\int_{X_c}^{X}\overline{\rho}(X')X'dX'.$$

We can then use the definition of Eq.(4.8) since the SSIM predicts its validity for any shell inside the analytical self-similar system (under the core radius r_s), which contains the range of integration thanks to the choice of r_c. It is to be noted that since r_c is fixed, $X_c = r_c e^{-\delta T}$ shrinks with time, reinforcing the strength of the flat potential hypothesis ($\frac{d\Phi}{dr}\big|_{r_c} = 0$). Thus Ext can be written (recall that we have taken G=1 and defined $\overline{\rho} \equiv 4\pi\overline{\rho}$)

$$\overline{Ext} = \lambda \int_{X_c}^{X} X'^{1-\frac{2}{\delta_0}} dX' = \begin{cases} \frac{\lambda}{(2-\frac{2}{\delta})}\left(X^{(2-\frac{2}{\delta})} - X_c^{(2-\frac{2}{\delta})}\right) & \delta < 1 \\ \lambda \ln\left(\frac{X}{X_c}\right) & \delta \geq 1 \end{cases}.$$

Forms of the potential and total energy

Self-similar contributions Using Eq.(4.8) to recover the mass, the form of the self-similar potential is given by

$$\overline{\Phi} - \overline{\Phi_c} = \begin{cases} -\frac{\lambda}{(3-\frac{2}{\delta})} X^{(2-\frac{2}{\delta})} - \frac{G\overline{M}_{central}}{X} + \frac{\lambda}{(2-\frac{2}{\delta})}\left(X^{(2-\frac{2}{\delta})} - X_c^{(2-\frac{2}{\delta})}\right) & \delta < 1 \\ -\lambda + \lambda \ln\left(\frac{X}{X_c}\right) - \frac{G\overline{M}_{central}}{X} & \delta \geq 1 \end{cases},$$

so that

$$\overline{\Phi} - \overline{\Phi_c} = \begin{cases} -\frac{\lambda}{(3-\frac{2}{\delta})} X^{(2-\frac{2}{\delta})}\left(\frac{1}{2(\frac{1}{\delta}-1)}\right) - \frac{G\overline{M}_{central}}{X} - \frac{\lambda X_c^{(2-\frac{2}{\delta})}}{(2-\frac{2}{\delta})} & \delta < 1 \\ -\lambda(1 - \ln(X)) - \frac{G\overline{M}_{central}}{X} + \ln(X_c) & \delta \geq 1 \end{cases}$$

because the various power law integrals are within quantities of the same Dimensions. Thus

$$\overline{\Phi} - \overline{\Phi_c} = \begin{cases} -\frac{G\overline{M}}{X}\left(\frac{1}{2(\frac{1}{\delta}-1)}\right) - \frac{G\overline{M}_{central}}{X} - \frac{\lambda r_c^{2(1-\frac{1}{\delta})}}{(2-\frac{2}{\delta})} e^{2(1-\delta)T} & \delta < 1 \\ -\frac{G\overline{M}}{X}(1 - \ln(X)) - \frac{G\overline{M}_{central}}{X} + \ln(r_c) - \delta T & \delta \geq 1 \end{cases}$$

which displays that that potential could be taken proportional to Chandrasekhar's definition. The extra, time dependent-only, terms can be considered nearly constant over the last stages of the self-similar phase, when the PDF is measured[1]: δ being very close to 1, the exponential of the steep case is slowly varying and we can neglect the variations of

[1]It can be noted that for our typical steep case, $\epsilon = \frac{5}{2}$, thus $\frac{\delta}{\alpha} = \delta = \frac{2}{3}\left(1 + \frac{1}{\epsilon}\right) = \frac{14}{15}$, the time dependence is then $e^{\frac{2}{15}T}$ and the proportionality constant is:

$$\left(\frac{1}{2(\frac{1}{\delta}-1)}\right) = 7.$$

For our typical shallow case, $\epsilon = \frac{3}{2}$, the index becomes $\frac{\delta}{\alpha} = \delta = \frac{2}{3}\left(1 + \frac{1}{\epsilon}\right) = \frac{10}{9}$, and the time dependence follows $-\frac{10T}{9}$

the shallow case's factor, all the more as the ranges of T usually span less than 2 units of T. Moreover, for the steep case, the power of r_c, very close to -0, is helping to limit the magnitude of the multiplicative constant when we take a very small r_c ($r_c \to 0$) which has then to be not too small. The reference potential can then be used to cancel the averages of the extra terms around the measurement times. For any case, if there is a central non-zero mass, the variation of the potential is dominated by that mass so taking $\overline{\Phi} = -\frac{G\overline{M}}{X}$ is just neglecting the corrections to the evolution with X due to $\overline{Ext}$. The magnitudes of those terms will be evaluated in section 4.2.4.

Presence of a central mass In the presence of a central mass, the evolution of the potential over the halo is essentially dominated by the evolution from the potential of the point mass: the radial derivative of the potential, considering that a finite mass initial perturbation density profile requires that $\epsilon < 3$ and thus that $\delta > \frac{8}{9} > \frac{2}{3}$, is dominated by the central mass term in the limit given below.

$$\frac{d\overline{\Phi}}{dX} = \begin{cases} \frac{\lambda}{(3-\frac{2}{\delta})} X^{(1-\frac{2}{\delta})} + \frac{\overline{M}_{central}}{X^2} = (\frac{\lambda}{(3-\frac{2}{\delta})\overline{M}_{central}} X^{(3-\frac{2}{\delta})} + 1)\frac{\overline{M}_{central}}{X^2} & \delta < 1 \\ \frac{\lambda}{X} + \frac{\overline{M}_{central}}{X^2} = (\frac{\lambda X}{\overline{M}_{central}} + 1)\frac{\overline{M}_{central}}{X^2} & \delta \geq 1 \end{cases}.$$

When the extra term is less than 1, the central mass dominates:

$$\frac{\lambda}{(3-\frac{2}{\delta})\overline{M}_{central}} X^{(3-\frac{2}{\delta})} < 1 \Leftrightarrow X < \left(\frac{(3-\frac{2}{\delta})\overline{M}_{central}}{\lambda}\right)^{\frac{\delta}{3\delta-2}}$$
$$\frac{\lambda X}{\overline{M}_{central}} < 1 \Leftrightarrow X < \frac{\overline{M}_{central}}{\lambda}$$

In other words taking $\overline{W_\Phi} = -\frac{G\overline{M}}{X} \simeq \frac{G\overline{M}_{central}}{X}$ is well justified in the presence of a central mass within the limit radii defined above. Outside of the limit radii, the cases without central mass apply. These radii are evaluated in section 4.2.4.

Steep case without central mass: consequences on the PDF measurements If there is no central mass and we ignore the time variations of X_c, our use of the form $\overline{W_\Phi} = -\frac{G\overline{M}}{X}$ as potential instead of $\overline{\Phi} = -\frac{G\overline{M}}{X}\left(\frac{1}{2(\frac{1}{\delta}-1)}\right)$ has an effect equivalent to shrinking the energy scale for the potential values. Equivalently it has the effect to shrink that scale when measuring the potential. With the definition of energy as $E = \frac{Y^2}{2} + \overline{W_\Phi}$, including the use of $\overline{W_\Phi} = -\frac{G\overline{M}}{X} = 2(\frac{1}{\delta}-1)\overline{\Phi}$, the modifications on the PDF measurements can come from two aspects: the PDF is calculated, in practice, using the phase space volume factor g(E) and the PDF is a function of the energy. Recall that

$$F(E) = \frac{\sum_{E_i \in [E \pm \Delta E/2]} m_i}{\Delta E g(E)}.$$

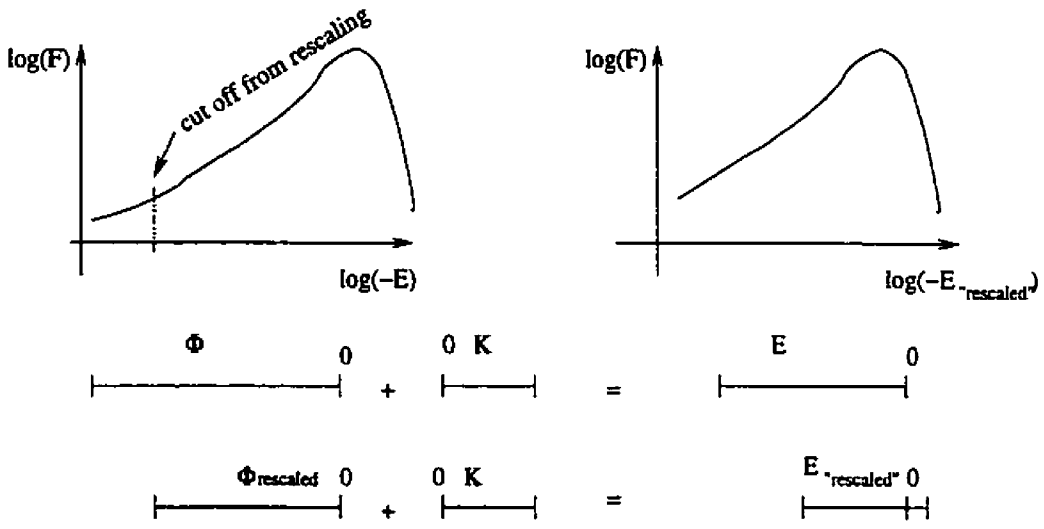

Figure 4.4: Energy rescalings from the use of Chandrasekhar's definition.

Rescaling the potential could first affect the phase space volume factor

$$g(E) = \int \sqrt{\frac{2}{E - \overline{W_\Phi}}} dX.$$

In fact this term remains unaffected since, in its definition, the consistent use of the rescaled $\overline{W_\Phi}$ and of E using the same $\overline{W_\Phi}$ leads to re-obtain $\sqrt{\frac{2}{E-\overline{W_\Phi}}} = \frac{2}{Y}$ as it is evaluated without rescaling the potential energy.

The second modification is more direct: not only the range of E is diminished indirectly through the shrinking of the range of $\overline{\Phi}$, but also the most unbound particles previously counted in the PDF measurement are cut off. Indeed, since the PDF measurement cuts off particles when their energies are measured positive, using $\overline{W_\Phi} = -\frac{G\overline{M}}{X} = 2(\frac{1}{\varsigma} - 1)\overline{\Phi}$ suppresses from the measurements particles which were very marginally bound when using the full potential definition. This reinforces the clarity of the results obtained with such approximation. The total operation on the energy ranges and the PDF is schematised on figure (4.4). We are justified in this approximation again by the SSIM: the real energy is given by

$$E = \overline{\Phi} + \frac{Y^2}{2}.$$

The "rescaled" energy used is

$$E_X = \overline{W_\Phi} + \frac{Y^2}{2} = \varsigma\overline{\Phi} + \frac{Y^2}{2},$$

where $\varsigma = 2(1/\delta - 1) < 1$. We can then write

$$\frac{E_X}{E} = \varsigma\frac{\overline{\Phi}}{E} + 1 - \frac{\overline{\Phi}}{E} = (\varsigma - 1)\frac{\overline{\Phi}}{E} + 1 = (\varsigma - 1)/\varsigma\frac{\overline{W_\Phi}}{E} + 1,$$

which can be considered nearly constant from the SSIM's construction: indeed, in the self similar phase, we can consider the radial energy distribution the same way that we have derived the density. Recall that the density comes from the following Dimensional analysis:

$$\left.\begin{array}{c}[\rho] = \left[\frac{M}{L^3}\right] \\ M \propto e^{\mu T} = e^{(3\delta-2)T} \\ X \propto e^{\delta T}\end{array}\right\} \Rightarrow \left\{\begin{array}{l}\rho \propto \frac{e^{\mu T}}{e^{3\delta T}} = e^{-2T} \\ e^T \propto X^{\frac{1}{\delta}}\end{array}\right. \Rightarrow \rho \propto X^{-\frac{2}{\delta}}.$$

In the same way, we can analyse the energy to get its radial dependence

$$\left.\begin{array}{c}[E] = \left[\frac{L^2}{t^2}\right] \\ t = e^T \\ X \propto e^{\delta T}\end{array}\right\} \Rightarrow \left\{\begin{array}{l}E \propto \frac{e^{2\delta T}}{e^{2T}} = e^{2(\delta-1)T} \\ e^T \propto X^{\frac{1}{\delta}}\end{array}\right. \Rightarrow E \propto X^{2(1-\frac{1}{\delta})}.$$

Together with the definition of the potential from the mass, which is integrated from the density

$$\overline{W_\Phi} = \frac{M}{X} \propto X^{3-\frac{2}{\delta}-1} = X^{2-\frac{2}{\delta}},$$

the ratio of energies is then

$$\frac{E_X}{E} = (\varsigma - 1)/\varsigma\frac{\overline{W_\Phi}}{E} + 1, \text{ with } \frac{\overline{W_\Phi}}{E} \propto \frac{X^{2-\frac{2}{\delta}}}{X^{2(1-\frac{1}{\delta})}} = 1,$$

so that apart from logarithmic corrections, it is constant. In the rest of this work, when dealing with PDFs, E_X will be noted E for convenience. For any other context, E will retain its classical definition.[2]

[2]The sign of $\frac{E_X}{E}$ is positive. This can be seen by considering that, $E < 0$, $|E| \underset{\sim}{<} |\overline{\Phi}|$. Therefore we can write (recall that $\varsigma\overline{\Phi} = \overline{W_\Phi}$)

$$\frac{\overline{W_\Phi}}{E} \underset{\sim}{>} \frac{\overline{W_\Phi}}{\left(\frac{\overline{W_\Phi}}{\varsigma}\right)} = \varsigma,$$

so the ratio is then assured to be positive:

$$\frac{E_X}{E} \underset{\sim}{>} \frac{(\varsigma - 1)}{\varsigma}\varsigma + 1 = \varsigma > 0.$$

ϵ	$\frac{3}{2}$	1.9	$\frac{5}{2}$	2.1
δ	$\frac{10}{9}$	$\frac{58}{57}$	$\frac{14}{15}$	$\frac{62}{63}$
μ_ϵ	2	2	$\frac{15}{7}$	$\frac{63}{31}$
λ_ϵ	1.35×10^4	1.31×10^4	4.21×10^3	7.47×10^3

Table 4.1: Power law proportionality constants measured from simulations using Eq.(4.10). In each case are given the initial power index ϵ, the self-similar class index δ and the final stable power law index μ_ϵ predicted by the SSIM.

Shallow case without central mass In this case, the radial drift or deviation from the Chandrasekhar's potential is neglected compared to its average value and then absorbed in the reference potential. The following section estimates the orders of magnitude of the neglected terms.

Orders of magnitude

The neglected terms can be partly included in the value of the reference potential. It is then of importance to evaluate the magnitude of their drifts with time and with radius. Using measured values of the density profile and their theoretical power laws, one can retrieve the values for the proportionality constants. Then from other given values of the simulations, the relative variations of the time drifts as well as the shallow case's radial drift can be obtained.

Power law density proportionality constants Measuring densities at $X = 10^{-2}$ and $X = 10^{-4}$ and assuming theoretical power laws, the proportionality constant λ_ϵ can be computed:

$$\lambda_\epsilon = \frac{\rho_2 - \rho_1}{X_2^{\mu_\epsilon} - X_1^{\mu_\epsilon}}. \tag{4.10}$$

For the four studied cases (shallow or steep, with or without central mass) we compute the values given in table 4.1.

Radial domain of influence of central masses In the evaluation of the SSIM with central mass, we distinguished two kinds of behaviours: when the central mass is given a real Schwarzschild radius, it is too tiny to allow the model to accrete mass onto that seed. The seed behaves then as a correction to the implementation reproducing the SSIM profile's central cusp otherwise difficult to model numerically. When the Schwarzschild radius is enhanced artificially, some self-similar evolution is perceived and the central mass acquires more shells. The corresponding radii of influence described in section

ϵ	1.9	2.1	1.9	2.1
effective speed of light c	$3 \times 10^8 m/s$	$3 \times 10^8 m/s$	$1.64 \times 10^5 m/s$	$1.64 \times 10^5 m/s$
central mass $m_\bullet$	0.1	0.1	~ 2	~ 2
values for X_{infl}	7.6×10^{-6}	8.9×10^{-6}	$\sim 1.5 \times 10^{-5}$	$\sim 2.0 \times 10^{-4}$

Table 4.2: Central mass radii of dominance for the potential.

ϵ	$\frac{3}{2}$	1.9	$\frac{5}{2}$	2.1
δ	$\frac{10}{9}$	$\frac{58}{57}$	$\frac{14}{15}$	$\frac{62}{63}$
form of $\overline{Drift}(T)$	δT	δT	$7.45 \times 10^4 e^{\frac{2}{15}T}$	$2.93 \times 10^5 e^{\frac{2}{63}T}$
$\overline{\Delta Drift}$	0.2	0.2	$1 - e^{-\frac{4}{15}} \simeq 0.23$	$1 - e^{-\frac{4}{63}} \simeq 0.062$

Table 4.3: Time relative drifts over the significant PDF measurement periods $\overline{\Delta Drift}$. For reference purpose the initial power index ϵ, the self-similarity class δ and the numerical form of the time dependent term $\overline{Drift}(T)$ are given.

4.2.4 are presented in table 4.2 with $X_{infl}(\epsilon = 1.9) = \frac{\overline{M}_{central}}{\lambda}$ and $X_{infl}(\epsilon = 2.1) = \left(\frac{(3-\frac{2}{\delta})\overline{M}_{central}}{\lambda}\right)^{\frac{\delta}{3\delta-2}}$.They all more or less represent tiny fractions of the system (the maximum radius of the system being of order 0.03).

Estimations of the time drifts For each case, the time drift comes from only one term:

$$\overline{Drift}(T) = \begin{cases} -\frac{\lambda r_c^{2(1-\frac{1}{\delta})}}{2(1-\frac{1}{\delta})} e^{2(1-\delta)T} & \delta < 1 \\ -\delta T & \delta \geq 1 \end{cases} . \tag{4.11}$$

Because the PDF measurements take place near the end of the self-similar phase we can evaluate the relative drift by normalising the difference of the Drift at two time bracketing the measurement period: for the steep case we take

$$\overline{\Delta Drift} = \frac{\overline{Drif}(15) - \overline{Drift}(13)}{\overline{Drift}(15)},$$

and for the shallow case, we restrict ourselves to

$$\overline{\Delta Drift} = \frac{\overline{Drif}(10) - \overline{Drift}(8)}{\overline{Drift}(10)}.$$

Since we have used $r_c = X_c(T = 0) = 1.5 \times 10^{-3}$, we can the compute the various cases (see table 4.3).

δ	$\frac{10}{9}$	$\frac{10}{9}$	$\frac{58}{57}$	$\frac{58}{57}$
T	10	8	10	8
$\overline{\Delta Drift}(X)$	$\frac{n}{36} \simeq 0.055$	$\frac{n}{34} \simeq 0.059$	$\frac{n}{13} \simeq 0.15$	$\frac{n}{11} \simeq 0.18$

Table 4.4: Radial maximal relative drifts obtained over the system using Eq.(4.12) for a given combination of self-similarity index δ and relevant measurement time T.

Estimation of the radial drift (shallow case) The shallow case requires to neglect a term in ln(X). In order to treat that term, considering the time drift associated with the full term to neglect ($\ln\left(\frac{X}{X_c}\right)$), a relative radial drift can be estimated using the maximum and minimum X that are primordial to the density and PDF measurements.

Considering that the self-similar cores are usually displaying a stable boundary $X_s \simeq 0.03$ and that we are interested in a radial range of two to three decades inwards, we can take $X \in [X_{min} = X_{max}10^{-n}; X_{max}]$ with $X_{max} = 0.03$ and n=2 to 3. Thus the spatial drift being defined by

$$\overline{Drift}(X) = \ln\left(\frac{X}{X_c}\right),$$

with $X_c = r_c e^{-\delta T}$ the relative drift can then be estimated as

$$\overline{\Delta Drift}(X) = \frac{\overline{Drift}(X_{max}) - \overline{Drift}(X_{min})}{\overline{Drift}(X_{max})} = \frac{n}{\ln\left(\frac{X_{max}}{X_c}\right)} = \frac{n}{\ln\left(\frac{X_{max}}{r_c}\right) + \delta T}. \quad (4.12)$$

Hence the relative drifts for the various cases studied at the edges of the measurement time spans are summarised in table 4.4.

All the drifts obtained being no larger than 20% or so, the terms they represent can therefore be neglected

Conclusion

Given the fact that our simulation reproduces the SSIM approximately, we have thus used the model's predictions to show that the presence of the extra terms in the physical potential with respect to that given by Chandrasekhar's definition can be neglected or absorbed in that definition if the system follows exactly the SSIM. Neglecting those term for the PDF measurements is then an artifact that also neglects large amounts of numerical noise introduced by the finiteness of the number of particles in our simulations, allowing for better resolution than would be allowed by our choice of N. This will be used only for PDF calculations.

4.3 The relation between ϵ_s and the timestep δt

We now have the tools for detailing the approaches to the smoothing length-timestep optimal tuning. This can be explored in the following ways, using the results from the SSIM.

4.3.1 Radial step constraint

Using the force law of Eq.(4.5), one can construct the function relating ϵ_s and $\delta t = f(\epsilon_s)$ from the condition that the relative radial step of all integration timesteps must be small,

$$\frac{\delta r}{r} \ll 1. \tag{4.13}$$

The small timestep approximation ($\delta r \approx v.\delta t \approx a\,(\delta t)^2$), together with the mass profile or mass inside of a given radius, iM, allows one to rexpress the radial step in terms of the acceleration law of Eq.(4.5) and δt:

$$\frac{a(\delta t)^2}{r} = \frac{iM}{(r^2+\epsilon_s^2)^{\frac{3}{2}}}(\delta t)^2 \ll 1.$$

From Eqs.(3.80), the mass profile during the self-similar phase can be written as

$$iM = M_{core}\left(\frac{r}{r_{core}}\right)^{3-\mu}, \tag{4.14}$$

where μ is the logarithmic slope given by Eqs.(3.80). The desired relation is obtained if the radial step condition is calculated at the smoothing scale ($r = \epsilon_s$): hence

$$\frac{a(\delta t)^2}{r} = \frac{M_{core} r_{core}^{\mu-3}}{\sqrt{2}^3}\epsilon_s^{-\mu}(\delta t)^2 \ll 1,$$

so choosing a constant $K \gg 1$ one can rewrite the previous inequality as an equation:

$$(\delta t)^2 = \frac{\sqrt{2}^3 r_{core}^{3-\mu}}{K M_{core}}\epsilon_s^{\mu}$$

or more importantly:

$$(\delta t)^2 \propto \epsilon_s^{\mu}.$$

Timestep versus Kepler's law

Another way of looking at integration constraints is to ask for the integration timestep to be small compared to a Keplerian circular orbit period down to the level of the smoothing scale. Using again Eq.(4.5) to balance a circular acceleration and the period for a circular orbit:

$$\begin{cases} T = \frac{2\pi r_c}{v_c} \\ \frac{v_c^2}{r_c} = \frac{iMr_c}{(r_c^2+\epsilon_s^2)^{\frac{3}{2}}} \end{cases},$$

one can then write, using Eq.(4.14) and taking the smoothing scale as the radius,

$$T^2 = \frac{4\pi^2\sqrt{2}^3}{M_{core}r_{core}^{\mu-3}}\epsilon_s^\mu \gg (\delta t)^2.$$

again, choosing a constant $K' \gg 1$ one can rewrite the previous inequality as an equation:

$$(\delta t)^2 = \frac{4\pi^2\sqrt{2}^3}{K'M_{core}r_{core}^{\mu-3}}\epsilon_s^\mu$$

or more importantly:

$$(\delta t)^2 \propto \epsilon_s^\mu.$$

Self-similar Dimensional analysis and Kepler's law

These results turn out to be similar, in terms of the interdependence of ϵ_s and the timestep. They could have been derived independently through Dimensional analysis, using the scalings of the SSIM from the same techniques as in Eq.(3.28), which already yielded Eqs.(3.26): from $d_M = \begin{pmatrix} 0 & 0 & 0 & 0 & 1 \end{pmatrix} \equiv \begin{pmatrix} -2 & 3 & 0 & 0 \end{pmatrix}$, Eq.(3.28) reads for the mass inside the radius of the core halo

$$iM \propto t^{(3\delta-2)} = e^{(3\delta-2)T}$$

(α is taken to be 1). From Eqs.(3.26), $r \propto t^\delta = e^{\delta T}$,thus $\epsilon_s \propto e^{\delta T}$ Kepler's law, on another hand yields, at the smoothing scale

$$T^2 \propto \frac{\epsilon_s^3}{iM} \propto \frac{\epsilon_s^3}{\epsilon_s^{3-\frac{2}{\delta}}} = \epsilon_s^{\frac{2}{\delta}} = \epsilon_s^\mu,$$

from Eqs.(3.80). So again, requiring the integration timestep to be small, leads to

$$(\delta t)^2 \propto \epsilon_s^\mu.$$

Monte Carlo determination

Eventually, since the previous calculations only give us indications without certainty on the proportionality constant, we tested the balance between timestep and smoothing length in a Monte Carlo survey of their parameter space. The accepted parameter sets correspond to those satisfying the condition of Eq.(4.13), which validity is here set within $\frac{\delta x}{x} < 2.10^{-2}$, for the whole duration of the system's evolution. Because of lack of time, only two survey were performed without checking for variations with angular momentum strength. Those presented here correspond to a moderate amount of angular momentum (see figure 4.5). Those results are assumed to be relatively robust to changes of self-similarity index (since the expected dependence on final density profile index should not vary very much) and angular momentum (it doesn't enter in the expected expression). One run was made at very small smoothing length to check for the influence of it on the dynamics of the relaxed system (see section 6.2.3). We otherwise used the smallest possible smoothing length corresponding to a manageable timestep.

4.4 Equations of motion and integration schemes

4.4.1 Smoothed equations of motion

From Eqs.(3.62), (4.6) and (4.5), the smoothed, self-similar, Lagrangian equations of motion of the system can be rewritten. Despite the fact that we are writing the fully self-similar version of the equations, we are expressing the interior mass and the angular momentum in their non-scaled versions and then scaling them to be used in the fully scaled equations. These are more useful representations of the mass and angular momentum for the following reasons: the former is conserved locally before shell-crossing — and even globally after shell-crossing, when considering the whole halo — and the latter is an integral of the motion. Further notational simplification is then used for the convenience of the programming by using the form

$$g_m = e^{(2-3\delta/\alpha)\alpha T}$$

for the mass scaling factor which translates real mass into self-similar mass according to $\tilde{m}_{self\,similar} = g_m \tilde{m}$, and

$$g_j = \frac{e^{2(1-2\delta/\alpha)\alpha T}}{g_m} = e^{-(\delta/\alpha)\alpha T}$$

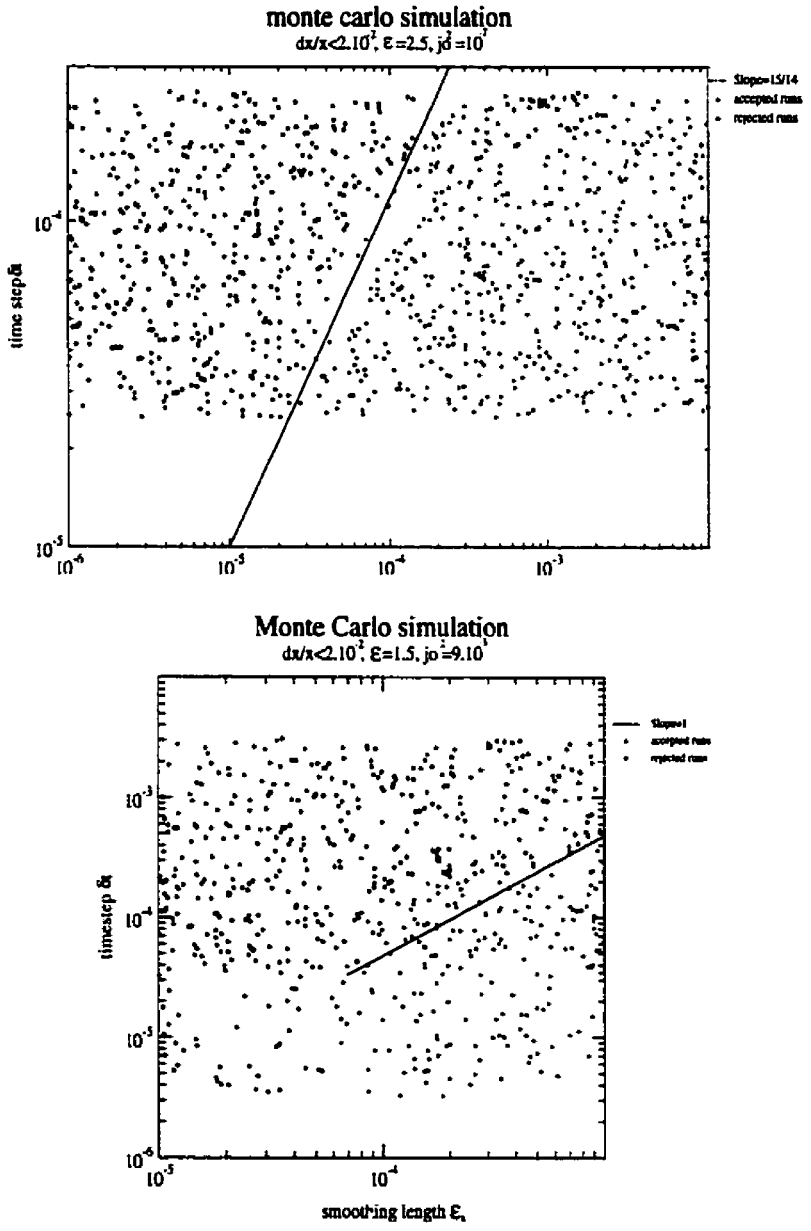

Figure 4.5: Monte Carlo explorations of acceptable timesteps for given smoothing lengths: left, for a steep initial density profile, right, for a shallow one

as a complementary factor that yields the angular momentum scaling ($Z = g_j \cdot g_m \cdot j^2$). The equations of motion then read:

$$\begin{cases} \frac{dY}{dT} = \left(\frac{j^2 g_j X}{(X^2+\epsilon_i^2)^2} - \frac{iMX}{(X^2+\epsilon_i^2)^{\frac{3}{2}}} \right) g_m + (\alpha - \delta) Y \\ \frac{dX}{dT} = Y - \delta X \end{cases}, \tag{4.15}$$

where we usually take α to be 1. Then the self-similarity index is represented by $\delta (\equiv \delta/\alpha)$ and can be related to initial conditions as stated in Eq.(3.67).

4.4.2 The second order Runge-Kutta integration scheme

Thanks to the self-similar expression of the equations of motion and to the Lagrangian treatment of the system, we are left with Ordinary Differential Equations(ODE) (Eqs.(4.15)).

Because of the need to avoid finer integration steps than the smoothing scale, the second order Runge-Kutta method is perfectly adapted for the simulations of our model. It can be expressed as a two step method where the derivatives are directly given by Eqs.(4.15). It should make use of the initial angular momentum distribution and of the calculation scheme of the mass interior to a shell, including self-interaction, from Eq.(4.4).

The Runge-Kutta integration scheme we used can be described as follows. First, we advance the whole N-body system of concentric mass shells to midstep, from T to T + $\frac{h}{2}$, for each shell using a simple Euler integration scheme (i.e. calculating the derivatives at starting point) on its phase space coordinates: for shell of Lagrangian index i,

$$\begin{cases} X_i(T + \frac{h}{2}) = X_i(T) + \frac{h}{2} \frac{dX_i}{dT}(T) \\ Y_i(T + \frac{h}{2}) = Y_i(T) + \frac{h}{2} \frac{dY_i}{dT}(T) \end{cases}.$$

Recall that the derivatives are evaluated using Eqs.(4.15) at the starting point of the timestep. Then the final step is made for each shell from the initial starting point using the derivatives calculated from the midstep state of the whole halo, which requires evaluating again the radial ordering of the shells at midstep,

$$\begin{cases} X(T+h) = X(T) + h \frac{dX}{dT}(T + h/2) \\ Y(T+h) = Y(T) + h \frac{dY}{dT}(T + h/2) \end{cases}.$$

Since the simulations are Lagrangian, it is useful to make it explicit and we did so by labeling the shells with their initial ordering in radius, evolving the physical quantities for each shell by this integration scheme. Because the Y derivative calculation in the integration scheme requires ordering the shells in radial hierarchy (to determine which shells are interior to a given one so that a mass profile can be established), this is done by ordering the shell's indices with their radius value (a detailed exposition of the Lagrangian treatment of the model is given in appendix C).

4.5 Initial conditions

The cosmological Einstein-de Sitter background imposes a choice of initial background density given by Eq.(3.64) and a Hubble initial flow given by Eq.(3.65). The constitution of an initial density profile, which determines the self-similarity index, was treated so as to leave some choice in the amplitude of the cosmological density perturbation.

The initial power law profile central singular cusp[3] of the cosmological density perturbation can be treated in two ways: either by smoothing the density to a constant value in the centre while keeping the same mass interior to the radius at which the density switches from a power law to a polynomial as if it still were constituted from the power law, or by collapsing that mass to a central point mass. The latter can be used to initiate a model of central black hole embedded in a CDM halo. The former can be designated by its treatment of the central cusp's singularity: namely the smoothed central cusp density profile implementation.

The value of the angular momentum can be set to 0 or specified as a non-zero free parameter in the case of the implementation of the angular momentum model, since it is conserved in purely spherical symmetry.

The initial conditions can involve a requirement on the evolution to stop at a certain stage. This allows one to prepare the system for the laying of an overdensity perturbation on the edges of the halo to implement the merger model.

These three last points will be dealt with in the respective chapters devoted to each model implementation. Here we will concentrate on the smoothed central cusp density profile implementation. This has been done in three different alternate ways for the cosmological initial conditions, plus with an additional non-cosmological condition without background. We have in general taken, in the implementation of the program, the cosmological perturbation strength parameter to be

$$A = \frac{1}{2}.$$

This choice of primordial density perturbation amplitude was driven by the constraints imposed on A by methods used in establishing the initial density profile. These methods and their constraints will be detailed in section 4.5.1. The choice of A made is then more a matter of convenience than a significant one. Indeed A governs the density profile's amplitude and therefore regulates the system's virialisation time scale.

[3]central part of a power-law profile that leads to an infinite central density. Cusp is one of the seven types of elementary mathematical catastrophe (Thom R;)

4.5.1 Cosmological perturbation

Initial density profile

We have adopted the following notation for the density profile in our simulations at initial times:

$$\rho = \rho_0(1 + \Delta_d(r, t_i)),$$

with the density contrast, for a central cusp smoothed by a second order polynomial, reading

$$\Delta_d(r, t_i) = \begin{cases} A(1 - B(r/r_{min})^2) & r < r_{min} \\ A(1 - B)(r/r_{min})^{-\epsilon} & r \geq r_{min} \end{cases} . \tag{4.16}$$

The scale of smoothing r_{min} is arbitrary but has to remain small compared to the total size of the halo, since the halo in this model is in theory infinite. However, in a cosmological context, it is limited by the extent of neighbouring halos. Therefore a maximum initial radius r_{max} was also imposed arbitrarily to handle the finite size of simulations. This arbitrariness allows for a scale-independent model which can then be matched to observations in order to determine the real values of the arbitrary units used.

We used the values $r_{min} = 0.5$ and $r_{max} = 15$. The value of B is set by requiring that the total mass inside r_{min} is the same as that which would obtain from keeping the power law cusp.

Initial mass profile

From the density profile given above the cumulative spherical mass inside a given radius is

$$\begin{cases} iM = \int_0^r \rho r^2 dr = \rho_0 r^3 (\frac{1+A}{3} - \frac{A.B(r/r_{min})^2}{5}) & r < r_{min} \\ iM = \int_0^r \rho r^2 dr = \rho_0 r^3 (\frac{1}{3} + \frac{A(1-B)(r/r_{min})^{-\epsilon}}{3-\epsilon}) & r \geq r_{min} \end{cases} . \tag{4.17}$$

These are both of the form:

$$iM = \rho_0 \frac{r^3}{3}(1 + 3.\Delta(r)).$$

The matching of boundary conditions at r_{min} yields the condition on B

$$\frac{A}{3} - \frac{AB}{5} = \frac{A(1-B)}{3-\epsilon} \Rightarrow B = \frac{5\epsilon}{3(\epsilon+2)}.$$

To determine the radii of the shells from this, we start from a grid which sets iM as a function of shell label. So to get non-regular shell spacings, we have to invert $iM(r)$ into $r(iM)$. For the power-law mass contrast ($\Delta(r) \propto r^{-p}$), this is done by Taylor expansion and back substitution. This can be generalised for more general mass contrasts to:

$$\left(\frac{3.iM}{\rho_0}\right)^{\frac{1}{3}} = r(1 + 3.\Delta(r))^{\frac{1}{3}} = r(1 + \Delta(r) + O(\Delta^2))$$

$$\Rightarrow r = \left(\frac{3.iM}{\rho_0}\right)^{\frac{1}{3}} (1 - \Delta(r) + O(\Delta^2)) \simeq \left(\frac{3.iM}{\rho_0}\right)^{\frac{1}{3}} (1 - \Delta(\left(\frac{3.iM}{\rho_0}\right)^{\frac{1}{3}})) \qquad (4.18)$$

which is valid if $3.\Delta(r) < 1$, 1 being the convergence radius of the series $(1+x)^\alpha = \sum_n \binom{\alpha}{n} x^n$.

Keeping this notation for the power law cosmological perturbation and the central smoothed part allows us to maintain without effort the continuity of radius distribution around r_{min}.

This condition on A appears in the following way: for the two domains,

$$3.\Delta(r) = \begin{cases} A(1 - \frac{3.B}{5}\left(\frac{r}{r_{min}}\right)^2) \\ 3\frac{A(1-B)}{3-\epsilon}\left(\frac{r}{r_{min}}\right)^{-\epsilon} \end{cases} \qquad (4.19)$$

with the continuity condition at $r=r_{min}$ $1 - B > 0 \Leftrightarrow 1 - \frac{5\epsilon}{3\epsilon+6} = \frac{6-2\epsilon}{3\epsilon+6} = \frac{2(3-\epsilon)}{3(\epsilon+2)} > 0$, which is always true for $0 < \epsilon < 3$. That condition on ϵ is also implied in the finiteness of the integration of the density, i.e. the finiteness of the total mass.

Hence the inequality governing the convergence of the series yields

$$\begin{cases} \frac{5}{3.B}(1 - \frac{1}{A}) < \left(\frac{r}{r_{min}}\right)^2 \\ r > r_{min}\left(\frac{2A}{(\epsilon+2)}\right)^{1/\epsilon} \end{cases}.$$

For the first domain it is always true if $A < 1$ (i.e. in our choice of A). Otherwise it holds for $r > r_{min}\sqrt{\frac{5}{3.B}(1 - \frac{1}{A})}$. For the second domain, this inequality leads to a validity all the way down to $r = r_{min}$ (the limit of the second domain) for $A < \frac{(\epsilon+2)}{2} (\in [1; \frac{5}{3}]$ when $0 < \epsilon < 3$). Remark that if A¡1 the expansion is always valid. The first shell of the halo at, say a radius r_1, must therefore give the limit on A from the first domain condition:

$$A < \frac{1}{(1 - \frac{3.B}{5}\left(\frac{r_1}{r_{min}}\right)^2)} = \frac{\epsilon+2}{2 + \epsilon(1 - \left(\frac{r_1}{r_{min}}\right)^2)} = A_{limit} < \frac{(\epsilon+2)}{2}$$

and furthermore, this form of limit can be shown to satisfy $A_{limit} > 1$.

In conclusion, the value of the cosmological perturbation strength parameter in the case of a non-constant initial shell spacing (i.e. requiring the inversion of $iM(r)$) is limited by $A < \frac{\epsilon+2}{2+\epsilon(1-\left(\frac{r_1}{r_{min}}\right)^2)}$, which is satisfied for our choice of A($=\frac{1}{2}$).

Shells initial masses and phase space position

The filling of the phase space by our model of discrete shells following Eq.(4.3) representing the continuous halo can be made in three different alternate ways. The first is to

displace the shells' positions after establishing a constant density background halo. The second is to set a constant shell spacing and fill the shell masses according to the modeled density profile. The third is to set the shell positions after distributing the mass of the halo evenly between shells.

In all cases, cosmological shells will follow an initial Hubble flow:

$$y_i = \frac{2}{3} x_i.$$

Then the distinction between methods comes from the use or not of the inversion of the mass profile described in Eq.(4.18), and from the constitution of the intended mass profile.

Constant shell initial density Historically, since the SSIM describes the halo coming from a perturbation of a cosmological constant background, a combination of the implementation of those two main physical ideas was used. First a constant density profile with regularly spaced shells was formed, representing the cosmological background. Then the shells' positions were displaced through Eq.(4.18) to simulate the cosmological perturbation.

Using the initial constant shell spacing the initial background shell positions are distributed evenly on the radial axis so that the number of shells falling inside r_{min} is proportional to its relative size compared with r_{max} (i.e. the number of shells inside r_{min} is $int\left(\frac{r_{min}}{r_{max}}n\right)$ and thus the number left for the power law region is $n - int\left(\frac{r_{min}}{r_{max}}n\right)$). The radial distribution of initial background shells is therefore given by:

$$x_i = \frac{(r_{min})}{int\left(\frac{r_{min}}{r_{max}}n\right)} i \qquad i \leq int\left(\frac{r_{min}}{r_{max}}n\right),$$

$$x_i = r_{min} + \frac{(r_{max} - r_{min})}{n - int\left(\frac{r_{min}}{r_{max}}n\right)} (i - int\left(\frac{r_{min}}{r_{max}}n\right)) \qquad i > int\left(\frac{r_{min}}{r_{max}}n\right).$$

Because of the change in the nature of the density profile at r_{min}, the shell spacing may be slightly different between the two portions of profile, but this scheme ensures that this difference is negligible when n is large (i.e. $\frac{\left(\frac{r_{min}}{r_{max}}n\right) - int\left(\frac{r_{min}}{r_{max}}n\right)}{int\left(\frac{r_{min}}{r_{max}}n\right)} \ll 1$). For the constitution of a Dirac-type density representation of the constant background density profile, that is to say modeled by the form of Eq.(4.3), the mass for Lagrangian shell labeled i is found as:

$$mass(i) = m_i = \rho_0 \frac{\left((x_i)^3 - (x_{i-1})^3\right)}{3}$$

with the convention $x_{i-1} = 0$ for i=1 (0th shell reduces to the central point), so the mass profile is

$$iM(x_i) = \rho_0 \frac{(x_i)^3}{3}.$$

Using then this mass profile in Eq.(4.18), the density perturbation imposed by the expressions for the mass contrast (Eqs.(4.19)) shifts the spacings according to:

$$x(i) = x_i(1 - A\left(\frac{1}{3} - \frac{B}{5}.\left(\frac{x_i}{r_{min}}\right)^2\right)) \qquad x(i) < r_{min},$$

$$x(i) = x_i(1 - \frac{A(1-B)}{3-\epsilon}.\left(\frac{x_i}{r_{min}}\right)^{-\epsilon}) \qquad x(i) \geq r_{min}.$$

The interest of this method lies in its link with the physical picture of primordial density perturbation. Indeed, the cosmological perturbation is represented by the density of shells along the radial axis, an even spacing meaning no perturbation. Its interest also lies in the increased mass resolution at the beginning of the self-similar accretion phase due to the decrease in mass for shells when going closer to the centre. This latter feature, because of the exponential growth of the accretion during the self-similar phase, will provide a more constant self-similar mass resolution (the growing real masses being more and more scaled down when considering their self-similar measure) than if the real mass resolution was kept constant.

The drawbacks of this method become obvious when the phase space population is measured, since each particle weighs differently. This is combined with the inaccuracy implied by the need for an approximate inversion to get the shell's radii.

Constant shell initial spacing With a constant initial shell spacing, there is no need for the approximate mass-radius inversion, and the benefits of increased mass resolution in the early stages of the evolution remain.

As for the previous case the shell positions are evenly spaced and distributed between the two domains divided by r_{min}. For shells inside r_{min},

$$x(i) = x_i = \frac{(r_{min})}{int\left(\frac{r_{min}}{r_{max}}n\right)}i \qquad i \leq int\left(\frac{r_{min}}{r_{max}}n\right).$$

The masses of shells reproducing the Eq.(4.3)-type density directly come from the difference between subsequent values of the appropriate initial mass equation from Eqs.(4.17):

$$mass(i) = m_i = \rho_0 \left[\frac{\left((x_i)^3 - (x_{i-1})^3\right)(1+A)}{3}\right.$$

$$-\frac{A.B\left((x_i)^5-(x_{i-1})^5\right)}{5r_{min}^2}\Bigg] \qquad r \leq r_{min}$$

with the convention $x_{i-1}=0$ for i=1 (0th shell reduces to the central point). For shells over r_{min},

$$x(i)=x_i=rmin+\frac{(r_{max}-r_{min})}{n-int\left(\frac{r_{min}}{r_{max}}n\right)}(i-int\left(\frac{r_{min}}{r_{max}}n\right)) \qquad i>int\left(\frac{r_{min}}{r_{max}}n\right).$$

Again, the masses of the shells are direct retranscriptions of the appropriate equation from Eqs.(4.17):

$$mass(i)=m_i=\rho_0\Bigg[\frac{\left((x_i)^3-(x_{i-1})^3\right)}{3}$$

$$+\frac{A.(1-B)\left((x_i)^{3-\epsilon}-(x_{i-1})^{3-\epsilon}\right)}{r_{min}^{-\epsilon}(3-\epsilon)}\Bigg] \qquad r>r_{min}.$$

If phase space densities are to be measured (e.g. to measure the PDF of the system) the extra variation coming from the different weighting of each shell makes it more difficult, so a constant mass for all shells is recommended.

Constant shell mass In that case, the mass distribution among shells is trivial,

$$mass(i)=m_i=smass=cst,$$

and so is the shell's inside mass distribution,

$$iM(i)=i.smass,$$

but at the cost of having to use the mass-radius inversion approximation (Eq.(4.18)):

$$x(i)=\left(\frac{3.i.smass}{\rho_0}\right)^{\frac{1}{3}}(1-A(\frac{1}{3}-\frac{B}{5}.\left(\frac{\left(\frac{3.i.smass}{\rho_0}\right)^{\frac{1}{3}}}{r_{min}}\right)^2)) \qquad x(i)<r_{min},$$

$$x(i)=\left(\frac{3.i.smass}{\rho_0}\right)^{\frac{1}{3}}(1-\frac{A(1-B)}{3-\epsilon}.\left(\frac{\left(\frac{3.i.smass}{\rho_0}\right)^{\frac{1}{3}}}{r_{min}}\right)^{-\epsilon}) \qquad x(i)\geq r_{min}.$$

4.5.2 Non-cosmological test of the dynamics

Since we know from Henriksen &Widrow [41] the behaviour of a pure power law initial condition without initial velocities, a good test of the validity of the simulation was performed by reproducing those results.

Initial density profile

Using the same definition as in Eqs.(4.16), the initial density distribution is set to

$$\rho = \rho_0 \Delta_d(r, t_i).$$

The same conditions on the mass profile around r_{min} used for the cosmological cases are applied here.

Initial mass profile

The cumulative spherical mass inside a given radius follows from the previous density profile

$$\begin{cases} iM = \int_0^r \rho r^2 dr = \rho_0 r^3 (\frac{A}{3} - \frac{A.B(r/r_{min})^2}{5}) & r < r_{min} \\ iM = \int_0^r \rho r^2 dr = \rho_0 r^3 (\frac{A(1-B)(r/r_{min})^{-\epsilon}}{3-\epsilon}) & r \geq r_{min} \end{cases}$$

Since we will only be using a constant shell initial spacing method, there is no need to invert the mass profile.

Shells initial masses and phase space position

As in Henriksen &Widrow [41], we assume no flow:

$$y(i) = 0$$

Constant shell spacing The choice of constant shell initial spacing is made because it is the simplest to implement. Shells are evenly placed along the radial axis according to the same scheme as in section 4.5.1. For shells within r_{min},

$$x(i) = x_i = \frac{(r_{min})}{int\left(\frac{r_{min}}{r_{max}} n\right)} i \qquad i \leq int\left(\frac{r_{min}}{r_{max}} n\right).$$

The corresponding mass, calculated similarly to the constant shell spacing implementation of section 4.5.1, reads

$$mass(i) = m_i = \rho_0 A.(\frac{\left((x_i)^3 - (x_{i-1})^3\right)}{3}$$

$$-B\frac{\left((x_i)^5-(x_{i-1})^5\right)}{5.r_{min}^2}) \qquad r \leq r_{min}$$

with the convention $x_{i-1}=0$ for i=1 (0th shell reduces to the central point). For shells over r_{min},

$$x(i)=x_i=rmin+\frac{(r_{max}-r_{min})}{n-int\left(\frac{r_{min}}{r_{max}}n\right)}(i-int\left(\frac{r_{min}}{r_{max}}n\right)) \qquad i>int\left(\frac{r_{min}}{r_{max}}n\right),$$

and the masses are even simpler

$$mass(i)=m_i=\rho_0.\frac{A(1-B)}{r_{min}^{-\epsilon}}\frac{\left((x_i)^{3-\epsilon}-(x_{i-1})^{3-\epsilon}\right)}{3-\epsilon} \qquad r>r_{min}.$$

Results and comparison with Henriksen & Widrow

The results of a test run using those non-cosmological initial halo conditions are shown in figure 4.6. the upper panel displays the virial ratio evolution with self-similar time, showing clearly the self-similar phase followed by the virialised phase. The middle panel gives the phase space distribution of equal mass shells near the end of the self-similar phase (recall that Y is the self-similar velocity and X, the self-similar radius). In contrast with simple cosmological SSIM, the stream of particles emerging out of the core for the first time seems to be submitted to stronger phase space instability. The lower panel shows the density profile to be reproducing well the r^{-2} law from Henriksen & Widrow [41], given that the initial density profile starts shallower than r^{-2}.

4.5.3 Density definition by shells and their positions

Once the system is modeled in the code, the density can be measured back from the halo. But one has to keep in mind the original definition of the shells: each infinitely thin shell represents the distribution of its mass over the volume contained between it and its radial predecessor. Then , depending on the presence of a background or not, can be measured the density contrast or the density relative to that of a reference de Sitter universe.

In addition we allowed for a certain non-linear averaging to smooth the measurements of density which showed up very noisy. If a number *smooth* of shells over which the density is smoothed is specified at the beginning of the simulation, all density measurements around shell "i" will use the mass of shell(s) specified as (E(n) being the integer part of n)

$$MASS_i=\sum_{i=b_{inf}=\max(i+E(smooth/2)-smooth+1,1)}^{b_{sup}=\min(i+E(smooth/2),n)} m_i,$$

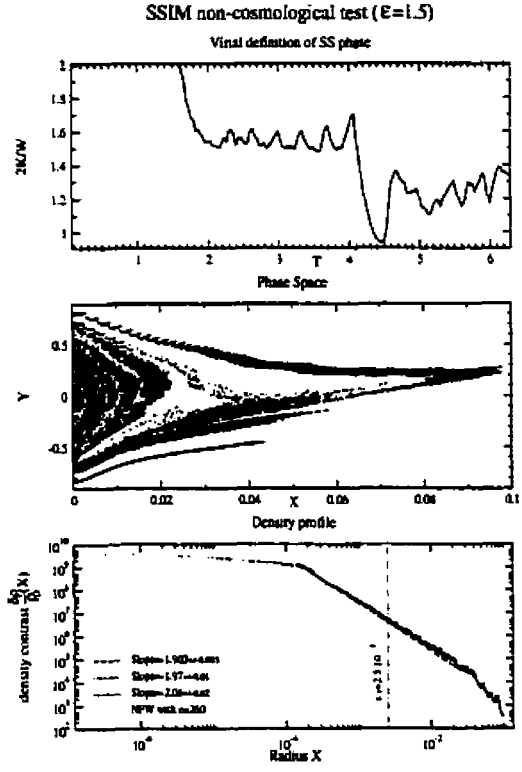

Figure 4.6: Non Cosmological SSIM halo simulation. The upper panel shows the evolution of the virial ratio, the middle one displays the system's phase space (self-similar radial velocity, Y, versus radius, X) at the end of infall and the lower panel gives the density profile. In the phase space representation, each dot stands for one simulated particle. The density profile is fit with power laws above and below the smoothing length ϵ_s. Since a logarithmic slope of about -2 is obtained in both cases, a fit is given for the whole halo which yields also -2. For comparison, an NFW profile fit is also displayed.

(which is the sum of the masses of a number *smooth* of shells centered on the measuring location shell "i") and the corresponding 'volume' of those shells is given by

$$VOLUME_i = x^3_{b_{\sup}} - \left\{ \begin{array}{cc} (x_{b_{\inf}-1})^3 & if\ b_{\inf} \neq 1 \\ 0 & otherwise \end{array} \right\}.$$

Density contrast with cosmological background

We measure the density contrast over a number of shells given by smooth according to the following definition:

$$\frac{\delta\rho}{\rho_0}(i) = \frac{MASS_i}{\frac{\rho_0}{3}(VOLUME_i)} - 1.$$

For a value of *smooth* equal to 1 (no smoothing), we find the elementary definition of the original density of the shell:

$$MASS_i = m_i,$$

and

$$VOLUME_i = x_i^3 - x_{i-1}^3,$$

then

$$\frac{\delta\rho}{\rho_0}(i) = \frac{m_i}{\frac{\rho_0}{3}\left(x_i^3 - x_{i-1}^3\right)} - 1.$$

Relative density without cosmological background

For the case of relative density, the de Sitter universe is just one with the constant density ρ_0. Using the same definitions, one can express the density relative to the smooth de Sitter model as:

$$\frac{\rho}{\rho_0}(i) = \frac{MASS_i}{\frac{\rho_0}{3}(VOLUME_i)},$$

which again yields the usual forms in the case without smoothing.

Chapter 5

SSIM Probability Distribution Function (PDF) and sensitivity to mergers

> You never go as far as when you don't know where you are going.
>
> OLIVER CROMWELL (1599-1658)

This chapter deals with the first explorations of the SSIM's power to bring light on the understanding of gravitational relaxation in Large Scale Structure Formation. In a first section, the specifications and problems encountered when measuring PDFs on our implementations of the SSIM and its extensions are laid out. Then, results on the SSIM's PDF from Henriksen & Widrow are confirmed, consolidated and extended in a second section. The third section explains the technical details of implementing our model for mergers[1] into the SSIM. Finally, the last section will describe the results from our study of the SSIM's sensitivity to merger perturbations.

5.1 Measurement of Probability Distribution Functions: Preliminary definitions, predictions and calibrations

The measurement of PDFs for evolved systems does not necessarily require the mass of individual shells to be constant, but a constant mass resolution is preferable for ensuring that the phase space distribution of particles reflects that of the phase space distribution

[1] recall that mergers points towards the merging of comparable sized haloes

in mass and for avoiding distortions from effects coming from the finite size of the mass of shells. This section will show how to extract the PDF from a discrete distribution of mass particles in phase space in the case of a purely radial spherical system, and of isotropic angular momentum. It will explain the importance of the phase space correction factor and its sensitivity to the effective gravitational potential energy. It will show the successful testing of the code respectively on a Plummer spherical model for isotropic velocity distribution, and on the purely radial Henriksen & Widrow spherical model.

5.1.1 Extraction of the PDF

The standard output that is available from simulations to measure a system's PDF is its collection of mass and phase space positions. The aim of this section is to link the general distribution function to its definition in terms of particles' masses and phase space positions. The terminology of probability introduces itself naturally in this phase space density context through the assumption of the ergodic hypothesis (the equivalence between presence probability at one point and number of occurrence of elementary systems in the large total number of systems approximation).

Definition of PDF

We are here only interested in PDFs that exclusively depend on the specific energy E integral of motion. The PDF is defined as the phase space mass density. Using the radial/tangential decomposition of the velocity differential and the spherical volume element, one can write the phase space elementary volume as $dV_{PhSp} = dV.dV_{\vec{v}} = dr.r^2 \sin\theta d\theta d\varphi dv_r dv_\perp v_\perp d\varphi_{v_\perp}$ (r,θ and φ are the usual spherical coordinates,v_r, $v_\perp$ and $\varphi_{v_\perp}$ are the radial velocity and the polar coordinates of the part of the total velocity orthogonal to the radial velocity), but because of spherical symmetry all angles are integrated over and the definition of angular momentum $j^2 = r^2 v_\perp^2$ simplifies the phase space volume element into $dV_{PhSp_{Sph}} = 4\pi^2 dr dv_r dj^2$. Because of the normalisation of the PDF, constants can be ignored until the end and we will use the system's self-similar variables phase space element $dXdYdj^2$ (where we don't use Z, the scaled version of j^2 for the conservation reasons discussed in section 4.4.1). The definition of the PDF then reads

$$F(E) = \left\langle \frac{d^3M}{dXdYdj^2} \right\rangle = \frac{d^3M}{dXdYdj^2} = \frac{\partial\Gamma}{\partial Y},$$

where we have defined the function $\Gamma = \frac{d^2M}{dXdj^2}$, and where the rescaled PDF F(E)=$4\pi^2 f e^{-(2\delta-\alpha)T}$, with the usual distribution function in spherical symmetry defined as $f = \frac{d^6M}{dV_{PhSp_{Sph}}}$, the elementary phase space volume in spherical symmetry being noted $dV_{PhSp_{Sph}}$. Since F

only depends on E, it is more convenient to select a measurement grid on the phase space in terms of E and thus estimate the following alternate PDF:

$$F_1 = \frac{d^3M}{dXdEdj^2} = \frac{\partial\Gamma}{\partial E}.$$

Recall that the specific energy is (the potential energy being here written as $W_\Phi(X)$)

$$E = \frac{Y^2}{2} + \frac{j^2}{2X^2} + W_\Phi(X) \Rightarrow Y = \pm\sqrt{2(E - W_\Phi) - \frac{j^2}{X^2}},$$

where the specific energy self-similar versions of Eqs.(4.7) and (3.11), the latter in its smoothed form derived from Eq.(4.5), have been used (respectively for the kinetic energy and Chandrasekhar's potential energy). The importance of F_1 lies in the fact that it can be directly estimated by choosing the mass contained in a restricted phase space volume around a given E and thus it singles out the dependence on E. To switch from one phase space representation to the other, we can use the differential of Γ defined above: with the velocity differential $dY = \pm\frac{dE}{Y} + \frac{\partial Y}{\partial X}dX + \frac{\partial Y}{\partial j^2}dj^2$, one can rewrite the differential from

$$d\Gamma = \left.\frac{\partial\Gamma}{\partial Y}\right|_{X,j^2} dY + \left.\frac{\partial\Gamma}{\partial X}\right|_{Y,j^2} dX + \left.\frac{\partial\Gamma}{\partial j^2}\right|_{X,Y} dj^2 = F(E)dY + \left.\frac{\partial\Gamma}{\partial X}\right|_{Y,j^2} dX + \left.\frac{\partial\Gamma}{\partial j^2}\right|_{X,Y} dj^2$$

as the energy, instead of velocity, dependent

$$\begin{aligned} d\Gamma = \left.\frac{\partial\Gamma}{\partial E}\right|_{X,j^2} dE + \left.\frac{\partial\Gamma}{\partial X}\right|_{E,j^2} dX + \left.\frac{\partial\Gamma}{\partial j^2}\right|_{E,X} dj^2 &= \frac{F(E)}{Y} dE + \left.\frac{\partial\Gamma}{\partial X}\right|_{E,j^2} dX + \left.\frac{\partial\Gamma}{\partial j^2}\right|_{E,X} dj^2 \\ &= F_1 dE + \left.\frac{\partial\Gamma}{\partial X}\right|_{E,j^2} dX + \left.\frac{\partial\Gamma}{\partial j^2}\right|_{E,X} dj^2 \end{aligned}$$

yielding the definition of F_1 as

$$F_1 = \frac{F(E)}{Y} = \frac{F(E)}{\pm\sqrt{2(E - W_\Phi) - \frac{j^2}{X^2}}}. \tag{5.1}$$

This will entail the development of a phase space transformation factor (based on the expression noted $\frac{1}{\sqrt{2(E-W_\Phi)-\frac{j^2}{X^2}}}$ and used above), which will reveal itself to be crucial later on. Recall that the definition of W_Φ is derived from the specific energy self-similar version of Eq.(3.11), in the smoothed form deduced from Eq.(4.5). Again, the need for such a transformation comes from the fact that even if F(E) only depends on E, this will not be apparent since E is a compound of F's variables, while E is an independent variable of F_1 and will therefore make clear the energy dependence in F.

From the measurement side, we also have access to a collection of masses with their E-sliced phase space discrete distribution:

$$F_1 = \frac{d^3M}{dXdEdj^2} = \sum_i m_i\delta(E - E_i)\delta(X - X_i)\delta(j^2 - j_i^2) \tag{5.2}$$

where i is the particle's label and δ is the usual Dirac distribution. All the expressions obtained above can be transformed into purely radial ones (their equivalent in the strict absence of angular momentum) by setting j^2 to 0 and replacing any derivation by j^2 with the identity operation.

Phase space factor and PDF

From Eq.(5.2), the integration over a patch of phase space yields a measurement of F_1 that can be related to F using Eq.(5.1):

$$2\int_{E-\Delta E/2}^{E+\Delta E/2} dE \int_{X-\Delta X/2}^{X+\Delta X/2} dX \int_{j^2-\Delta j^2/2}^{j^2+\Delta j^2/2} dj^2 F_1 = \sum_{\substack{i \\ |X-X_i|\leq \Delta X/2 \\ |E-E_i|\leq \Delta E/2 \\ |j^2-j_i^2|\leq \Delta j^2/2}} m_i.$$

The factor 2 comes from the integration over E as one value of energy corresponds to two values of velocity (positive and negative). But for F depending only on E, the integration can be extended over the full ranges of radius and angular momentum belonging to the same energy range. Then F can be reached through a sum of masses, contained in the corresponding phase space patch, following

$$\sum m_i = 2\int dE dX dj^2 \frac{F(E)}{Y} = 2\int dE.F(E) \int \frac{dX dj^2}{Y},$$

so around $E = E_0$, assuming that $2F(E)\int \frac{dXdj^2}{Y}$ varies slowly with E, and noting the phase space factor $g(E) = 2\int \frac{dXdj^2}{Y}$, one can integrate over E by the use of Rolle's theorem, also known as the mean value theorem

$$\sum m_i = \Delta E.F(E_0).g(E_0).$$

The phase factor then contains the only discrimination between various geometries of infall in this otherwise general expression.

Phase space factor in radial orbits The simplest measurement come from radial orbits, present in the original SSIM Henriksen & Widrow model and the present work's extensions with an overdensity and in the radial halo surrounding a black hole. In this case, the phase space factor only comprises an integration over all allowed radii

$$g(E) = 2\int_{X_{min}}^{X_{max}} \frac{dX}{\sqrt{2(E-W_\Phi)}}, \tag{5.3}$$

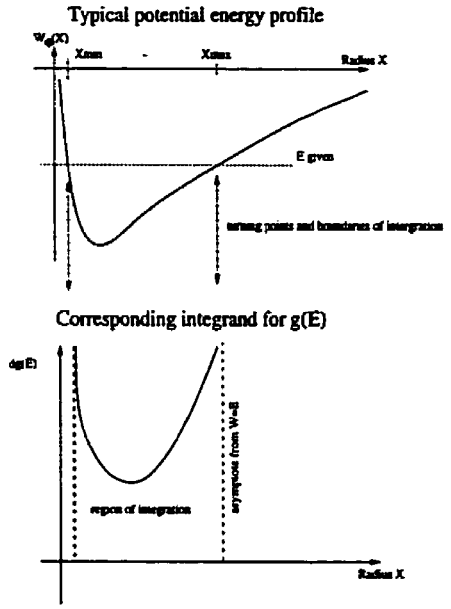

Figure 5.1: Typical behaviour of the integrand for the radial phase space density of states factor.

the lower limit being different from 0. This lower limit springs out of the modeling of the mass distribution by finite size masses. At small radius, the quality of the modeling degrades when the number of particles within a given radius becomes negligible compared with the number of particles in the halo. Because of the degradation of the quality of the modeling , this definition induces a cut off in the potential energy which tends to 0 at the origin, even in cases where the theoretical potential energy should diverge. Those boundaries are set by the need for the square root argument in the integral of Eq.(5.3) to be strictly positive at fixed E:

$$W_\Phi = E \Leftrightarrow (X = X_{min} \text{ or } X_{max}).$$

the integration corresponds to finding the area between the two boundaries and the X-axis and the curve (or integrand)

$$dg(E) = \frac{2}{\sqrt{2(E - W_\Phi)}}$$

which typically has an asymptote at each boundary (see figure 5.1).

Phase space factor in isotropic orbits If the orbits depart from radial infall but the velocity distribution is isotropic with respect to the centre of the halo, Henriksen &

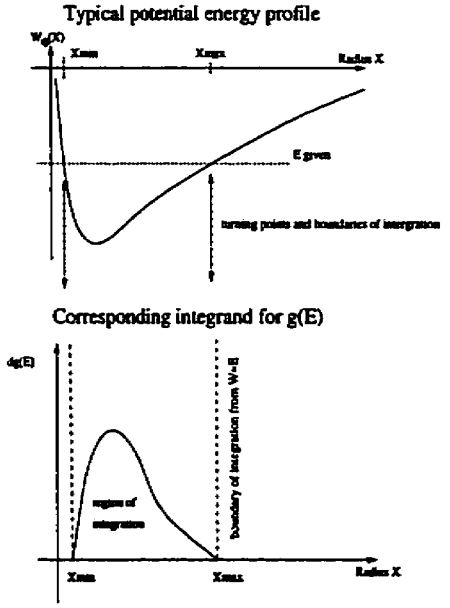

Figure 5.2: Typical behaviour of the integrand for the isotropic phase space density of states factor.

Widrow [44] have shown that an equilibrium state would admit a PDF depending only on the energy. The phase space factor then reads

$$g(E) = 2\int_{X_{min},0}^{X_{max}\, j^2_{max}} \frac{dX dj^2}{\sqrt{2(E - W_\Phi) - \frac{j^2}{X^2}}},$$

but the integration over the angular momentum can be performed analytically. The maximum value for angular momentum is imposed by the condition that the square root in the integrand keeps a positive argument. Thus the angular momentum can only reach up to $j^2_{max} = 2(E - W_\Phi(X))X^2$ at fixed E and X. The phase factor then yields

$$g(E) = \int_{X_{min}}^{X_{max}} dX 4\sqrt{2(E - W_\Phi)}X^2, \tag{5.4}$$

which integrand is better behaved than in the radial case since no asymptotes are present here (see figure 5.2).

Phase space factor in anisotropic orbits Even though the anisotropic case was not developed in the present work, thought was given to its requirements for PDF measurements. This may allow for fast developments of anisotropic, spherically symmetric PDF

measurements in the near future. In this case, F=F(E,j^2) so the approximations made have to be restricted by weaker assumptions: the mass distribution can be rewritten

$$\sum m_i = 2 \int dE dX dj^2 \frac{F(E,j^2)}{Y} = 2 \int dE dj^2 . F(E,j^2) \int \frac{dX}{Y}.$$

Thus, around $E = E_0$ and $j = j_0$, assuming that $2F(E,j^2) \int \frac{dX}{Y}$ varies slowly with E and j, and writing again the phase space factor $g(E) = 2 \int \frac{dX}{Y}$, one can integrate over E and j^2 by Rolle's (or mean value) theorem

$$\sum m_i = \Delta E \Delta j^2 . F(E_0, j_0^2) . g(E_0, j_0^2).$$

The phase space factor then becomes

$$g(E,j^2) = 2 \int_{X_{min}}^{X_{max}} \frac{dX}{\sqrt{2(E - W_\Phi(X)) - \frac{j^2}{X^2}}}, \tag{5.5}$$

and again the integrand diverges on the boundaries in a fashion similar to the radial case, at fixed E and j^2 (refer to figure 5.1).

Because of the double variable dependence of the measurements, each measurement implies that a smaller number of particles has been used than for the single variable cases, leading to mass resolution problems.

Indeed, simulations model a continuous mass distribution in phase space with a discrete set of point particles by having each of them represent a small density patch. Liouville's Theorem tells us that the evolution of the system should conserve the phase space volume of those patches but certainly not their shape. Evolution should then deform those patches so trying to hold on to the original tiling is not a practical method. The measurements done then superimpose on the phase space another tiling of patches corresponding to the double variable mean field approximation region $\Delta E \Delta j^2$ (see figure 5.3). If those new patches are large enough compared to the discretisation ones, the measurement behaves as if the model distribution was continuous. If its size starts to compare with the discretisation patches, the measurement becomes poor and unreliable.

5.1.2 Models' predictions

For each of the three symmetries discussed above, some models of static equilibrium can yield predictions for their measurements. Henriksen & Widrow [44] made predictions on self-similar static models that can be applied here: static states can be seen as end products of the self-similar evolution for which the transition to virialisation seems to conserve their main features.

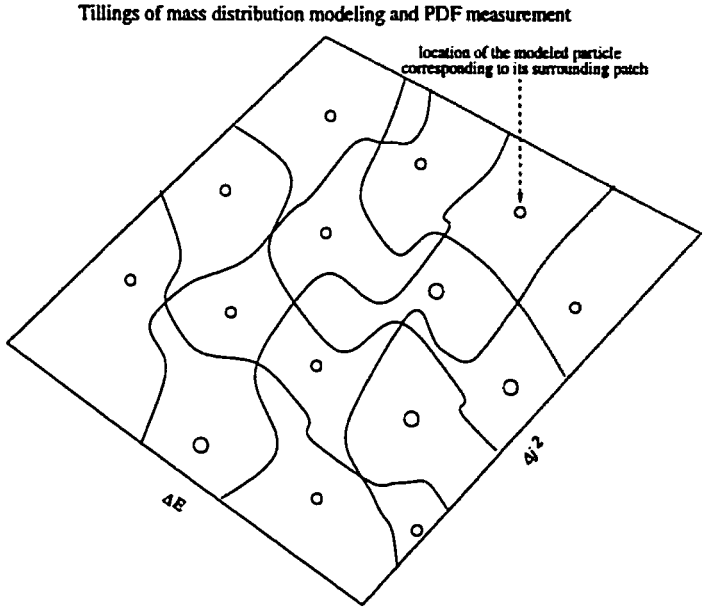

Figure 5.3: The regular outer boundaries of the diagram represent the PDF measurement tiling, the inner boundaries represent the tiling from the mass distribution resolution deformed by the Liouville flow. Because of the low number of mass particles in this particular example, a similar configuration should yield a poor and unreliable PDF measurement.

In the pure radial case, they found a density profile and distribution function that are only functions respectively of radius and specific energy in the form:

$$\rho \propto r^{-\frac{2\alpha}{\delta}}$$
$$F(E) \propto (-E)^{\frac{1}{2}},$$

which is also obtained in their dynamical exploration of the radial collapse in [42], although their measurement of the PDF only spans a decade in energy.

Another radial equilibrium system appears in Binney & Tremaine [87] p281, which is improperly qualified as the only one in this symmetry (the HW self-similar system being another one), is the Fridman-Polyachenko system. It follows

$$\rho \propto \begin{cases} r^{-2} & r \leq r_0 \\ 0 & r > r_0 \end{cases}$$
$$F(E) \propto \begin{cases} |E - E_0|^{-\frac{1}{2}} & E \leq E_0 \\ 0 & E > E_0 \end{cases},$$

where E_0 is the minimum specific energy a particle can have. Because this system's dependence on E is different than the power law form expected in measurements on the SSIM, it was eventually not used for calibrations of the measuring code. All in all, it seems that the Fridman-Polyachenko system fills the $\delta/\alpha = 1$ gap left in the static Henriksen & Widrow continuum of solutions by their choice of δ ($\delta_{HW95} = \frac{\delta}{\delta-\alpha}$with δ and α from our present choice of values: it appears then that $\delta/\alpha = 1$ cannot be treated by HW95's choice since it corresponds to $\delta_{HW95} = \infty$).

In the isotropic case, polytropes yield a simple example of PDF, in particular, the Plummer's spherical model. Rasio *et al.* [99] use that polytrope in terms of the density and distribution function to test their pure phase space approach to spherical collapse PDF evolution, Binney & Tremaine [87] describe Plummer's model as a polytrope with index n=5:

$$\rho \propto \left(1 + \frac{r^2}{a^2}\right)^{-\frac{n}{2}}$$
$$F(E) \propto \begin{cases} |E|^{n-\frac{3}{2}} & E < 0 \\ 0 & E \geq 0 \end{cases}.$$

This model was used to calibrate the measurement code for isotropic systems. Henriksen & Widrow's self-similar static solutions also constitute an isotropic solution of the following form

$$\rho \propto r^{-\frac{2\alpha}{\delta}}$$
$$F(E) \propto (-E)^{\frac{3\delta-\alpha}{2(\delta-\alpha)}},$$

but an isotropic velocity distribution was not set up (only an isotropic angular momentum distribution was implemented).

The anisotropic case leads Henriksen & Widrow [44] to predict a distribution function of the form

$$F(E, j^2) = j^{-\frac{3\delta-\alpha}{2\delta-\alpha}} \overline{F}(\xi)$$
$$\xi = j^{-2} |2E|^{\frac{2\delta-\alpha}{\delta-\alpha}}$$

where $\overline{F}$ is an arbitrary function. As stated in the previous section, measurements of this distribution function are submitted to the impoverishment of the statistics compared to the univariate measurements and were not implemented.

5.1.3 The potential energy

We have used the Chandrasekhar definition of potential energy throughout this work. The nature of our systems and the stability of this definition justifies this choice: the systems we deal with are finite in size. They don't extend to infinity. They are also not isolated in general: there exists an essential mass flux through their boundary during the self-similar phase. These two properties generate non-vanishing surface terms in any calculations, modifying the equivalences between classical definitions of the potential energy ($W \propto \int |\nabla\Phi|^2$, $\int \rho\Phi$ *or* $\int \rho r \nabla\Phi$). Moreover, Binney & Tremaine [87], p68, already give an account of the potential energy of a spherically symmetric system in terms coming from the Chandrasekhar definition (Eq.(3.11)). That is why this work has used that definition, which with its gradient of the potential, makes the contributions to the potential from the outside shells vanish in the potential energy. Therefore the specific potential energy of one shell in the systems is given by

$$W_\Phi = -\frac{iM(X_i)}{X_i}.$$

This form is also confirmed *a posteriori* by the successful reproductions of the Plummer and Henriksen & Widrow models as a calibration of the code (see figure 4.3).

In addition we must take into account the fact that the systems studied involve a smoothing length which softens the potential energy. Now the PDF measurement is an independent snapshot of the state of the system, so we can introduce the smoothing length at the level of the potential energy independently from the dynamics of the simulation. This contrasts with the introduction of ϵ_s in the dynamical integration, for which the force law has to derive from the same source as the potential energy in a consistent way. Introducing the smoothing length at the level of the potential energy, the simplest way is to replace the square of the radius by a smoothed radius as follow:

$$W_\Phi = -\frac{iM(X_i)}{\sqrt{X_i^2 + \epsilon_s^2}},$$

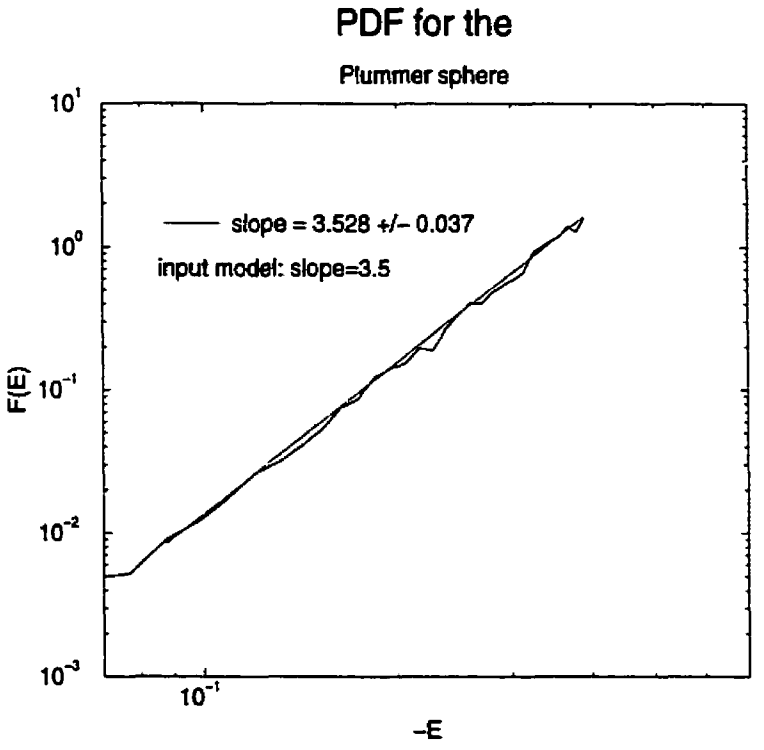

Figure 5.4: Reproduction of Plummer's model PDF from its phase space (data from Merrall, T., personal communication [100]).

the mass tending to 0 at the origin, the energy will do so at the same rate instead of with a power of X.

5.1.4 Testing the methods

In order to check the validity of the measurements of subsequent system's PDF, The method was confronted with data generated from well known and well behaved models.

The first model to be reproduced was the PDF for a Plummer's sphere, since its phase factor, given in Eq.(5.4), is easier to compute because of its well behaved integrand. We used also the simulation's form for the smoothing of the potential (see figure 4.3), but the best results were obtained with the definition of the previous section (5.1.3). The phase space realisation of the Plummer model was granted by my fellow student, Tom Merrall [100]. Its results can be seen on figure 5.4.

The second test concerned the fully radial infall PDF measurements. Its singular phase factor Eq.(5.3) is the only difference in its calculation from the isotropic measurement

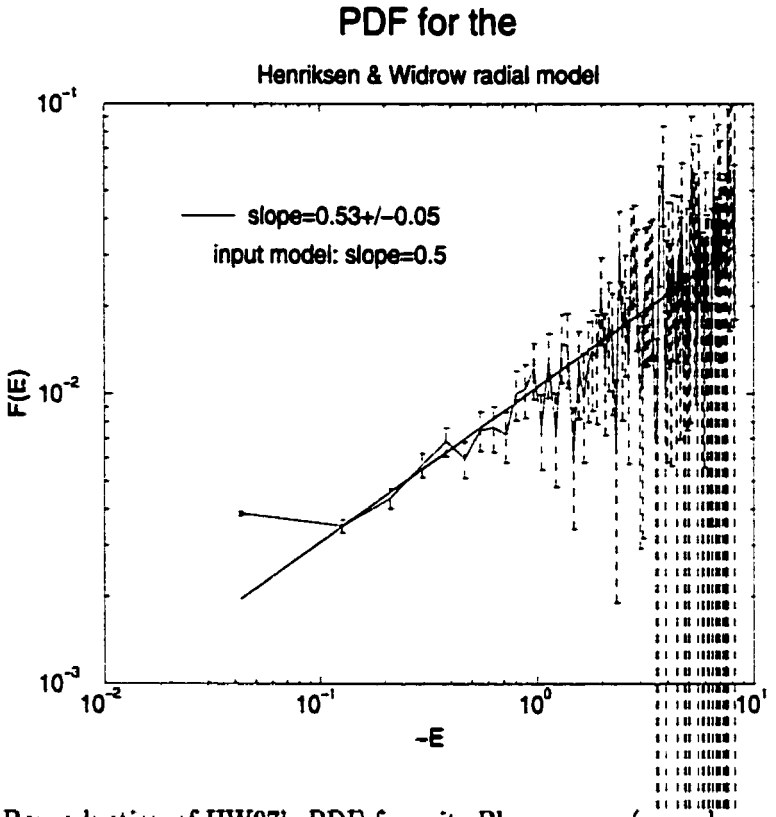

Figure 5.5: Reproduction of HW97's PDF from its Phase space (error bars are Poisson-like estimates)

ascertained with the Plummer's sphere results. As stated in section 5.1.2, we used the Henriksen & Widrow solution for testing the measurement code. A realisation of the phase space was generated from the model's PDF to be reproduced by the code. It consisted of a random realisation of the discrete modeling of the phase space mass distribution using the Henriksen & Widrow solution PDF as a generating probability function. The PDF measurement program was then applied on this distribution of particles in the same way as it can be applied to snapshots of the integration of a modeled halo. Some difficulties, from mass resolution limitations (see figure 5.3 and corresponding discussion), were encountered in reproducing the PDF. At that point, a constant mass was adopted for any PDF measurement as a preferable configuration, and a Poisson error was generated from the number of particles involved in each energy bin ($F(E_{bin}) = F(E_{bin})_{measured}(1 \pm \frac{1}{\sqrt{N_{bin}}})$) where N_{bin} is the number of particles included in the energy bin centered on E_{bin}. These difficulties with the mass resolution indicated that the anisotropic measurement would require simulations much heavier than the ones already available. The result of the radial Henriksen & Widrow model's PDF reconstruction from its generated phase space can be seen on figure 5.5.

The PDF measurement code was then considered reliable enough to be used on the required phase space outputs from simulations.

5.2 Measurement of Probability Distribution Functions: Refined results for the SSIM

In their exploration of the SSIM from cosmological, non-self-similar initial conditions, Henriksen & Widrow [42] predicted that self-similarity would induce a PDF with power law dependence on the specific energy for the relaxed system. This was verified by their N-body simulations of the SSIM, but only crudely and over less than a decade in energy.

They argued that the transition between the quasi-stationary self-similar accretion phase that establishes itself shortly after the formation of an accretion core and the relaxed virialised phase of the system should be smooth enough to maintain the equilibrium configuration of the self similar model in the end product of the evolution.

They eventually followed MTJ [60] in conjecturing a negative temperature exponential cut-off accompanying the power law in energy, to represent the effect of incomplete — or violent — relaxation. To support this view, they display a remnant correlation in energies between initial and final states of the system.

This calls for more investigations on the PDF produced by SSIMs and on the energy correlation that can mark a relic of moderately (or not) violent relaxation. This section will explore the results of measurements made with the code described in the previous

section on an extension of the Henriksen & Widrow [42] model. Even though several values of the self similarity index were explored, only two representative cases will be presented, standing for their generic qualitative behaviour: as shown in Henriksen & Widrow, the initial density profile sets the value of the self-similarity index and profiles shallower than r^{-2} lead to the final state attractor characterised with $\rho \propto r^{-2}$, while steeper profiles lead to a continuum of attractors depending on initial primordial fluctuation power law index. In a first section, general remarks surrounding the measurements of PDFs will be presented that are useful for the interpretation of the results. In a second section, the shallow and the steep case results will be presented, discussed and explained. Then the low energy cut off in the PDF will be interpreted and confronted to some other authors' results. Eventually, a summary of this section's results will be given.

5.2.1 Preliminary remarks on the SSIM's PDF measurements, initial and potential energy and self-similar virial ratio

remarks related the PDF measurements

Measurements of the PDF over the self-similar phase were performed on the SSIM. Since those include a binning of mass shells within ranges of specific energies, a Poisson type error was ascribed to each bin from the number of mass shells involved in the PDF evaluation. This Poisson type error becomes large with more negative energies (see figure5.5). On another hand, the self-similar phase is a stationary state when expressed with the use of self-similar variables. In order to reduce the error and because of the stationary nature of self-similar physical quantities, which includes the scaled PDF, that PDF was averaged over several measurements at different epochs obtained from the part of the self-similar phase for which it looked stationary.

In addition, the evaluation of the phase factor has been seen as limited by the finite mass resolution (see section 5.1.1). Indeed, the potential energy measurement used in its evaluation may become questionable near the centre of the halo, at what may become the more negative energies evaluation of $g(E)$. Monitoring of the phase factor was then mirrored to the PDF so as to judge when the more negative energies PDF evaluation should not be trusted anymore.

According to the cosmological set up and measurement of energies used here (see sections 4.5.1 and 4.2.3) the Einstein-de Sitter background with a Hubble flow translates into a net energy coming only from the primordial density perturbation. The initial self-similar specific energy as a function of self similar radius can then be expressed as

$$E_i = \frac{Y_i^2}{2} - W_\Phi(X_i) = \frac{H^2}{2}X_i^2 - \frac{GM_i(X_i)}{X_i} = \frac{H^2}{2}X_i^2 - 4\pi G\rho_0\left(\frac{X_i^2}{3} + \frac{X_i^{2-\epsilon}}{3-\epsilon}\right),$$

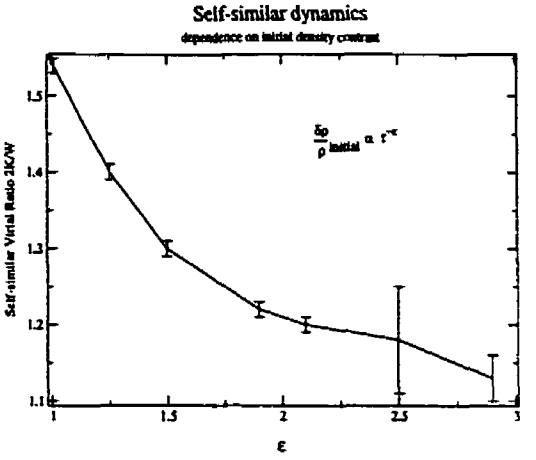

Figure 5.6: The evolution of the virial ratio with the concentration of initial halo

with the cosmological Einstein-de Sitter set up equating the factors of kinetic and potential terms in X_i^2. Therefore, the initial energy can be written

$$E_i \propto -X^{2-\epsilon}. \tag{5.6}$$

In addition the real energy before shell-crossing is conserved for each particle. This is because of spherical symmetry and Gauβ's theorem: before shell-crossing, each spherical shell is in free fall under the influence of the mass inside its own radius, which is constant until shells start crossing each other.

Also, according to the SSIM model's exploration by Henriksen & Widrow, an initial density contrast $\delta\rho/\rho_{background} \propto X^{-\epsilon}$ sets the self similarity class for each shell at their turn-around radius and time to the value $\frac{\delta}{\alpha} = \frac{2}{3}\left(1+\frac{1}{\epsilon}\right)$. This leads to a self-similar density profile

$$\rho_{ss} \propto X^{-\mu}, \; with \; \mu = \begin{cases} 2, & \epsilon \leq 2 \\ \frac{2\alpha}{\delta} = \frac{3\epsilon}{1+\epsilon}, & \epsilon > 2 \end{cases}, \tag{5.7}$$

which in turn yields a self-similar potential energy profile (up to logarithmic corrections) of the form:

$$W_\Phi \propto X^{2-\mu}. \tag{5.8}$$

A trend in the self-similar virial ratio

Explorations were performed for initial density profile indices spanning over a full range ($\epsilon \in \{1.01, 1.25, 1.5, 1.9, 2.1, 2.5, 2.9\}$), recalling that this index is defined by $\delta\rho/\rho_{background} \propto X^{-\epsilon}$. Typical representative for the shallow and the steep case were chosen respectively as $\epsilon = 1.5$ and $\epsilon = 2.5$.

An interesting result was obtained by monitoring the level of the virial ratio during the quasi-equilibrium self-similar phase: there seems to exist a trend wherein the initial halo with a more concentrated density distribution displays smaller kinetic to potential ratios (see figure 5.6). This remains consistent with the fact that shallower[2] self-similar cores tend to be more stirred up by their self-similar mass flux than their steeper[3] counterparts, since they start with less mass in the centre and more accretion is to be made in order to absorb all the surrounding halo. Thus we can expect that they will display a larger amount of kinetic energy, therefore a larger virial ratio. The other remarkable result of this observation is that the virial self-similar ratio does not seem to clearly tend to the isolated gravitational equilibrium value of 1, distinguishing the isolated system equilibrium from the infall-driven self-similar quasi-equilibrium.

5.2.2 Typical Measurements of PDF, energy correlations and other dynamical informations on the SSIM

This section is divided according to the separation by the density profile behaviour of Eq.(5.7):The first part is devoted to the dynamical informations characterising the shallow initial density profile ($\epsilon \leq 2$), and the second part to that of the steep initial profile ($\epsilon > 2$).

The shallow initial density profile case

Measurements of the PDF for the SSIM with any initial density profiles shallower than r^{-2} yield qualitatively the same kind of results, detailed hereafter for an initial density fluctuation on an Einstein-de Sitter background $\delta\rho/\rho_0 \propto r^{-\epsilon}$ with $\epsilon = \frac{3}{2}$.

PDF and Phase Space factor The PDF was measured and fitted by a power law with negative temperature cut off , as conjectured in Henriksen & Widrow [42] ($F(E) \propto |E|^p e^{\frac{E}{E_{cut\,off}}}$ to fit and check the value of the power of E in Henriksen & Widrow's $F(E) \propto |E|^{\frac{1}{2}} e^{aE}$). The cut off energy was then used to select a region where the power law was fitted more precisely. This is shown in figure 5.7's upper and lower left panels respectively. The right panels display a higher resolution view in energies of the PDF and phase space factor $g(E)$, respectively on the upper and lower panel. The phase space density of state factor $g(E)$ corresponds to the phase space volume associated with a given energy. At a given energy binning, it is inversely proportional to the PDF. From the scatter on the $g(E)$ measurement at the more negative energies, a last statistical confidence level is determined, which reflects the limitation induced by finite mass resolution on the accuracy of the measurement. This directly reflects on the PDF measurement but allows for enough

[2],than the isothermal initial profile (see Fillmore & Goldreich),

[3],than the isothermal initial profile (see Fillmore & Goldreich),

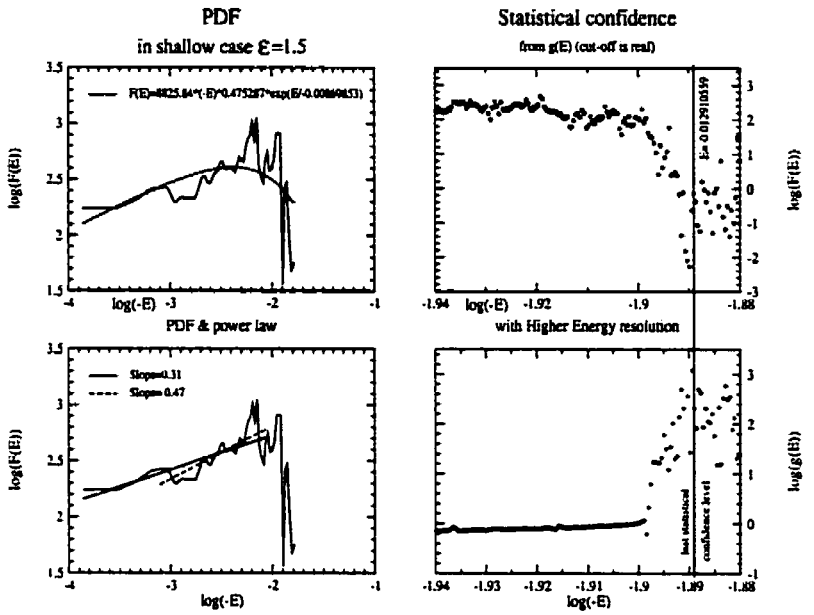

Figure 5.7: PDF measurement averaged over the self-similar phase and evaluation of the last confidence level in energies from the phase space factor

energy range of confidence to confirm the evidence for a cut off in the PDF at the more negative energies. The nature of this cut off, though, is not clearly exponential, as can be seen in figure 5.7's upper left panel. On another hand, its lower left panel displays a clear power law dependence beyond the cut off region and within the relaxed region, over the range of a full decade. It is to be noted that the power law fit on the relaxed region is closer to the predicted value of 0.5 from Henriksen & Widrow than the fit including the non-relaxed region.

Energy correlations and potential energy The relaxed region corresponds to the energy range where the phase mixing streams from the infall have been washed out by the gravitational instability. Some violent relaxation is caused here in the system and the instability in this region particular is the mechanism by which it is expressed. This region is apparent in phase space (figure 5.9's lower left panel) by exclusion of the margin of recently incorporated shells which retain their Lagrange-Liouville[4] stream coherence. This margin of shells defines the relaxation region, where the phase space instability is brewing the self-similarity of the system.Some violent relaxation is caused here in the system and the instability in this region is the particular mechanism by which it is

[4]Lagrange-Liouville stream: Lagrangian particles gathered in a Liouville phase space flow.

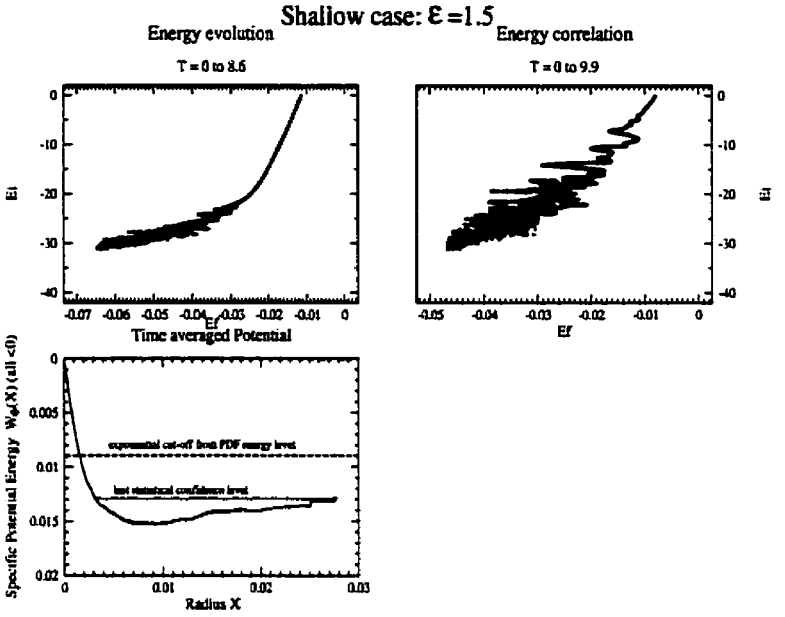

Figure 5.8: Energy correlation between initial and final times at the beginning (upper left panel) and at the end (upper right panel) of the stable PDF portion of the self-similar phase; the potential energy profile is illustrative of the phase factor calculation

expressed. It can be also identified in the first hump at high energy in the PDF because of the similarity between characteristics, reproduced by the Lagrange-Liouville streams, and energy contours (see the characteristics of Eq.(3.29) in section 3.1.2). Those streams therefore represent an accumulation region in energy space before they get spread in the relaxed core. In the energy correlation diagrams (figure 5.8's upper panels) the relaxed region is characterised as the range of initial energies for which a correlated scatter of final energies appears available but where the correlation is not too strong (contiguous initial energy shells do not find their final energy contiguous as well). In contrast, the relaxation region can be characterised in these diagrams by its strong local (shell to shell) contiguous correlation coupled with the instability marked by the strong wiggling of the correlation line thus drawn

In the left panel (which corresponds to the epoch of beginning of stable PDF in the self-similar phase) the stream of incoming particles is still evident as the vertical tail of correlated energies on the upper part of the diagram. Because initial energies are monotonic in radius (see Eq.(5.6)), and conserved until shell-crossing, it is possible to identify the shells along the Lagrangian-Liouville stream by their initial energies. Then, following the stream down in the upper part of the diagrams both right and left, the relaxation of the shells that have just fallen into the core takes the form of the strong

wiggling of the correlation line in a horizontal smear in the upper parts of the upper panels of figure 5.8.

Despite the scattering of energies, there is an obvious correlation equal to that the spread of final energies seem to concentrate not arbitrarily far from the initial ones. Compared with the correlation obtained by Henriksen and Widrow [42], marking that violent relaxation is moderate. In addition, the sharp cut off in energy is apparent in the correlation diagrams as an accumulation boundary at lower final energy (highest negative energy) in the left, bottom part of the top panels of figure 5.8. This is most visible in the right panel.

According to Eq.(5.8), in the shallow case characterised by a final $\mu = 2$, the potential energy profile should be constant up to logarithmic corrections. Apart for the central innermost radius region which is discussed in section 5.1.1, the lower panel of figure 5.8 seems to agree well. This panel is presented as an illustration of the process of calculation, detailed in section 5.1.1 and exemplified in figure 5.1, for a valid $g(E)$: the last statistical confidence level derived from the scattering in figure 5.7's lower right panel seem to coincide with the approach of the energy level E, involved through Eq.(5.3) in the calculation of $g(E)$, towards the almost constant value of the potential energy. The scatter can then be attributed to the departure of W_Φ from its constant value because of the finite mass resolution involved in its determination: following figure 5.1, the surface between W_Φ and $E = cst$ is getting so small compared to less negative energies evaluations that the resulting integration surface for $g(E)$ is blowing up, getting more sensitive to inaccuracies in the potential energy (refer to figure 5.1).

Virial ratio, phase space and density profile The virial ratio is given in the upper left panel of figure 5.9 and confirms the reproduction of Henriksen & Widrow's SSIM results. Note that the use of constant mass shells in order to improve the PDF measurements leads to a coarser mass resolution than with unequal mass shells in the central part of the halo, which also corresponds to the set of shells that forms the core or first enters it. In Henriksen & Widrow, the SSIM was modeled with shells of unequal masses, regularly carved out of the cosmological background and which boundaries were then displaced to model the initial mass profile of a primordial power law mass fluctuation (see section 4.5.1's first paragraph). Using the same method, or an even better one not requiring an approximate mass inversion (section 4.5.1's second paragraph), the quasi-equilibrium self similar state can be achieved almost as soon as the core forms (see figure 4.1). However, with equal mass shells, this cannot be achieved as gracefully. Comparatively with unequal shell set ups, the constant mass innermost particles will have a much larger self-similar mass than their unequal mass counterparts. This results in a poor modeling of the theoretical constant self-similar mass flux needed to maintain self-similarity for the accretion

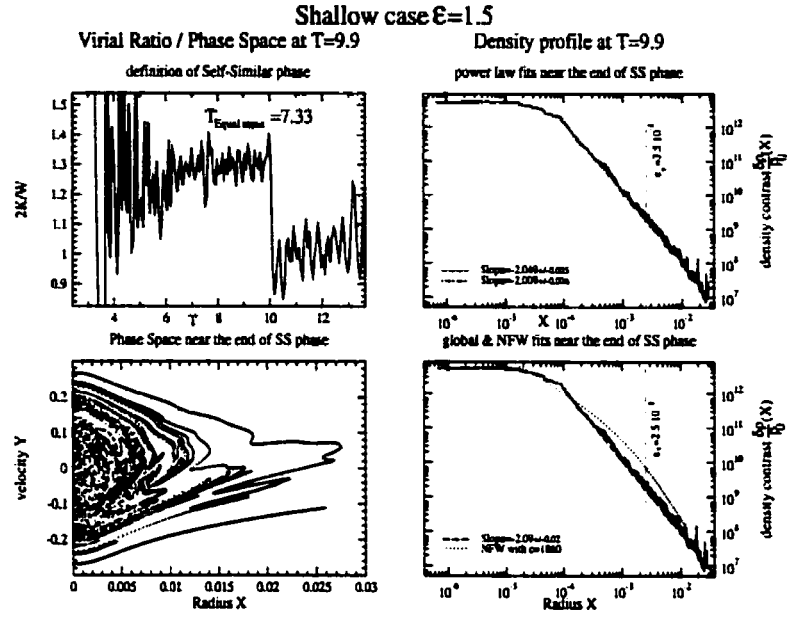

Figure 5.9: Virial ratio, Phase Space diagram and Density profile Diagrams at the end of the self similar phase for the $\epsilon = \frac{3}{2}$ case

of innermost shells into the core, each shell acting almost as an overdensity perturbation to the previously established core and throwing it out of self-similar equilibrium until it is digested or the next perturbation enters the core (for a more detailed discussion of the effect of overdensity perturbations, refer to section 5.4.2 bellow). This conjecture was successfully tested by measuring the time at which a shell of the same mass as for the equal mass setting, but evolving in an unequal mass construction of the same initial density profile, was entering the core of the halo. This time, referred to as $T_{Equal\ mass}$, corresponds indeed to an epoch when the virial ratio, which marks the dynamical stability of the system, is well established at its self-similar value (here $T_{Equal\ mass} = 7.33$). In fact that ratio seems stable a little before $T_{Equal\ mass}$. That can be accounted for by the fact that at these earlier stages, the self-similar masses start to be small enough to model the continuous flux, thanks to the exponentially decreasing scale factor for masses (recall $M_{ss} = M_{real}e^{\mu T}$, where $\mu = 3\delta - 2\alpha$ is the mass cofactor in the rescaling algebra for which G is kept constant).

The phase space diagram (figure 5.9's lower left panel) reflects Henriksen & Widrow's combination of phase mixing and instability which displays this almost continuous phase space distribution of mass particles.

The density profile of the SSIM is also successfully reproduced on figure 5.9's right

panels for this shallow case where the theoretical logarithmic slope is -2: the upper right panel displays power law fits which hint that our simulations are accurately reproducing the SSIM not only above but also inside the smoothing length ϵ_s. Indeed, a simulation involving a smaller smoothing length, following the guidelines for integration reliability from Monte Carlo simulations presented in figure 4.5, was performed in the context of angular momentum implementation. Its results show that the smoothing length is not a limit to the validity of the simulation's density profile, but rather that it is limited by the mass resolution. This will be discussed in more detail in section 6.2.3, devoted to this specific, smaller smoothing length, angular momentum simulation. The lower right panel of figure 5.9 presents as a comparison a power law fit over both ranges (bellow and above the smoothing length) together with the best possible fit using the NFW profile. Of course it is not possible to obtain a satisfactory NFW fit. All power law fits are made inside the self-similar core. This is ensured by limiting the fitting range to the density profile within regions inside the radius of the core as displayed in the phase space diagram.

The steep initial density profile case

Any member of the continuum of attractors for the SSIM, for which the initial density profile is steeper than r^{-2}, even though each initial profile generates a different attractor, yields qualitatively the same kind of results. Therefore measurements of the PDF for an initial density fluctuation on an Einstein-de Sitter background $\delta\rho/\rho_0 \propto r^{-\epsilon}$ with $\epsilon = \frac{5}{2}$ are used here as a generic exponent of the SSIM's behaviour.

PDF and Phase Space factor In the steep initial density profile case, evidence for the low energy cut off in the PDF is not decisive. From a superficial examination of figure 5.10's left panels, there is an indication of a cut off in the PDF at lowest energies. But the reliability of the measurements in that range is subject to the phase space volume factor behaviour over that range. Indeed, figure 5.10's lower left panel shows that the possible cut off is deep inside a zone of dubious measurements from the phase factor $g(E)$. A higher energy resolution investigation of the end region is provided for the PDF and phase factor respectively in the upper and lower right panels of figure 5.10. The lower panel is used to define the last statistical confidence energy level, which in turn is used in upper left panel to define the fitting region for the third power law. The first two ones are fitting in red, dashed line and green, long dashed line, respectively the whole range of energies and the inner range which excludes the non relaxed region. The fit made over the whole well behaved range of the phase factor (above the last statistical confidence level, over two decades) is the closest to the predicted power law of 0.5, although it is clear that the relaxed, $g(E)$-well behaved region admits a steeper power law. Here the relaxing region seems to gather a larger population as can be traced in the phase space

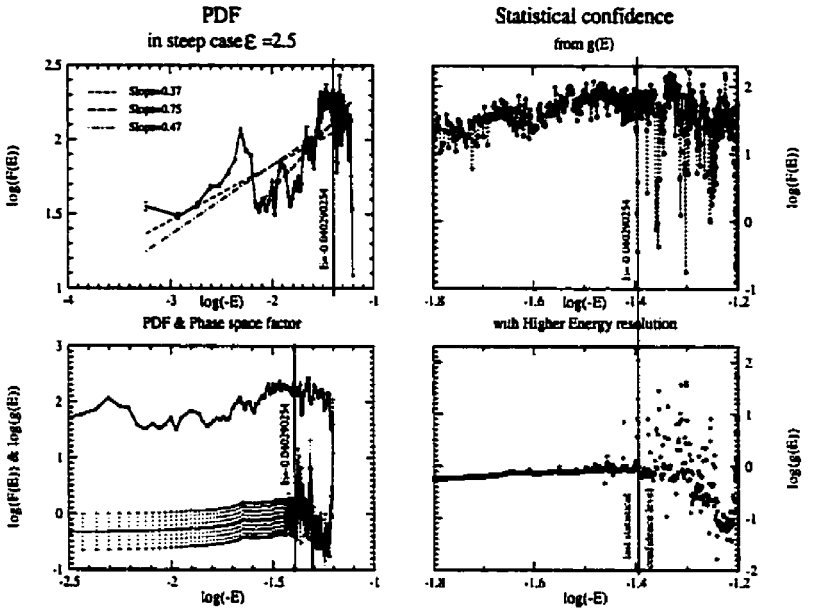

Figure 5.10: PDF measurement averaged over the self-similar phase in the steep initial density profile configuration and evaluation of the last confidence level in energies from the phase space factor

diagram (lower left panel, figure 5.12) and its importance depletes as much the relaxed halo. The steep initial profile is more concentrated, so the already formed core is able to stir up the freshly incoming particles more efficiently, but these shells eventually would settle down in the core once the system virialises. The PDF and phase factor have been presented with their Poisson error bars reduced from the averaging process. Their almost invisible size lead us to discard them form other PDF plots (e.g. figure 5.7).

Energy correlations and potential energy The relaxed region is also detected in the energy correlation diagrams for the steep case. There is no fundamental difference in their aspect,apart from a tighter correlation visible in the steep case The initial energies trace again the Lagrangian-Liouville stream of shells. Indeed, the stream of incoming particles is manifest in figure 5.11's upper panels, as the vertical tail on the upper part of the diagram.

The relaxation process can again be seen in the shells just fallen into the core in the strong wiggling of the correlation line in a horizontal smear. Nevertheless, both at the beginning and at the end of the stable self-similar phase (upper left and right panels of figure 5.11), the spread of final energies of the relaxed core seems to concentrate around initial real energies, indicating energy correlation, thus that the system experiences mod-

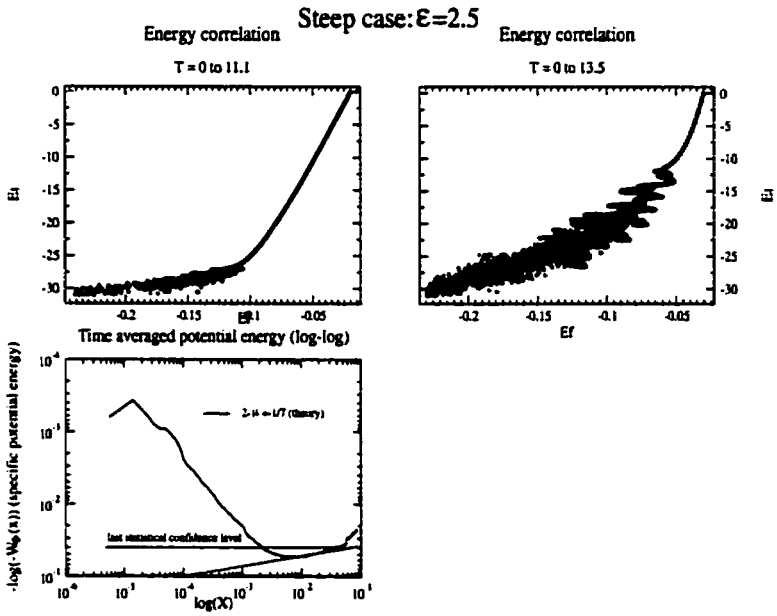

Figure 5.11: Energy correlation between initial and final times at the beginning (upper left panel) and at the end (upper right panel) of the stable PDF portion of the self-similar phase; the potential energy profile is given in logarithmic scale for comparison with Eq.(5.8) and is illustrative of the phase factor calculation

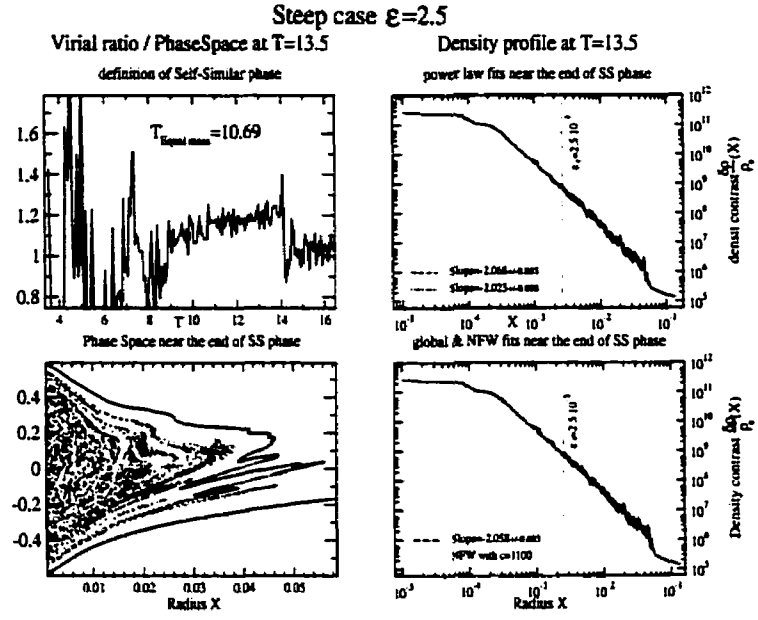

Figure 5.12: Virial ratio, Phase Space diagram and Density profile Diagrams at the end of the self similar phase for the $\epsilon = \frac{5}{2}$ case ($T_{Equal\ mass} = 10.69$)

eration in its violent relaxation, as in Henriksen & Widrow [42]. Furthermore, the same display of a more negative energy cut off at a fixed value of the final energy is visible in the correlation diagrams as for the shallow initial profile case.

Figure 5.11's lower panel presents the core's potential energy in logarithmic presentation, with a fit using the theoretical slope of Eq.(5.8) in the studied case. The fit is good in the relaxed region, excluding the central, innermost radius region as discussed in section 5.1.1. The last statistical confidence level from figure 5.7's $g(E)$ is indicated here to show that it again corresponds to levels yielding integration surfaces coming from the inverse of a very small region which boundaries may suffer from numerical noise: when the energy level E gets too close to the minimum value of potential energy possible, variations of the surface between $E = cst$ and the W_Φ curve caused by the curve's departure from its theoretical value, when that surface becomes tiny, are inducing noise in $g(E)$ (refer again to figure 5.1).

Virial ratio, phase space and density profile The state of gravitational equilibrium reflected by the virial ratio on figure 5.12's upper left panel is again confirming Henriksen & Widrow's results on the quasi-static self-similar phase experienced by the SSIM. As discussed in paragraph 5.2.2, the initial delay in establishing the self-similar virial ratio

can be understood in terms of the ill-appropriate equal mass setting with respect to early central mass resolution. The time for the equal mass characteristic shell to enter the core matches again that at which the system has reached dynamical stability as measured by the virial ratio. In parallel to the shallow case of paragraph 5.2.2, stability can be considered to be achieved approximately a little earlier than $T_{Equal\,mass}$, and this earlier stability allows for the same explanations as in paragraph 5.2.2 to apply.

In this case, the phase space diagram (figure 5.12's lower left panel) appears more relaxed (its phase space winding stream structure being more washed out by the instability) than in the shallow case (figure 5.9's lower left panel) in its innermost regions. Though, its instability region, where the shells more recently incorporated in the core are undertaking violent relaxation instabilities, seems more pronounced, as reflected in the PDF (figure 5.10's left panels). This is probably caused by the fact that the steepness of the density profile leads most of the mass to start very close to the centre and therefore to get included quickly into the core, leaving a more tenuous stream for late incoming particles. These particles thus feel less swung back inwards to the centre by the weight of the very latest incorporated particles from the incoming stream, spending more time in the relaxation region. The importance of this relaxation region is related to the establishment of the density profile and its validity inside the smoothing length and will be discussed in more detail in section 6.2.3. The aspect of the phase space is again conforming to its study by Henriksen & Widrow.

The theoretical slope of the density profile in this steep case is given for the self-similar relaxed density according to section 5.2.1 by $\mu = \frac{15}{7} \simeq 2.14$. Figure 5.12's right panels presents the current work's evaluation, which seems to follow only approximately the prediction. Nevertheless, the tiny difference of slope (about +0.07) and the noise in the relaxing region can account for that discrepancy above the smoothing length, while the difficulty to decide on the flattening radius caused mainly by the mass resolution can explain the discrepancy of the region inside of the smoothing length. Indeed, if one should level off the noise peaks in the relaxing region, the effects would seem to be a slight decrease of the negative slope of the power law fit. The lower right panel in figure 5.12 displays the power law fit over both ranges around the smoothing length, and shows again the difficulty associated with an NFW fit to the SSIM. Again all power law fits were limited to the core region with he help of the phase space diagram.

5.2.3 Interpretation of the cut off at low energy in the PDF

To this point, we have re-obtained the phase space, density profile, virial evolution and energy correlation diagrams from Henriksen & Widrow [42] and have enhanced their results on the PDF with numerical confirmation of the form of the distribution.

The PDF measurements have shown, at least for the shallow initial density perturbation case, the existence of a cut off at low energy. The attraction of the PDF formalism to the understanding of Large Scale Structure formation studies in the form of a generic dark matter halo is the insight it brings in the dynamics of the path such a system takes to a static or quasi static state in the simplest terms possible, sifting down the details of the system into its essential elements. For an isolated system, the PDF will depend only on the integrals of motion, which contain the essential dynamical information on the state of the system. For a forming dark matter halo, the picture is more complex since it is accreting or merging with neighbouring haloes. Studies like Henriksen & Widrow's [42] have shown that, if the secondary accretion mechanism is the main tool for dark halo formation, it will settle into a self-similar quasi-static accretion mode, which betrays a very peculiar yet generic mode of relaxation for such a halo. These studies indicate that relaxation of such a system is violent enough to wash out the finer phase space structures but moderate enough to retain some memory of initial conditions of the system. They also conjectured the existence of an exponential cut off in the system's PDF, characterising this moderately violent relaxation. In addition, the self-similar quasi-static mode of relaxation is characterised in the system's PDF by its energy power law dependence.

This work has confirmed those studies in their results in every point. The energy correlations imply a moderately violent relaxation, as found in Henriksen & Widrow. The energy power law dependence of the PDF is confirmed over a decade or more. And the existence of a cut off at low energy has been shown, at least for the shallow initial density profile case.

The cut off in the shallow case

To understand the establishment of the cut off for the shallow case, one may use the initial energy radial distribution. Indeed, Eq.(5.6) indicates that initial energy is monotonically decreasing with radius(when considering the definition used for the PDF calculations). Since the collapse occurs first with innermost shells, the turnaround radius progressing inside out, the last particles to fall in the system at the end of the self similar phase have the most negative initial energies. Even if the finite size of the simulated halo is primarily a consequence of finite computing power, it also represents the finite cosmological accretion basin available for each primordial fluctuation, and so is a real effect. The interruption of the flow of particles of lower and lower energy, imposed by the existence of neighbouring accretion basins for other primordial density fluctuations, appears then as the main factor in the establishment of the PDF low energy cut off. However, this picture is only providing a limit to the pool of initial energies available and the energy 'processing' observed in the energy correlation diagrams (top panels, figure 5.8) is clearly taking a strong role in

maintaining the sharpness of the cut off.

The cut off in the steep case

Since the evidence presented here are not conclusive about the low energy cut off in the PDF for the steep initial density profile cases, the discussion on its establishment can only be conditional (linked with the reality of the cut off). Supposing that the cut off indeed does exist, its establishment cannot proceed from the same effects as for the shallow case: in the steep case, initial lowest energies are incorporated in the system at the beginning of its evolution because they correspond to the innermost radial part of the collapsing halo. The limitation in the lower energies achieved in the simulation are coming from, on one hand, the finite mass resolution at the center, and on the other hand, from the regularisation around the centre, which prevents infinite theoretical central density to be achieved. Even though on a practical level the first limitation does indeed have an effect, increasing the mass resolution would change the cut off energy level. On the contrary, the second limitation is independent of mass resolution. Its physical justification can be seen as coming from the inescapable scale limitation on the central primordial density peak resolution, an offspring of Heisenberg's uncertainty principle which, in the inflationary model of the primordial density fluctuation formation, is zoomed together with quantum fluctuations during the inflationary phase. However, its implementation here comes from an arbitrarily chosen central scale. In addition, the maintenance of a sharp cut off would also be subject to the 'processing' of energies in the relaxation region. The energy correlation diagrams (top panels, figure 5.11) are hinting at traces of such a cut off after relaxation.

Other cut offs and PDFs

This work is not alone in dealing with a cut off at lower energy in the PDF of self-gravitating systems. In early works on self-gravitating star systems using the Collisionless Boltzmann's Equation coupled with Poisson field equation, Hoffman *et al.* 79 [104] directly evolved distribution function's collapses to equilibrium without N-body simulation and found the exponential cut off of a Maxwellian final PDFs. More recently the same methods were extended by Rasio *et al.* 89 [99] with initial conditions of perturbed Plummer's sphere. The non cuspy density profile of the Plummer polytrope induces an effective energy cut off in the PDF, conserved in the Liouville flow. But the N-body results of Hanyu & Habe 00 [101] display very good indications of a cosmological halo exhibiting a low energy cut-off in its PDF. Nevertheless, comparison of all these models with the SSIM are subject to the difference in angular momentum treatment: in this chapter, the SSIM does not include any angular momentum, whereas these other approaches all

include isotropic velocity dispersions. Other works discussing the cut off are using the presence of a black hole as a trigger for its population inversion, but this will be discussed in the section on the implementation of a central black hole in the SSIM (section 6.4).

5.2.4 Summary of the results

In conclusion to this section, it appears that this work was successful in reproducing Henriksen & Widrow's results with definite improvements. The power law in the PDF was successfully confirmed over one or more decades, with the small reservations that, in the steep initial density profile case, the relaxation region should be taken into account. Eventually, a new result confirming the existence of a low energy cut off in the PDF was obtained in the shallow initial density profile case, and indication of its existence in the steep case. A preliminary result was also discovered in the dependence in the self-similarity class of the value of the virial ratio during the self-similar infall phase.

5.3 The establishment and integration of an overdensity perturbation: Preliminary definitions, calibrations and set up

> "...And now for something completely different."
>
> THE MONTHY PYTHON'S

The modeling of the effect of repeated mergers on a CDM halo in the frame of the SSIM can be performed by adding on the edges of the core or halo a region of shells that is made overdense with respect to the original halo (cosmological background with a central perturbation). This is performed by evolving the halo first to obtain a self-similar quasi-equilibrium.

5.3.1 Initial situations of the core and overdensity

The first aim of the merger modeling within the SSIM is to set the conditions for which the halo is sufficiently evolved to have developed into its self-similar infall phase. Then a prescription has to circumscribe the nature of the overdensity that will merge with the self-similar system (or core) using significant parameters. Eventually, the system will be prepared and receive the chosen implementation of that overdensity before resuming its evolution.

The halo in which the overdensity is deposited

In order to decide when to interrupt the preliminary evolution of the halo, the definition of what is in the self-similar core is needed. From that knowledge, the mass fraction of the core compared to the total halo simulated, $Mfcore$, can be measured. The value of that fraction for which the halo can be considered sufficiently evolved into its self-similar infall phase will be retained. It was determined in an initial run for which initial conditions involved equal shell spacing. That way, the mass resolution allowed for the self-similar phase to establish itself very rapidly. Hence, the choice of the size of the core at the laying of the overdensity was made so as to leave a large enough halo to yield sufficient accretion time.

Since the self-similar quasi-equilibrium was re-obtained after some time, but not for all overdensities for lack of halo infall time, some tuning of the extent of the halo was performed and 10 000 shells were settled on.

To define the system we used the Lagrangian index of the last particle to cross the centre of the core (see Eq.(4.2)). Nevertheless, this does not reflect entirely the gravitational scope of the system: inward going shells which are not yet in the core from the previous definition can still act on core shells if they are located under the radially outermost core shell. Thus a fully effective description of the system requires the addition of that outermost shell's Lagrangian index. That task entails the establishment of the bijection between Lagrangian indices and radially ordered indices of the shells, noted $indx : i_{radially\ ordered} \longmapsto indx(i_{radially\ ordered}) = i_{lagrangian}$. Henceforth, the Lagrangian index of the outermost core shell can be calculated according to

$$i_{max}(icore) = indx(\sup\{i | indx(i) \leq i_{core}\}).$$

Figure 5.13 illustrates how the core and outermost core particles are defined, as well as how the evolution of the initial halo leads to a pause: the core is defined by the Lagrangian index of the latest particle that crossed the center of the halo for the first time (see also figure 4.2). The outermost core particle is shown on figure 5.13 as that which gets the largest radius measured within core particles. This figure also shows at a given time the radius under which the cumulated mass sums up to $Mfcore.iM(indx(n)) = Mfcore.M_{total}$, where $M_{total}is$ the total mass of he halo simulated. The pause in the evolution of the initial halo is declared when these two radii (that of the core and the one just defined with $Mfcore$) cross for the first time. They do so when the fraction $Mfcore$ of the simulated initial halo is included in the self-similar core.

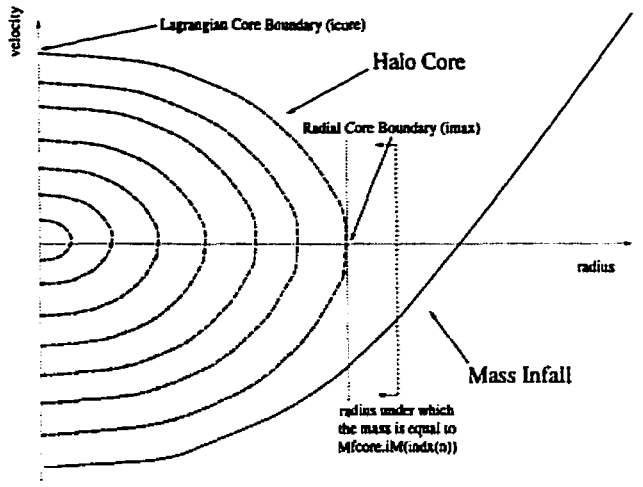

Figure 5.13: Definition of the gravitational core boundary from its Lagrangian definition.

Initial conditions of the overdensity

Once the halo presents a self-similar core, the overdensity can be established. First, its location is set in the same terms as the test for pausing the evolution of the primordial system: the fraction of mass of the initial halo inside of all overdensity shells. This is the part of the halo which gravity is felt throughout the overdensity. That gives the position of the inner shell of the satellite model.

Then the shape of the density profile over the range of the overdensity is defined by two parameters and the choice of adding the central part of a gauβian density distribution on top of the halo mass distribution at the location of the overdensity: the ratios of the mass and average density of the overdensity over its parent core, noted M_{ratio} and D_{ratio}. These input parameters share the same definitions as those measured below. Placing the overdensity far from the core allowed for evolution to take place, but it proved profitable to keep more control on the final input parameters of the overdensity entering the core to create it close to the core.

The ratio of the two parameters, M_{ratio}/D_{ratio}, defines the volume ratios between the core and the overdensity. Thus the radial range that will be included in the overdensity is fully determined. With M_{ratio}, the target mass of the satellite can be compared to that of the preexisting halo. Since we are interested only in adding mass on top of the halo in the range of the overdensity, this target mass must be larger than that of the preexisting halo over the same region. Otherwise the parameters have to be changed. All the gauβian density distribution constants can be derived from those primary parameters, with some general considerations such as how negligible is a given integer or how centered is the

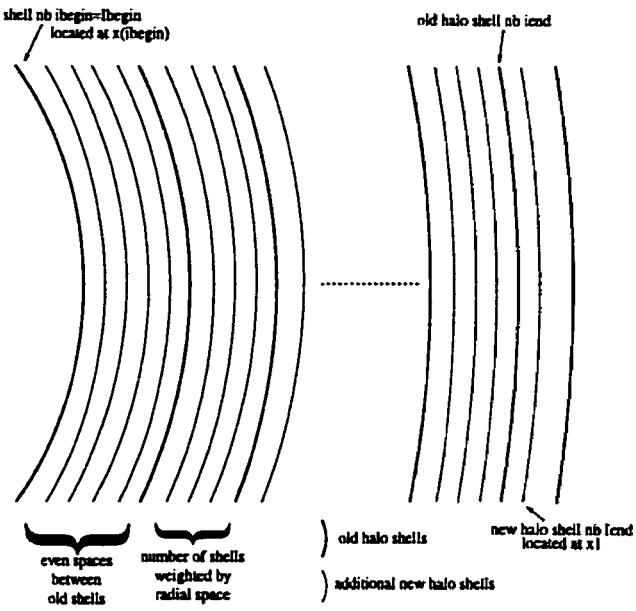

Figure 5.14: Subdivision of shells in the overdensity

gauβian to be.

We are also interested in following the shells belonging to the overdensity. To refine the resolution of the simulations over the range of the initial overdensity, the preexisting halo is fitted so as to subdivide evenly each of its original shell (see figure 5.14). Then the desired density profile is obtained by adding to the fits the chosen gauβian distribution.

All the procedures on the core and the initial overdensity definitions mentioned above are detailed with more precision in appendix F to allow for reproducibility of the numerical experiments.

5.3.2 Coherence of overdensity

We want to measure the cohesiveness of the overdensity's structure. We first need to define the overdensity with time. Then we will measure the coherence through two opposing tendencies: the tidal disruption exerted by the halo on the overdensity and the binding acceleration of the overdensity on itself.

Definition of overdensity region

We define the overdensity region as being the set of all shells originally in the overdensity added with the ones that have been accreted until it reached the edge of the core (or a definite very small distance to the core).

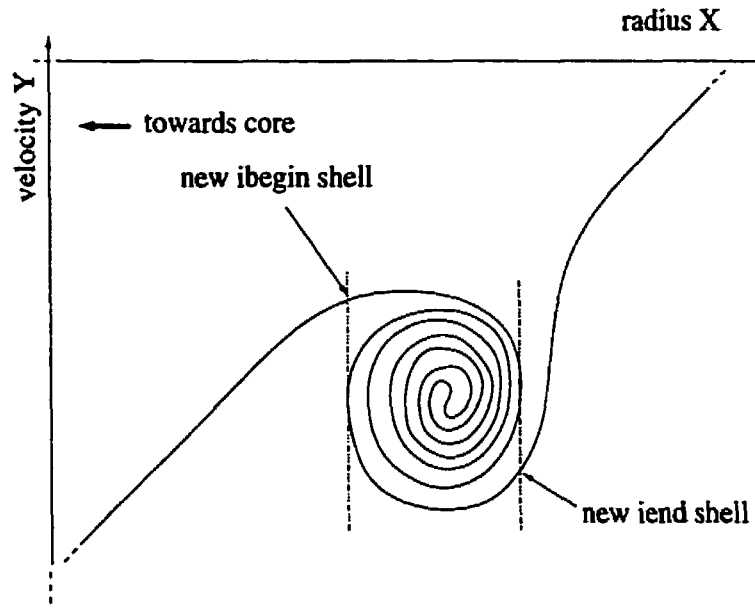

Figure 5.15: Phase space view of evolved overdensity

The accretion of shells by the overdensity can be observed as a characteristic winding of the phase space sheet, similar to the one of the core (e.g. in sketch 5.15, also seen in figure 3 of Sikivie *et al.* 97 [51], or in the example phase space evolved overdensity presented in figure 5.16). This winding accretion of the phase space sheet follows the influence of the mass distribution shift induced by the overdensity: because of the extra mass at the locus of the overdensity, the mass inside each shell of that overdensity grows faster with increasing radius than if the halo was unperturbed. Under the gravity of this growing mass excess, each shell is falling faster than it would have without overdensity. Thus outer shells would tend to fall faster than inner shells on the overdensity range, catching up with them until they cross around the centre of the overdensity and leading to the winding observed, like a wave breaking on a beach. As for the rest of the halo which envelopes the whole of the overdensity, it behaves according to the inside halo being heavier. To summarise the consequences of the overdensity on the rest of the infall, its effect on the halo outside of the overdensity is to shift the phase space sheet towards lower velocities. That translates into the shells near the inner edge of the overdensity falling slower towards the core than those inside of the overdensity region, and the shells near the outer edge of the overdensity falling faster towards the core than the stream below the overdensity, inducing this winding effect on the overdensity and the shifting on the phase space sheet (see figure 5.16).

The accretion of new shells into the overdensity as illustrated in the sketch 5.15 is

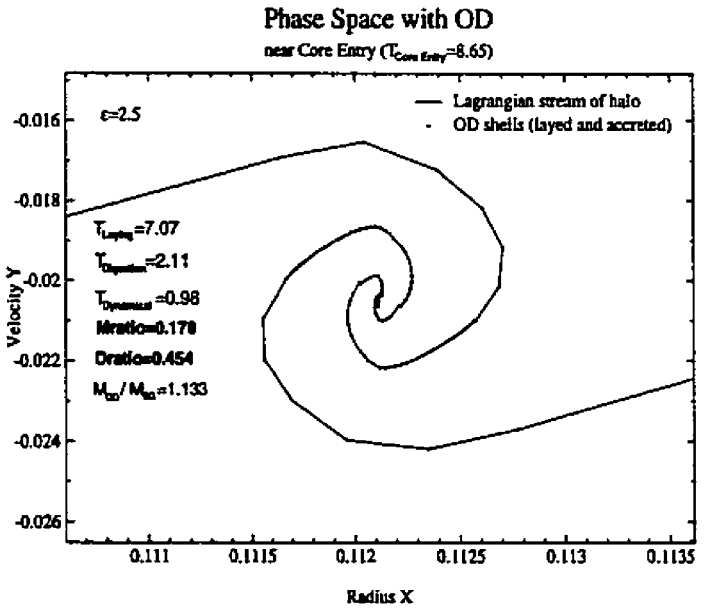

Figure 5.16: Example of simulation's evolved overdensity. The accreted shells appear as more spaced on the Lagrangian-Liouville stream (also referred to as phase space sheet) than the original overdensity ones. All the indicated parameters point to one of the cases which results will be given in section 5.4.

accounted for through a redefinition of the edges of the accreting region. This redefinition procedure makes use of the Lagrange-Liouville stream to calculate new Lagrangian indices for the edges i_{end} and i_{begin}. Density caustics frame the limits of the accreted region and point towards the new edges without ambiguity. Figure 5.15 is showing the construction of such new edges and figure 5.16 illustrates how it worked on a real overdensity.

We stop the evolution of the overdensity when it comes too close to the core. That is ensured by allowing only one more timestep evolution of the overdensity once its lower edge has fallen towards the core at a distance less than its width from the outer edge of the core as illustrated in figure 5.17.

It can be noted that, at this stage, the core and overdensity strongly resemble one another: the only topological difference between the two comes from the need for the winding of the core to be split and mirrored in the middle in order to accommodate for the non existence of negative radii. Figure 1 of Sikivie & Ipser 92 [103] illustrates this point by showing an artificial representation of the phase space core collapse which includes a mirror image in negative radii of the halo. Their picture is remarkably similar to our figure 5.15, the satellite growth in figure 3 of Sikivie *et al.* 97 [51], or our's in figure 5.16.

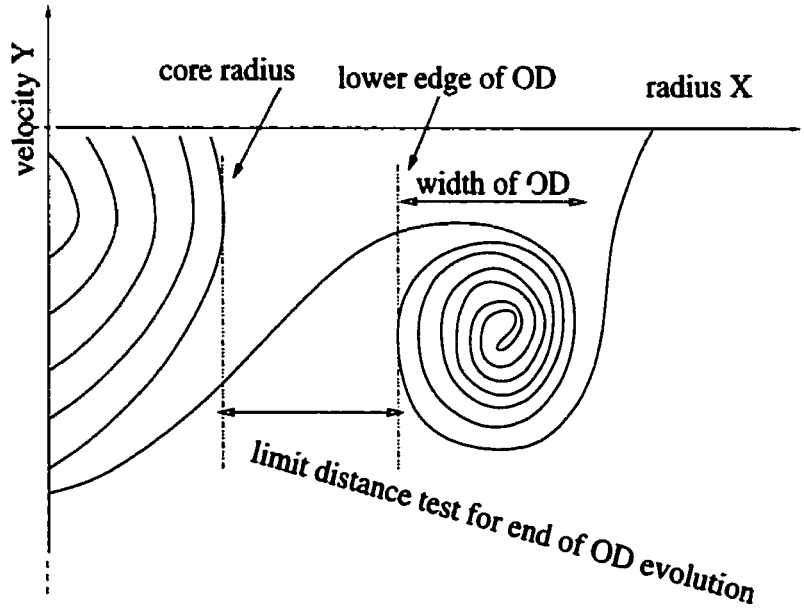

Figure 5.17: End of overdensity evolution test

Figure 5.17 illustrates the definition of the overdensity at core entry.

Density and Mass ratios

The original motivation for this modeling of repeated merger through overdensity shells aimed at comparing the Syer & White [33] model with the effect of a perturbation of a kind similar to a merger on the smooth SSIM. Indeed, the Syer & White model advocates the dynamical origin of a universal density profile through non smooth repeated mergers, while the SSIM features a continuous stream of smoothly infalling mass.

Their argument can be summarised as follow: primordial cold dark matter haloes have a characteristic density and a characteristic radius respectively decreasing and increasing with halo mass. When merging, a satellite halo can either have a higher or lower characteristic density at its characteristic radius than its parent halo at the same radius. Dynamical friction will make the satellite sink towards the centre of its parent halo. Tidal stripping will disrupt the satellite's outer envelopes until its average density is higher than the parent halo at the satellite's remaining radius or it is completely disrupted. The distribution of the stripped material follows the parent-satellite's resonant radii: the characteristic orbit frequency of material is proportional to the square root of the average density contained in its radius. Thus if material in a satellite, with a given satellite average density, sinks down under dynamical friction to a parent's radius for

which the parent's average density equals that of the satellite, resonance will strip that layer of material from the satellite and spread it in the parent at that radius. The interplay between tidal stripping and dynamical friction leads denser satellites to enhance the core's logarithmic slope and shallower ones to flatten it by spreading over the whole parent. Repeated mergers will then dynamically lead to a universal profile, the attractor of this negative feedback mechanism.

Nevertheless the Syer & White argument's feedback mechanism might still have its relevance in the frame of their interpretation, even if the main reason for the emergence of a profile in the SSIM remains the self-similarity. The relevance of tidal stripping and dynamical friction as mechanisms present in the one-dimensional model of the SSIM will be discussed in section 5.3.3.

The Syer & White argument bases itself on the comparison of some characteristic density between the two merging haloes. In this context we chose to monitor the overdensity by its relative mass and average density with respect to the core and to explore those two parameters in order to detect any behaviour indicative of the Syer & White argument.

The mass and density ratios were measured once the accretion of new shells on the overdensity has been computed for the last time, according to the criteria described in the previous section.

The mass ratio represents how much of a perturbation the overdensity will produce when absorbed inside the core. This is equivalent to gauging if the merger was between two almost equivalent haloes or if it was a matter of a central halo absorbing one of its satellites. The density ratio reflects a measurement of the same nature as the Syer & White characteristic density, in the sense that a more concentrated overdensity would tend to resist more to tidal stripping and sink to the inner regions of the core through dynamical friction, if their model still applies to a secondary infall.

Calculation of the mass ratio was performed by recognising the shells corresponding to the radial edges of the core, the inner overdensity shell and the outer overdensity shell. Then it is just a matter of using the mass profile:

$$M_{ratio_{real}} = \frac{iM(i_{end}) - iM(i_{begin})}{iM(i_{core})}.$$

We measured the density ratio simply by determining the radii of the core x_{core}, the innermost over density shell x_{begin} and the outermost one x_{end}, then using them to compute the volume ratio as described below:

$$D_{ratio_{real}} = \frac{iM(i_{end}) - iM(i_{begin})}{iM(i_{core})} \frac{x_{core}^3}{x_{end}^3 - x_{begin}^3}.$$

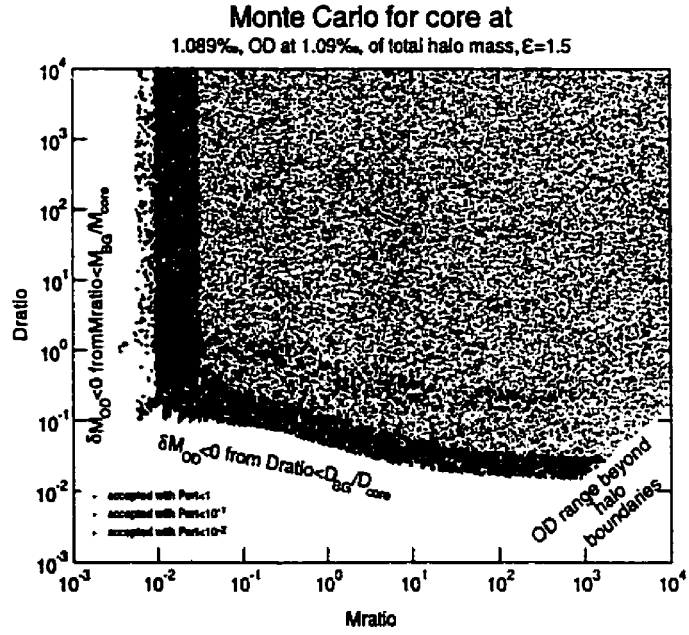

Figure 5.18: Monte Carlo exploration; shallow initial density profile

Experimentation with the distance from the core to the overdensity led us to prefer control over the ratios by placing the overdensity close to the edge of the core. Evolved overdensities did not seem to affect significantly the dynamics of the encounter with the core.

Monitoring the ratios, it appeared that a region of this parameter plane should be excluded since we were only interested in positive mass additions on the overdensity (see discussion in section 5.3.1, or, for a more detailed description, in section F.2.3): indeed, simulation of merger meant the encounter between a parent halo and its satellite. Thus a Monte-Carlo simulation was performed to select the initial values of the ratios that would produce interesting merging scenarii. A steep case and a shallow case were chosen from the original, unperturbed SSIM. The results from the shallow case yielded the following plot (figure 5.18): the colour coding limits the ranges for which the overdensity remains a perturbation over the unperturbed halo background, the rejections were motivated by the need to add a positive mass to the halo and the finite size of the simulation's initial halo r_{max}. The parameter points of figure 5.18 which are coloured in blue have the mass ratio of the added overdensity upon its location's undisturbed halo background, noted hereafter $Pert = \frac{\delta M_{OD}}{M_{background\ halo}}$ (also noted M_{OD}/M_{BG} on the figures of section 5.4) as in perturbation, less than or equal to 10^{-2}. Those in green have their ratio $Pert \leq 10^{-1}$

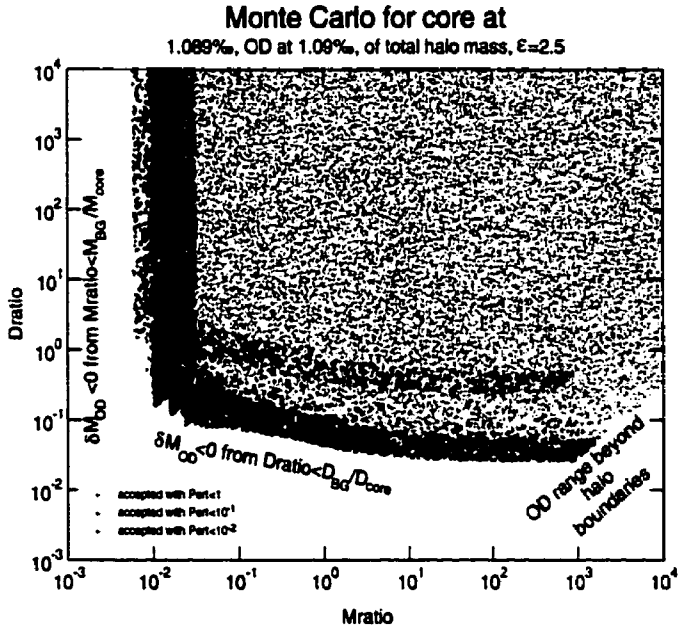

Figure 5.19: Monte Carlo exploration; steep initial density profile

and those in red yield a ratio of comparable masses of $Pert \leq 1$. All other accepted parameter points designate overdensities which are strong additions to the original halo and thus strongly departing from a secondary infall merger. This pointed us to the exploration of two series of simulations at high and low density ratio for various mass ratio. There appears to be an echo of the coloured regions. That can be seen as a result of the non-linear definitions of the ratios: if one assumes the background halo at overdensity laying to have a power law density in radius $\rho = \rho_{00} x^{-k}$, defining for instance the density (D_{ratio}) and the $Pert$ ratio to be constant, the freedom in mass ratio leads to a polynomial equation if the power law is rational (which is always the case when treated by a computer) which leads to several roots and thus several possible bands in the Monte Carlo graph (see appendix D). The steep case exploration yields a similar plot (figure 5.19): The notations referring to the core and the overdensity placements are expressed in terms of "per-thousand-age" (noted $^o/_{oo}$) ratio out of the total initial mass of the simulated halo.

5.3.3 Tidal stripping and dynamical friction in the one-dimensional SSIM

In this section, the soundness of using the terms dynamical friction and tidal stripping in the frame of the SSIM will be argued despite the one-dimensional nature of the model

that can be opposed *a priori* to the multidimensional ($d \geq 2$) definitions proposed in the field.

Tidal stripping

In order to simplify the argument, the influence of the smoothing length in the modeled gravitational force will be neglected.

Tidal acceleration on a test particle The tidal acceleration on a test shell can be defined as the differential acceleration between its boundaries; it can be understood as the acceleration felt on one edge in the rest frame of the other.

The accelerations under and above a given shell can be written (with an inwards orientation)

$$F_1 = \frac{GM}{r^2}$$
$$F_2 = \frac{G(M+m)}{(r+\Delta r)^2} ,$$

where m is the mass of the shell and r+Δr is the upper radius of the shell. M is the total mass under the lower radius r of the shell. Using the linear approximation for the shell's thickness ($(r+\Delta r)^2 \simeq r^2(1+2\frac{\Delta r}{r})$), the tidal acceleration can be obtained:

$$T = F_2 - F_1 \simeq \frac{GM}{r^2}(\frac{m}{M} - 2\frac{\Delta r}{r}) = \frac{Gm}{r^2} - 2\frac{GM\Delta r}{r^3},$$

which can be decomposed into a cohesive (attractive) term involving the mass of the shell and a disruptive (repulsive) term involving the spread of the shell in the radial direction.

Because the mass distribution of shells has a radial dependence, a continuous model argument is more adapted to bring out the characteristic behaviours of the SSIM under tidal stripping.

Tidal acceleration on an infinitesimal shell From the uniformity of spherical shells of the SSIM, the mass of an infinitesimal shell of thickness dr is given with the density distribution ρ as:

$$m = 4\pi\rho r^2 dr.$$

Thus the elementary tidal acceleration reads

$$dT \simeq \frac{GM}{r^2}\left(\frac{4\pi\rho r^2 dr}{M} - 2\frac{dr}{r}\right) = G4\pi\rho dr - 2\frac{GMdr}{r^3}.$$

Defining the cumulative average density profile by the expression

$$\langle\rho\rangle_r \equiv \frac{M}{V_r} = \frac{M}{\frac{4\pi r^3}{3}} \Rightarrow \frac{M}{r^3} = \frac{4\pi}{3}\langle\rho\rangle_r ,$$

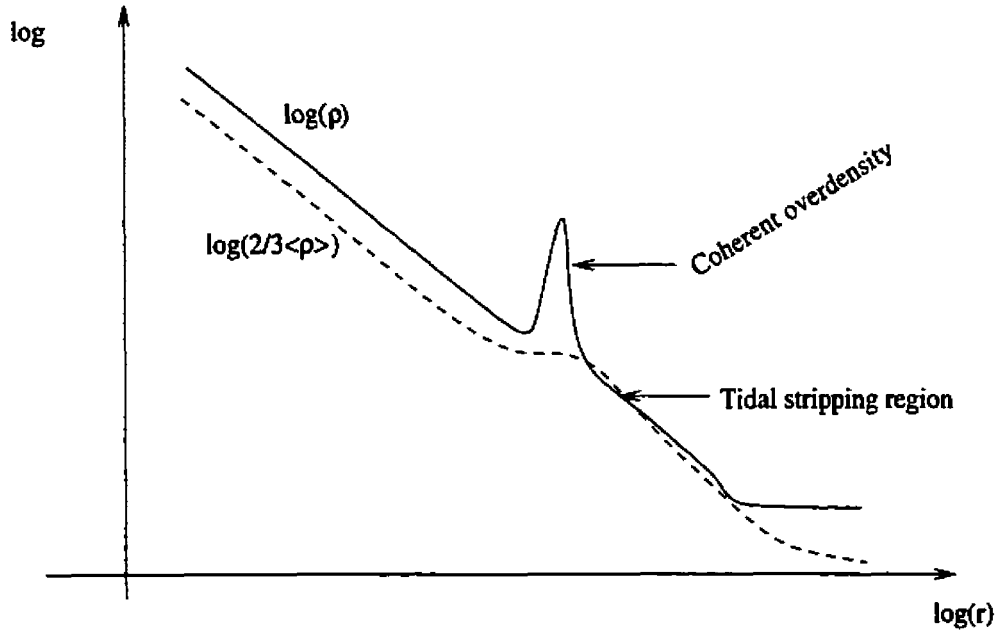

Figure 5.20: Tidal disruption of an overdensity on a power law background

the tidal acceleration can be interpreted using the cumulative density profile with the form

$$dT \simeq G4\pi dr \left(\rho - \frac{2}{3}\langle\rho\rangle_r\right).$$

It is clear that peak regions of density springing over the cumulative average ($\rho < \frac{2}{3}\langle\rho\rangle_r$) will experience a net disruptive acceleration with the effect of spreading apart shells in those regions (see figure 5.20).

Dynamical friction in one dimension

Classical definitions Dynamical friction is defined as a result of a transverse velocity of a gravitating body diminished in the process of two bodies scattering, cumulated over the collective of a dense medium of gravitating bodies.

It can be alternately seen as the dragging on a body crossing a dense gravitating medium created by the wake of pulled-in bodies behind that test particle. (see, e.g. Binney & Tremaine [87]).

These definitions appear to intrinsically require at least two dimensions: one for the direction of propagation of the test particle, and one for the oscillations of the wake particles (or alternately for the scattering away from the initial trajectory).

One-dimensional interpretation By analogy, it is still possible to describe qualitatively as a dynamical friction the phenomena that lead for shells to spiral deeper and deeper around the Fillmore & Goldreich trajectory.

Analogy to the wake phenomenon When a massive particle is falling into and traveling through the medium formed by the particles in the core of the SSIM, each of those shells crossed by the massive particle is feeling more gravitational attraction. This sudden increase of each shell's inwards acceleration pulls the medium tighter inwards, similarly to the wake that creates dynamical friction in multiple dimensions.

In the same fashion, after the massive shell has crossed the center (this is happening because of spherical symmetry and the lack of collision in dark matter's definition) and when it is moving outwards, each medium particle it crosses ceases to feel the massive shell's gravity and thus moves comparatively less inwards under the influence of the rest of the core. This brisk decrease of the inwards acceleration and the subsequent motions reproduces the impression of a wake behind the outwards moving massive shell.

Thus a massive shell creates behind it in the one-dimensional SSIM the analog of a wake of shells.

Analogy to the wake's dragging effect The effects of those relative wakes, whereas the test particle is moving inwards or outwards can also lead to relative dragging interpretations: their gravitational pull excesses relative to the average core pull can be interpreted as having a dynamical effect.

For the case of the massive particle moving inwards, the gravity of the wake cannot be felt directly because of spherical symmetry: the wake being outside of the massive shell cannot affect it. Nevertheless, in its journey, less and less particles are featured inside the massive shell so there is a relative diminishing of the inwards pull felt by it. This can be interpreted as an outwards net (averaged) pull which can be labeled as dragging.

In addition, the wake created by the inwards moving massive shell when it almost reaches the center can serve as an already constituted lump of additional inwards-pulling material for the outwards crossing when that massive shell will have crossed the origin.

The massive particle, when moving outwards, does feel the effect of gravity from the wake: more and more particles fall inside the massive shell so there is a relative increase of inwards pull felt by it. This again can be translated as dragging.

5.4 The establishment and integration of an overdensity perturbation: Results

Modeling mergers with a secondary infall model could appear as an oxymoron. In fact the very implementation of the SSIM into its numerical realisation, due to the need to discretise the mass distribution, is already a sort of repeated mergers model with the hope that the size of the satellites will be small enough to be negligible compared with the core (see the counter example of this hope for the equal mass implementation of the innermost shells in paragraph 5.2.2).

It is generally accepted in the field of Large Scale Structure formation that repeated mergers should play an important role in the relaxation of dark haloes and the constitution of their density profile. This is all the more important in the view of the possibility of a universal density profile (NFW [32], Moore *et al.* [71]) to determine how important mergers are to dark haloes density profile construction and to challenge the Syer & White [33] picture which relies only on mergers.

Phenomenologically, one would expect both secondary infall and mergers to occur during the formation of a dark halo. The SSIM teach us that depending on the primordial density fluctuation profile, a semi-universal profile arises for dark haloes. Syer & White [33] explain a universal profile solely with a repeated merger feedback mechanism. Challenging the consensual paradigm as well as articulating the two main growth factors for dark haloes was the purpose of this investigation.

In a first section, preliminary remarks will set the scene of this introduction of mergers in the SSIM. In a second section will be presented the effect the model merger has on the equilibrium of the system and conversely how is the overdensity affected by the system once settled in. Then the impact of merger on the density profile will be explored through the mass profile, which is a more stable indicator. Eventually a summary of the results will close the chapter.

5.4.1 Preliminary remarks

This exploration has used an implementation of the semi-analytical model which assign uneven masses to shells, but initially space them evenly along the radial direction. This implementation allows for a stable self-similar quasi-equilibrium to settle down as soon as the central system forms, which then can be easily halted to introduce the various overdensities needed for this exploration.

Three values for the initial power law index of the primordial density profile were used to inquire about the diversity of impacts merger has on the SSIM. One ($\epsilon = \frac{3}{2} = 1.5$) was taken to stand for the initial density profiles shallower than r^{-2}, which admits a

universal density profile attractor at $\rho \propto r^{-2}$. This class of system is also expected to be not very concentrated, leading to less tidal stripping according to the Syer & White argument. In order to confront the continuum of attractors displayed by the SSIM's density profiles starting with steeper initial density profiles, two values were used: one was taken to represent typical behaviours of that class of initial conditions ($\epsilon = \frac{5}{2} = 2.5$), the other was used to test the extreme region of the continuum of attractors ($\epsilon = 2.9$, recall that the class of steep initial profiles relates initial $\delta\rho \propto r^{-\epsilon}$, where $2 < \epsilon < 3$, to final $\rho \propto r^{-\mu(\epsilon)}$). Those systems are expected to be more concentrated, the latter in an extreme way, so that the Syer & White argument would forecast more disruption for the overdensity.

Using the Monte Carlo simulations of figures 5.18 and 5.19 as a guide to the shallow case for the first and to both steep cases for the second respectively, a range of mass and density parameters were explored within each intermediate overdensity initial condition (each evolved primordial halo proposed as initial game field for overdensity explorations). Represented here for each primordial density profile case are three instances of combinations of higher and lower overdensity relative masses and average densities that are allowed by our criteria of adding a positive mass on top of the preexisting overdensity region's halo mass, but which shouldn't be too strong a perturbation of the already constituted core and a reasonable perturbation of the preexisting halo. In addition, it was found that even with a minimal amount of time left for evolution of the overdensity, the halo would strongly act upon overdensities with too extreme parameters, resulting in a difficulty to control exactly the Core Entry values of the mass and density ratios.

The density profile is directly related to the mass profile. Because of its integral nature, and for historical reasons, we chose in this section to use the mass profile to characterise the mass distribution in the system examined. For a density profile of the form $\rho \propto r^{-\mu}$, the mass profile is integrated into $iM \propto r^{3-\mu}$. So the shallow SSIM class of initial density profile leads to mass profiles following $iM \propto r$, whereas steep initial profiles ($\delta\rho \propto r^{-\epsilon}$, where $2 < \epsilon < 3$) yield mass profiles of the form $iM \propto r^{\frac{3}{1+\epsilon}}$. In the cases explored here, respectively $\epsilon = \frac{3}{2}$, $\frac{5}{2}$, 2.9, the mass profiles logarithmic slopes predicted by the SSIM are $3 - \mu = 1$, $\frac{6}{7} (\simeq 0.857)$, $\frac{10}{13} (\simeq 0.769)$.

5.4.2 Mutual relaxation of the system and the overdensity

The first striking feature of the effect of merger on the SSIM is how the measure of its self-similar quasi-stable evolution gets affected by the accretion of a bigger lump than its usual self-similar mass flow. Then it is the monitoring in phase space of the overdensity at the end of the self-similar phase and/or the beginning of the virialised phase which reveals how the overdensity retains some coherence after being ingested by the core.

ϵ and order	M_{ratio}	D_{ratio}	M_{OD}/M_{BG}	$T_{digestion}$	$T_{dynamical}$	$\frac{T_{digestion}}{T_{dynamical}}$
$\frac{3}{2}$, upper panel	0.751	0.282	1.173	2.50	0.70	3.57
$\frac{3}{2}$, middle panel	4.25×10^{-2}	7.10×10^{-2}	9.38×10^{-2}	0.13	0.73	0.178
$\frac{3}{2}$, lower panel	6.92×10^{-2}	0.168	1.453	0.13	0.71	0.183
$\frac{5}{2}$, upper panel	0.889	5.51×10^{-2}	0.319	4.21	1.21	3.48
$\frac{5}{2}$, middle panel	0.439	5.54×10^{-2}	0.290	3.07	1.12	2.74
$\frac{5}{2}$, lower panel	0.178	0.454	1.133	2.11	0.98	2.15
2.9, upper panel	0.753	9.19×10^{-2}	0.416	4.83	1.17	4.13
2.9, middle panel	0.407	0.641	1.118	4.94	1.10	4.49
2.9, lower panel	0.301	9.71×10^{-2}	0.344	3.07	1.11	2.77

Table 5.1: Defining parameters for the examples of merger with the SSIM

Merger from the SSIM core's perspective

It is first important to precise that the mass and density ratios given here are measured at the time defined as $T_{Core\ Entry}$ in section 5.3.2 and with figure 5.17 whereas those same ratios are used as initial input parameters to constitute the overdensity at the moment of its laying. The three examples for each of the three primordial density profiles used here makes nine sets of defining parameters, presented in table 5.2. The reference to the order of each simulation points to their positions in the corresponding figures. They are grouped by primordial density contrast power law index and then presented on top of each other. Each figure displays on each line, corresponding to one simulation, the virial ratio of the system and its phase space near the end of the self-similar phase for which the particles in the overdensity as defined at $T_{Core\ Entry}$ in section 5.3.2 with figure 5.17 are singled out so as to access to their phase space configuration once the system has relaxed. Figure 5.21 contains the results of mergers starting with a self-similar core evolved from a shallow initial density profile at $\epsilon = \frac{3}{2} = 1.5$. These simulations are taken to be generic for the shallow case. The steep initial density profile case is represented in figure 5.22 by the results of mergers starting from a self-similar core at $\epsilon = \frac{5}{2} = 2.5$. Because of the results these simulations show for the mass profile (see section 5.4.2), confirmation runs were performed at an extreme value of the initial density contrast's power law index to see the effects of changing self-similarity class within the same steep self-similarity category. Those run's virial evolution and phase space are presented in figure 5.23.

The first remarkable feature springing out from the virial evolutions is the presence of a sometimes drastic trough in the self-similar phase, which eventually returns to the **original** self-similar value of the initial core, as it can be undeniably checked on figure 5.21's upper left panel, all of figure 5.22's left panels or figure 5.23's lower left panel (the

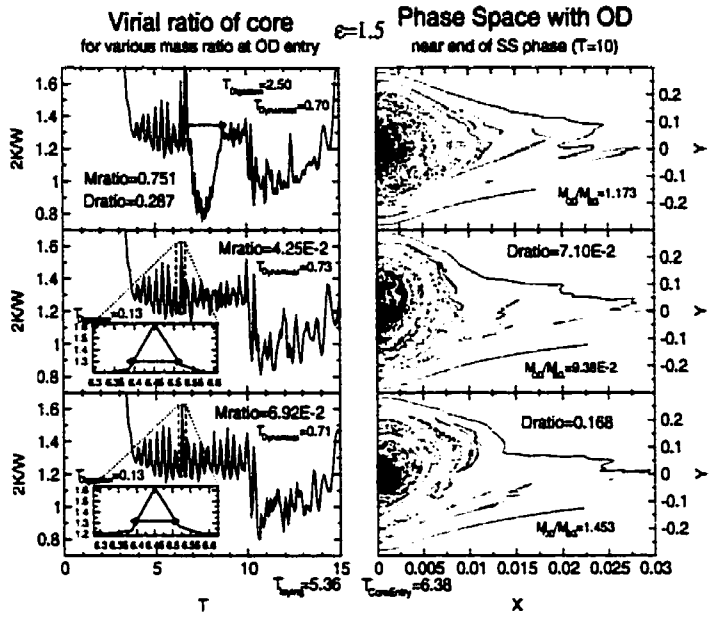

Figure 5.21: Shallow case: Virial ratio and phase space diagrams at the end of the self-similar phase, including an emphasis on digested overdensity shells for various overdensity parameter values in the semi-universal attractor SSIM case ($\epsilon = \frac{3}{2} = 1.5$). The middle and lower left panels also contain each a zoomed encapsulation of the small spike provoked by the absorption of the overdensity for those weaker perturbations.

latter's upper panel being less clear on that point, probably for lack of time left to the system in the self-similar phase, and the first's lower panels not displaying a trough). A close examination of the various simulations presented here reveals that the presence (figure 5.21's middle and lower left panels do not display a trough and figure 5.22's lower left panel just shows a very mild one because of their lower mass ratios than that which seems needed for the perturbation on the core to give rise to a clear trough) and deepness of the trough primarily depend on the mass ratio between the frozen overdensity (figure 5.17) and the corresponding self-similar core, and in a lesser measure, a deeper trough can be obtained from a combination of a high mass ratio and a high average density ratio (figure 5.23's middle left panel). Self-similar class seems to be affecting the threshold mass ratio at which a trough is visible in the sense that it seems the shallow case is more resistant to the establishment of high mass overdensity with a high density ratio, the tendency being to spread denser overdensities, hence the more successful simulations for the steep case in obtaining a trough in the virial ratio. This can be understood in terms of the more empty halo surrounding steeper initial profiles which acts less on any additional mass.

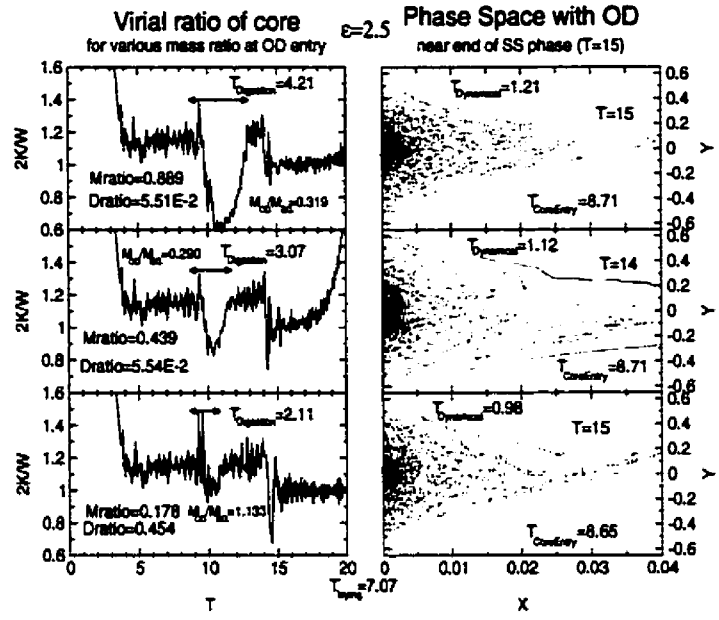

Figure 5.22: Steep case: Virial ratio and phase space diagrams at the end of the self-similar phase, including an emphasis on digested overdensity shells for various overdensity parameter values in the SSIM continuum of attractors case ($\epsilon = \frac{5}{2} = 2.5$)

Then the trough can be quantified by defining the digestion time for the core to return to its self-similar virial phase from Core Entry. A close examination of the virial behaviour in this range shows another distinction between shallow and steep cases: the troughs in the steep case all display at diverse degrees a first decrease in the virial ratio right after $T_{Core\ Entry}$, followed by a steep increase of the virial ratio which later dips into the trough until recovery of the initial self-similar value whereas the shallow case displays little of the initial decrease but shows two spikes before the trough itself. The evolution of the virial ratio under the influence of the overdensity can be understood according to the following scenario: because of the definition of the core (figure 5.13), and that of the time $T_{Core\ Entry}$, after that time exists three status for the overdensity. The first corresponds to the very brief time before its lower boundary effectively crosses the radius of the core, for which there is no effect on the core. The second occurs after that and before the overdensity's lower boundary reaches the centre of the halo. For this stage, the only effect the overdensity can have on the core is through its contribution to gravitational energy, since it is not yet being counted in the core, but gravitational energy counts all the mass inside a given radius. The effect of that stage on the virial ratio is expected to be that first dip observed on steep profile cases, because only the magnitude of the potential

energy is increased in those circumstances. From phase space diagrams (figures 5.21, 5.22 and 5.23's right hand side panels) it can be conjectured that this absence of dip could come from the smaller size of shallower cores compared to steeper ones, leaving no time for the shallow core to reflect this stage. The third status corresponds to the entrance of the overdensity into the system. A first order phenomenological calculation on the impact of an overdensity on the virial ratio shows that an overdensity more dominated by kinetic energy (more hot) than the core could explain the spike(s) at the beginning of its digestion. It can be seen as follows: noting the core and overdensity's total, kinetic and potential energy respectively E, K, -W, E_{OD}, K_{OD}, $-W_{OD}$, and the half virial ratios for the core, the overdensity and the total system respectively A, A_{OD} and A_T, and assuming the crude model of instantaneous absorption of the overdensity 'as is' by the core, as well as that $\frac{K_{OD}}{W}$ and $\frac{W_{OD}}{W}$ are first order quantities, the total system's energy ratio then reads:

$$A_T = \frac{K + K_{OD}}{W + W_{OD}} \simeq \left(A + \frac{K_{OD}}{W}\right)\left(1 - \frac{W_{OD}}{W}\right) \simeq A + \frac{K_{OD}}{W} - A\frac{W_{OD}}{W}$$

$$\Rightarrow A_T \simeq A + (A_{OD} - A)\frac{W_{OD}}{W},$$

thus $A_T > A$ when $A_{OD} > A$.

Then, keeping this simple model, before the overdensity relaxes with the system, it can be seen crudely that keeping the kinetic energy roughly constant, the potential energy should increase each time the overdensity runs through the centre, allowing for additional spikes in the shallow case, where the phase space shows the system to be less relaxed in general, and needing perhaps more dynamical mixing turns in the edge of the system for the overdensity to get relaxed in the system. Eventually, relaxation of the overdensity in the medium of the core seems to combine this increase of the total potential energy with a decrease in kinetic energy probably manifesting an over-reaction of the system under the addition of the overheated clump of extra mass, contracting temporarily until the overdensity gets digested by the system.

In order to assess the time it takes for the halo to digest an overdensity, the dynamical time was evaluated for the farthest overdensity shell at $T_{Core\ Entry}$. Because the definition of a dynamical time typically involves an isolated system ([87], p37), which the SSIM is not, a self-similar version of the argument is used to extract a dynamical time adapted to the system. The argument goes as follows: consider a test particle placed at the same radius in a spherical model as the shell considered (here the last overdensity shell at Core Entry) falling under the pull of the mass contained in that shell, but spread as a constant density distribution (here in self-similar variable) that is assumed to be stable. The dynamical time is then defined as the free fall time for that test particle in this test system to reach its centre (see appendix E). Applying this definition to the studied

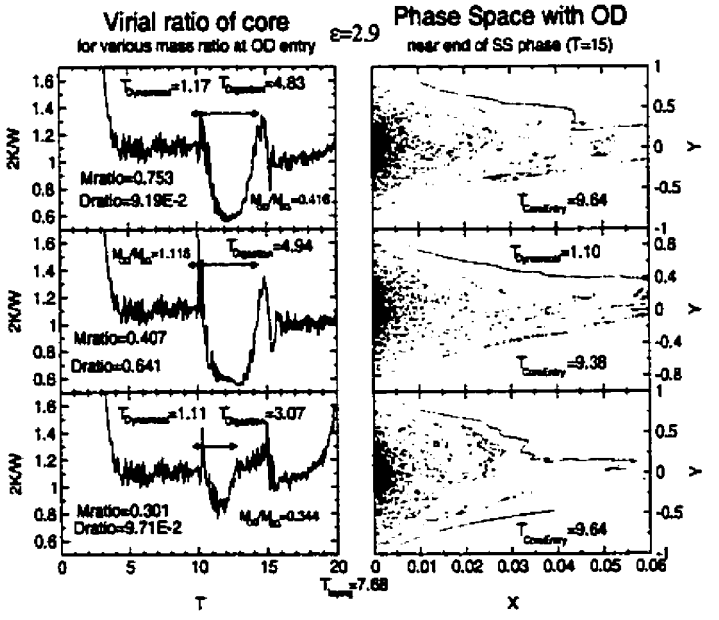

Figure 5.23: Extreme steep case: Virial ratio and phase space diagrams at the end of the self-similar phase, including an emphasis on digested overdensity shells for various overdensity parameter values in the SSIM continuum of attractors case ($\epsilon = 2.9$)

systems it was found that the digestion times of the overdensities by the haloes, apart from the two cases where the definition of the digestion time was problematic (middle and lower left panels of figure 5.21), is on average 3.33 times the dynamical time with a standard deviation of the ratio $\frac{T_{digestion}}{T_{dynamical}}$ of 0.767 (from the data in table 5.2). This indicates that the system needs of the order of 2 to 4 passages of the overdensity in the relaxation region to be completely assimilated, which seems comparable to the number of Lagrangian-Liouville streams present in the relaxation region of the phase space. There are still questions on the correlation between the digestion time and the mass and density ratios, but the small number of good, exploitable data prevent from a more thorough study.

The virial ratio also presents an interesting peculiarity on its virialised phase for the steep initial profile cases: from figure 5.22's upper and lower left panels as well as figure 5.23's two upper left panels, it seems that heavier masses, but also a combination of moderately heavy mass and higher density, tend to stabilise the integration on the virialised system while the use of self-similar variables translate into a shrinking of the system and a less and less trustworthy integration (the smoothing length doesn't shrink!). A close examination of the simulations' s corresponding phase space diagram reveals that each of these cases display the presence of overdensity particles right down to the centre of the system, whereas the non stabilised ones have a depleted centre of their phase space. This points to the fact that most of the instability in the SSIM comes from the scattering of incoming particles by the strongest gravitational field region at the centre of the halo and the jittering that may be induced on those scattering particles (recall that the SSIM with its PDF cut off is depleted of its most stable, central particles), which would then be damped by the presence of some stable additional mass.

Finally, the overall behaviour of the virial evolution under the influence of an overdensity inspires one to reflect upon the representation of the SSIM by a discrete computer model: instead of a continuous stream of mass, the model presents a repeated bombardment of finite mass shells which can be seen as small overdensities. Indeed, in the light of the behaviour of the virial ratio under the influence of lighter overdensities (figure 5.21's lower panels) the spikes appear as little more than overgrown noise features that are displayed throughout the rest of the simulations. It then appears that this very noise in the viral evolution is merely the ripples from repeated micromergers from each and everyone of the model's shells.

Mergers from the overdensity's perspective

The effect of the merger on the overdensity is reflected on its spread in the final phase space displayed for each simulation on the right corresponding panel of each figure. Two

features are crucial in the phenomenological description of the overdensity's fate: its spread along the halo, or conversely its compactness within the halo, and the presence of some or all of its particles at the origin of the system's phase space. This reflects on the reading grid used by Syer & White to develop a discourse on merger, divided between tidal stripping, which would tend to spread the overdensity throughout the halo, and dynamical friction, which would tend to pull the overdensity towards the centre of the halo.

Thus, a high density ratio seems the primary factor for compactness of the overdensity in the steep initial density profile case (figures 5.22's lower right panel and 5.23's middle right panel), which could be interpreted as good resistance to tidal stripping. Conversely a high mass ratio is the main factor to ensure presence of overdensity shells in the centre of phase space (figures 5.21's upper right panel, 5.22's lower and upper right panels and 5.23's two upper right panels), indicating that at least some of the overdensities with a high mass which sinks under the influence of dynamical friction to the centre has survived tidal striping.

Now all possible behaviours are available: a weak mass and density leads to a scattering of the overdensity shells throughout the halo without reaching the centre (figure 5.21's middle right panel). A weak mass but high density can prevent any part of the overdensity to sink to the centre but keep the tidally stripped shells in the same compact neighbourhood (figure 5.21's lower right panel). A weak density but high mass, if the density is high is high enough, can present a very scattered overdensity but still contribute to the central parts of the overdensity (figures 5.21's upper right panel, 5.22's upper right panel and 5.23's upper right panel), whereas if the density is too weak or the mass not high enough, the scattering may be too strong for a central contribution to survive (figures 5.21's middle right panel, 5.22's middle right panel and 5.23's lower right panel). But if both mass and density are strong enough, the overdensity can survive almost intact in the centre of the halo (figures 5.22's lower right panel and 5.23's middle right panel). Here we start to see the limits of the 'weak', 'strong', 'high' and 'low' denominations to qualify the density and mass ratios. At the same time, a picture involving some kind of threshold taking into account both the mass and density ratio emerges to account for the survival of some or all of the overdensity to the halo's tidal stripping in its journey to the centre under the influence of dynamical friction. The simplest conjecture compares the product of the two ratios to find whether a consistent threshold picture emerges from the data. Table 5.2 presents each model with its mass/density product. Indeed, if we divide the ranges between the steep initial density profile and the shallow one, a coherent picture emerges where the steep profiles require probably a higher parameter than a threshold contained between 6.920×10^{-2} and 8.081×10^{-2} to reach the centre intact of tidal stripping and another one between 2.923×10^{-2} and 4.898×10^{-2} to have some of overdensity

ϵ and order	$\frac{3}{2}$, upper panel	$\frac{3}{2}$, middle panel	$\frac{3}{2}$, lower panel	$\frac{5}{2}$, upper panel
$M_{ratio}.D_{ratio}$	0.212	3.017×10^{-3}	1.163×10^{-2}	4.898×10^{-2}
$\frac{5}{2}$, middle panel	$\frac{5}{2}$, lower panel	2.9, upper panel	2.9, middle panel	2.9, lower panel
2.432×10^{-2}	8.081×10^{-2}	6.920×10^{-2}	2.609×10^{-1}	2.923×10^{-2}

Table 5.2: Conjectured Survival parameter of the overdensity ($M_{ratio}.D_{ratio}$) for the examples of merger with the SSIM

reach the centre, and below which tidal stripping completely tears it apart, whereas the available data only allows for the second threshold to be bracketed in the shallow case, between 1.163×10^{-2} and 0.212. It is remarkable that the shallow case requires a higher threshold than the steep one. It can be understood, though, as a manifestation of the less concentrated nature of the shallow case's density distribution, which leaves a higher level material for the overdensity to cross for a longer radial range in its journey under the influence of dynamical friction, which would exert a stronger tidal stripping.

From here on the product $M_{ratio}.D_{ratio}$ will be referred as the strength of the overdensity and cases with a higher product value will be referred as stronger overdensities, and conversely, a lower product value will be referred as a weaker overdensity.

To summarise, the understanding of mergers in terms of dynamical friction and tidal stripping presented in Syer & White [33] appears to be relevant to the fate of an overdensity in the frame of the SSIM, the difference between the secondary infall and repeated mergers accretion formation residing essentially in a quantitative size of the merging satellites.

5.4.3 Effect of merger on the SSIM's final density profile

The aim of the Syer & White argument [33] is to provide an explanatory frame for the observation that a universal density profile should arise for CDM haloes from repeated mergers, as first found by NFW [32]; but this argument would retain its validity even for other forms of universal profiles (Moore *et al.* [71]) provided that repeated mergers are indeed essential to the formation of CDM haloes density profiles. The goal of this section is to assess how and if mergers are modifying the density profile of the SSIM in its nature and shape.

The first step in this endeavour was to check for each of the actualisations of the SSIM presented here that they were indeed following the SSIM's predictions. This was effected in figures 5.24, 5.25 and 5.26's left panels by displaying for every realisation of the SSIM the mass profile it presents once it has reached the time defined above as $T_{Core\ Entry}$, at which the overdensity has evolved and fallen down to the brink of entering the system's

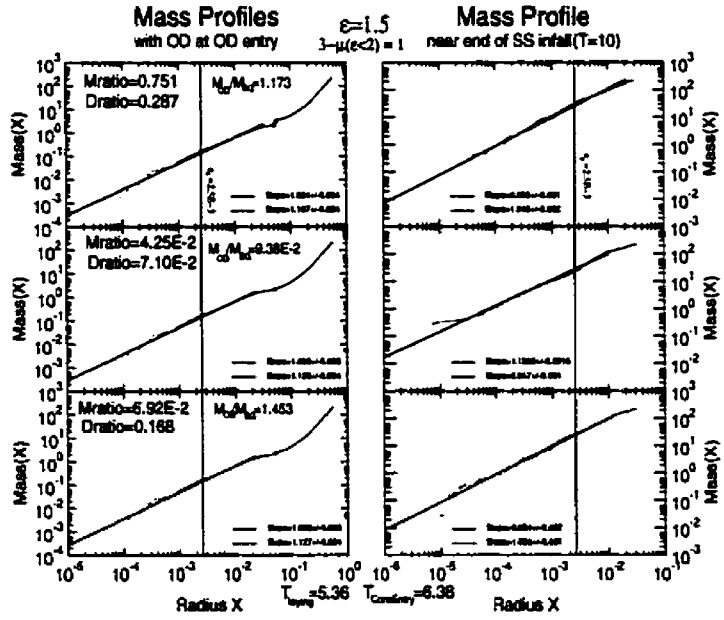

Figure 5.24: Shallow case: Mass profiles comparison between the time of first absorption of the overdensity by the system and the end of the self-similar phase, including an emphasis on digested overdensity shells for various overdensity parameter values in the semi-universal attractor SSIM case ($\epsilon = \frac{3}{2} = 1.5$)

radius. Each profile is fitted by power laws, first over the region of the core above the smoothing length (green fits) then over the whole core (blue fits). The core region was defined with the help of the phase space diagram. As invoked above in section 5.2.2, the limitation of validity of the density profile is not coming from the smoothing length for reasons which will be discussed in more details in section 6.2.3. In the top centre of each figure is indicated the initial density contrast power law index and the SSIM predicted slope of the mass profile $3-\mu$ where μ is the power law index of the self-similar density profile. The shallow initial density profile set reproduces the prediction above the smoothing length, but displays a departure from them when taking the whole halo into account, reflecting a flattening of the density profile in the centre (which translate in the mass profile as a steepening, from the $3-\mu$ correspondence; we will use the mass profiles here but discuss the density profiles, assuming the slope translation is exact). The same problem arises in the extreme steep initial profile set which reproduces the SSIM's predictions better with the fit above the smoothing length, flattening occurring which spoils the whole core fit. On another hand the regularly steep initial profile displays the opposite behaviour, the mass profile fit above the smoothing length being probably flattened by the inclusion of some out-of-the-core shells in the fit, picked up in the manual method of selecting fitted regions. All in all, these departures from the predictions of the SSIM are very minor, as can be observed on figures 5.24, 5.25 and 5.26's fits and the check was considered successful.

Then the outputs from the digestions of the overdensity by each core can be examined. It can be first read in terms of the power law fits. The shallow case doesn't seem to be much affected even though the slopes are all slightly inferior to their counterparts before the ingestion of the overdensity (compare figure 5.24's right panels slope with their left panel counterparts; though, the middle panel shows an increase in the outer slope). Considering the changes and the weaker overdensity's discrepancy (middle panel), the conclusion that nothing much is changed is therefore natural. One detail springs out as a minor trend from the overdensity: the weaker overdensities produce a stronger flattening in the centre of the density profile and the stronger one marks a flattening of the mass profile. But the innermost profile is subject to the unreliability of the discrete shell modeling of a continuous density in the centre when the number of shells contributing becomes small and has to be taken with caution.

The $\epsilon = \frac{5}{2} = 2.5$ initial density profile set tells a different story: there is a definite steepening trend of the mass profiles towards the shallow-type semi-universal profile of the SSIM, which is markedly more pronounced for the stronger overdensity. At the same time, the stronger the overdensity gets, the more pronounced the morphology of the density profile gets from an almost pure power law to a varying power index profile with a flatter core and a steeper envelope, as observed in full N-body simulations and in the

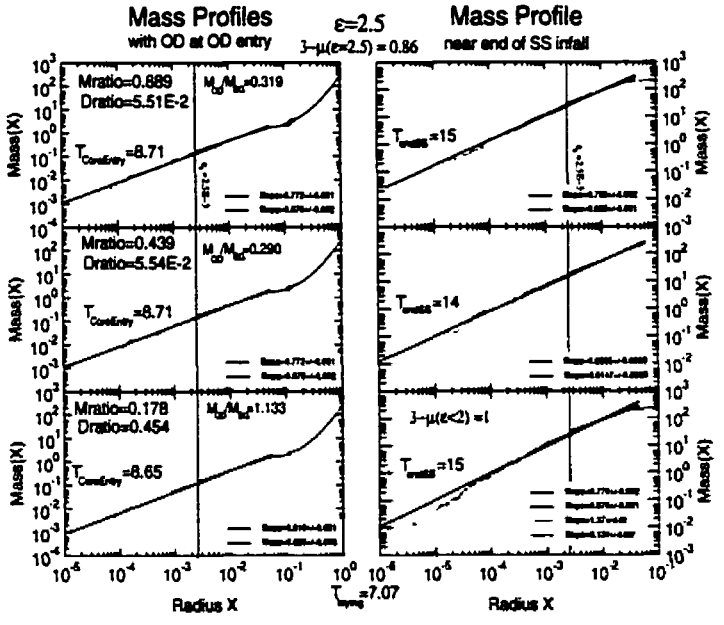

Figure 5.25: Steep case: Mass profiles comparison between the time of first absorption of the overdensity by the system and the end of the self-similar phase, including an emphasis on digested overdensity shells for various overdensity parameter values in the SSIM continuum of attractors case ($\epsilon = \frac{5}{2} = 2.5$)

universal profiles fit (NFW, Moore *et al.*, Hernquist). Nevertheless this bending doesn't concern the bulk of the profiles and NFW profiles were not even close to fit the stronger overdensity. Instead, the bent edges of the stronger overdensity case were fitted with power laws as indications of their asymptotic slopes (see figure 5.25's lower right panel).

These results would tend to suggest a picture where one merger event seems to contract the already narrow continuum of attractor density profiles outputted from the SSIM (recall that for initial density contrast indices $\epsilon \in [2;3]$, the corresponding self-similar classes range $\delta = \frac{2}{3}\left(1+\frac{1}{\epsilon}\right) \in \left[\frac{8}{9};1\right]$ and the final attractor density profile indices build as $\mu = \frac{2}{\delta} \in \left[2;\frac{9}{4}\right]$), leading to a picture where repeated mergers would eventually bring the SSIM's semi-universal density profile to a unique attractor isothermal profile, that is $\mu = 2$, reminding the picture of Syer & White [33]. This picture has to be modified, because the central density nor the total mass can be infinite contrary to the isothermal sphere, with the peculiar deviations at the edges of the profile. This leads the attractor slope to eventually lose its meaning since the asymptotic slopes of the edges would be the most prominent features of the final profile.

The extreme steeper initial density profile set ($\epsilon = 2.9$) was then used to confirm this effect from a merger simulation on the SSIM. The steepening of the mass profile is confirmed, but in this set, the weaker overdensities are getting the stronger steepening. The deviations at the edges of the density profile, though seem to follow the previous pattern, and the stronger overdensity's inner slope was measured to be about the same as for the less steep initial profile case. The outer bending was less conspicuous and therefore was not measured (see figure 5.26).

The trend contradiction displayed here with the more moderate steep initial profile set can mean two things: either the SSIM range of final slopes is already so narrow that logarithmic slope measurements are differing by little more than the measurement noise, or the extremely concentrated initial density profile contains an instability that would tend to flatten it under the slightest of the circumstances, and stronger overdensities are just tending to contribute more to the central density distribution, slowing the flattening process. The latter is the most likely explanation. It is also remarkable that the deviations at the edges would be qualitatively similar to the changes of logarithmic slope observed in N-body simulations haloes.

5.4.4 Mergers and the SSIM

Exploration of the SSIM with a model of merger has brought us a great deal of insight into the formation of CDM haloes: from a dynamical point of view, it has allowed us to probe into the intricate details of the impact of a merging satellite on the SSIM of a halo. It seems that, even though the density profile resulting from the merging event would tend

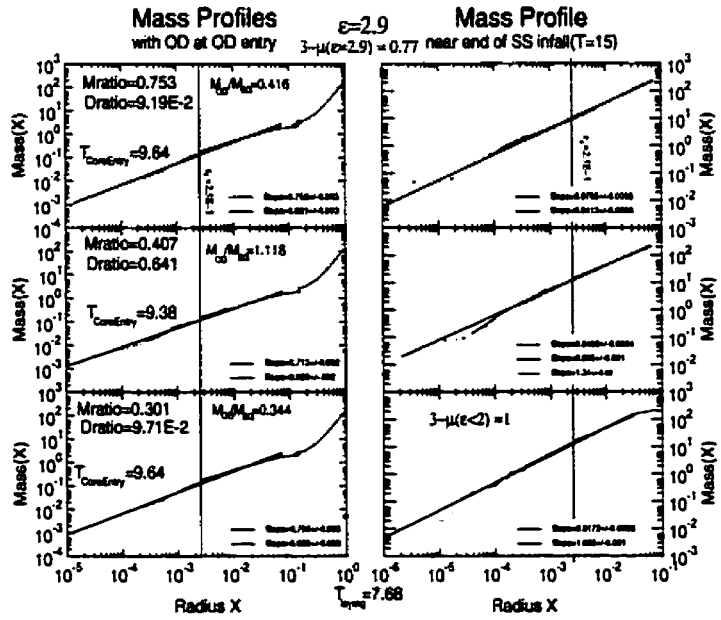

Figure 5.26: Extreme steep case: Mass profiles comparison between the time of first absorption of the overdensity by the system and the end of the self-similar phase, including an emphasis on digested overdensity shells for various overdensity parameter values in the SSIM continuum of attractors case ($\epsilon = 2.9$)

to point to a destruction of the scale-free unique power law of the SSIM, the continuation of the secondary mass infall seems to bring the system back into the energetic quasi-stable state of the SSIM. In other respects, this 'merger probe' into the intimate modeling of the SSIM shows the lack of distinction between the SSIM and repeated mergers where satellites are small enough compared to the parent, and the number of mergers frequent enough to maintain a strong mass flux through the system's boundary.

From the constitution of the density profile, the SSIM has taught us that indeed, repeated strong mergers could be the driving force that build the kind of two components profiles seen in large N-body simulations, but this study should be extended if it were to yield more precise prediction on the inner and outer profile logarithmic slopes. Nevertheless, departure from the unique power law profile is not a monopoly of the merger events and literature has shown that the central flat slope observed is concomitant with a certain amount of non-radial motion, suggesting that rotation could also be a driving force to get the two components density profile. Eventually, the observations of real density profiles suggesting that inner slopes even flatter than the ones obtained in pure CDM N-body calculations is suggesting that something more is needed than just cold dark matter to explain haloes profiles.

Alternate take: Besides, this probe of a merger into the intimate modeling of the SSIM shows that there is no distinction between the kind of merging where satellites are small enough compared to the parent, and the number of mergers frequent enough, and the SSIM.

Chapter 6

Implementation of angular momentum and a central black hole in the SSIM

> Celui qui proclame l'existence de l'infini, et personne ne peut y échapper, accumule dans cette affirmation plus de surnaturel qu'il n'y en a dans les miracles de toutes les religions, car la notion de l'infini a le double charactère de s'imposer et d'être incompréhensible.
>
> LOUIS PASTEUR (1822-1895)

The previous chapter allowed us to realise that the SSIM had much more explanatory potential than was expected. Despite its symmetry restrictions and the well accepted paradigm of repeated mergers for CDM halo formation, it was able with secondary accretion to give insight into the workings of (moderately) violent relaxation of haloes, as well as to bridge the gap between the merger paradigm and the opposite one of secondary accretion.

Nevertheless, unconstrained N-body simulations strongly question the radial infall limitation of the SSIM, as well as, to a lesser degree, its spherical symmetry. The latter point can be ignored with arguments such as the fact that we can consider models of simplified geometry to understand the principles of CDM halo formation. Exploring more restricted geometries helps to circumscribe those principles. Spherical symmetry can be seen more simply, as put forward by Sikivie *et al.* [51], as a model of an average halo

representing the mean over all halo orientation. The former objection, though, is more problematic (e.g. the qualitative differences between radial and less restricted N-body simulations in Huss *et al.* [66]) and calls indeed for some urgent investigations.

In parallel, observations seem to be pointing towards a much flatter density profile central cusp for dark matter haloes (Kravtsov *et al.* [31], Stil [75]) and purely collisionless CDM seems unable to explain that in itself. One way, of producing such a cusp is through the presence of a central black hole in the middle of the halo as was done first by Peebles 72 [82], Young 80 [83], Quinlan *et al.* [84], and, more successfully as far as flattening the central cusp is concerned, by Nakano & Makino 99 [85] and Henriksen & Le Delliou [86].

This chapter will tackle those issues by modifying the SSIM. The first section will give the tools by which the SSIM can be made to model angular momentum's effects. The second section will detail the changes angular momentum implies for the results of the SSIM. The third section will present the implementation of a growing black hole in the non-relativistic context and the last section will be devoted to the results from such a simplified model.

6.1 Angular momentum implementation: the initial radial dependence

The introduction of non-radial motion in dark matter halo models has followed several forms, from full 3D N-body simulations to a radial model with transverse velocity dispersion ([45], [46] and [55]). These include spherically symmetric angular momentum shell distribution, with just a constant angular momentum magnitude per shell, a single shell angular momentum magnitude distribution ([51]), and ad hoc source terms that switches off at turnaround ([52]).

The importance of non radial motion in the formation of dark matter haloes in other works has been discussed in section 3.2.1. This section will first summarise the issue of vorticity in dark haloes, as well as its presence in spherical symmetry, and then detail the implementation of angular momentum in the numerical modeling of the SSIM.

6.1.1 Dark haloes and angular momentum

Dark haloes and galaxies are believed to acquire their angular momentum from neighbouring anisotropies of the density distribution. Neighbouring haloes, when forming, first compete for accretion of mass at the edges of their accretion basins. Because of the irregular shapes of these basins coming from anisotropies in the primordial density distribution, each halo would in general not be spherical. That means that their tidal torques on their neighbourhood are in general not symmetric, thus imprinting vorticity

(see Peebles 80 [8] pp 107-110, or Longair 98 [105] pp 477-479).

In the spherical symmetry of the SSIM, introduction of angular momentum has to be ad hoc: indeed, the symmetry imposes that angular momentum is conserved for each shell at all times. This can be done by introducing a heuristic source term as in White & Zaritsky [52] until the turnaround for each particle, or by assigning an angular momentum distribution at turn around time (Sikivie *et al.* [51], whereas the distribution respects self-similarity or follow some statistics). The radial SSIM teaches us that self-similarity can be expected as an intermediate stage of evolution of dark haloes. In this work, a form of angular momentum was assigned at the beginning of the collapse such that the establishment of self-similarity is ensured at turnaround. Recall that the self-similarity is established analytically by the asymptotic logarithmic slope of the turnaround radius as a function of time (Henriksen & Widrow [42]). This form of angular momentum distribution will be referred below as self-similar angular momentum or SSAM.

6.1.2 Implementation in the SSIM's shell model

The introduction of angular momentum in the simulations takes place at the setting of initial conditions, but it obeys, for half of the explorations, a constraint which allows for the Fillmore & Goldreich [35] self-similarity to establish itself at turnaround. This constraint is similar to the condition at turnaround used by Sikivie *et al.* [51] on angular momentum to ensure self-similarity but it is used to establish an initial form of angular momentum (Eq.3.73). The other half of the explorations uses an asymptotically scale-free power law form inspired by the previous form. The slight departure from the so-called self-similar form of the angular momentum, or SSAM, was found to be natural and useful.

Together with the establishment of the shell's masses, initial positions and velocities, the initial angular momentum is set to a non-zero value and account is to be taken of this in the calculations of accelerations for each shell according to Eqs.(4.15). It also modifies the calculations of kinetic energy for each shell according to the full expression of Eq.(4.7).

Angular momentum implementation in the SSIM requires us to follow the form given by Eq.(3.73). Translated into the variables used in the problem, it means that for each shell, there is a value attributed of the angular momentum according to the expression

$$j^2(i) = \rho_0 \frac{\lambda}{3q} x_i^{4-\epsilon} \left[1 - \sqrt{1 - 4J^2 \left(1 + q \frac{x_i^\epsilon}{\lambda} \right)^2} \right]$$

$$\lambda = [A(1-B) r_{min}^\epsilon]$$

$$q = (1 - \frac{\epsilon}{3})$$

and that the subsequent angular momentum profiles will follow from the shells' radial phase mixing during infall, spherical symmetry excluding any evolution of the individual shell's angular momentum (recall that a spherically symmetric system obeys equations of motions without angular momentum evolution). In fact we will use an expression from which the previous equation is derived since the mass profile is already computed at that stage of the simulation:

$$j^2(i) = iM(x_i).x_i.\frac{\left[1-\sqrt{1-4J^2\left(1+q\frac{x_i^i}{\lambda}\right)^2}\right]}{\left(1+q\frac{x_i^i}{\lambda}\right)}, \tag{6.1}$$

keeping the same definitions for q and λ. This expression is just a calculation step before the previous one, the simple substitution of $\frac{a}{x}$ in Eq.(3.70). It will be referred to in the rest of this work as the self-similar form of angular momentum, or SSAM form. It is also based on the same constraint used by Sikivie *et al.* [51] after the turnaround time of each of their shells.

It is important to note that this expression has been computed for an initial angular momentum distribution that would not disturb the self-similarity so much that the Fillmore & Goldreich self-similar radial density profile would not be valid anymore. This is translated into the presence of a squareroot factor whose argument must remain positive if the solution is to be valid. A negative argument just manifests that the strength of the angular momentum represented by the constant factor J^2 is too large to respect that constraint. This sets a limit on the strength of j^2 which may prevent fruitful explorations. Indeed it proved difficult to obtain results interestingly different enough from the classic SSIM ones.

Using Eq.(6.1) as a starting point, this work also explored a form of the initial angular momentum that is not preserving self-similarity to compare its effect on the core of the SSIM. In Eq.(6.1), the factor $iM(x_i).x_i$ is dictated by Dimensional considerations whereas the rest of the expression just reflects the constraints to keep the SSIM results together with the presence of j^2. To obtain a new profile that can compare with Eq.(6.1) but is not limited in amplitude, one can take the limit of the extra factor when the amplitude J^2 is very small and then extrapolate it for any value of J^2. Such a profile would be close to scale-free (the initial mass is just a power law perturbation on top of a constant background) and still motivated by Dimensional arguments, but the modulation factor

would write:

$$\frac{\left[1-\sqrt{1-4J^2\left(1+q\frac{x_i^\epsilon}{\lambda}\right)^2}\right]}{\left(1+q\frac{x_i^\epsilon}{\lambda}\right)} =$$

$$\frac{\left[1-\sqrt{\left[1-2J\left(1+q\frac{x_i^\epsilon}{\lambda}\right)\right]\left[1+2J\left(1+q\frac{x_i^\epsilon}{\lambda}\right)\right]}\right]}{\left(1+q\frac{x_i^\epsilon}{\lambda}\right)} \underset{J^2\sim 0\,(heuristically)}{\simeq},$$

$$\frac{\left[1-\sqrt{1-2J\left(1+q\frac{x_i^\epsilon}{\lambda}\right)}\right]}{\left(1+q\frac{x_i^\epsilon}{\lambda}\right)} \underset{J^2\sim 0}{\simeq} \frac{\left[1-\left(1-J\left(1+q\frac{x_i^\epsilon}{\lambda}\right)\right)\right]}{\left(1+q\frac{x_i^\epsilon}{\lambda}\right)} = J$$

and thus allow for arbitrary amplitude of angular momentum (of course the third step is not rigorous but we are just looking for a **heuristic justification** of the factor here). Since J is a constant that we can redefine freely in our expression as J^2, the resulting initial angular momentum profile takes the form

$$j^2(i) = J^2 iM(x_i).x_i = J^2\rho_0\frac{\lambda}{3q}x_i^{4-\epsilon}\left(1+q\frac{x_i^\epsilon}{\lambda}\right). \tag{6.2}$$

This profile will be referred to as the 'power law' angular momentum profile, or PLAM. We will see (section 6.2.3) that the PLAM is able to reproduce an NFW profile. In order to place it into perspective, a section (section H.6) of appendix H is devoted to computing characteristics of the rotation of the model.

6.2 Angular momentum implementation: Results

The picture of a purely radial infall of matter is evidently contrived, especially when compared to observed galaxies or group of galaxies, which are most probably tracing motion in their dark matter halo. Observation of N-body codes output from various groups also points towards the need to include non-radial motion in any dark halo model.

This section will present the SSIM's picture of the influence of angular momentum, but first a discussion of non-radial motion from other works will be presented, followed by the present exploration.

6.2.1 Recall of motivations for modeling non-radial motion

N-body simulations offer a picture of collisionless collapse unbiased by the geometric constraints involved in the present work. The cores they obtain for dark matter haloes are a principal indication of the presence of non-radial motion. The importance of that

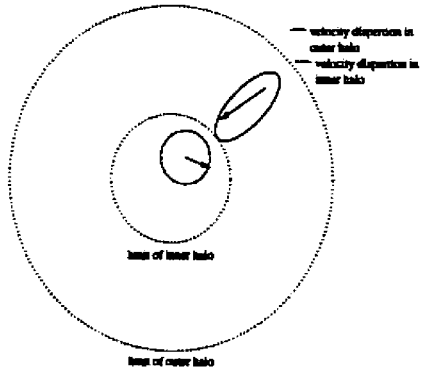

Figure 6.1: Picture of the velocity dispersions in Tormen *et al.* [55] as a function of halo depth.

kind of motion in the formation of the density profile has been shown for instance in Huss *et al.* 99a [66] and 99b [67]. Already Tormen *et al.* [55] had found N-body haloes to have elongated velocity dispersions in their outer parts but isotropic ones in their innermost parts (see figure 6.1) .

Other works have related central flattening of the density profile with dimensionality of the infall, or available phase space: Teyssier *et al.* [54] relate the difference in behaviour of dark matter with gas by the dimensionality of available phase space, pressure making the gas velocity distribution isotropic. Moutarde *et al.* [39] use a semi-analytical model formed with three orthogonal sinusoids initial density perturbation evolved in an N-body code to show how a system in which symmetry appears intermediate between spherical and cylindrical can give rise to a central cusp (of logarithmic slope 1.8) intermediate between the SSIM's prediction for those symmetries (e.g. Bertschinger [36], between 2 for spherical, and 1 for cylindrical symmetry). Their model implies a link between primordial caustic[1] intersections[2], dimensionality of available phase space and effective dimensionality of the collapse.

Models starting from the SSIM have also been explored for some sort of angular momentum accounting. Moutarde *et al.* [39]'s central slope is reminiscent of results from Ryden & Gunn's extension of the SSIM [47][3], where they included eccentricities and oblateness in the distribution of trajectories to find that, if a slope of 1.5 was found for

[1]caustics are singularities formed by the folding on themselves of non-singular continuous fields.

[2]In the theory of the largest scale structures offered by the Zel'Dovich approximation, the primordial velocity field leads to the formation of density caustics, or pancakes. Even in the CDM frame, velocities derived from the linear density perturbation form those caustics when considering very large scale structures. These pancakes define planes at which intersections form stronger caustics, called filaments, themselves intersecting into nodes that represent dominant haloes.

[3]Ryden & Gunn used adiabatic invariant with probabilistic methods in their explorations of the SSIM.

purely circular orbits, 1.8 was reached for random (isotropic) velocities. Indeed Ryden [53] has found with a perturbation model of a SSIM halo using Legendre polynomials that self-similar solutions to the infinite accretion stream model in axial symmetry yield central slopes shallower than the Fillmore & Goldreich [35] or Bertschinger [36] solutions, down to a slope of 1.5.

An earlier look at unconstrained spherically symmetric infall by White & Zaritsky [52] in an open background universe had an artificial angular momentum source building up rotation until turnaround. Their results show flatter halo mass profiles than isothermal without detailed central slope explorations.

Various semi-analytical methods seeking self-similar solutions to the Collisionless Boltzmann's Equation and its moments, coupled with Poisson's Equation (Subramanian *et al.* [45] and Subramanian [46]), or to the Lagrangian Newtonian Equations (Sikivie [51]), show inner cusps. These lie between an extension of the continuity of self similar attractors to shallow initial density profiles, expressed using this work's conventions by $\mu = \frac{3}{1+\frac{1}{\epsilon}}$,even for $\epsilon < 2$, (notice then that following the results from [47], a slope of 1.5 implies $\epsilon = 1$, and 1.8 comes from $\epsilon = \frac{3}{2}$) and the usual SSIM semi-universal slope of 2 for these shallow cases. If, for the Subramanian *et al.* model ,which includes isotropic tangential plus radial velocity dispersion, intermediate slopes were found, Sikivie *et al.* find the inner cusp to follow exactly the extension of the SSIM's continuum of attractors in the version of their model when the angular momentum is of constant magnitude over one shell. But those models are solving for pure self-similar solutions, that only involve phase mixing[4] (like Fillmore & Goldreich and Bertschinger), thus not taking phase space instability[5] into account.

6.2.2 Narrowing the exploration

In our exploration of our SSIM's version with an angular momentum radial distribution, it appeared difficult to find magnitudes of the angular momentum (parameter noted J^2 in Eqs.(6.1) and (6.2) governing more or less directly the amplitude of each shell's angular momentum) which would not have a negligible effect on the SSIM (in both cases of the SSAM form of Eq.(6.1)and 'power law' angular momentum of Eq.(6.2)) but which would be small enough to maintain self-similarity or even the formation of a central core (for Eq.(6.2)). Indeed the exploration of the non-self-similar[6] form of j^2 was triggered by

[4]Phase mixing is the action involved in non-linear dynamical system that lead to the closening of initial phase space points that were arbitrarily remote and vice-versa.

[5]We describe as phase space instability the arisal of turbulent-like behaviours in the phase mixing process.

[6]Here the self-similarity, when qualifying the form of the angular momentum profile, refers to the form that allows to conserve the Fillmore & Goldreich solutions in a 0 order approximation.

this difficulty. When the parameter was too small, the SSIM behaviour were recovered unchanged, whereas when it was too large, either in the self-similar j^2 distribution the squareroot in Eq.(6.1) was negative, indicating that an angular momentum with such a magnitude couldn't be self-similar, or the innermost shells' angular momentum was so large that they would never cross the origin and form a self-similar core but instead display tiny cores of phase mixed Liouville sheet. Moreover these tiny cores would never develop instabilities for lack of material and most of the halo's initial mass would maintain itself outside of the core (recall that cosmological initial conditions give Hubble flow halo particles). The systems presented here were then those with angular momentum magnitude tuned in the range which yielded a clear departure from the classical SSIM behaviour. With the SSAM, this was more difficult to obtain and the systems presented are still very close to the SSIM behaviour.

This chapter also comprises the test simulation studying whether the density profile is strongly influenced by changes of the smoothing length, and thus if its validity lies strictly outside the smoothing length or if it can be extended until ultimately the mass resolution sets an inner validity limit.

The representation of the full three-dimensional phase space (3 for radius, radial velocity and angular momentum) also sheds light on the dynamical behaviour and the relaxation process endured by the system under the influence of the two angular momentum distributions adopted here.

6.2.3 The influence of angular momentum on the cosmological SSIM

This section will present the angular momentum influence on the SSIM. In a first part, the persistence of a quasi-equilibrium self-similar phase and the effects of angular momentum on the SSIM's relaxation will be explored. The focus will turn, in the following section, to the formation of the density profile under the influence of angular momentum. A test simulation of reduced smoothing length (hereafter RSL) will then be discussed. Eventually the three-dimensional phase space of each explored case will be analysed as well as a correlation in the final angular momentum profile.

Relaxation and initial angular momentum distribution

Presented here are the results from four series of simulations involving two values of the initial density contrast power law index combined with the two initial angular momentum distributions used in this work. The values of the initial power law indices are taken as $\epsilon = \frac{3}{2}$ and $\epsilon = \frac{5}{2}$ which represent the SSIM's initial shallow and steep density profile respectively. The angular momentum strength is adjusted in Eq.(6.1) so as to minimise the squareroot term for the furthest shell (for that shell, the expression $4J^2\left(1+q\frac{x_i^\epsilon}{\lambda}\right)^2$ is

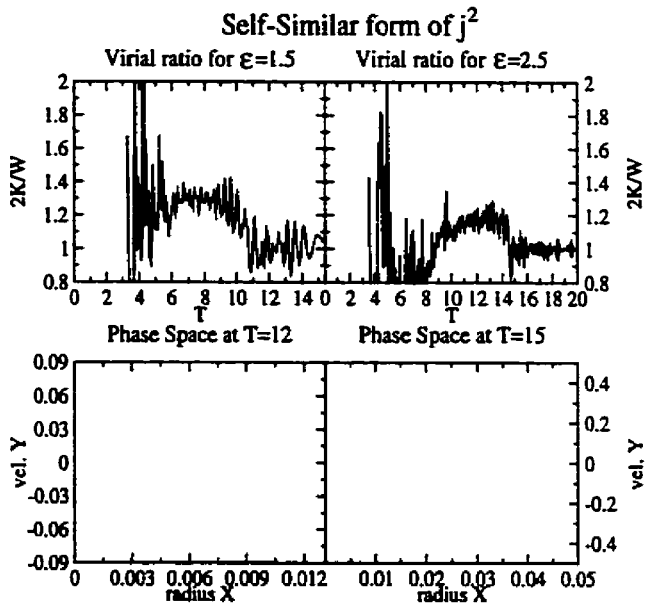

Figure 6.2: SSAM: virial ratios and phase space projections in the radius/radial velocity plane near the end of the self-similar quasi-equilibrium phase for critical values of the angular momentum in the shallow ($\epsilon = \frac{3}{2} = 1.5$) and steep ($\epsilon = \frac{5}{2} = 2.5$) initial density profiles cases

the largest). Thus, the squareroot factor is always defined but reaches 0 for the outermost shell. This corresponds to the strongest SSAM distribution allowed. In the shallow case the value is adjusted close to $J^2 \simeq 2.82 \times 10^{-6}$ up to machine precision, and close to $J^2 \simeq 4.60 \times 10^{-9}$ for the steep case (the magnitude being smaller in the steep case since the maximised expression grows faster in the steep case), corresponding to the approach to the limit $J^2 \leq \frac{\left(1+q\frac{\epsilon^2 h_0 l_0}{\lambda}\right)^{-2}}{4}$,before the argument of the squareroot of Eq.(6.1) becomes negative. For the 'power law' angular momentum of Eq.(6.2), the values adopted are respectively $J^2 = 9 \times 10^{-3}$ and $J^2 = 10^{-3}$, and are chosen in the range discussed in section 6.2.2.

The shallow and steep case results are presented side by side, showing that their reactions to angular momentum are similar, after taking their original SSIM behaviour differences into account. The virial ratios on figures 6.2 and 6.3's upper panels display the characteristic 'equal mass modeling initial stabilisation time' discussed in paragraph 5.2.2. The main difference with the SSIM resides in the transition from self-similar accretion to isolated virial ratios. Despite the limitation of angular momentum strength in figure 6.2, there still is a visible smoothing compared with the SSIM's sharp transition: instead of

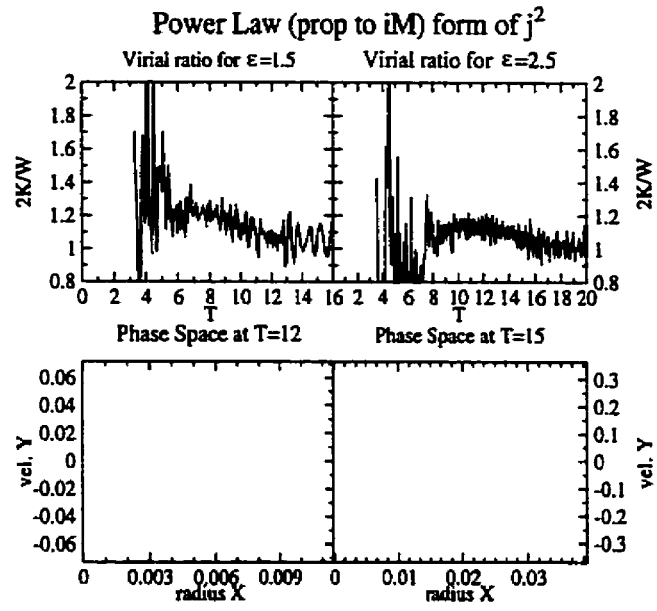

Figure 6.3: 'Power law' angular momentum (PLAM): virial ratios and phase space projections in the radius/radial velocity plane near the end of the self-similar quasi-equilibrium phase for critical values of the angular momentum in the shallow ($\epsilon = \frac{3}{2} = 1.5$) and steep ($\epsilon = \frac{5}{2} = 2.5$) initial density profiles cases

falling almost instantly from the self-similar value to the virialised unity when that last shell falls in the centre, the presence of angular momentum seems to yield a slow decrease from the self-similar value to the isolated one, beginning earlier than the SSIM's end of self-similar phase corresponding epoch and finishing later than that epoch. Moreover, the phase space projections (figures 6.2 and 6.3's lower panels display the phase space distribution of shells in the radius-radial velocity plane, projection along the angular momentum direction) reveal that there remains a stream of outer particles for which the angular momentum is so large that they will never fall into the core (their rotational kinetic energy makes them unbound). In a similar way as for the initial 'stabilisation time', this can be interpreted in terms of the mass flux at the boundary of the system. Indeed, the initial angular momentum distribution is monotonically increasing with radius, the angular momentum is conserved exactly throughout the simulations and the initial radial ordering is conserved until shells reach the core, so near the end of the self-similar phase, the shells with increasingly large angular momentum are just contributing to the mass flux. Considering that, given higher and higher angular momentum, there is a point at which it induces an inner turn around radius at the size of the self-similar core, shells

with a smaller angular momentum will be able to enter the core but with a reduced radial velocity compared with the radial SSIM. Since the increase of angular momentum with shell is gradual and concomitant with the shells coming at later and later epochs in the core, the mass flux can be pictured as diminishing gradually. And this gradual extinction of the mass flux through angular momentum is gradually shifting the system from its intermediate quasi-static phase to its final virialised (dynamically isolated gravitational stationary state) phase without the hiccup of a sudden interruption.

Eventually, the presence of angular momentum seems to stabilise the virialised stage of the system even when expressed in growing self-similar variables with a smoothing length that is fixed in those variables. Indeed, compared with the virial ratios of the radial SSIMs (figures 5.21's upper left panel and 5.22's middle left panel), those of the angular momentum SSIM appear much better behaved at late epochs (figures 6.2 and 6.3's upper panels), and that was obtained in almost every exploratory simulation involving angular momentum. This stabilisation effect can be understood by considering the centrifugal effect of angular momentum. Particles which are likely to escape the core after having their energies artificially boosted in the non-conservative dynamics zone[7] near the centre tend to deplete that region when ascribed angular momentum, leading to more stability of the system at later times.

Apart from the difficulty, in the SSAM simulations, to reach high enough values of non-radial motion to exhibit as clear an evidence of gradual self-similar to virialised state shifting as in the "power law" ones, their phase space aspect strikes one as less homogeneous in the relaxed regions in figure 6.2's lower panels, compared with figure 6.3's. In fact the self-similar j^2 figures exhibit much less smearing from the phase space instability in their inner parts than the radial SSIM or even the "power law" j^2 model: it is peculiarly noticeable for the shallow case that the winding of the phase space sheet, although not as exact as in the self-similar solutions, say from Sikivie *et al.* [51], is still visible in a smeared form, denoting a less complete relaxation than for the non-self-similar case.

Angular momentum and the density profile

This more moderately violent relaxation picture for the SSAM form of angular momentum is consistent with the comparison of the density profiles. These are presented, respectively for the SSAM and for the "power law" angular momentum form in figures 6.4 and 6.5's left and right panels for the shallow and steep initial density profile cases respectively. Each panel presents, together with the density profile, the size of the smoothing length used

[7]The smoothing length induces the possibility of energy conservation to be broken for particles inside of it, for there, the calculation of gravitational forces departs from Newton's law artificially.

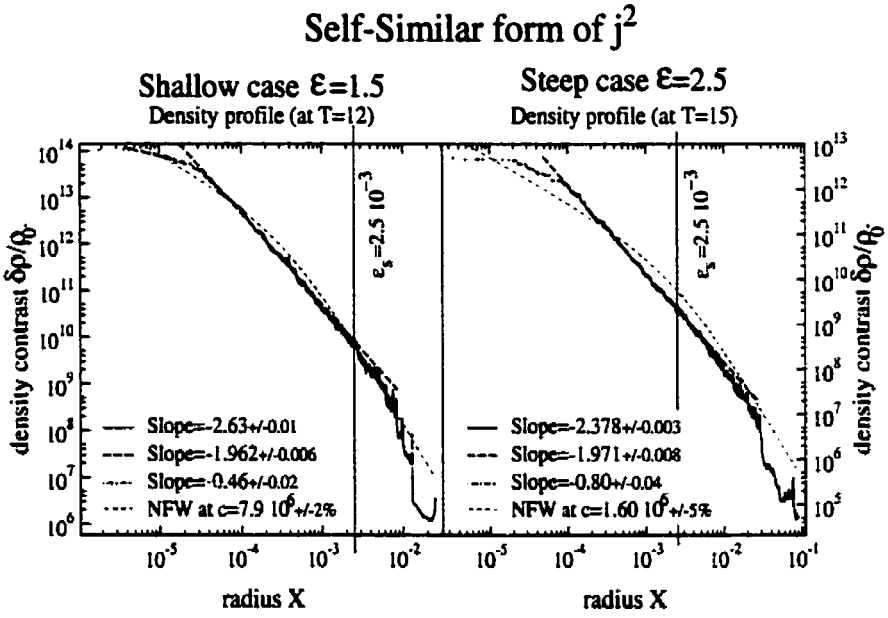

Figure 6.4: SSAM: density profiles for critical values of the angular momentum near the end of the self-similar quasi-equilibrium phase in the shallow ($\epsilon = \frac{3}{2} = 1.5$) and steep ($\epsilon = \frac{5}{2} = 2.5$) initial density profiles cases

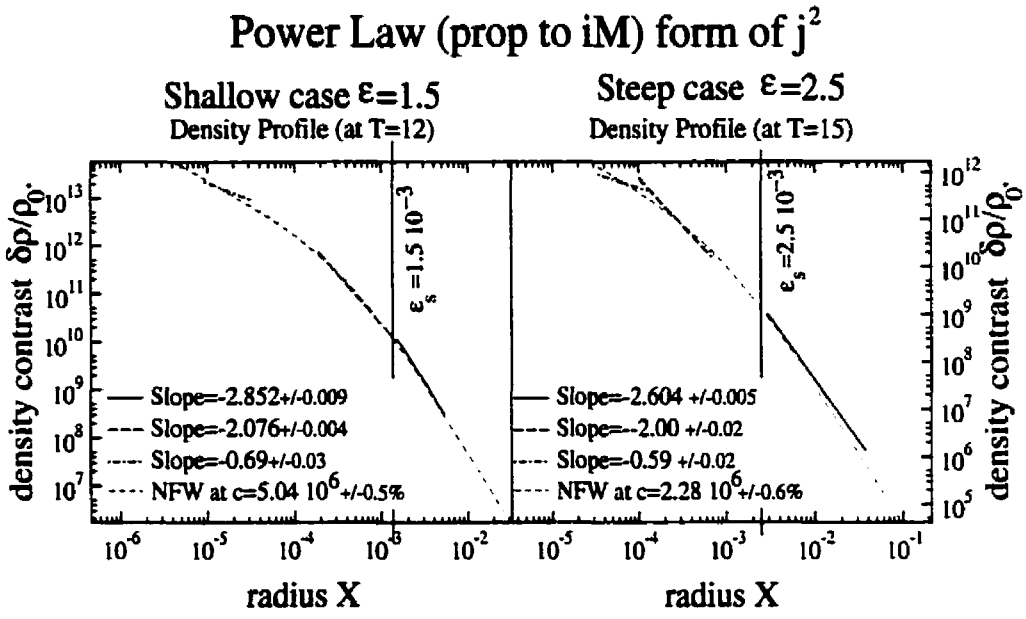

Figure 6.5: 'Power law' angular momentum (PLAM): density profiles for critical values of the angular momentum near the end of the self-similar quasi-equilibrium phase in the shallow ($\epsilon = \frac{3}{2} = 1.5$) and steep ($\epsilon = \frac{5}{2} = 2.5$) initial density profiles cases

and power law fits to the core above and below the smoothing length. The core region is limited again with the help of the phase space projection. In addition the innermost parts of the density profile are fitted in blue (dot-dashed line), and an NFW profile is fit (in orange, small dashed line) to the overall behaviour of our modified SSIM. Each power law fit logarithmic slope is indicated and an estimate of the NFW concentration parameter is given for the fit.

The first comparison should be made with the radial SSIM (figures 5.9 and 5.12's right panels). The presence of angular momentum set up to respect self-similarity seems to yield a very minor change in the density profile: very questionable in the steep case, the shallow case displays a moderate amount of flattening in the centre of the halo as well as steepening in the outermost parts of the system. Similarly to the radial SSIM, the central flattening could be interpreted as showing the limitations from our mass resolution so the innermost fit cannot hold more than an indicative value. Nevertheless, the increased convexity of the logarithmic density profile reveals itself through the slope differences around the smoothing length: even though division of the density profile at the smoothing length is artificial, ϵ_s having no major impact on the density profile (see section 6.2.3), its midpoint position reveals that the slopes above it are noticeably steeper

that those below it, by contrast with the radial SSIM, confirming that angular momentum indeed tends to deplete the centre of the halo and to smooth out the transition between the outer halo and the inter-halo medium.

The second comparison then ought to be between the convexity of the density profile with the so-called SSAM (figure 6.4) and that of the 'power law' version of the model (figure 6.5). In parallel with the more relaxed aspect of their phase space projections, the "power law" models display even more convex density profiles than the self-similar ones. This is so to the point that in the "power law" cases, the NFW fit looks a much better model for the density profile at the end of the self similar phase, which exhibits more of a smoothly varying logarithmic slope than of a piecewise power law profile. The innermost power law fit is again subject to the limited mass resolution and therefore at most indicative, but would suggest a flatter inner core than that given by the NFW profile. The central power law fit is close to isothermal in both self-similarity classes (steep and shallow cases) and the outer fit tends towards the Keplerian profile. The NFW fits show the steeper self-similarity classes to have smaller concentration parameters, but that is offset by the excess of mass over the NFW fit displayed by the steeper classes in their centre. In the 'power law' simulations with a shallow initial density, the smoothing length has been adjusted from the 2.5×10^{-3} value to $\epsilon_s = 1.5 \times 10^{-3}$, all other parameters kept constant, without a change. By continuity, the inner profile's slope for the "power law" models would be more compelling than that of the SSAM. On that assumption, it is to be noted that the slopes obtained are steeper than -0.5 but shallower than the ones obtained with the merger model of the SSIM, the Moore99 profile (slope of -1.5) and the NFW profile (slope of -1).

These results show that using the SSIM as a basis from which to relax slightly, such as allowing for some form of spherically symmetric angular momentum, offers the promise to circumscribe the exact nature of the physical elements involved in the formation of dark matter halo profiles. At the same time, self-similarity needs to be relaxed if a 'realistic' profile is to obtain (realistic in the sense that it can be fitted by a profile which represents the shape of full blown 3-dimensional N-body collisionless simulations). On the one hand, the irrelevance of the smoothing length for the validity of the density profile calls for a thorough evaluation of the effects of the mass resolution on that profile, which has yet to be done, and probably an enhancement of it in order to produce trustworthy innermost logarithmic slopes that can be compared with observations (numerical or physical). On the other hand, more effort should be put at understanding theoretically this necessary departure from the self-similar behaviour and , maybe, predict those slopes.

The effect of reduction of the smoothing length

Studies have been previously made (Knebe *et al.* [110]) on the effect of resolution on N-body dissipationless cosmological numerical simulations that emphasise the importance of a good coordination between the dynamical resolution of the force's smoothing length and the mass resolution, once the timestep has been adjusted to the integration of the force. The mass resolution represents the size of the phase space volume element associated with particles. Indeed, Knebe *et al.* [110] point out that if the smoothing length is smaller than the characteristic size of the phase space volume associated with a particle, such particle will not model a continuous mass distribution as it is expected to do but will behave like a point mass in two body encounters.

The numerical implementation of the SSIM's semi-analytical model implies the use of a smoothing length to avoid inducing through the central force singularity a scattering which would not respect the comoving size induced by finite mass shell modeling (section 4.1.1). Throughout this work, the range of values used for the smoothing length has been kept almost constant, due to computational time limitations (see the effect of varying the size of ϵ_s on the timestep, thus on the computation time, in sections 4.1.4 and4.3) and it is the aim of this section to explore the variation of such a smoothing length and show that its effects on the SSIM are minimal as used in this work. Because of the order of magnitude difference in computation time, one case of high interest involving the implementation of angular momentum with an initial radial distribution proportional to the mass profile times radius, referred to as " power law" implementation, was run.

First, the suspicion that the smoothing length should not affect much the SSIM is backed up by the theoretical exploration of a sort of coarse-graining of the SSIM's equations: Henriksen ([106]), in a development of the self-similar Collisionless Boltzmann's Equations (CBE) in powers of $1/\alpha$ has shown that the 0th order perturbation, while devoid of any dynamical term, nevertheless yields the same predictions as the SSIM (in its radial form) in terms of density profile (refer also to Henriksen & Le Delliou 01 [112]). In other words, once the self-similarity class is established from initial conditions and the mechanics of the turnaround radius and time given for each shell before shell-crossing by the gravity of the rest of its inner shells, the dynamics has no role in the establishment of the density profile other than maintaining the self-similar evolution. The density profile being then only superficially affected by the dynamics, its validity is not subject to the limitations of valid dynamics above the smoothing length.

Testing for these conjectures and predictions was effected and compared with the high smoothing length version of the model . Figures 6.6 and 6.7 present on their left panels the large smoothing length model ($\epsilon_s = 1.5 \times 10^{-3}$, $\epsilon = \frac{3}{2}$, $J^2 = 9 \times 10^{-3}$) on which the corresponding graphs for the smaller smoothing length ($\epsilon_s = 3 \times 10^{-4}$) are superimposed

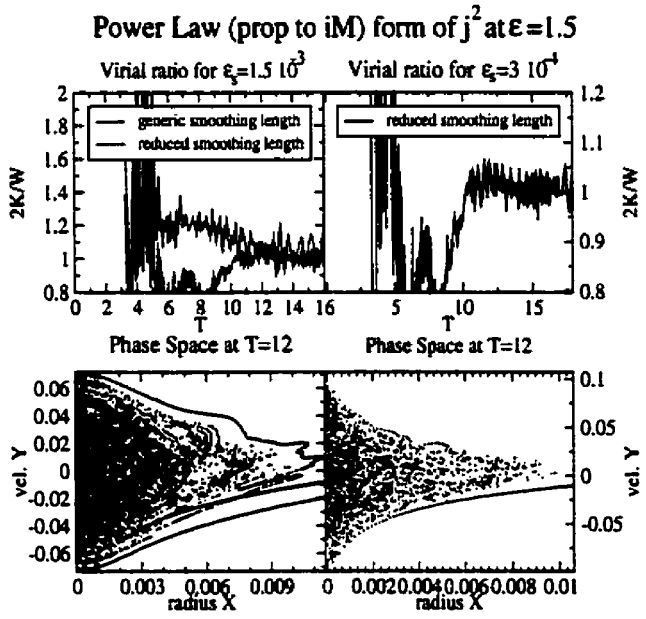

Figure 6.6: Smaller smoothing length ϵ_s test run: virial ratios and phase space projections in the radius/radial velocity plane near the end of the self-similar quasi-equilibrium phase for critical values of the angular momentum in the shallow ($\epsilon = \frac{3}{2} = 1.5$) initial density profiles cases using the 'power law' form of angular momentum

in red. These corresponding graphs are also repeated on the adjacent right panels of figures 6.6 and 6.7 for clarity (figure 6.6) and to allow for similar analysis (figure 6.7).

The main difference in behaviour of the virial ratio of the reduced smoothing length (RSL) simulation (figure 6.6's upper panels) resides in its longer period of stabilisation which encompass almost all of the self-similar phase. The right panel indicates that there still is a period where the ratio is slowly decreasing from a higher value than 1. Interpretation of this lengthened initial relaxation phase is problematic: its understanding in terms of reaching the 'mass flux resolution' in order to establish a stable self-similar quasi-equilibrium doesn't imply that a reduction of the smoothing length should slow down the process. In fact a reduced smoothing length (RSL) means that the region of reversing acceleration due to the mean potential inside the original smoothing length gets the maximum acceleration felt by particles in the centre boosted when that region is reduced; that increase in central acceleration should shorten the time spent by shells in the centre, tending to slightly shorten the 'equal mass time', not lengthen it. But the same increase of acceleration in the central parts also means that scattering of shells will be much stronger, making it more difficult for the system to settle down. This indicates that the mass flux resolution, though not sufficient to account for the stabilisation delay, still provides a good basis of understanding . The previous evidence of the correspondence between the stabilisation delay and $T_{equal\,mass}$ is not supported here. One might think that this is an indication that the mass resolution (see figure 5.3) should follow the smoothing length reduction in order to minimise inertial noise induced by high acceleration excitations of individual shells. The larger smoothing length has been thoroughly explored in an empirical fashion to yield the best account of dynamics and was monitored on the virial ratio in doing so. It can then be viewed as an optimum balance between the mass, force and time resolutions. Nevertheless, figure 6.6's upper right panel shows that there is still a decrease in the virial ratio of the RSL simulation, paralleling that of the generic one.

It is also remarkable that the noise in the virial ratio (the amplitude of its fluctuations, evident in figure 6.6's upper left panel) is diminished with the smoothing length, which shows that if on one hand the equilibrium is achieved slower, it is on another hand of a more stable nature.

Adding to this picture of a more efficient relaxation accompanying the smaller smoothing length, the phase space of the smaller ϵ_s simulation appears more relaxed than its larger ϵ_s counterpart, the relaxation region at the edges of the system being restricted to the first outer stream of the system and all traces of the intricate SSIM phase space mixing being washed out (figure 6.6's lower right and left panels). That relaxation explains why the smaller ϵ_s simulation's phase space is slightly wider in radial velocity and has its first outcoming particle stream inside of its counterpart's. This can also been observed

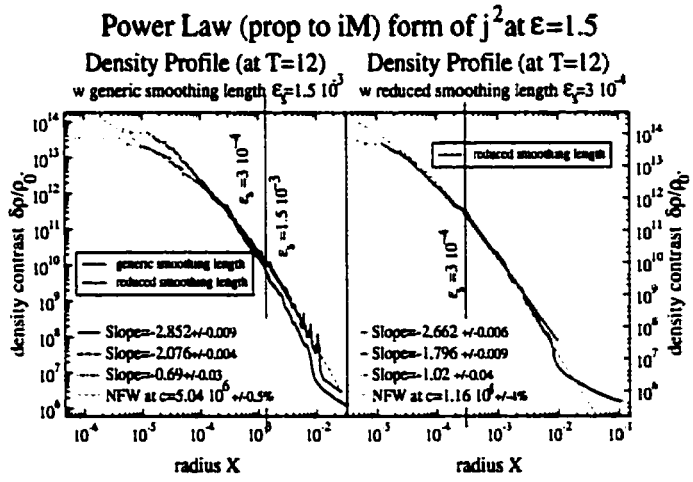

Figure 6.7: Smaller smoothing length ϵ_s test run: density profiles for critical values of the angular momentum near the end of the self-similar quasi-equilibrium phase in the shallow ($\epsilon = \frac{3}{2} = 1.5$) initial density profiles case using the 'power law' form of angular momentum

in the NFW fit which is slightly more concentrated with a smaller ϵ_s.

The comparison between the two density profiles resulting from the two ϵ_s on figure 6.7's left panel shows that little has changed in the operation. The outermost caustics, marking the relaxation region, are not present anymore, and the profile is slightly depleted on the edge while denser in the centre. All this denotes the higher degree of relaxation achieved by having a more detailed interaction for shells first crossing the origin. The fact that the power laws measured above and below ϵ_s are shallower than for the larger ϵ_s case are merely due to the change in position of the divide. It is notable that the innermost power law is steeper (and fully compatible with the NFW inner slope) in the RSL case. Thus the NFW profile could be explained entirely by the SSIM when angular momentum acts.

In brief, reducing the smoothing length doesn't affect drastically the behaviour of the system, even though the corresponding more detailed time integration allows for a stronger relaxation, a more stable evolution and an increase in the central slope. Exploring the fully 3-dimensional phase space (of the one-dimensional system plus angular momentum) then appeared of interest to check how the relaxation of the system was populating the angular momentum degree of freedom.

Interpreting these results in the light of N-body studies like Knebe *et al.* [110], it appears that our simulations have been using a smoothing length much larger than the mass resolution would prescribe, in order to stay on the safe side as far as the possible inaccuracy in the dynamics, induced whenever two body scattering becomes too important. The limitation on accuracy of the description by the mass resolution as well as the smoothing length-timestep relation sheds light on the low smoothing length cut off[8] particularly clear on figure 4.5's right panel, and with which this work has struggled to get an acceptable low ϵ_s simulation. Nevertheless, the nature of relaxation in the SSIM leads to the density profile being accurate even below its smoothing length, but only a

[8] An example of calculation for an estimate of the mass resolution length scale coming from this simulation can be written as follows: the constant mass of one shell is given in the simulation's unit as $m_{1shell} = 2.10^{-2}$. The maximum density contrast on figure 6.7 can be taken as $\frac{\delta\rho}{\rho_0} = 4.10^{13}$. Because of its high value, the density contrast, which can be noted in short δ in this note, can be identified with the density itself

$$\frac{\delta\rho}{\rho_0} = 4.10^{13} \gg 1 \Leftrightarrow \frac{\delta\rho}{\rho_0} \equiv \delta \simeq \rho.$$

Thus, the volume of innermost shells can be evaluated as

$$\delta \simeq \rho = \frac{m_{1shell}}{V_{1shell}} \Rightarrow V_{1shell} \simeq \frac{m_{1shell}}{\delta},$$

so the characteristic length scale of a shell in the centre is given by

$$L_{1shell} \simeq^3 \sqrt{\frac{m_{1shell}}{\delta}} =^3 \sqrt{\frac{2.10^{-2}}{4.10^{13}}} =^3 \sqrt{5.10^{-16}} =^3 \sqrt{0.5}10^{-5} \simeq 7.9 \times 10^{-6}.$$

few times above its mass resolution characteristic length. This is caused by the fact that relaxation in the SSIM essentially occurs in the few dynamical times that particles are freshly incorporated into the self-similar core, mainly around the secondary turnaround radii, i.e. near the radial boundary of the core.

The structure of three-dimensional phase space

This section explores the nature of the mass distribution in the radius-radial velocity-angular momentum phase space for systems with a shallow ($\epsilon = \frac{3}{2}$) initial density profile, starting with the RSL simulation. Then it is compared with the larger ϵ_s version of the simulation, to finish with that of the SSAM form of angular momentum. All of the phase space maps presented are measured at T=12 which corresponds to a clear end of the self-similar infall phase and beginning of the isolated system virialised phase.

In the low smoothing length and shallow case, projections along the axes were first attempted but it was not enough to get a clear view of the topology of the phase space distribution. Figure 6.8 (a)'s three different projections can show that shells are spread for all velocities at a given angular momentum small range (left panel), that higher radii are only available to the highest angular momenta (upper right panel) and that the j^2 projection has the structure of the 2-dimensional radial phase space (lower right panel).

To get a complete sense of the topology of the winding and relaxation of the original Liouville stream of Hubble flow shells, tilted projections of the (X,Y,j^2) space are required. Angular momentum conservation explains the population of all radial velocity values with the picture of this weaving distaff of mass flow being pulled along circuits stretched further and further in radius with increasing j^2 (i.e. initial kinetic energy). Figures 6.8 (b), (c) and (d) allow for a finer analysis: (b) shows a clear relaxation among the smallest radii and angular momentum shells which accumulate along the velocity axis at the smallest possible radii. Figure 6.8 (c) shows more clearly that the relaxation region is still present but unresolved in the j^2 projection since it is then projected on the boundary of the system. The most striking revelation that is made clear in figure 6.8 (d) is that gathering of shells takes place on a thin surface of phase space: the system seems constrained in a 2-dimensional sheet of the 3-dimensional phase space in the shape of a soaring bird, the neck and beak pointing towards high radius and angular momentum, the wings spreading over all values of j^2 towards the high ends of radial velocity and the body covering all values of Y into low X and j^2. That general shape as well as the 2-dimensional nature of the constrained phase space sheet is also present in the larger smoothing length simulation presented on figure 6.9 except that the high velocity wings are more progressively spread, only the highest angular momentum reaching the largest radial velocities. The accumulation of shells at low radius is also more shaped into the

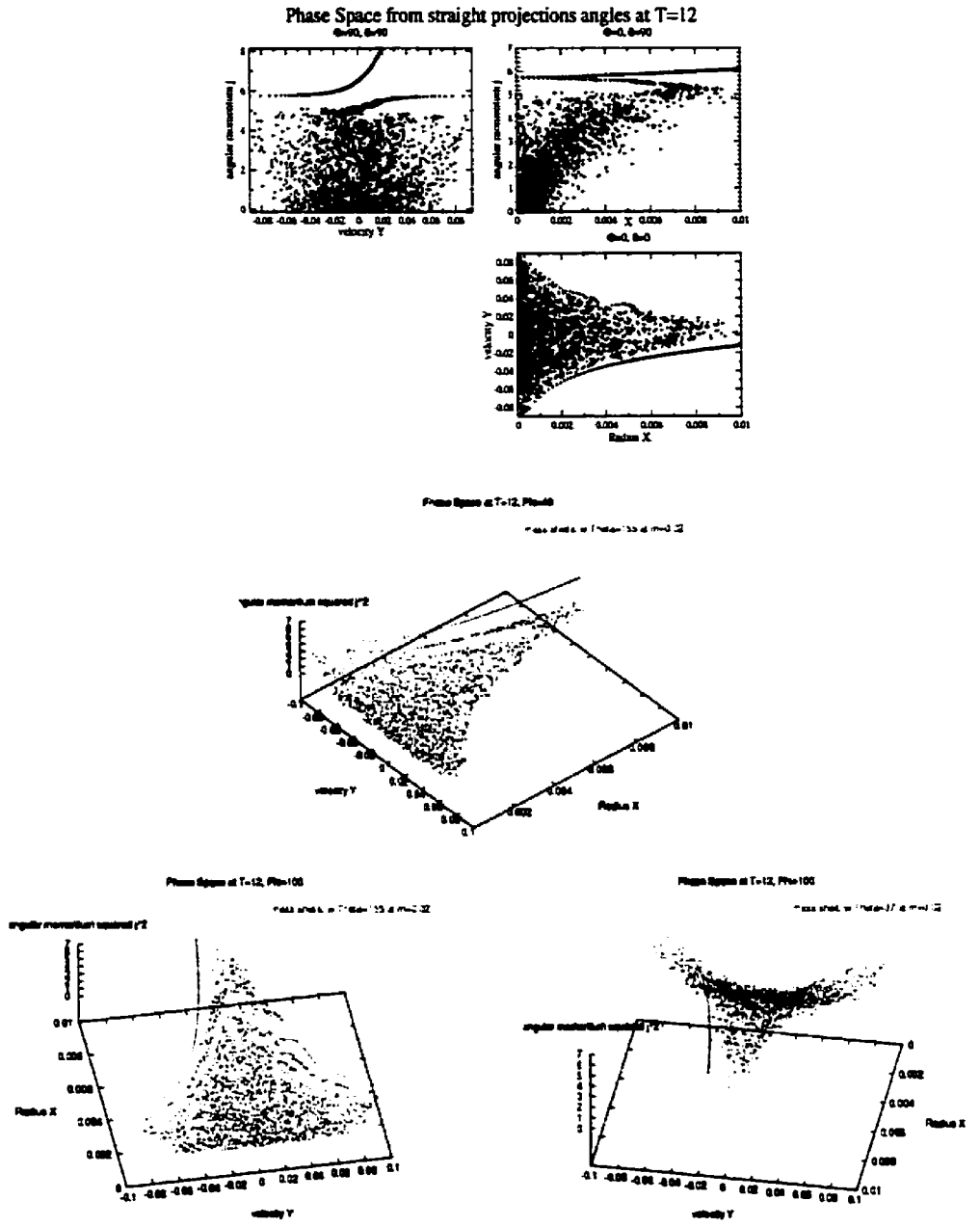

Figure 6.8: Full Phase space exploration for smaller smoothing length ϵ_s test run near the end of the self-similar quasi-equilibrium phase (shallow initial density contrasts $\epsilon = \frac{3}{2} = 1.5$ using the 'power law' form of angular momentum). Upper figure: projections along negative X (front view) and j^2 axes and positive Y (side view) axis; 3d views from top to bottom right: side view from underneath;front view from underneath;front view from above

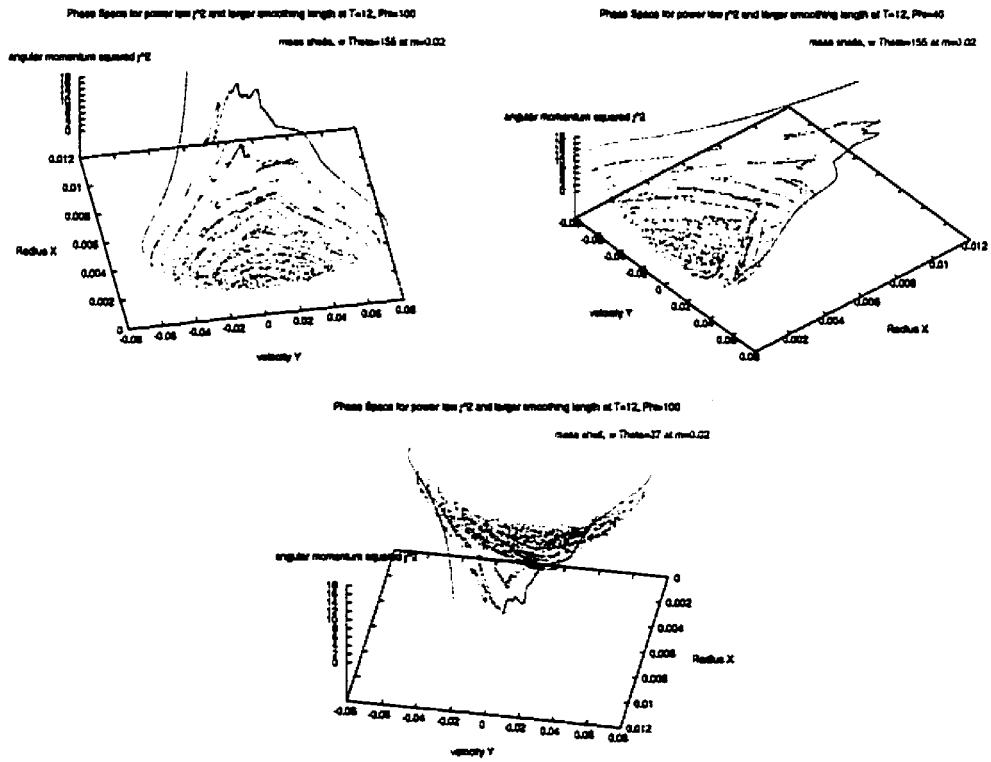

Figure 6.9: Phase space exploration using the 'power law' form of angular momentum near the end of the self-similar quasi-equilibrium phase (shallow initial density contrasts $\epsilon = \frac{3}{2} = 1.5$). 3D views from top left to bottom: front view from underneath; side view from underneath; front view from above

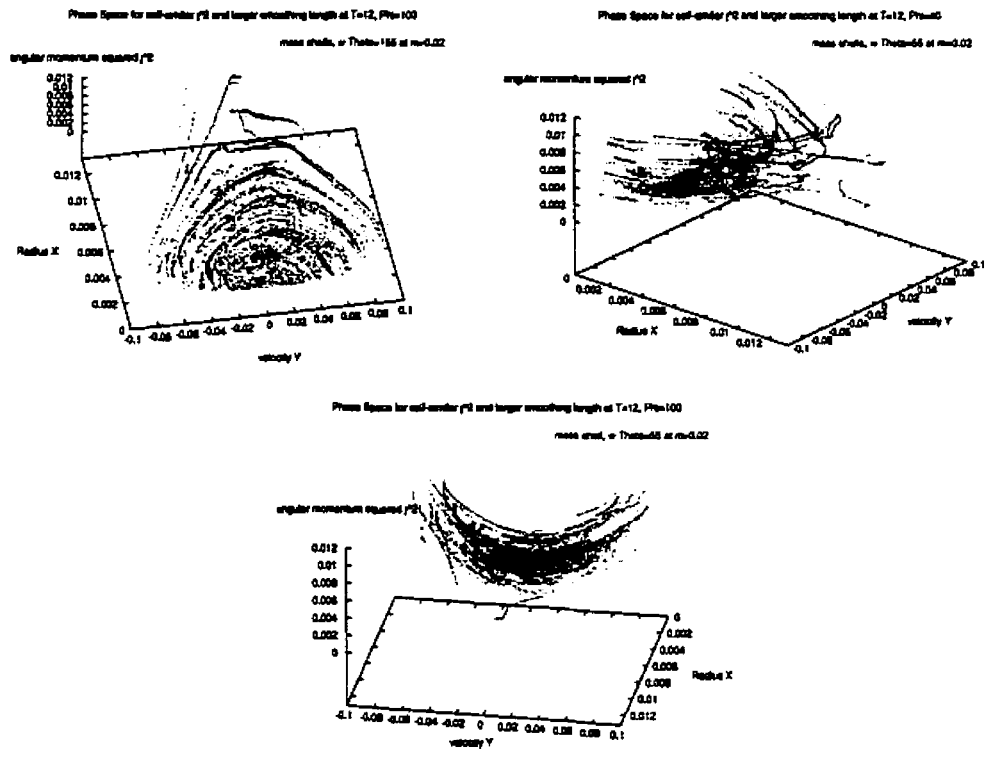

Figure 6.10: Phase space exploration using the self-similar form of angular momentum near the end of the self-similar quasi-equilibrium phase (shallow initial density contrasts $\epsilon = \frac{3}{2} = 1.5$). 3d views from top left to bottom: front view from underneath; side view from underneath; front view from above.

form of a flat basin than of a moderately steep incline. Finally the relaxation region streams are more prominent and spread in radius and velocity. In both of the 'power law' phase space distributions, the shells inside the relaxation, or instability, region and belonging to thee relaxed region appear very relaxed and homogeneous, no phase space stream structure surviving the relaxation process. On the contrary, phase space from the SSAM initial angular momentum distribution displays much more Liouville stream structure in its projection along the j^2axis. Figure 6.10 reveals that the distribution of shells, though it gathers around the same surface as that of the 'power law' initial angular momentum distribution of figure 6.9, spreads itself over a substantial volume of phase space. Echoing the importance of available phase space volume pointed out by Tormen *et al.* [55], Teyssier *et al.* [54] and Moutarde *et al.* [39] in the final state of dark matter haloes, the SSAM angular momentum distribution seems to open the third dimension to the spread of the system, at the same time reducing the influence of each

individual shell on the phase space volume so that violent relaxation becomes less efficient, leaving the structure of the Liouville stream winding almost immune from phase space instability. This diffusion away from the surface present in figure 6.9 could be interpreted as a consequence of the artificial nature of the overconstrained form of the self-similar j^2, setting the system in an unstable state which is transformed into this access to extra layers of the phase space.

Angular momentum and mass correlation?

The existence of this phase space sheet suggests the possibility for a correlation in the angular momentum profile. Indeed phase space can be projected along the radial velocity axis to reveal the angular momentum profile. This has been done for the three systems studied in the previous section. One group have even claimed to find a universal angular momentum profile in N-body simulations in terms of a halo's cumulative mass (Bullock *et al.* 2000 [113]) according to

$$M(<j) = M_v \mu j/(j_0 + j), \tag{6.3}$$

where μ and j_0 are correlated characteristic scales and M_v is the halo's virialised mass. They also find a power law describing the correspondence between angular momentum and radially cumulative mass ($j(M) \propto M^s$ where $M = M(<r)$ and $s = 1.3 \pm 0.3$).

Dimensional analysis (for instance of Eq.(3.70)) and defining the final density profile as $\rho \propto r^{-\mu}$ leads one to approximate the self-similar model's results with power laws for the angular momentum ($j^2 \propto r^{4-\mu}$) and for the mass profiles ($M \propto r^{3-\mu}$). Thus, s can be predicted to be $s = \frac{4-\mu}{2(3-\mu)}$, with the SSIM giving the final profile index as a function of the initial one as:

$$\mu = \begin{cases} 2 & \epsilon \leq 2 \\ \frac{3\epsilon}{1+\epsilon} & \epsilon > 2 \end{cases}.$$

Of course, in the presence of enough angular momentum, the radial SSIM results are altered as seen above, but it is remarkable that the shallow initial density profile yields $s = 1$. The largest deviation from that is given for $\epsilon = 3$, since then $s = \frac{\epsilon+4}{6} = \frac{7}{6} \simeq 1.17$, which is also within error from the Bullock *et al.* [113] value.

Even though the cumulative mass $M(<j)$ is not the same as $M(<r)$, approximating the former by the latter allows to construct $M(<j)$ with the help of the angular momentum and density profiles and the approximate relation $M \propto \rho r^3$. Nevertheless, the previous section warns us that a correlation in the j^2 profile shouldn't come from a simple regression, but should try to fit the constrained surface from which the phase space configuration unfolds. In fact, the caustic formed in the projection of phase space in the $j^2 - X$ plane appears a reasonable candidate for the correct angular momentum

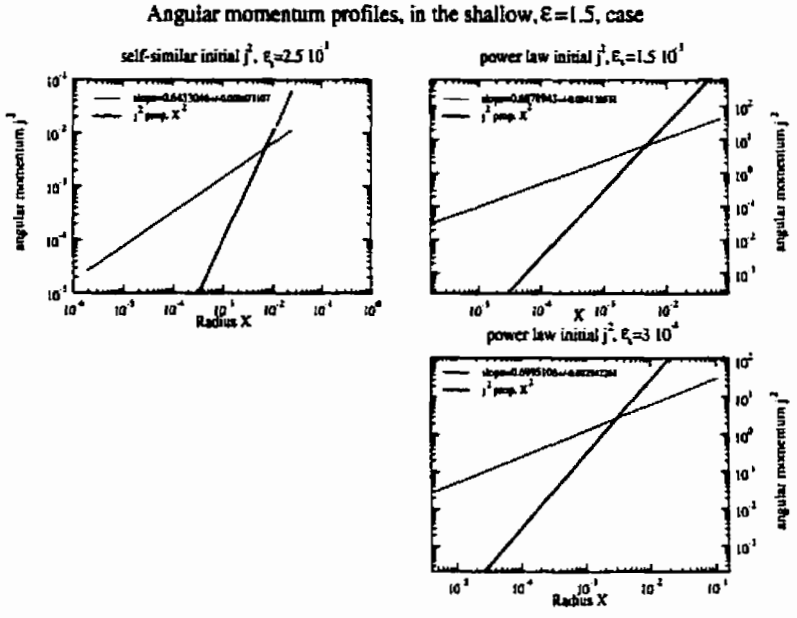

Figure 6.11: Three angular momentum profiles and their correlations

profile. Figure 6.11 illustrates the angular momentum profile correlations: the thin red lines are mere power law fits to the whole core of the system, and their values do not reflect the self-similar calculations. On the contrary, a $j^2 \propto X^2$ fit of the phase space caustic illustrates the predictions for the shallow case. Moreover, the density profiles showing some steepening on the outer edges of the halo, that translates into indications for a flattening of the mass profile, as in Eq.(6.3).

The most remarkable result of this section is the correlation of the phase space surface caustic in the radial velocity projection, displaying $j \propto X$ for both the SSAM and PLAM initial angular momentum and for the regular and RSL simulations.

6.2.4 Angular momentum in the SSIM

It is now clear that angular momentum has a profound impact on the state of dark matter haloes. Fueled by independent studies pointing out that impact from various theoretical, numerical and observational points of view, the extension of the SSIM to include angular momentum proves full of surprises.

The first surprise comes from the smoothed transition induced by angular momentum between the system's self-similar quasi -equilibrium and virialised states, while the former seems to persist even without a fully constrained initial system. That latter remark adds to the power of attraction of self-similarity as an intermediate dynamical stage.

The second surprise springs from how well the density profile of the modified SSIM with 'power law ' initial angular momentum profile fits the general shape of N-body simulations haloes. This , together with the results of the merger model in the SSIM, tends to favour non-radial motion against repeated mergers as the main driving force towards purely collisionless dark matter haloes density profiles.

The third surprise comes from the comparative topology of the phase space between the self-similar and a less constrained form of initial angular momentum distribution. It gives rise to an interesting correlation in the angular momentum profile. This calls for more investigation.

6.3 Black Hole in radial infall: preliminaries

Scientist confounded from the apparition (outbreak) of a black hole

Le trou noir
JEAN-VINCENT SÉNAC

The previous chapter allowed us to realise that the SSIM had much more explanatory potential than was expected. Despite its symmetry restrictions and the well accepted paradigm of repeated mergers for CDM halo formation, it was able with secondary accretion to give insight into the workings of (moderately) violent relaxation of haloes, as well as to bridge the gap between the merger paradigm and the opposite one of secondary accretion.

The SSIM has thus shown its capacity by explaining the NFW profile with a Dimensionally justified initial angular momentum distribution. The power of attraction of the enhanced SSIM promises more results when we turn to the problem of the density profile's central cusp. As mentioned earlier, some observations point towards a much flatter density profile central cusp for dark matter haloes (Kravtsov *et al.* [31], Stil [75]) than purely collisionless CDM can explain. The introduction of a central black hole coupled with a

population inversion in the PDF has proved able to produce such a flat cusp (Nakano & Makino 99 [85] and Henriksen & Le Delliou [86]) but the question of the population inversion, manifest in a low energy cut off, remains problematic. The purpose of this section and the next is to verify if the observed cut off in the original SSIM persists when such a central black hole is introduced and if it induces the predicted cusp.

The implementation of a black hole in the centre of the radial (1-dimensional, with 2d phase space) infall requires two changes: the first is to replace the region of the smoothed central cusp density profile by a collapsed central, tunable mass.Note that this mass does not necessarily equal the mass that would be contained in that central region if the power law profile were continued to the centre. The second change is to define the size of the black hole's mass and Schwarzschild radius at any given timestep. This latter task requires to derive the growth of the mass considered to be inside the black hole at any time. The difficulty comes from spherical symmetry, in which all the shells will eventually cross the origin, whereas a real black hole would swallow anything crossing its Schwarzschild radius. Since all shells entering the core of the halo for the first time by crossing the origin would define the core to be equal to the black hole, a way to limit and account for the shells really considered to have fallen into the black hole must be provided. It is important to mention that we are not concerned with the initial formation of the central black hole, and are dealing only with the growth of an initially already formed black hole seed.

6.3.1 Initial conditions for collapsed central mass

Initial conditions for the set up of a central mass differ from the simple SSIM initial halo by their handling of the central part. Instead of a smoothing of the central cusp, the density profile's central singularity is replaced by a point mass, with the power law extending outside the radial parameter r_{min}.

Cosmological halo

Initial density profile The model is again reproducing, above r_{min}, a density profile constituted with a constant background and a power law primordial overdensity. The central space is initially empty, except for the central mass sitting still at the origin (with X=Y=0):

$$\rho = \rho_0(1 + d_0.r^{-\epsilon}) \; r \geq r_{min}.$$

The constants are defined in more detail in appendix G.

Initial mass profile The resulting cumulative mass inside a given radius, if one remains outside the central region, is thus

$$iM = \int_0^r \rho r^2 dr = \rho_0 r^3 (\frac{1}{3} + \frac{d_0 r^{-\epsilon}}{3-\epsilon}) + \delta M_\bullet \qquad r \geq r_{min},$$

where $\delta M_\bullet$ is the extra mass in the black hole compared with the mass the power law density would yield in the central region. For radii inside that central region, the mass is constant and given by

$$iM = centralMass = m_\bullet = \rho_0 r_{min}^3 (\frac{1}{3} + A) + \delta M_\bullet.$$

All the constants are again defined in appendix G.

Shells initial masses and phase space position The set up of individual shells in phase space is implemented in a similar way as in section 4.5.1, with the density distribution modeled by Eq.(4.3) and the initial halo obeying the Einstein-de Sitter Hubble flow:

$$y(i) = \frac{2}{3} x(i).$$

The same variety of methods can then apply: constant shell initial density, constant shell initial spacing or constant shell mass. The detail of the implementations can be read in appendix G.

Density definition by shells and their positions

The measurements of density are similar to the regular SSIM definitions. The main distinction is the presence, for the initial time only, of an innermost shell boundary different than the origin. The formulations of density profiles and relative density are detailed in appendix G.

6.3.2 Time dependent definition of the central black hole

The key issue in this model is the definition of the possibly evolving central mass.

Definition of the black hole

Because of the purely radial infall, all particles hypothetically cross the horizon of the central black hole. Of course this is just a model with restricted radial spherical symmetry and classical gravity and should be compared with a full representation of the properties of an embedded black hole with caution.

The simple SSIM points us towards a straightforward interpretation: since the structure of phase space allows to define particles which are approximately on streams, we can exploit the predictability of those streams. There appear to be streams that would turn around before the Schwarzschild radius, once it is given. All particles on those streams can therefore be assumed inside the Schwarzschild radius, and thus in the black hole. Particles which belong to streams which would lead them to escape the Schwarzschild radius are considered as if they were outside of it, whereas particles whose streams remain inside the Schwarzschild radius are considered to have entered the black hole and their masses are therefore collapsed onto the black hole at the origin.

Even though the particles from escaping streams can be found at radii less than the Schwarzschild radius, the reasoning is such that without the presence of the horizon's trap they would turn around, at a later time, farther from the centre than the horizon and are therefore considered to be excluded from the black hole until their projected turnaround radius falls under the horizon.

Practically, this means that we have to keep track in the simulations of shells which are crossing the origin, and thus jumping streams to their radial mirror image as shown on figure 6.12, and which are subsequent to the last shell incorporated in the black hole in the original stream order. Winding up along this stream we can track the first shell to cross the Schwarzschild radius at the new timestep. This will define the first stream not yet swallowed by the black hole. The stream shifting shell just preceding that escaping one then defines the new outer boundary of the black hole in the Lagrange-Liouville stream, as illustrated in figure 6.12. Then the new black hole shells are collapsed onto the central mass and the integration can advance one more timestep.

Definition of the Schwarzschild radius

The Schwarzschild radius can be defined from its expression out of the General Relativistic static black hole description, but it also can be defined using Newtonian theory, like Laplace (in 1798, see Misner, Thorne & Wheeler 73 [92] p872, or d'Inverno 92 [93] p224), and Michell (in 1783, see Caroll & Ostlie 96 [107]; they were the first to calculate the radius for a body with Solar density to have its escape velocity equal to that of light) did first: if an object admits such a density that the escape velocity at its surface is the speed of light, then it resembles a black hole. This can be expressed as the condition for marginal binding in terms of specific energy with a kinetic energy using a velocity equals to c:

$$\frac{1}{2}c^2 - \frac{GM_\bullet}{R_{Sch}} = 0 \Leftrightarrow R_{Sch} = \frac{2GM_\bullet}{c^2},$$

which is the same expression as the real Schwarzschild radius coming from a General Relativistic treatment.

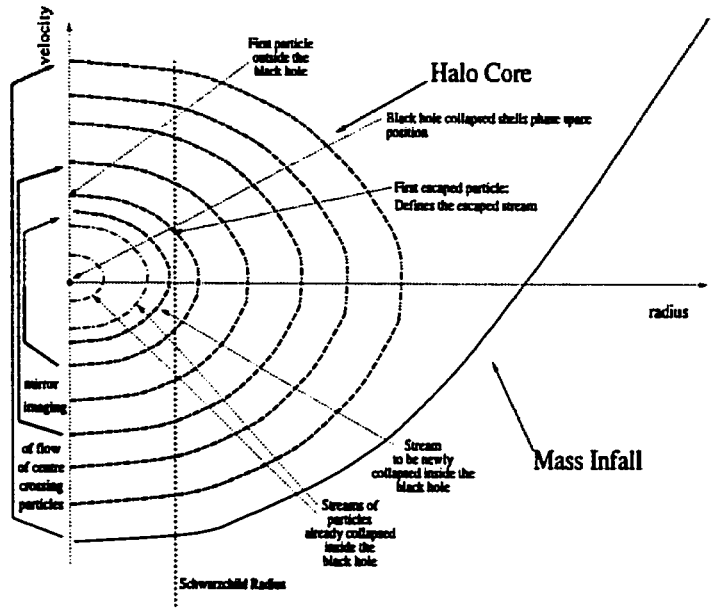

Figure 6.12: Algorithmic definition of the black hole shells

But this expression has to be fitted into the self-similar treatment of the halo. In real units, c is a constant, but in the time varying self-similar variables, it cannot be maintained constant except for the special case when the time and length rescalings are equal (self-similarity index $\frac{\delta}{\alpha} = 1$, i.e. $\epsilon = 2$). On top of that, the initial units, which are not rescaled, are arbitrary and must be mapped onto real values. The treatment of units and subsequent determination of the scaled Schwarzschild radius are given in appendix H.

6.4 Black Hole in radial infall: Results

Vous nain, vous avez fait l'infini
prisonnier.

La légende des siècles La comète
VICTOR HUGO

In the wealth of collisionless N-body simulations, the consensus of the density profile calculation for dark matter haloes tends to indicate the presence of a pronounced central cusp (as steep as r^{-1} for NFW and up to $r^{-\frac{3}{2}}$ for the Moore99 type profiles) for the innermost density that seems unavoidable. On another hand, as pointed out by Kravtsov *et al. [31]* and Stil [75], some observations do not favour such a steep cusp.

This section will devote itself to the exploration of one possibility for generating a shallower inner cusp in collisionless self-gravitating dark matter haloes, within the framework of the SSIM: the presence in the halo of a central black hole. It will first briefly describe the analytical expectations from Henriksen's calculations in Henriksen & Le Delliou [86] on the SSIM together with a brief argument for the inclusion of a black hole in the centre of dark matter haloes. Its second part will set the stage for this work's results with preliminary remarks. Then the SSIM's alteration by a central black hole will show its resulting relaxation through the PDF and energy correlations. The consequences on the density profile will be explored in the fourth part of this section, followed by an examination of the evolution of its relaxation and central black hole with time. Eventually this will trigger a model exploration of a reduced speed of light so that the Schwarzschild radius is larger.

6.4.1 Analytical predictions and short review

The recent enhanced interest in the behaviour of a collisionless self-gravitating halo embedding a central black hole has been driven by the need to bridge the divide between pure dark matter simulations and observation of shallow cusps in halo density profiles.

Henriksen & Le Delliou [86] show that a self-similar secondary accretion with a central black hole is capable of explaining the kind of shallow cusps observed by Stil [75]. In the analytical exploration of [86], the radial infall of the SSIM already gives the promise of a shallower cusp: from the undisturbed (by the black hole) semi-universal density profile of the SSIM $\rho \propto r^{-2}$, or steeper, the presence of the self-similarly growing black hole combined with a population inversion of the halo (expressed in a cut-off of the PDF at large negative energies) induces a universal central cusp with $\rho \underset{r \to 0}{\propto} r^{-\frac{3}{2}}$. This prediction is tested in the present work. Nevertheless, Henriksen shows that if the cut-off is absent or too soft in the PDF, a simple negative temperature exponential model for the PDF ($F(E) \propto e^{aE} \quad a > 0$) yields a logarithmic slope of $-\frac{5}{2}$ and the Henriksen & Widrow [42] prescription of a negative temperature cut-off on the self-similar equilibrium power law PDF ($F(E) \propto |E|^{\frac{1}{2}} e^{aE} \quad a > 0$) yields a slope of -3.

But the most interesting predictions in Henriksen & Le Delliou [86] concern the cusps of the SSIM with a central black hole and the presence of angular momentum: in the absence of energy cut-off or if it is too soft, the central cusp yields again a slope of $-\frac{3}{2}$, whereas a sharp enough cut-off brings the cusp within observations to a slope of $-\frac{1}{2}$.

The only other work known to show inner cusps compatible with the observations is that of Nakano & Makino 99 [85], who find a King-type[9] PDF and also observe a

[9] i.e. leading to the King density profile.

population inversion in energies after evolving an initial non-adiabatically disturbed halo, by an off-centre black hole. Other even more recent studies have not displayed such success, such as Leeuwin & Athanassoula 2000 [111], whose axial model doesn't allow for a population inversion to develop, starting from a modified Plummer model (featuring an infinite possible range of energies) whose softened potential provides too soft a cut-off to escape the formation of the $-\frac{3}{2}$ cusp.

6.4.2 Preliminary remarks

The decision method used to grow the central black hole with time, illustrated in figure 6.12, turned out to exhibit no growth when using the Schwarzschild radius induced by our model. Indeed, the initial self-similar Schwarzschild radius reveals itself to be too tiny compared to the size of the core: it is smaller than all radial steps in simulation, and that is aggravated by the exponential decay of X_{Sch} when the mass $m_\bullet$ is constant (refer to the discussion in section 6.4.5 and the lower left panels of figure 6.19 in the shallow case and figure 6.20 in the steep case). This is so even when the growth method is simplified to include any shell-crossing the Schwarzschild radius, without possibility of escape. Indeed, the scaled initial Schwarzschild radius is so small, when using the regular value for c, that it falls way inside the dynamical radial jumps effected by shells in one timestep, so none ever reach such tiny radii.

This work first presents results using that cruder method of growth, because they don't differ from the method exposed in section 6.3.2 and that method imitates better the relativistic behaviour of a black hole. The lack of black hole growth, though, left unanswered the question of its self-similarity. Conditions on the Schwarzschild radius allow for a significant mass growth of the central black hole, if the value of the speed of light c, an external parameter for this non-relativistic model, is relaxed. A reduced c induces, all other parameters kept unchanged, the desired increase in initial Schwarzschild radius, leading to the growth of the black hole mass in a significant way, as recorded from the last series of simulations.

6.4.3 Black hole and the system's relaxation

The SSIM presents itself with a clear behaviour demarcation between initial density profile shallower than isothermal, leading to a self-similarity class whose index is larger than 1 and converging to the isothermal profile; and steeper than isothermal, with index smaller than 1 and that admits a continuum of density profile attractors. This demarcation is used as a guideline for explorations throughout this work.

The error evaluation and remarks on energy and potential energy from section 5.2.1 are still valid here. Of course, the PDF and energy measurements were made for the

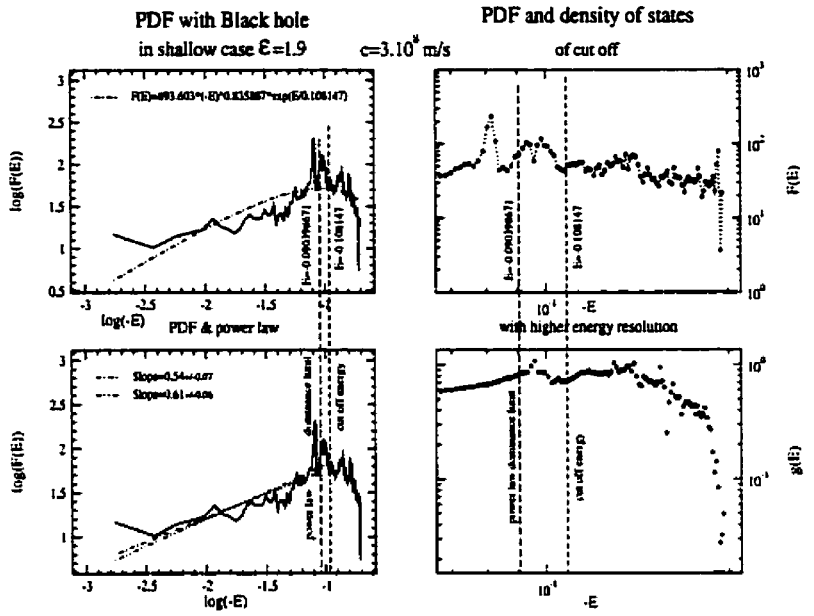

Figure 6.13: Black hole PDF measurement (shallow case: $\epsilon = 1.9$, regular speed of light) averaged over the self-similar phase and evaluation of the power law dependence in energy. The phase space factor is well behaved for all energies.

surrounding halo, excluding from them the shells inside the black hole.

PDF and energy correlation of a black hole embedded in a diffuse initial halo

Choosing the embedding halo in the shallow range, one can compare its results with those given in section 5.2.2 for a simple SSIM halo.

PDF and Phase Space factor The exponentially cut off power law suggested by Henriksen & Widrow [42] was fitted to the time averaged PDF in the same fashion as for the non-singular mass halo ($F(E) \propto |E|^p e^{\frac{E}{|E_{cutoff}|}}$ was fitted on the higher left panel of figure 6.13 to the halo as a general family that includes Henriksen & Widrow's $F(E) \propto |E|^{\frac{1}{2}} e^{aE}$). Compared with the non-singular mass halo of figure 5.7, the power law appears steeper, but the cut off is clearer, preceded by a slow decline after the rise of the power law (higher left panel of figure 6.13). But this fit is merely an indicator for the value of the cut off: the lower left panel of figure 6.13 displays more accurate power law fits to the less negative energies. This confirms a slight steepening which can be attributed to the approach of the critical self-similarity index value corresponding to the initial halo at $\epsilon = 2$ by the present initial halo set at $\epsilon = 1.9$. Because of the presence

of the slow decline, but foremost because of several spikes around the maximum PDF, before the sharp cut off, giving more leveling weight to the high negative energy end of the fit, the limit of the exponential energy cut off yields a steeper power law than the predicted $\frac{1}{2}$, in the lower left panel of figure 6.13. That is why another boundary was proposed, corresponding to the real power law behaviour region for the exponentially cut off power law fit of the higher panel. This cut off also corresponds to a horizontal tangent to the initial power law-exponential fit. That new fit yields a good confirmation of the power law value away from the cut off, and seems to be valid over more than one and a half decades. The characteristic hump of the relaxation region also appears less pronounced, but the most striking feature lies in the enhanced energy resolution figures of the right panels of figure 6.13, which display no sign of statistical noise comparable to those in figure 5.7. Indeed the energy cut off seems genuinely confirmed, all the more as the behaviour of the density of state $g(E)$ would tend to oppose the decline of the PDF ($F(E) \propto \frac{\sum m_i(E)}{g(E)}$ so the declining $g(E)$ would induce a rising $F(E)$ at constant mass population of the energy bins, thus indicating a genuine and sharp decline in population).

This stabilisation of the results from the SSIM can be attributed to the presence of the central mass. As for the non-singular mass halo SSIM, evidence for an exponential cut off is quite weak, but the presence of a sharp cut off seems well established. Even if an explanation of this cut off involves initial conditions, more constraints act during the relaxation period, involving energy 'processing' of shells in the relaxation region. These are also apparent in the energy correlation diagrams of figure 6.14.

Energy correlations and potential energy The correlation between initial versus final energy for all shells is plotted in figure 6.14's top panels for two final epochs to indicate the evolution in time of the energy spread. Those two epochs correspond again to the first and last sampling for the PDF time averaging. The relaxation region can be seen on the top of those diagrams, and corresponds to shells just fallen in and not fully relaxed: their violent relaxation translates into the wiggling in the range of final energy of the strongly correlated line of particles. The Lagrange-Liouville stream of incoming particles not yet entered in the system is present at the initial less negative energies (top of figure 6.14's upper left panel). The correlation of energy with radius until shell-crossing allows for shells outside of the system to be traced in their energy.

The bulk of the particles inside the system are in the relaxed region, characterised by a correlated scatter of final energies, less contiguous compared to the relaxing shells. Some definite correlation in the relaxed shells' energy is then present, showing thus moderation in violent relaxation, as in Henriksen & Widrow's simulations with comparable smoothing length. In addition, the sharp cut off can be detected in the energy diagram as the accumulation limit at the bottom left of the energy diagrams.

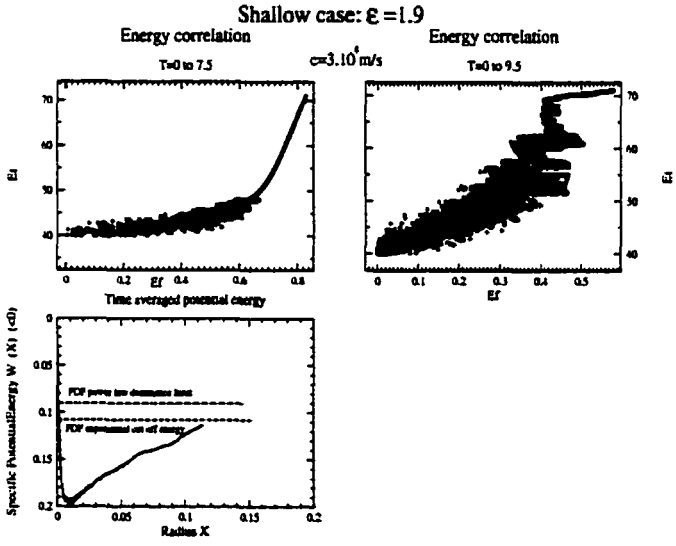

Figure 6.14: Black hole Energy correlation (shallow case: $\epsilon = 1.9$, regular speed of light) between initial and final times at the beginning (upper left panel) and at the end (upper right panel) of the stable PDF portion of the self-similar phase; the potential energy profile is given for comparison with Eq.(5.8) with an added contribution from the central mass and is illustrative of the phase factor calculation

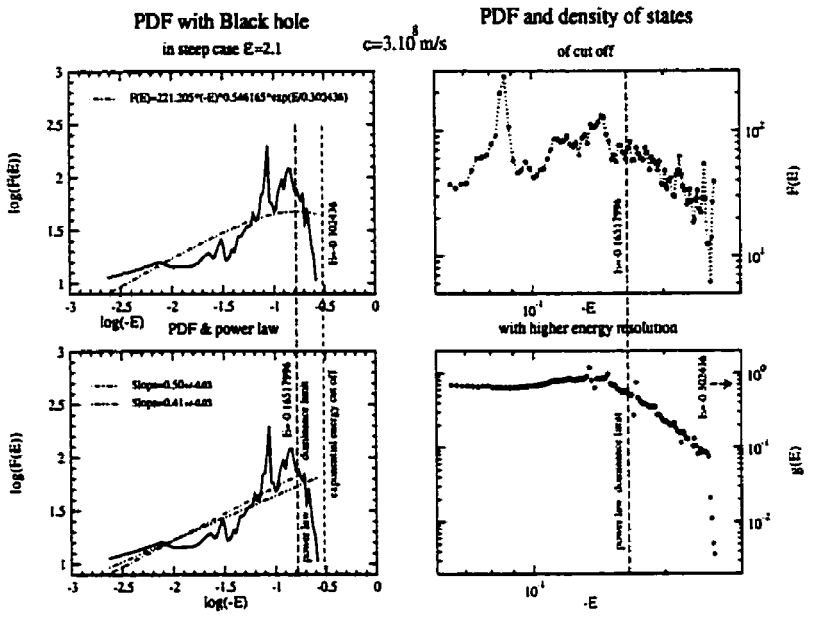

Figure 6.15: Black hole PDF measurement (steep case: $\epsilon = 2.1$, regular speed of light) averaged over the self-similar phase and evaluation of the power law dependence in energy. The phase space factor is well behaved for all energies.

The potential energy displayed in the bottom panel of figure 6.14 differ from its non-singular mass halo SSIM counterpart which is constant, up to logarithmic corrections because it here is added to the potential energy resulting from the central point mass. It then, as expected, follows an inverse radial law adjusted by a constant from the halo's potential energy. The levels of the energy cut off and validity limit for the power law fit are indicated as references. The central part behaviour still follows section 5.1.1's expectations.

PDF and energy correlation of a black hole embedded in a more concentrated halo

Comparison of the steep initial density profile case with the simple SSIM halo of section 5.2.2 can again be made with the embedded black hole halo.

PDF and Phase Space factor The fundamental difference between the steep non-singular mass halo SSIM PDF and that of the embedded black hole halo lies in the clear presence of an energy cut off at the lowest end of the energy distribution. Even though it is weaker than in the shallow case (it doesn't plunge far below the level of the rest of

the halo's PDF), it still exhibits the same clear slow decline before the sharp cut off at highest negative energy.

Nevertheless, the exponentially cut off power law finds it hard to reproduce a shape which roughly looks more like a log-normal distribution (see figure 6.15's upper left panel) and the fit is more useful as an indication of the cut off to use for a pure power law fit. Indeed the exponential cut off from the fit is even located off from the energy range of the PDF and we used again the limit of the real power law behaviour of the fit (lower left panel of figure 6.15). Using that range restriction, which also make sense since it eliminates the decline from the fitted region, the Henriksen & Widrow [42] prediction of a power law $F(E) \propto |-E|^{\frac{1}{2}}$ is here confirmed over almost two decades!

In contrast with the non-singular mass halo SSIM PDF but in concordance with the shallow embedded black hole PDF, the characteristic hump of the relaxation region almost vanishes, reinforcing the strength of the power law fit. This is quite spectacular when compared to the very strong hump of the simple SSIM.

In parallel with the shallow embedded black hole, the emergence of the cut off is free from statistical noise experienced in the non-singular mass halo SSIM (right panels of figure 6.15). This, though, is a radical qualitative change with the simple SSIM and sheds new light on its original conclusions. Instead the slight evidence for a cut off in the non-singular mass halo SSIM PDF, is supported by these results.

The exponential nature of the cut off has very weak support in the embedded black hole halo model presented here, but the presence of a cut off in the steep case also seems well established.

Energy correlations and potential energy The relaxation process involved in the formation of the system equilibrium as measured in the PDF can be studied with the energy correlation diagrams, presented for two epochs in figure 6.16's top panels. These indicate the evolution in time of the energy spread. In this case again, the relaxation region corresponds to shells just fallen in and not fully relaxed: their violent relaxation translates into the same wiggle of the correlation line in the narrow range of final energy. Again, the initial energy correlation with radius before shell-crossing accounts for the tail of the Lagrange-Liouville stream of incoming particles not yet entered in the system, which is found this time at the top of the first correlation diagram presented here (bottom of figure 6.16's top left panel.

Most of the particles inside the system are again in the relaxed region, where the correlated scatter of final energies is less contiguous than that of the relaxing shells. A moderately violent relaxation diagnostic can be extracted from the obvious correlation in the relaxed shells' energy, as in Henriksen & Widrow's simulations with comparable smoothing length. The cut off can also be detected in the energy diagram in the

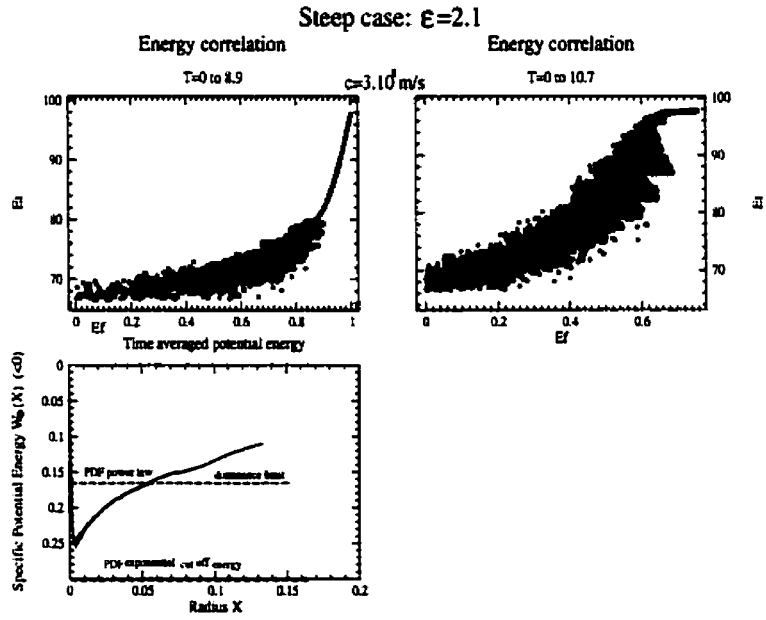

Figure 6.16: Black hole Energy correlation (steep case: $\epsilon = 2.1$, regular speed of light) between initial and final times at the beginning (upper left panel) and at the end (upper right panel) of the stable PDF portion of the self-similar phase; the potential energy profile is given for comparison with Eq.(5.8) added with the central mass contribution and is illustrative of the phase factor calculation

accumulation of shells along the bottom left of the energy diagrams.

The potential energy of the bottom panel of figure 6.16 differs again from its non-singular mass halo SSIM counterpart because the added r^{-1} potential energy resulting from the central point mass dominates over the halo potential ($W_{\Phi_{halo}} \propto r^{2-\mu}$ with $\mu \in]2; \frac{9}{4}]$, so $2-\mu < 1$). The levels of the energy cut off and validity limit for the power law fit are indicated as references. The central behaviour still follows section 5.1.1's expectations.

Stabilisation, black hole evolution and SSIM

Because of the absence of black hole growth, the absence of evolution of the black hole mass translates into the scaling exponential decrease of the self-similar Schwarzschild radius (see the discussion in section 6.4.5 and the lower left panels of figure 6.19 for the shallow case and figure 6.20 for the steep case), the only difference between the non-singular mass halo SSIMs and this work's resides in the presence of one extra particle of mass sitting still in the centre of the halo. Since this mass is comparable to individual shells (it is not orders of magnitude heavier) and negligible compared with the final halo's, it can be regarded as just a cluster of particles without motion at the centre.

The stabilisation of the halo under these circumstances can be well understood as the effect of this central mass: it suppresses the continual tugging of shells each time they cross the centre by the previous jittering of the innermost shell (in fact, they usually jump in one integration step over the central radius and are folded back into positive radii). There is no more possible slingshot effect on new incoming shells because the innermost shell is now the black hole itself, which has no motion. In other words, the previous time-varying innermost gravitational potential is dominated now by the stable black hole central potential.

Again, the PDF cut off can be explained in the same way (see section 5.2.3): from initial energy radial distribution and conservation of energy outside the core of the shallow initial profile, the last infalling particles also carry the most negative energy. When the last particle falls in, the feeding of more and more negative energy to the core is abruptly cut off.

For the steep initial profile, the initial energy radial distribution shows the reverse trend, and the more negative energy shells are located in the centre and fall first into the core. The presence of a cut off in the PDF can then be attributed, as in section 5.2.3, to the regularisation of the central density in the implementation of the model.

These indicate already mechanisms for the PDF cut off to arise, the pool of initial energies being finite and limited. But there is more than this constraint acting during the relaxation because of the energy 'processing' of shells in the relaxation region, which

is apparent also in the energy correlation diagrams of figures 6.14 and 6.16.

Eventually, comparing the outcome of the SSIM with and without this single central mass we can change our point of view of the system: instead of seeing the point mass as a black hole, we acknowledge that it simply imitates the singularity expected from the self-similar density profile. This helps the numerical modeling to achieve a cusp in the centre of the halo. Hence, despite the lack of evidence in the simple SSIM simulations, the central mass SSIM's steep case exhibits the presence of a low energy cut off in its PDF.

6.4.4 Resulting density profiles

By the self-similar quasi-equilibrium infall phase, the system is establishing a stable mode through this 'processing' of energy. In the simple picture of the radial SSIM, the self-similar density profile depends on the initial density contrast and is divided between a semi-universal attractor $\rho \propto r^{-2}$ for contrasts shallower than itself, and a continuum of attractors $\rho \propto r^{-\mu}$ with μ depending on the value of steeper contrasts than the semi-universal one.

Explorations of the asymptotic behaviour of the density using the characteristics of the Collisionless Boltzmann's Equations (CBE) and the presence of a central self-similarly growing mass at the centre of the halo (black hole), Henriksen [86] predicts that the density profile will develop a central cusp of a different slope than the bulk of the halo. In the case of a radial infall, considering that the PDF exhibits a sharp low energy cut off, the predicted cusp follows $\rho \underset{r \to 0}{\sim} r^{-\frac{3}{2}}$.

From diffuse initial embedding halo

The density profile of the system near the end of the self-similar infall phase and the virialised phase (T=8.5) reflects the state of the system and provides a link to its observational consequences. In figure 6.17, the scaled radius of the embedded black hole at that time is so small that it is indicated as lying outside of the plot.

From the point of view of the radial SSIM, the self-similarity will drive the density profile from a shallow logarithmic slope with $\epsilon = 1.9$ towards the semi-universal attractor $\mu = 2$. A power law fit to the whole of the core indeed yields (blue, long dashed line in figure 6.17) almost that slope ($\mu \simeq 2.03$). It can be verified on that figure (6.17) that if the NFW profile fit (dotted purple line) fails to reproduce the density distribution of the SSIM embedded black hole, the single power law fit only gives an approximation for the whole profile.

There is clearly a two power law profile coming out of the examination of the core:

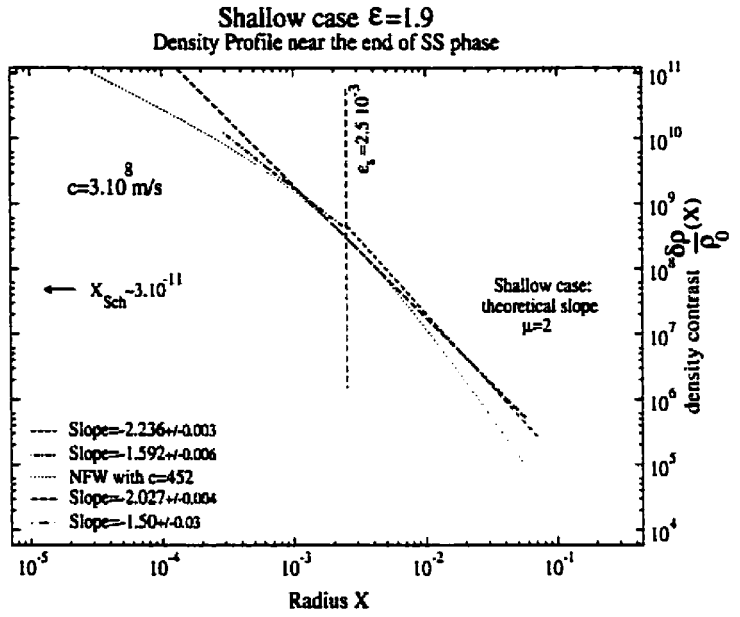

Figure 6.17: Black hole Density profile Diagram (shallow case: $\epsilon = 1.9$, regular speed of light) at the end of the self similar phase.

fitting the density outside of the smoothing length shows that the outer profile admits a steeper slope than the semi-universal one ($\mu \simeq 2.24$, for the red dashed line of figure 6.17) whereas a fit of the second slope, between ϵ_s and the mass resolution inner break of the slope appears to confirm the Henriksen & Le Delliou [86] prediction of $\frac{3}{2}$ for the radial black hole embedding SSIM with a sharp PDF cut off at large negative energies.

The measured inner slope of the cusp doesn't reach 1.5 (it remains around 1.592 ± 0.006), when fitted over a range including the smoothing length. Though the ϵ_s delimitation is not physically relevant (see discussion in section 6.2.3), the change of slope seems to occur not so far inside that limit. In fact the break seems to occur at a somewhat smaller radius, hinting towards a slightly flatter inner slope. The difficulty in defining a proper measurement range makes the error on the regression not as relevant as the range of slopes obtainable. In addition, selecting the range of the power law fit in a careful way (between the main slope break and a slight upward inflection, as measured by eye), one can obtain the value of 1.5 within regression error. All in all, the slope can be estimated at 1.6 ± 0.1, confirming the prediction of $\frac{3}{2}$.

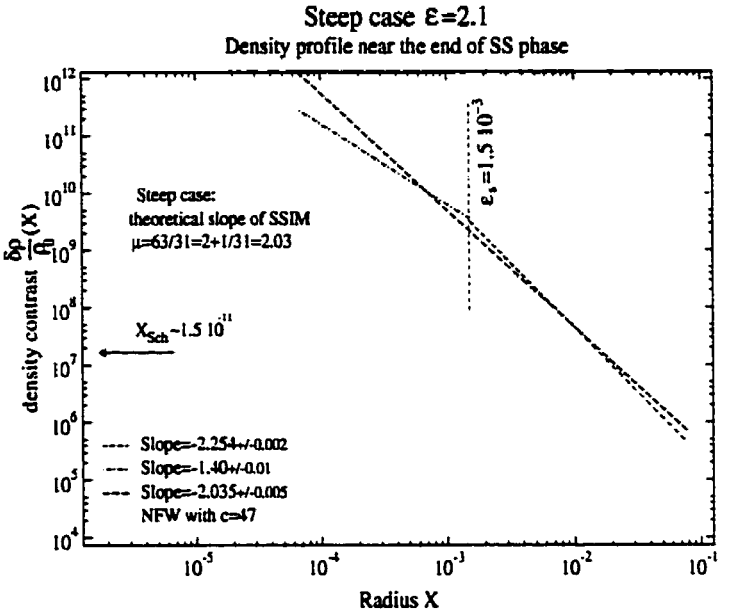

Figure 6.18: Black hole Density profile Diagram (steep case: $\epsilon = 2.1$, regular speed of light) at the end of the self similar phase.

From a more concentrated initial embedding halo

The density profile of the system, evolved from an initial density contrast steeper than the isothermal profile, is represented in figure 6.18 at the end of the self-similar infall phase and near the virialised phase (T=10.1). The scaled radius of the embedded black hole at that time is again so small that it lies outside of the plot.

In the radial SSIM, the self-similarity would drive the density profile from a steep logarithmic slope with $\epsilon = 2.1$ towards the corresponding self-similar attractor $\mu = \frac{3\epsilon}{1+\epsilon}$. This time, a power law fit to the whole of the core yields (blue, long dashed line in figure 6.18) exactly that slope ($\mu \simeq 2.03$). The NFW profile fit here too fails to reproduce the density distribution of the SSIM embedded black hole (figure 6.18, dotted brown line). Close examination reveals also that the single power law fit is again only here an approximation for the whole profile.

The core here can also be fitted by a two power law profile, and this time there is a clear break coinciding with the smoothing length. Fitting the density outside of the smoothing length shows that the outer profile admits a steeper slope than that of the self-similar attractor ($\mu \simeq 2.25$, for the red dashed line of figure 6.18), when a fit of the slope between ϵ_s and the mass resolution inner break of the curve yields an even steeper slope than the Henriksen & Le Delliou [86] prediction. That prediction of $\mu = \frac{3}{2}$ for the

radial black hole embedding SSIM with a sharp PDF cut off at large negative energies is supposed to be independent of the self-similarity class, but here we find $\mu \simeq 1.40$. A close look at the density profile compared to the inner slope measurement shows that the uncertainty on the slope here is much greater than indicated from the χ^2 regression and that the inner part's curve is not as sharply modeled by a unique power law as the preceding shallow case. Again, a careful selection of the fitting range can yield the predicted slope. Here there seems to be a sharp change of slope located at the smoothing length, though the ϵ_s delimitation is not physically relevant (see the same discussion in section 6.2.3). Because of the uncertainty on the inner slope it is difficult to pinpoint exactly the decisive change of slope and an examination of figure 6.17's density at the smoothing length reveals the trace of a similar variation in the profile. The break at ϵ_s can then be understood as a natural manifestation of the change of dynamical regime. It is due to the presence of the central mass. The measured inner slope, compared with that of the shallow case (1.60) seems to point towards an error of the order of 0.1, and the limit of ϵ_s even if irrelevant for the SSIM density profile, by altering the dynamics inside of it, affects the efficiency of the central mass potential in driving the halo profile's inner cusp to the predicted slope.

6.4.5 Relaxation of the halo and growth of the black hole

The object of the previous section on the embedded black hole in the SSIM is to check the effect of the central mass on the SSIM's self-similar relaxation history through the virial ratio, and examine the topology of its phase space under this new influence. A monitoring of the scaled Schwarzschild radius shows that the central mass is not able to accrete.

For a diffuse initial halo

The virial ratio of the system has been shown to reveal in the SSIM a quasi-equilibrium phase during the self-similar mass infall marked by a virial ratio slightly larger than the stationary value for gravitational equilibrium. A comparison between the behaviour of that ratio for the simple SSIM and that for the black hole embedding SSIM (figures 5.9 and 6.19's upper left panels) allows one to detect comparatively the effects of the central mass on the SSIM. Because of the different values of the self-similar class of the two initial shallow density profile systems presented in the regular SSIM and here respectively, the comparison remains qualitative but the results of the comparison are not different from that of the present system with an equivalent simple SSIM simulation.

The first striking feature resides in the similitude of the two virial evolutions: they both start with a period of unsettled variations due to the equal mass modeling resolution

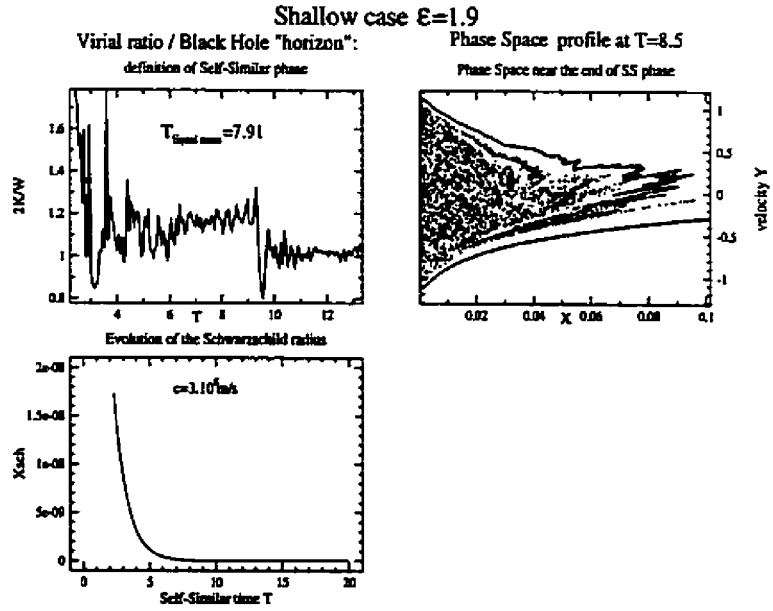

Figure 6.19: Black hole Virial ratio (shallow case: $\epsilon = 1.9$, regular speed of light) and Schwarzschild radius evolution, and Phase Space diagram at the end of the self similar phase

in the self-similar mass flux, the central mass acting merely as an already established core, then disturbed by the successive incoming extra shells in the same fashion as by repeated mergers of overdensities, as discussed in the paragraph of section 5.2.2. Even their stabilisation characteristic times are comparable:

$$T_{Equal\,mass}(\epsilon_{simple\,SSIM} = 1.5) = 7.33$$
$$T_{Equal\,mass}(\epsilon_{SSIM+\bullet} = 1.9) = 7.91$$

On the other hand, they differ in the virialised phase in the respect that the presence of the central mass is again stabilising the evolution of the system, inducing a clearer virialisation for which the growth of noise in the self-similar variable treatment is more controlled.

This stabilisation is also visible in the comparison of the phase space structure in figures 5.9's lower left and 6.19's upper right panels: the presence of the black hole, at the same force resolution seems to reinforce the destruction of streams by phase space instability and wash out more structure than obtained in the absence of central mass. In fact it resembles more the kind of phase space structure obtained in the exploration of the effect of an increased force resolution (see figure 6.6). We have seen that the reduction of the smoothing length ϵ_s allows for more relaxation because it entails a more detailed

integration. Similarly, the innermost time varying gravitational potential is dominated by the stable central mass potential which allows for the resulting smoother dynamics to be integrated more accurately.

The evolution of the scaled Schwarzschild radius of the present model of a central black hole embedded in the radial SSIM halo shows a blatant lack of black hole evolution (figure 6.19's lower left panel): the exponential decrease shown here of the scaled radius corresponds to a constant real radius, according to the scaling of length in the self-similar variables (refer to section 3.1.2, especially Eqs.(3.26) for the scalings of radius, radial velocity and angular momentum in spherical symmetry). Thus, from the relationship between the Schwarzschild radius and the black hole mass (Eqs.(H.1) and (H.2), for the scaled and real versions respectively), it is clear that no accretion has taken place here. Although understandable in terms of the size of the radial integration steps followed by the system compared to the Schwarzschild radius, this lack of evolution prevents this work, under these circumstances, to test the prescription of a self-similar mass growth of the central black hole made in Henriksen & Le Delliou [86]. Conversely, it shows that the mere presence of a stationary central mass is enough to yield the expected flattening of the density cusp, in the presence of a sharp cut off at large negative energy in the PDF of the system for the SSIM. Eventually, this called for the exploration of an altered version of this model for which the initial scaled Schwarzschild radius would be large enough to allow for some accretion of the halo's shell onto the central mass.

For a more concentrated initial halo

The virial ratio of the system has been shown to reveal in the SSIM a quasi-equilibrium phase during the self-similar mass infall marked by a virial ratio slightly larger than the stationary value for gravitational equilibrium.

The virial ratio comparison between its behaviour for the simple SSIM and that for the black hole embedding SSIM (figures 5.12 and 6.20's upper left panels), in the steep initial density profile cases, reveals approximately the same structures, and in comparison to the shallow case, exactly the same effects of the central mass on the SSIM. Because of the different values of the self-similar class of the two systems, the comparison remains again qualitative (the virial phase is longer for $\epsilon = 2.5$, $T \simeq 14$, than for $\epsilon = 2.1$, $T \simeq 10.1 - 10.2$) but its results are not different than the comparison with the equivalent simple SSIM simulation.

Therefore, as in the shallow case, the two virial evolutions are strikingly similar: they both start with a period of unsettled variations due to the equal mass modeling resolution in the self-similar mass flux (see again the discussion in the paragraph of section 5.2.2). These periods of settling into the self-similar phase mirror each other

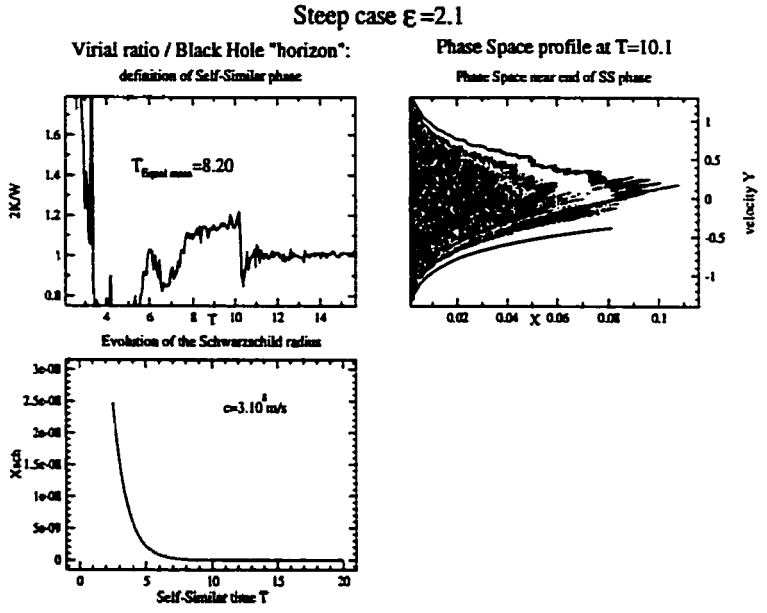

Figure 6.20: Black hole Virial ratio (steep case: $\epsilon = 2.1$, regular speed of light) and Schwarzschild radius evolution, and Phase Space diagram at the end of the self similar phase

to the point that they both feature the same last sharp decrease before reaching the self-similar quasi-equilibrium (the black hole SSIM is also displaying it more clearly, due to the smoothing of dynamical noise by the central mass). The central mass SSIM stabilisation characteristic times is again agreeing with the time for the establishment of the self-similar phase (compare the settling in the top left panel of figure 6.20 with the time $T_{Equal\,mass}(\epsilon_{SSIM+\bullet} = 1.9) = 8.2$). The difference in the stability of the virialised phase between the simple and black hole SSIMs can also be found here, reinforcing the indications on the stabilising effects to the evolution of the system in the presence of the central mass.

This stabilisation is again visible in the phase space structure differences between figures 5.12's lower left and 6.20's upper right panels: the phase space structure seems again to be more washed out and the phase space instability reinforced in the presence of the black hole, at the same force resolution. As for the shallow case, the phase space resembles more, keeping in mind the qualitative difference of self-similarity behaviour, the structure obtained in the exploration of the effect of an increased force resolution (see figure 6.6).

The scaled Schwarzschild radius of the central black hole embedded in the radial SSIM halo evolves in the same way as its shallow counterpart (see figure 6.20's lower

left panel): its exponential decrease translates again the lack of evolution of a constant real radius, according to the same self-similar length scaling (section 3.1.2, especially Eqs.(3.26) for the scalings). The relationship between the Schwarzschild radius and the black hole mass (Eqs.(H.1) and (H.2), for the scaled and real versions respectively)proves that no accretion has taken place again here. The same interpretations as in the shallow case can equally been drawn here, as well as the need to explore an altered version of this model for which the initial scaled Schwarzschild radius would be large enough to test the prescription made in Henriksen & Le Delliou [86].

6.4.6 Summary

Thus the effect of this embedded black hole, though it is not growing and feeding on the halo, is to stabilise the SSIM. The SSIM's self-similar evolution is still present in the new system which displays every aspects of the SSIM in a clearer way (see Henriksen & Le Delliou 01 [112]) because of this stabilisation. But there are also important differences: the potential energy profile is dominated by the central point mass (figures 6.14 and 6.16's lower panels) which then induces, through a PDF population inversion (PDF low energy cut off in figures 6.13 and 6.15) the flattening of the innermost density profile (Henriksen & Le Delliou [86], and figures 6.17 and 6.18). The evolution of the system is less noisy, leading to a clearer virialisation, and a more relaxed phase space(figures 6.19 and 6.20). Nevertheless, the self-similar evolution of the Schwarzschild radius is not tested in this version of the model.

6.4.7 A self-similar black hole growth?

The need for testing the kind of evolution undergone by a black hole whose linear size would compare with the size of the halo requires us to increase the Schwarzschild radius without affecting too much the system by mass. The solution came from the value of the velocity of light, which is an outside parameter in this non-relativistic model of gravity. This avoids having to improve drastically the mass resolution, which would make the integration time unmanageable, all other parameters remaining the same. In this way, only the evaluation of the Schwarzschild radius is affected by the tuning of c and allows therefore the tuning to involve a (marginally) sufficient number of orbits to get captured by the initial central mass: if the initial radius is too small, no evolution occur, but if it is too large, each and every single shell gets absorbed at its first crossing of the centre, which defeats the purpose of our moderate black hole accretion model (see section 6.3.2 and figure 6.12). This tuning was achieved in both qualitative cases with $c \sim 1.64 \times 10^5 m/s$.

This section presents the effects of modifying the magnitude of the velocity of light (i.e. the initial Schwarzschild radius) while keeping any other parameter constant in the

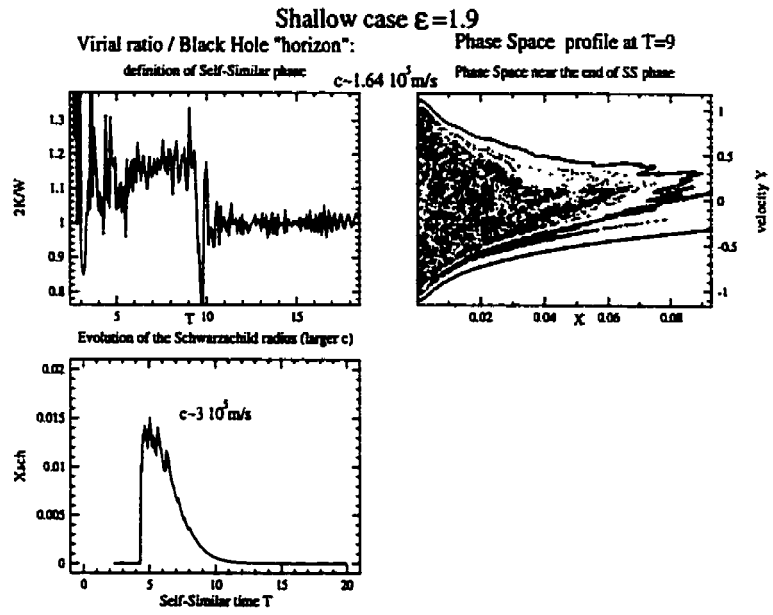

Figure 6.21: Black hole Virial ratio (shallow case: $\epsilon = 1.9$, reduced speed of light) and Schwarzschild radius evolution, and Phase Space diagram at the end of the self similar phase

shallow and steep initial density profile models of the embedded black hole SSIM.

Virial ratio, Phase space and evolution of the Schwarzschild radius

The virial and phase space diagrams of both shallow and steep cases seem almost unaffected by the accretion taking place with this larger black hole. The virial ratios just confirm an even more stable virialised phase. One difference though in the virial ratio for the steep case is the smoothing of its last trough before the stable self-similar virial phase visible as a noisy but regular rise in figure 6.22's top left panel, compared with its corresponding range in the top left panel of figure 6.20. This can be seen as a result of the reinforcement of the stabilisation effect of the central mass by its growth and the capture of some shells in the centre. As for the phase space diagram, there are no major differences between the steep case accreting and non accreting black hole simulations (top right panels of figures 6.22 and 6.20). On another hand, the phase space representation of the shallow case shows a stronger smearing of its structures, noticeable in the vanishing of most of its secondary Lagrange-Liouville stream: the inner second layer of shells wrapping around the system visible in the top right panel of figure 6.19 is almost absent in that of figure 6.21.

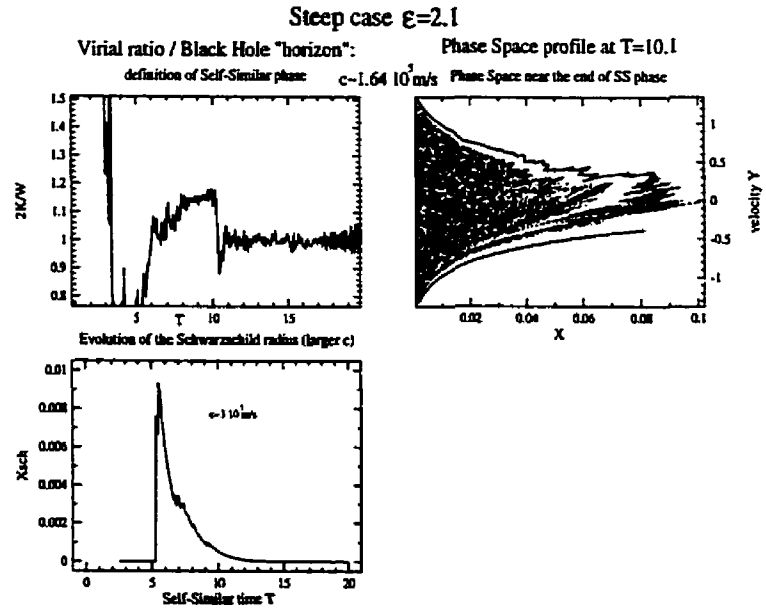

Figure 6.22: Black hole Virial ratio (steep case: $\epsilon = 2.1$, reduced speed of light) and Schwarzschild radius evolution, and Phase Space diagram at the end of the self similar phase

The remarkable feature of this model is the evidence for some self-similar accretion on the black hole at the beginning of the core formation for the diffuse initial halo, which then disappears at approximately the same time as the system stabilises in its self-similar phase (compare top and bottom left panels of figure 6.21). In fact a correspondence can be drawn between the central mass accretion and a last decline in the virial ratio before stabilisation. The steep case also displays some central mass accretion around the beginning of the core formation, until approximately the same time as the system stabilises in its self-similar phase (see top right and bottom panels in figure 6.22), albeit not as strongly as the shallow case. The indication for self-similar accretion (i.e. accretion in a quasi-equilibrium self-similar infall, as detected in the virial ratio) is also quite dim in the steep case, some hint being more noticeable around the same time as the last noisy regular rise before the stable self-similar phase, in the virial ratio.

A possible interpretation of the lack of accretion displayed is that the efficiency of the phase space instability rapidly washes away any trace of even remnants of the Lagrange-Liouville stream, on which the accretion algorithmic decision test is built (see section 6.3.2 and figure 6.12). Before the system settles, these streams are not too disturbed so as to break down the accretion, in the same manner as the disturbed Poincaré tori around equilibrium orbits (K.A.M. theorem). But when those streams are destroyed, like

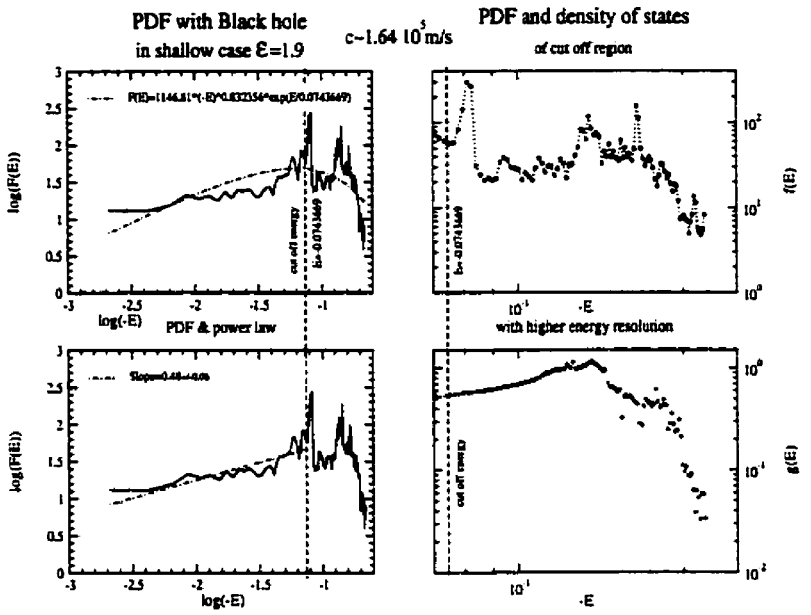

Figure 6.23: Black hole PDF measurement (shallow case: $\epsilon = 1.9$, reduced speed of light) averaged over the self-similar phase and evaluation of the power law dependence in energy. The phase space factor is well behaved for all energies.

the Poincaré tori, a sea of chaos is left, invalidating the decision test to accrete a shell on the central mass, thus failing to grow the black hole anymore. As for the difference of the steep case behaviour with the shallow case, namely the less clear self-similar accretion, the self-similar evolution of the scaled Schwarzschild radius with the steep case self-similarity class has been shown to follow an exponential decrease. This decrease, though, has a very small log-linear slope (see Eqs.(H.3)'s second line). It tends to suppress shells' accretion since it diminishes the scaled radius which in turn is capturing less orbits. Nevertheless, some hints of self similar accretion can be seen in the suggestion of a noisy almost constant evolution before the length scaling exponential decay wins over.

PDF and phase space density of states

The behaviours of the PDF and phase space density factor of the growing black hole systems exhibit very similar features as the system with a regular speed of light. Comparing the growing and non-growing black hole cases carefully, some minor differences emerge.

The shallow case's high energy PDF displays a slightly shallower slope than its higher speed of light counterpart, actually narrowing slightly tighter around the predicted power law slope of $\frac{1}{2}$ (lower left panel in figure 6.23). This narrowing is also perceptible in the

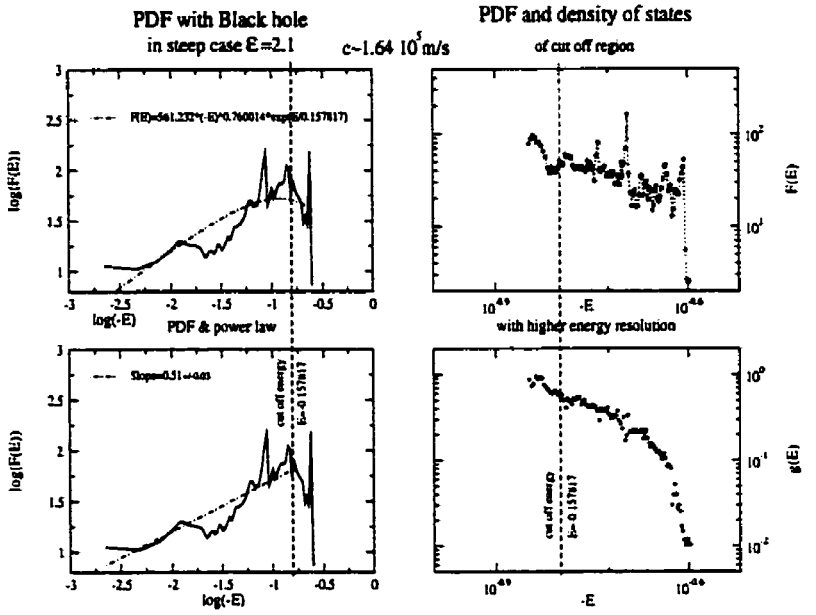

Figure 6.24: Black hole PDF measurement (steep case: $\epsilon = 2.1$, reduced speed of light) averaged over the self-similar phase and evaluation of the power law dependence in energy. The phase space factor is well behaved for all energies.

steep case's apparent measured power law, but the deviation with the actual high energy PDF is stronger than without accretion: the relaxation hump and subsequent trough are more pronounced here than in the non-accreting case.

The reinforcement of the relaxation hump reflects the shift in the phase space (figure 6.22's top right panel) of the instability outer layer towards larger radii. Also the cut off seems slightly sharper than for the model's regular c counterpart. That seems to reflect the enhancement of the lowest energy range of the phase factor, leading to a last spike in the PDF (see the two right panels of figure 6.24 compared with those of figure 6.15, which one can explain in turn with the softening of the potential energy turn around at low energy, compared with the corresponding potential energy of the non-accreting model (lower panels in figures 6.26 and 6.16).

Otherwise, the exponentially cut off power law is easier to fit in the shallow case (top left panel in figure 6.23), allowing the exponential cut off to fall before any turnaround of the slope and yielding a good limit for the power law estimate. This is due to the slight softening of the still sharp cut off, as observed on the higher energy resolution plots (top right panel in figure 6.23). This softening could be interpreted as a slight enforcement of the evidence for an exponential form of the cut off.

In other respects, this reduced speed of light model displays the same effects and

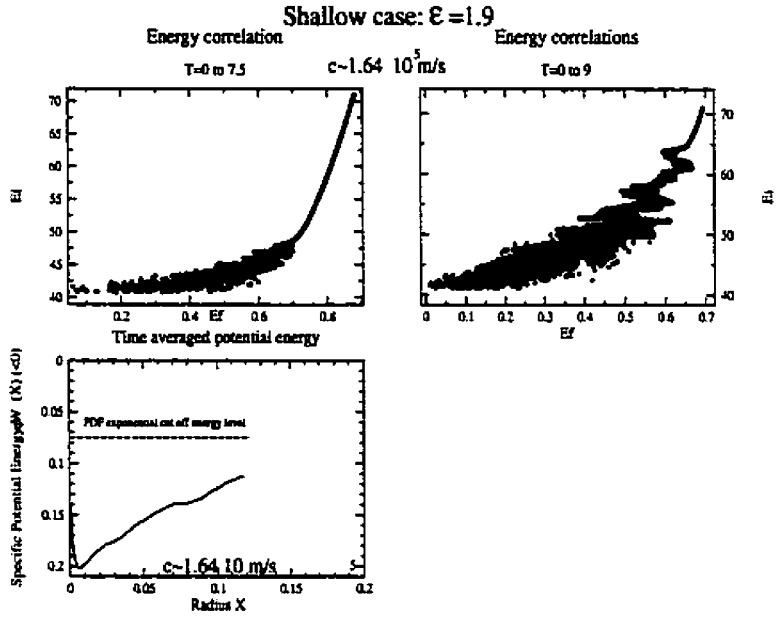

Figure 6.25: Black hole Energy correlation (shallow case: $\epsilon = 1.9$, reduced speed of light) between initial and final times at the beginning (upper left panel) and at the end (upper right panel) of the stable PDF portion of the self-similar phase; the potential energy profile is given for comparison with Eq.(5.8) added with the central mass contribution and is illustrative of the phase factor calculation

entails the same conclusions, compared to the simple SSIM, as the regular c black hole model.

Energy correlations and potential energy

Similar observations can be drawn from the energy correlation diagrams presented above than for the reduced velocity of light black hole embedding halo models (top panels in figures 6.25 and 6.26), but the cut off limit, seen in the bottom, leftmost part of each diagram, that was detected in the previous shallow case exploration to be correlated with initial energy of shells is no longer manifest as if the most bound energies were depleted by the presence of a strong back hole. This reinforces the previous result of a cut off, all the more as it was clearly detected for the simple SSIM's shallow case.

The aspect of the shallow case's energy diagram also shows a tighter energy correlation than for the regular c black hole model. This could be understood in terms of the stabilisation of the system by the higher central mass available. Similarly, the steep case's resulting energy correlation is tighter than that of its regular c counterpart.

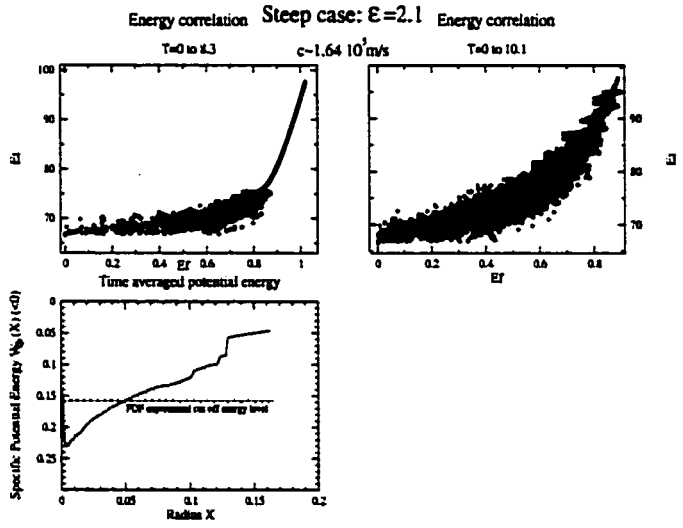

Figure 6.26: Black hole Energy correlation (steep case: $\epsilon = 2.1$, reduced speed of light) between initial and final times at the beginning (upper left panel) and at the end (upper right panel) of the stable PDF portion of the self-similar phase; the potential energy profile is given for comparison with Eq.(5.8) added with the central mass contribution and is illustrative of the phase factor calculation

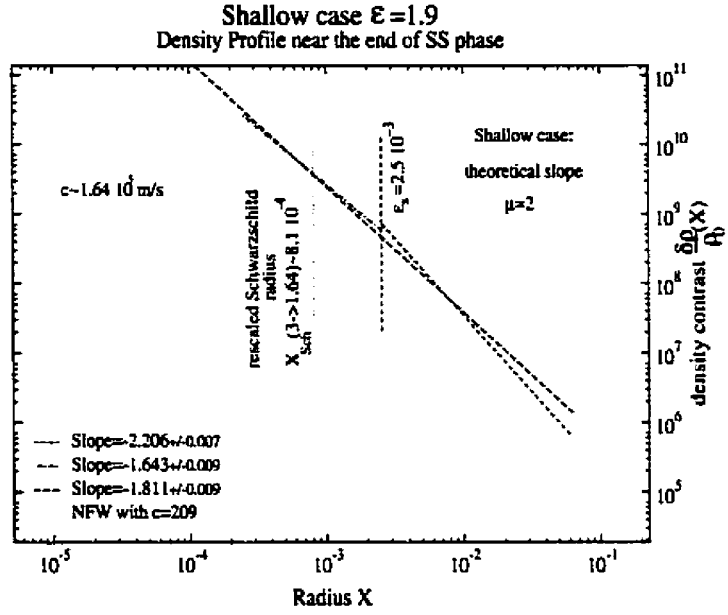

Figure 6.27: Black hole Density profile Diagram (shallow case: $\epsilon = 1.9$, reduced speed of light) at the end of the self similar phase.

The incoming particles energy outer streams are otherwise remarkably clear near the end of the infall phase, in the top right part of the diagrams (top parts of the energy correlations) compared to their regular c counterparts. Finally, the relaxation region is more delineated from the core (relaxed particles) correlation compared to the regular c case. This could indicate that the energy processing is more efficient since it wiggles shells more in the relaxation stage.

The potential energy diagrams illustrate (lower panels in figures 6.25 and 6.26), as for the regular central mass models, that the potential is dominated by the central mass. A slightly softer break of the potential energy power law behaviour at small radius can also be detected, compared with the regular central mass models.

Density profiles

Eventually, the density profiles display a much smoother change of slope between their inner and outer slopes. Nevertheless the NFW profile could still not be properly fitted (brown, dotted lines in figures 6.27 and 6.28). The steep case's regular c central mass model's cusp detected at the smoothing length is no longer apparent here, reinforcing its accidental nature. On another hand, the smoothness of the slope change makes it even more difficult to set its limits.

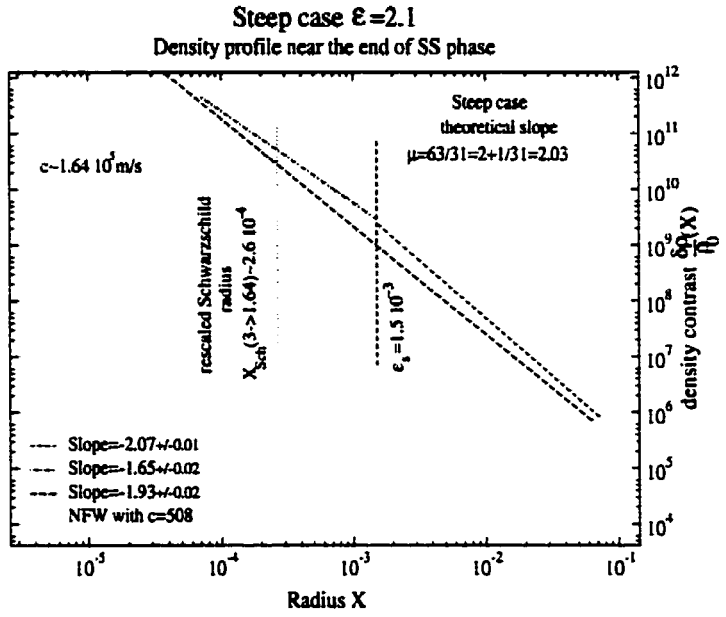

Figure 6.28: Black hole Density profile Diagram (steep case: $\epsilon = 2.1$, reduced speed of light) at the end of the self similar phase.

The global power law fit finds it all the more difficult to reproduce the theoretical SSIM slope ($\mu \simeq 1.81$ instead of 2 for the shallow case long dashed, blue line in figure 6.27 and $\mu \simeq 1.93$ instead of approximately 2.03 for the steep case, long dashed, blue line in figure 6.28). However, in the steep case, the outermost fit reveals more promise on that level ($\mu \simeq 2.06$, dashed, red line in figure 6.28). On another hand, this is quite a departure from the regular central mass model (for which $\mu \simeq 2.25$ for the same range of fit). Conversely, the outer slope from the smoothing length for the shallow case is close to the regular speed of light model ($\mu \simeq 2.21$ compared to 2.24, for the dashed, red line in figure 6.27), albeit being unable to fit the outermost density slope (there the NFW profile fit hints at an outer slope of $\mu = 3$).

The inner slopes encounter the same kinds of difficulties on their innermost parts. The estimated value of 1.64 (green, dotted dashed line in figure 6.27) can be questioned from the point of view of the accuracy of the fit (since the slope is changing continuously). The steep case's measures at an intriguingly similar value (green, dotted dashed line in figure 6.28, $\mu \simeq 1.65$ compared to 1.64 in the shallow case). There is also a question regarding its range of validity, the fit being calculated over particles which are inside the new Schwarzschild radius.

6.4.8 Black hole and density cusps

In the variety of ways to possibly understand the flat central density cusps observed in dwarf and low surface brightness galaxies, models embedding a central supermassive black hole hold serious promises. While other approaches encounter problems, like the lack of central radiation levels that would result from self-annihilation of self-interacting dark matter, shallow cusps are predicted for CDM black hole embedding haloes (Nakano & Makino [85] and Henriksen & Le Delliou [86]). The aim of this work was to explore the SSIM's inclusion of a central growing black hole calculated by Henriksen & Le Delliou, 2001 [86].

This introduction was made in a radial infall only, leaving non-radial modeling around the black hole for later works. Evaluations of the Schwarzschild radius required the use of some galaxy-size dark halo mapping of the model. The resulting radius represents a very small black hole accretion region compared to the cosmological halo scales and numerical treatment lead to no observed accretion. An enhanced Schwarzschild radius model was studied to evaluate the rate of accretion if the sizes of the halo and black hole were comparable.

This study has shown four major points: the cusp in haloes can be explained with the very elementary SSIM and do not require more than the presence of a central black hole and a regular accretion basin (contrary to Nakano & Makino [85]). The population inversion, or sharp cut off, just comes from the initial conditions of the system and the 'energy processing' of self-similar accretion, which occurs naturally in the SSIM. This cut off is therefore not necessarily a result of the central black hole: even though the black hole is responsible for the initial cut off in the steep initial density profile in the SSIM, that cut off originates in the limits of the dark halo accretion basin for the shallow initial conditions.

Self-similar accretion still appears very prominently in CDM halo formation as an intermediate stable quasi-equilibrium stage, even in the presence of a central black hole, and confirms itself as a primary principle of explanation for Large Scale Structure formation.

The analytical results in Henriksen & Le Delliou [86] are confirmed to hold in the radial infall model: the density cusp is verified, within the limits of accuracy of the simulations, to follow predictions and the method allowed for some weak evidence of the self-similar mass accretion by the black hole. The shallower cusps require a sharp cut off and results from Leeuwin & Athanassoula [111], with an arguably softer cut off, reveal even more decisively that importance.

From a reversed point of view, this work has also shed some new light on the SSIM itself: the presence of a simple central mass, by imitating the natural power law cusp of the SSIM, has shown a stabilised behaviour of the model. It has revealed that the cut off

in the PDF is present in both qualitative cases of the SSIM. The mass accretion of the central black hole just accentuates those results.

Chapter 7

Conclusions

This is the way the world ends
This is the way the world ends
This is the way the world ends
Not with a bang but a whimper

T.S.ELLIOTT

In modern, physical cosmology, the understanding of the formation of Large Scale Structures involves the exploration of Cold Dark Matter haloes. From the wealth of questions raised in the study of those objects, this work has focused on answering two main problems: what are the fundamental elements involved in the formation of CDM haloes density profiles, and what can characterise the relaxation state of equilibrium haloes.

This chapter will survey the implications of the present work: in a first section, the motivations that sparked it will be reviewed. The second section will clarify its achievements and the last section will point to questions left unresolved and directions for further research.

7.1 Why explore the SSIM?

> Nous ne savons encore presque rien et nous voudrions deviner ce dernier mot qui ne nous sera jamais révélé. La frénésie d'arriver à une conclusion est la plus funeste et la plus stérile des manies.
>
> *lettre à Louis Bouilhet* GUSTAVE FLAUBERT

Indeed, can such an old and simple model as the SIM still be of use in the understanding of CDM haloes already explored by large and complex N-body simulations? This work has shown how sophisticated second-generation versions of the SSIM answered questions coming from three main impulses: the theoretical drive for understanding fundamental concepts involved in the study of collisionless CDM halo's; the numerical drive of questions produced by results of N-body simulations; and the observational drive by new objects defying the predictions of N-body, self-gravitating purely collisionless matter

7.1.1 Theoretical drive

Exploration of the properties of self-gravitating collisionless matter is of utmost theoretical interest. The dominance of the bottom-up paradigm of CDM clustering and results from N-body simulations tend to emphasize the existence of hierarchical merger clustering and triaxial (as opposed to this work's radial or spherically symmetric) mass accretion of CDM haloes. To evaluate the importance of these processes in the formation of haloes is the goal of the study of Large Scale structure formation. In other words, are mergers necessary processes for the formation of CDM haloes (as advocated by Syer & White [33]) and if otherwise, what are the fundamental elements of CDM gravitational collapse?

Intimately linked with the modes of mass accretion is the problem of relaxation. The impossibility for a finite collisionless and self-gravitating system to reach a thermodynamical equilibrium, as discussed by Lynden-Bell [34], opens the question of the so-called 'violent relaxation' and the problem of its mediation in such systems.

Such questions have been successfully dealt with by the careful modelisation of the SSIM.

7.1.2 Numerical drive

The study of the results yielded by cutting edge N-body simulations allows one to probe the nominal behaviour of cosmology's hypothetical CDM, otherwise directly undetectable

by definition. This reveals that those haloes typically form by clumping surrounding matter and swallowing neighbouring lesser clumps in a highly non-radial way. These features pose profound questions as to whether these observed modes of formation are fundamental to CDM haloes properties or if they are just accidents of those detailed simulations of no great impact.

Present research focuses on the radial mass density distribution, or density profile, of CDM haloes. Some groups (led by Navarro, Frenk & White [32]) are finding what could be a universal — single, when applied to appropriately scaled haloes — profile in N-body simulations for any halo, commonly called NFW. Others are finding a different universal profile, like the one this work refers to as Moore99 [71] or the Hernquist profile [63], used earlier in theoretical description of stellar systems and elliptical galaxies. Some groups even disagree with the universality of those profiles (Jing [69], Jing &Suto [70]).

This interest in the density profile is fueled, on one hand, by the information it could contain about the initial conditions of the primordial density fluctuations and the accretion and relaxation processes it has undergone. Indeed, universality entails a loss of memory of initial conditions, but also implies sufficiently violent relaxation. Several groups have already worked on using some variant of the SSIM to explain the density profile of CDM haloes. The study of the equilibrium of CDM haloes has also led some groups to borrow the PDF, or Probability Distribution Function, formalism from stellar group dynamics and kinetic theory (for a more complete review see sections 2.2 and 3.2).

On the other hand, the possibility for observation to be linked indirectly to this CDM halo density profile also contributes to its interest. In fact, if it can be argued that full three-dimensional N-body simulations play a role similar to observations for theoretical understanding of the intimate relaxation and collapse mechanisms, then they reflect the limits of the purely collisionless CDM paradigm when confronted with real observations.

7.1.3 Observational drive

Such confrontations between N-body results, or broad paradigmatic models, and observations have already permitted the exclusion of the Hot Dark Matter scenarios as good models of Large Scale Structure formation in the universe.

More recent observations of density profile central cusps on haloes of dwarf and Low Surface Brightness galaxies, which can be derived with such tracers of mass as the Sunyayev-Zel'Dovich effect, disagree with all the density profiles obtained in N-body simulations. Some responses extending the simple CDM model in terms of self-interacting dark matter run into problems like the lack of central radiation levels that would result from the self-annihilation of such self-interacting dark matter (Flores & Primack 94 [79]). Other directions, like adding the effect of baryonic gas proposed by N-body numericists,

introduce a lack of simplicity and dissolve subtle understanding into maximalist N-body simulations. Besides, studies like Teyssier *et al.* [54] forecast that such efforts are unlikely to yield results much different than those obtained with rotating collisionless matter. A more promising departure from simple CDM models — the exploration of the effects of a central supermassive black hole — is the option followed in this work.

7.2 Advances

Confronted with these unresolved problems in the field of primordial halo formation, we adopted the strategy of reducing the complexities of the problems and distilling them into an elementary model: the SSIM. Mending its shortcomings led us to new territories of understanding both of the nature of the SSIM and of the nature of hierarchical collapse and CDM halo formation.

7.2.1 SSIM:PDF and virial states

In a first part of this project, we established our capacity to successfully reproduce Henriksen & Widrow's ([42]) unconstrained SSIM results, apart from a weaker energy correlation. This weaker energy correlation indicates a less moderate violent relaxation than previously found. That success, together with thorough explorations of some important parameter variations, served to confirm the validity of our numerical explorations. The SSIM thus displays its usual semi-universal density profile with initial profiles shallower than the isothermal density profile converging to $\rho \propto r^{-2}$ and steeper initial profiles each admitting a separate attractor not very far from isothermal ($\delta\rho_{initial} \propto r^{-\epsilon}$ with $\epsilon > 2$ leads to $\rho \propto r^{-\mu}$ with μ related to the self-similarity class $\frac{\delta}{\alpha}$ and thus to the initial profile by $\mu = 2\frac{\alpha}{\delta} = \frac{3\epsilon}{1+\epsilon}$). In cosmological terms, in the SSIM Einstein-de Sitter background, if the initial power spectrum is scale free ($P(k) = \left\langle |\delta_k|^2 \right\rangle \propto k^n$) and assuming the density profile to be proportional to the correlation function (through the spherically averaged rms mass fluctuation), the initial profile can be reformulated as $\delta\rho_{initial} \propto \left\langle \delta_R(\vec{x})^2 \right\rangle^{1/2} \propto R^{-(n+3)/2}$, and the resulting similarity class and final density profile can be defined as

$$\frac{\delta}{\alpha} = \frac{2}{3}\left(\frac{n+5}{n+3}\right);$$

and

$$\mu = \begin{cases} 3\left(\frac{n+3}{n+5}\right) & n > 1 \\ 2 & n \leq 1 \end{cases}.$$

But this exploration of the SSIM was also an opportunity to refine our understanding of the SSIM.

The importance to the relaxation of the system of the most recently fallen particles confined in the outer limits of the phase space and PDF of the SSIM is made clear in the energy correlation diagrams. Our understanding of violent relaxation in the SSIM is therefore improved: it occurs very rapidly and is more mediated by phase space instabilities (see Henriksen & Widrow [42]) than by the central part of the halo's potential. This has also been confirmed by a higher force resolution simulation in the presence of angular momentum.

Even if the exponential nature of the cut off at high negative energy in the PDF prescribed by Henriksen & Widrow, after Merritt *et al.* [60] was not established firmly, a new result was however obtained: the existence of such a sharp cut off was proven in the shallow initial density profile case, with similar indications in the steep case. The proof for an $F(E) \propto (-E)^{1/2}$ behaviour at high energy in the PDF was also reinforced over one or more decades.

Eventually, a preliminary result was also produced: the value of the virial ratio during the self-similar infall phase decreases with increasing primordial density profile power law index. Since that index, related to the self-similarity class, reflects the initial concentration of the halo, this trend just represents the reduction of the outer halo in favour of the centre, which in turn increasingly resembles a virialised system when reaching the quasi-equilibrium of the accretion phase. However, the trend does not asymptote to the regular isolated equilibrium value and the accretion phase retains its irreducible quality.

7.2.2 Mergers: Modeling of a merger event

Mergers are commonly believed to hold a predominant position in hierarchical clustering, disfavouring the secondary accretion model of the SSIM. Syer & White [33] published a discussion in which repeated mergers, in a feed back mechanism between dynamical friction and tidal stripping of merging satellites, explained the emergence of the NFW universal profile as a dynamical attractor.

The simple SSIM with its semi-attractor and self-similarity as a driving force presents itself as a serious candidate to explain some universality in density profiles. It only appears to lack the merger paradigm. Taking on the paradigm of repeated mergers, we included a model of its effect on the SSIM.

From this model we have established that the SSIM density profile is affected by the impact of a merger in an interesting way: the average power law continuum of attractor gets shrunk (from $\mu_{SSIM} \simeq 2.143$ to $\mu \simeq 2.024 \pm 0.001$ and from $\mu_{SSIM} \simeq 2.231$ to $\mu \simeq 2.095 \pm 0.001$ for strongly disruptive mergers) after the digestion of the satellite by the parent halo. Some indication of an outer steeper profile is visible for strongly disruptive mergers, getting close to Keplerian ($\mu_{outer} \simeq 2.866 \pm 0.007$). And some indications of

a flatter cusp can be obtained more clearly from the strongly disruptive mergers (e.g. $\mu_{inner} \simeq 1.63 \pm 0.02$ for the moderately steep parent halo). Thus a picture closer to the Moore99 profile as an attractor emerges from the repetition of mergers; this would increase the shrinking of the range of the SSIM attractors into being indistinguishable from a unique one.

Although this picture points towards the destruction of the scale-free unique power law of the SSIM by the introduction of a scale from the merging satellite, a very interesting dynamical result is obtained: the continuation of the secondary mass infall brings the system back into the energetic quasi-stable state of the SSIM! Despite the destruction of its scale-free features, the self-similar rescaling of the system also continues to hold. This robustness of the SSIM to merger disturbances of comparable mass and density proves the interest of self-similarity as a general intermediate attractor of the behaviour of the system and the value of self-similarity as an explanatory principle for the behaviour of DM haloes.

This exploration also contains an unexpected insight into the SSIM: it shows the lack of distinction between the SSIM and repeated mergers where satellites are small enough compared to the parent, and the number of mergers frequent enough to maintain a strong mass flux through the system's boundary. The difference between the two paradigms is then shown to be a progressive and quantitative one, rather than the distinct division commonly held.

Nevertheless, mergers are neither the only nor the most efficient mechanism leading to the central flattening and peripheral steepening of the density profile. Evidence for non-radial motion in the centres of haloes, both numerical and observational, points towards another, or at least a mixed, explanation. Moreover, the flattening obtained is not sufficient to reach the very flat cusps observed. Thus more investigations were begun, extending the limits of the SSIM in order to answer those further questions.

7.2.3 Modeling of halo angular momentum

Taking its origin from differential asymmetric torques of external haloes, non-radial motion is omnipresent in any realistic account of observations. Modifying the radial infall of the SSIM to accommodate for some form of spherically symmetric angular momentum was therefore necessary if the SSIM was to hold any claim to model the principles of dark halo formation.

Of the two forms of angular momentum distribution retained, one proved to be very important: the Dimensionally motivated 'power law' angular momentum profile proves capable of producing smoothly varying two-slope density profiles of the type made in fully three-dimensional collisionless N-body simulations. In fact the most important result of

this work on pure CDM haloes is that the NFW profile can be fitted extremely well to one of the realisations of the 'power law' angular momentum SSIM. Compared with the results from the merger model, the SSIM shows that non-radial motion probably plays the primary role in the constitution of the density profile. The shrinking of the continuum range by mergers is not so important when considering the difficulty of discriminating the initial range from the isothermal attractor ($\mu \in [2; \frac{9}{4}]$ so the maximum deviation from 2 is only 0.25).

The second main result from the modeling of dark haloes with the SSIM is the extreme robustness of the model: despite the perturbation of the angular momentum distribution, which sets a scale at the inner turnaround of particles, the scaling and relaxation features of the SSIM are almost unaffected. Remarkably, the virial ratio measuring the quasi-equilibrium stable self-similar accretion phase slips smoothly into its isolated equilibrium value in the presence of angular momentum instead of dropping after the last incoming particle is accreted. Overall, the robustness of the SSIM makes it a very convincing and attractive model for the principles of CDM halo formation. In addition, this version of the SSIM was chosen to test the robustness of the results under a change in the dynamical resolution (force smoothing length). The induced better time integration, and therefore dynamical relaxation, did not have a major impact on the model, confirming that most of the relaxation occurs in the outskirts of the system, in the previously characterised relaxation and energy processing region.

Eventually, the study of the relaxation of the shallow initial density profile systems reveals, surprisingly, that the more constrained form of angular momentum turns out to be less efficient at reaching relaxation. The shape in phase space of that distribution leads to the discovery of traces in the SSIM of what another group claims to be a universal angular momentum profile (see Bullock *et al.* [113]). More investigations are needed on those matters.

7.2.4 Modeling of central black hole

Armed with the confidence bestowed upon the SSIM by its success in explaining pure dark halo behaviours, we can now turn to our attempt to augment the SSIM. The need for more than purely collisionless DM modeling is driven by shallow central cusps observations (Kravtsov *et al.* [31], Stil [75]). We have chosen to study the effect of a central black hole on the SSIM as a natural and elegant extension of the model. Henriksen & Le Delliou [86] have shown that the analytical SSIM model with a self-similar growing central black hole is able to explain the shallow cusps observed.

In this work, a central mass was left to accrete in a radial infall. A more complete model would have included non-radial motion as well, but this was left for future works.

The simple radial model allowed us to concentrate on the effects specific to the central mass presence. The need for physical scalings of the model in order to implement a Schwarzschild radius called for an evaluation of the model as a galaxy-size halo. Despite using a peculiarly large central mass, this evaluation demonstrates how tiny supermassive black holes are compared to their halo. That scale difference combined with our mass resolution led the central mass to remain unable to accrete. In this classical model, the speed of light is an external constant. Adjusting its value allowed us to enlarge the original Schwarzschild radius so the effects of accretion were also studied.

From these explorations, Henriksen & Le Delliou's analytical predictions of a cusp with slope -1.5, in the radial infall model, are confirmed. Indeed, measured inner cusps are found with slopes around -1.5 ± 0.1. Instead of a smoothly varying density profile, the radial infall retains the SSIM's results as an average slope of a two-slope behaviour with a sharp transition between the inner cusp and the outer envelope. Analytical calculations (Henriksen & Le Delliou [86]) combined with these results allow us to be confident that an angular momentum implementation of this central mass SSIM should yield the shallow 0.5 central cusp. Of course this is to be confirmed in a future development of the model. Thus the simplicity of the SSIM added to the presence of a central mass is a sufficient condition to explain the observed density cusps.

Moreover, contrary to what Nakano & Makino [85] propose, the population inversion, or sharp cut off in the PDF, occurs naturally in the SSIM due to its initial conditions and relaxation properties. The cut off is thus not a direct result of the presence of the central mass: although the initial cut off in the steep initial density profile proceeds outwards from the black hole, the shallow initial conditions produce an initial cut off inwards from the limits of the dark halo accretion basin. In our model the shallower cusps require the population inversion to yield a sharp cut off. It can be argued that other attempts to include a central supermassive black hole cannot reproduce the same flat cusps (see e.g. Leeuwin & Athanassoula [111]), and our calculations even predict the cusp they display.

Finally, all the energetic, phase space and relaxation results of the simple SSIM model are even more distinctly reproduced here. The central mass allows for the numerical model to produce a real central cusp, which imitates the SSIM's natural power law cusp and thus stabilises the behaviour of the simulation. Thus the steep initial profile's PDF cut off can be confirmed thanks to that stabilisation. In fact, one can adopt the perspective of the SSIM and treat these results as a stabilised version of the simple SSIM and the best indicator of its properties. The evidence for a self-similar accretion through the enlarged Schwarzschild radius is just indicative, but accretion only reinforces the stabilisation of the simulation.

7.2.5 General picture of a dark halo from the SSIM and its extensions

The SSIM, when properly enhanced, contains all the elements essential for the understanding of the various behaviours in CDM halo formation.

The picture it presents of CDM haloes explains large N-body simulations and indirect observations of real haloes alike. From its exploration, because we did not assume self-similar accretion but allowed for it to develop and used coordinates that make it evident, self-similar accretion appears very prominently in CDM halo formation as an intermediate stable quasi-equilibrium stage. It thus confirms itself as a primary principle of explanation for Large Scale Structure formation.

We now understand the primordial importance of non-radial motion in the constitution of dark haloes' density profiles. The merger paradigm appears as a secondary but non-trivial addition to the picture, driving the halo towards a unique attractor, even in the absence of angular momentum. The introduction of a central black hole offers itself as a simple and natural way to explain the strong flattening of observed density cusps.

Understanding of the violent relaxation involved in cold collapse is refined in the light of the SSIM. Relaxation occurs continuously during the infall, but in a few dynamical times for any given shell. It is mainly located in the peripheral regions of phase space. It is effected by phase space instability after enough phase mixing has occurred. It is moderately violent, a clear energy correlation remaining after relaxation, and is characterised by a sharp population inversion in its Distribution Function. The origin of this cut off probably lies in initial conditions but it is remarkably maintained through the strong energy 'processing' of violent relaxation.

The power of explanation of self-similarity as an intermediate attractor is thus strongly illustrated and promises more developments.

7.3 Moving beyond

'Il est encore fécond, le ventre qui a vu naître la bête immonde'

La résistible ascention d'Arturo Ui
BERTOLD BRECHT

Prediction is very difficult, especially about the future.

NIELS BOHR (1885-1962)

In the present picture, the SSIM shows that the density profile of CDM haloes is determined by non-radial motion and the presence of a central supermassive black hole. Repeated mergers of hierarchical clustering are not necessarily primordial in the constitution of those density profiles, contrary to the Syer & White argument for the establishment of the NFW profile. Self-similarity points towards the existence of a universal profile, and for purely collisionless secondary accretion haloes, the NFW profile is favoured over the Moore99 profile. The dynamics of gravitational collapse involve moderately violent relaxation mediated through phase mixing and instability. But the present project has left open numerous questions.

The treatment of angular momentum reveals that a higher mass and dynamical resolution exploration of the SSIM could separate the NFW profile from the Moore99 beyond doubt. A study of the rotational velocities involved in the present model in terms of realistic halo measurement should be conducted. An angular momentum profile derived from a careful model of inter-halo tidal torques could be confronted with the previous a priori results. Moreover, a careful study of the velocity anisotropy could confirm N-body results and reinforce the grounds of the SSIM. Some preliminary measurements of PDF in the presence of angular momentum were performed during the course of this work. Since they were using the assumptions either of radial infall, or of isotropic velocity field, which are contrary to and not guaranteed by, respectively, the present use of angular momentum, they were not reported. Nevertheless, similarities of the isotropic velocity PDF measurements with that of other works (e.g. Hanyu & Habe [101]) are promising new results. Given an isotropisation that we conjecture but has to be tested, the one-dimensional energy dependent PDF could be measured and compared with those works.

The central mass results clearly show that a more careful control over the mass resolution length scale is needed to get the correct inner cusp as the limiting slope of density profile. A higher mass resolution might even yield a real size black hole accretion. But a more robust accretion test has to be imagined if the radial model is to produce a correct view on the subject.

In the end, the central black hole model needs to be addressed in more realistic terms with the inclusion of angular momentum. This will allow for the black hole to accrete in a more natural manner. The resulting profile should also be confronted with the observed very flat cusps and halo profiles.

The exploration of mergers presented here has yielded some promising conjectures on the final density attractor. A logical extention of the work should conduct a model of the repetition of mergers by iterating the process: once the overdensity is digested by the core of the SSIM, a second overdensity should be added on its edges, and the halo extended to allow for a new round of digestion. The combinatoric possibilities dictate also some additional experiments: the effect of angular momentum on the merging process with the

SSIM could be explored, as well as the impact of a merger on the accreting central mass model, or even a complete angular momentum with central black hole model could be perturbed by a merging satellite.

Other questions regarding the SSIM itself remain unanswered: a more complete study of the virial function dependence on the initial profile index should compare the numerical results with the predictions calculated from Henriksen & Widrow [42]. Further explorations could address the main objection to this work: the strength of the primordial density peak, kept constant here, could be modulated and its effects carefully studied. We used to describe the system a set of scaled variables so as to obtain a steady state when the system reaches self-similarity. In these variables, at a fixed class of self-similarity, the size of the self-similar core in phase space seems constant under changes involving mergers, central accreting mass and angular momentum perturbations of the SSIM. This poses the following question: what governs size of system in rescaled phase space?

Eventually, leaving the framework of the spherical shell code, the SSIM in particular and the collisionless self-gravitating collapse in general can be studied using the self-similar formulation to better detect the onset of self-similarity, using the evolution of the PDF by the Collisionless Boltzmann's Equation, as in simulations conducted by collaborators (Merrall [102]), or using this formulation to analyse the results from fully three-dimensional N-body simulations.

The SSIM has demonstrated its richness by offering a solid interpretation of self-gravitating dark haloes collisionless collapse, but its possibilities are far from exhausted. subfigure

Appendix A

Glossary

- **BBGKY=Bogoliubov-Born-Green-Kirkwood-Yvon hierarchy equations**: statistical description of a fluid originating from plasma physics .
- **BBKS=Bardeen, Bond, Kaiser & Szalay**: 1986 [22], extension of PS using density peaks.
- **BBN=Big Bang Nucleosynthesis**: The part of the BB scenario which computes the ratio of primordial light elements from nuclear reactions in the hot, early universe.
- **BCEK=Bond, Cole, Efstathiou & Kaiser**: 1991 [25], extension of BBKS to various mass scales.
- **CBE=Collisionless Boltzmann's Equation, also coined Vlasov Equation**: governing statistical equation for a collisionless system.
- **CMBR=Cosmic Microwave Background Radiation**: relic radiation of light from near the beginning of the universe (in fact from the Recombination epoch, when electrons were captured by nuclei).
- **CH91=Carter & Henriksen**: 1991 [43]. First systematic presentation of self-similarity in Newtonian mechanics.
- **DM=Dark Matter**: Generic term for electromagnetically quiet mass which would constitute most of the mass of the universe.
- **CDM=Cold Dark Matter, also referred as SCDM=Standard CDM**: DM with non-relativistic velocities. Yields bottom up LSS formation scenarii.

- **HDM=Hot Dark Matter**: DM with relativistic to ultra-relativistic velocities. Yields top down LSS scenarii.
- **CHDM=mixed Hot and Cold DM**: intermediate scenario with the two types of DM present.
- **WDM=Warm Dark Matter**: DM with almost relativistic velocities. they are large enough to have an influence but not enough to dominate the LSS formation.
- **ΛCDM=Cold Dark Matter mixed with Λ**: CDM scenario with the addition of a cosmological constant.
- **FG84=Fillmore & Goldreich**:1984 [35], first presentation of the SSIM.
- **HS85=Hoffman & Shaham**: 1985 [37], first attempt at linking the SSIM to the cosmological spectrum of density fluctuations.
- **Hot Big Bang Cosmology, or BB (Big Bang) Cosmology**: standard cosmological scenario where the universe was much denser and hotter in the past.
- **HI gas= Hydrogen type I= neutral hydrogen**: astronomer designation for atomic hydrogen present in the interstellar medium around galaxies.
- **IBP=Integration By Part**: mathematical method.
- **LSBs and DMDGs=Low Surface Brightness galaxies and DM dominated Dwarf Galaxies**: two types of galaxies exhibiting evidences for a very shallow central density cusp (or none at all).
- **LSS=Large Scale Structures**: The departures from uniformity that range from galaxies to superclusters of galaxies. by extension to their cause, the DM haloes themselves.
- **MACHOs=MAssive Compact Halo Objects**: one kind of DM made of normal matter (baryonic) but not luminous enough to be detected directly (mostly made of Jupiter-type massive objects).
- **MTJ=Merritt, Tremaine & Johnstone**: 1989 [60], heuristic argumentation for the PDF
- **MoND=Modified Newtonian Gravity**: an alternative approach to the mass measurement discrepancy than DM, by modifying the long range acceleration term in Newtonian gravity.

- **NFW=Navarro, Frenk & White**: 1996 [32], can refer to the paper or the universal density profile that is proposed in the paper.
- **PDF=Probability Distribution Function**: the statistical measurement characteristic of a stationary self-gravitating system.
- **PLAM='Power Law' Angular Momentum**: Introduction of an initial angular momentum in the SSIM which is motivated by Dimensional arguments.
- **PS=Press & Schechter**: 1974 [27], first paper giving a heuristic argument for the Excursion set formalism.
- **RSL=Reduced Smoothing Length**: explorations of the SSIM with a smaller smoothing length, i.e. with an increased force resolution.
- **SIM=(Spherical) Secondary Infall Model**: model of smooth accretion (in spherical symmetry).
- **Specific (potential, kinetic or total) Energy**: energy (potential, kinetic or total) per unit mass
- **SSIM=Self-Similar Secondary Infall Model**: SIM where the collapse is self-similar.
- **SSAM=Self-Similar Angular Momentum**: Introduction of an initial angular momentum in the SSIM which preserve the system's Fillmore & Goldreich self-similar characteristics.

Appendix B

Simplectic mechanics of the SSIM

B.1 Lagrange Equations in Spherical symmetry

B.1.1 Definitions

The Lagrangian functional's definition reads

$$\mathrm{L} = T - m\Phi(r) \tag{B.1}$$

with

$$T = \frac{1}{2}m\vec{v}^2 = \frac{1}{2}m\left(v_r^2 + v_\theta^2 + v_\varphi^2\right)$$

and the relationships between the velocities and the coordinates being

$$\begin{aligned} v_r &= \dot{r} \\ v_\theta &= r\dot{\theta} \\ v_\varphi &= r\sin\theta\dot{\varphi} \end{aligned} \quad .$$

The dots denote derivation with respect to time.

B.1.2 Lagrange equations:

The Lagrange equations then read

$$\begin{aligned} \frac{\partial L}{\partial r} = m(\frac{j^2}{r^3} - \frac{\partial\Phi}{\partial r}) = \frac{d}{dt}\left(\frac{\partial L}{\partial \dot{r}}\right) = m\ddot{r} \\ \frac{\partial L}{\partial\theta} = mr^2\sin\theta\cos\theta\dot{\varphi}^2 = \frac{d}{dt}\left(\frac{\partial L}{\partial\dot{\theta}}\right) = m\left(r^2\dot{\theta}\right)^{\cdot} \\ \frac{\partial L}{\partial\varphi} = 0 \Leftrightarrow \frac{\partial L}{\partial\dot{\varphi}} = cste = m.l = mr^2\sin^2\theta\dot{\varphi} \end{aligned} \quad . \tag{B.2}$$

The first one is Newton's law, where the angular momentum is

$$j^2 = (\vec{r}\wedge\vec{v})^2 = r^2\left(\left(r\dot{\theta}\right)^2 + (r\sin\theta\dot{\varphi})^2\right) = \left(r^2\dot{\theta}\right)^2 + r^2l\dot{\varphi} = \left(r^2\dot{\theta}\right)^2 + \frac{l^2}{\sin^2\theta}. \tag{B.3}$$

The second and third ones yield the conservation of angular momentum:

Eqs.(B.2:2,3)$\Longrightarrow$

$$\left(r^2\dot{\theta}\right)\dot{} = \frac{l^2}{r^2\sin^2\theta}\cot\theta, \tag{B.4}$$

so the time derivative of Eq.(B.3) yields

$$j.\dot{j} = \left(r^2\dot{\theta}\right).\left(r^2\dot{\theta}\right)\dot{} - \frac{l^2}{\sin^2\theta}\cot\theta.\dot{\theta} = 0.$$

B.2 Hamilton's Equations in Spherical Symmetry

B.2.1 Momenta definitions and the Hamiltonian

from Lagrange Eqs.(B.2):

$$\begin{aligned} p_r &= \frac{\partial L}{\partial \dot{r}} = m\dot{r} \\ p_\theta &= m\left(r^2\dot{\theta}\right) \\ p_\varphi &= m.l \end{aligned}$$

and therefore the Hamiltonian reads:

$$H = p_i\dot{r^i} - L = m\left(\dot{r}^2 + r^2\dot{\theta}^2 + r^2\sin^2\theta\dot{\varphi}^2\right) - L$$

$$\Longrightarrow H = \frac{1}{2}\left(\frac{p_r^2}{m} + \frac{p_\theta^2}{mr^2} + \frac{p_\varphi^2}{mr^2\sin^2\theta}\right) + m\Phi.$$

B.2.2 Hamilton's equations

The Hamilton's equations are then giving back Lagrange's equations plus the momenta definitions:

$$\begin{aligned} \frac{\partial H}{\partial r} &= -\frac{\frac{p_\theta^2}{m} + \frac{p_\varphi^2}{m\sin^2\theta}}{r^3} + m\frac{\partial\Phi}{\partial r} = -\dot{p_r} \\ \frac{\partial H}{\partial p_r} &= \frac{p_r^2}{m} = \dot{r} \\ \frac{\partial H}{\partial\theta} = -\frac{p_\varphi^2}{mr^2\sin^2\theta}\cot\theta &= -\frac{m.l^2}{r^2\sin^2\theta}\cot\theta = -\dot{p_\theta}\ . \\ \frac{\partial H}{\partial p_\theta} &= \frac{p_\theta}{mr^2} = \dot{\theta} \\ \frac{\partial H}{\partial\varphi} &= 0 = -\dot{p_\varphi} \\ \frac{\partial H}{\partial p_\varphi} &= \frac{p_\varphi}{mr^2\sin^2\theta} = \dot{\varphi} \end{aligned} \tag{B.5}$$

Defining the angular momentum again and using Eqs.(B.5:4,6)

$$j^2 = r^2\left(\left(r\dot{\theta}\right)^2 + \left(r\sin\theta\dot{\varphi}\right)^2\right) = r^4\frac{p_\theta^2}{m^2r^4} + \left(r^2\sin\theta\right)^2\frac{p_\varphi^2}{m^2(r^2\sin^2\theta)^2} = \frac{p_\theta^2}{m^2} + \frac{p_\varphi^2}{m^2\sin^2\theta} \tag{B.6}$$

So using Eqs.(B.5:1) and (B.6) one can get back Eq.(B.2:1), Eqs.(B.5:3,4) yielding Eq.(B.2:2), or more exactly a combination of that and Eq.(B.4) and Eqs.(B.5:5,6) reproduce Eq.(B.2:3). Eq.(B.6) also allows to write the Hamiltonian in the form:

$$H = \frac{1}{2}\left(\frac{p_r^2}{m} + \frac{m.j^2}{r^2}\right) + m\Phi. \tag{B.7}$$

Appendix C

Lagrangian indices and the Lagrangian treatment of the system

In our implementations of the SSIM, the spherical system of mass distribution is treated in Lagrangian coordinates, that is to say coordinates independent of the material described, designating the instantaneous positions of each elementary part of the material described. This is to be opposed to Eulerian coordinates which are a canvas filling the whole available space and allowing for a fluid, or field, description of the material's physical properties, such as position, velocities, etc..., within this available space. In our case, the SSIM is described in terms of Lagrangian elementary mass shells.

The Lagrangian index values are labeling shells throughout the entire simulation. They are established initially by ordering the shells according to their initial radius: indexing of quantity Q (where n is the total number of shells used in the code) reads

$$Q(i),\ at\ T=0\ such\ as\ \forall i,j \in |[1;n]|\ X(i)_{T=0} < X(j)_{T=0} \Rightarrow i < j,$$

which means for $Q = X$ that

$$X(1) \leq X(2) \leq \cdots \leq X(i) \leq \cdots \leq X(n).$$

Intermediate times need then to be reordered according to the new positions of the shells. This generates a *new set of indices* that are related to the Lagrangian indices by the function called *indx* : that yields an additional indexing scheme for any physical quantity according to

$$Q(indx(i)),\ at\ T\ such\ as\ \forall i,j \in |[1;n]|\ X(indx(i))_T < X(indx(j))_T \Rightarrow i < j,$$

where $indx(i)$ is the Lagrangian index value of the i^{th} shell in the radial ordering existing at T. Again for $Q = X$, that translates into

$$X(indx(1)) \leq X(indx(2)) \leq \cdots \leq X(indx(i)) \leq \cdots \leq X(indx(n)).$$

Appendix D

Echoes in the overdensity Monte Carlo map

D.1 Definitions

The mass ratio is noted M for this appendix. the density ratio is noted D. The ratio noted *Pert* will be called A. The mass and volume of the core at that time are noted M_C and V_C. The average core density is then $\langle\rho\rangle_C = \frac{M_C}{V_C}$ The total mass of the overdensity is M_{OD}, that of the added mass on it is δM_{OD}, while the background is M_{BG}. This allows for M_{OD} to be written in a simple way:

$$M_{OD} = (1+A)M_{BG}.$$

We assume a power law density with rational index:

$$\rho = \rho_0 x^{-k},$$

so the mass of the background halo can be written as

$$M_{BG} = \int_{x_{begin}}^{x_{end}} \rho x^2 dx = \rho_0 \frac{x_{end}^{3-k} - x_{begin}^{3-k}}{3-k}.$$

D.2 Fixing a case : D is constant

Thus, maintaining D and A constant, will still allow for freedom on M. The number of possible choice of M will tell if there is one, many or no system satisfying those conditions. In fact, the freedom on M transfers to a freedom on x_{end} in our notations. We will simplify them by noting x instead of x_{end}.

The condition on the density then yields:

$$D = M\frac{3V_C}{x^3 - x_{begin}^3} = cst$$

$$\Leftrightarrow D(x^3 - x_{begin}^3) = 3\rho_0\frac{(1+A)}{\langle\rho\rangle_C}\frac{(x^{3-k} - x_{begin}^{3-k})}{3-k}. \tag{D.1}$$

This latest equation admits at least one trivial root: $x_{end} = x_{begin}$, but that is not a retainable value for creating an overdensity, because then $M_{OD} = (1+A)M_{BG} = (1+A)\rho_0\frac{x_{end}^{3-k} - x_{begin}^{3-k}}{3-k} = 0$. Instead by assuming there exist at least another root, one can rewrite Eq.(D.1) into

$$\left(\frac{D(x^3 - x_{begin}^3)}{(1+A)}\frac{\langle\rho\rangle_C}{\rho_0}\frac{3-k}{3} + x_{begin}^{3-k}\right)^p = x^{p(3-k)}.$$

Depending on the rationality of k, there exist one lowest integer p which allows the previous equation to lead to a polynomial, accepting an integer number of roots. At most, $\max(3p, kp)$ roots (degree of the polynomial if $3-k > 0$ or $3-k < 0$), therefore the possibility of $\max(3p, kp) - 1$ solution bands. Here we see two bands, that could correspond to k integer less than 3 (then p=1) which yields 2 solution bands.

Appendix E

Self-Similar Dynamical Time Calculation

Considering the SSIM mass distribution at a given radius, the self-similar time it takes for a test particle to free fall from rest into the centre when the SSIM mass distribution is replaced by a constant average density model of the mass under the test particle is called the self-similar dynamical time.

E.1 Equations of motion

We start from the SSIM equations of motion: following Eq.(3.62) without angular momentum, noting with a dot differentiation with respect to self-similar time

$$\begin{cases} \dot{Y} = -\frac{M}{X^2} + (1-\delta)Y \\ \dot{X} = Y - \delta X \end{cases} \Leftrightarrow \begin{cases} \dot{Y} = \ddot{X} + \delta\dot{X} \\ \Rightarrow \ddot{X} + \delta\dot{X} + \frac{M}{X^2} + (\delta - 1)\left[\dot{X} + \delta X\right] = 0 \end{cases} . \tag{E.1}$$

The Poisson equation is replaced by the constant self-similar density approximation, settled by the test particle's initial radius, noted X_{Ce}

$$M = \rho_{Ce} X^3 \; where \; M_{Ce} = \rho_{Ce} X_{Ce}^3. \tag{E.2}$$

Thus, combining Eqs.(E.1) and (E.2), we obtain a linear second order ordinary differential equation for the test particle's radius as a function of time

$$\ddot{X} + (2\delta - 1)\dot{X} + \left[(\delta - 1)\,\delta + \rho_{Ce}\right] X = 0. \tag{E.3}$$

E.2 Solutions

Depending on the value of the self-similar density, Eq.(E.3) admits three types of solutions: using the notation $\Omega = -(\delta - \frac{1}{2})$, $\omega = \sqrt{|\rho_{Ce} - \frac{1}{4}|}$, the convention $i = \sqrt{-1}$, and the constants of integration X_1, X_2, for the general expressions, or A_i, B_i, with $i \in [1;3]$ for the detailed expressions, the solutions can be written as

$$\begin{array}{ll} X = X_1 e^{\Omega T} e^{\sqrt{-(\rho_{Ce}-\frac{1}{4})}T} + X_2 e^{\Omega T} e^{-\sqrt{-(\rho_{Ce}-\frac{1}{4})}T} & for\ \rho_{Ce} \neq \frac{1}{4} \\ X = X_1 e^{\Omega T}(1 + X_2 T) & for\ \rho_{Ce} = \frac{1}{4} \end{array} .$$

They also can be presented in the more practical form, detailing the three types of solutions

$$\begin{array}{ll} \bullet X = A_1 e^{\Omega T} \cos\omega(T + B_1) & for\ \rho_{Ce} > \frac{1}{4} \\ \bullet X = A_2 e^{\Omega T}(1 + B_2 T) & for\ \rho_{Ce} = \frac{1}{4} \\ \bullet X = A_3 e^{\Omega T}(\cosh\omega T + B_3 \sinh\omega T) & for\ \rho_{Ce} = \frac{1}{4} \end{array} . \qquad \text{(E.4)}$$

In the case of the evaluation of the self-similar dynamical time, the initial conditions are used to settle down the values of the constant of integration. They are given by imposing the definition of free fall from the test particle's initial radius:

$$\begin{array}{c} X(T = T_{Ce}) = X_{Ce} \ , \\ Y(T = T_{Ce}) = 0 \end{array}$$

which translates, through the expressions for X and its first derivative in T found in Eqs.(E.4) and (E.1), into three cases by

$$\begin{array}{ll} X_{Ce} = A_1 e^{\Omega T_{Ce}} \cos\omega(T_{Ce} + B_1) & X_{Ce} = A_2 e^{\Omega T_{Ce}}(1 + B_2 T_{Ce}) \ , \\ -\delta X_{Ce} = X_{Ce} - \omega X_{Ce} \tan\omega(T_{Ce} + B_1) & -\delta X_{Ce} = X_{Ce} + B_2 \frac{X_{Ce}}{1 + B_2 T_{Ce}} \\ for\ \rho_{Ce} > \frac{1}{4} & for\ \rho_{Ce} = \frac{1}{4} \end{array}$$

$$\begin{array}{l} X_{Ce} = A_3 e^{\Omega T_{Ce}}(\cosh\omega T_{Ce} + B_3 \sinh\omega T_{Ce}) \ . \\ -\delta X_{Ce} = X_{Ce} + \omega X_{Ce} \frac{\tanh\omega T_{Ce} + B_3}{1 + B_3 \tanh\omega T_{Ce}} \\ for\ \rho_{Ce} < \frac{1}{4} \end{array} \qquad \text{(E.5)}$$

E.3 Dynamical times

Armed with the general solutions Eqs.(E.4), the definition of dynamical time leads us to find the first time after T_{Ce} at which the test particle following one of the solutions reach the centre of the halo, namely $X = 0$. That leads to the three solution for the time

of collapse to the centre:

$$\begin{aligned} T_{final} &= \tfrac{\pi}{2\omega} - B_1 && for\ \rho_{Ce} > \tfrac{1}{4}\ , \\ T_{final} &= -\tfrac{1}{B_2} && for\ \rho_{Ce} = \tfrac{1}{4} \\ T_{final} &= -\tfrac{\operatorname{argtanh}\frac{1}{B_3}}{\omega} && for\ \rho_{Ce} < \tfrac{1}{4} \end{aligned}$$

which leads, after some calculations using the initial conditions in Eqs.(E.5) for the time derivative of X (and in the third case using the logarithmic definition of argtanh and the exponential definition of tanh), to the dynamical time as defined earlier by $T_{Dynamical} = \Delta T = T_{final} - T_{Ce}$, for the three cases

$$\begin{aligned} T_{Dynamical} &= \tfrac{\frac{\pi}{2} - \arctan(\frac{\delta+1}{\omega})}{\omega} && for\ \rho_{Ce} > \tfrac{1}{4} \\ T_{Dynamical} &= \tfrac{1}{\delta+1} && for\ \rho_{Ce} = \tfrac{1}{4} \\ T_{Dynamical} &= \tfrac{\ln\left(\frac{\delta+1+\omega}{\delta+1-\omega}\right)}{2\omega} && for\ \rho_{Ce} < \tfrac{1}{4} \end{aligned} \tag{E.6}$$

Appendix F

Semi-Analytical set up of an overdensity on the SSIM

F.1 Initial situation of the core

The criterion retained to decide when to stop the preliminary evolution of the halo was to choose a given mass fraction of the core compared to the total halo simulated $Mfcore$. The preliminary simulation was stopped when that mass fraction was reached by the system defined by the self-similar core.

F.1.1 Gravitational core boundary

The definition of the self-similar system (or core) is given by the Lagrangian index of the last particle to enter the core (see Eq.(4.2)). Gravitationally speaking, though, all the mass present inside the largest shell of the core is contributing to the dynamics of the core. Therefore a way of defining the acting mass of the core is through the Lagrangian index of the outermost shell belonging to the core: using the core definition provided by Eq.(4.2), and establishing the bijection between Lagrangian indices and radially ordered numbering of the shells, noted $indx : i_{radially\ ordered} \longmapsto indx(i_{radially\ ordered}) = i_{lagrangian}$, the Lagrangian index of the outermost core shell is given by

$$i_{max}(icore) = indx(\sup\{i | indx(i) \leq i_{core}\}).$$

This is illustrated in figure 5.13.

F.1.2 Decision test

Then the decision that the core is evolved enough to lay the overdensity perturbation is made by comparing the mass inside shell i_{max} to the prescribed mass for the core. This prescribed mass is computed by multiplying the prescribed mass fraction of core versus halo $Mfcore$ by the total mass of the halo. That prescribed mass, when bracketed by the mass of shells inside i_{max} and that inside the shell immediately above i_{max}, triggers the recording of quantities to be transmitted to the next step and the pause in the simulation, to be resumed after laying the overdense outer shells. That condition reads

$$\left.\begin{array}{c} iM(i_{max}) \leq Mfcore.iM(indx(n)) \\ iM(i_{max}) + mass(indx(indx^{-1}(i_{max}) + 1)) > Mfcore.iM(indx(n)) \end{array}\right\}.$$

$$\Rightarrow T = T_{end}; i_{core} = i_{core0}$$

It translates on figure 5.13 into the time at which the dashed line of the prescribed core mass falls under the dotted line of the radial core boundary.

F.1.3 Transmission to next step

All the physical parameters of the halo are then recorded in the radial order yielded at overdensity laying time:

recording of X, Y, Mass, initial energies as a function of shell radial order will follow the pattern (A stands for any physical quantity, say X)

$$A_{recorded}(i) = A(indx(i)).$$

Time will also be kept for restarting the run with same conditions. Eventually recording of the core Lagrangian index at that time, i_{core0}, will avoid unnecessary recalculations.

F.1.4 Extending the halo

In the case of a constant shell spacing, it was necessary to extend the halo radius, without changing the system in order to add time to the infall period and extension to the halo. This was necessary so as to embed overdensities completely inside the halo when otherwise they were too extended compared to the halo boundary. This was done by ensuring that the definitions of the state of the core at overdensity laying time and of the position of the beginning of the overdensity region would remain the same.

At constant shell spacing, extending the halo means to add shells on the outside. If the initial total radius of the simulated halo shifts from r_1 to r_2, then correspondingly,

must the number of shells n_1 increase to n_2, keeping the intershell spacing constant:

$$\frac{r_1}{n_1} = \Delta r_1 = \Delta r_2 = \frac{r_2}{n_2} \Rightarrow \frac{r_2}{r_1} = \frac{n_2}{n_1} = k \Rightarrow \begin{cases} r_2 = k.r_1 \\ n_2 = k.n_1 \end{cases}.$$

Keeping the same definitions for the core at laying and inferior range of the overdensity involves modifying the ratios Mfcore (decision test relative mass of the core) and MfBump (relative mass fraction for the laying of the inner boundary of the added overdensity). Since at initial time the mass profile behaves like

$$M \propto r^{3-\epsilon} \Rightarrow M_{total_2} = M_{total_1} k^{3-\epsilon}$$

$$\Rightarrow \begin{cases} Mfcore_2 = \frac{M_{core}}{M_{total_2}} = Mfcore_1 k^{\epsilon-3} \\ MfBump_2 = \frac{M_{halo\ under\ OD}}{M_{total_2}} = MfBump_1 k^{\epsilon-3} \end{cases}.$$

F.2 Placement and parameterisation of the overdensity

At first all physical quantity are retrieved from the prerun into temporary storages X(i),Y(i),mass(i) and initial energies, and we begin with the core defined by $i_{core} = i_{core0}$.

F.2.1 Initial situation of inferior shell of overdensity

We define the position of the first shell of the overdensity in the radius-ordered space. The position of this shell is defined by prescribing an initial mass fraction out of the total halo. This in turns sets the amount of mass of the halo which should lie underneath this first overdensity shell in a similar way as was defined the decision test core mass:

$$\left.\begin{array}{c} iM(i) \leq Mfbump.iM(n) \\ iM(i+1) \geq Mfbump.iM(n) \end{array}\right\} \Rightarrow i_{begin} = i.$$

There is no need to reorder the shells with radius since their new Lagrangian indexing after the prerun is already ordered in radius at the beginning of the overdensity run.

F.2.2 Corresponding superior shell

To circumscribe the superior shell of the overdense region in order to add a gauβian overdensity on top of the preexisting halo, one has to define two fractional quantities. The mass ratio of the overdensity with respect to the core of the halo is

$$M_{ratio} = \frac{Mass\ of\ overdensity\ region}{Mass\ of\ core} = \frac{iM(i_{end}+1) - iM(i_{begin})}{iM(i_{core0})}.$$

The average density ratio between these same entities reads

$$D_{ratio} = \frac{\langle\rho\rangle_{overdensity}}{\langle\rho\rangle_{core}}.$$

Of course these two ratios are related:

$$D_{ratio} = \frac{\langle\rho\rangle_{overdensity}}{\langle\rho\rangle_{core}} = \frac{\frac{M_{overdensity}}{V_{overdensity}}}{\frac{M_{core}}{V_{core}}} = M_{ratio} \cdot \frac{V_{core}}{V_{overdensity}}.$$

Using the expressions for those two volumes, one can invert $V_{overdensity}$ to get the radius of the last shell satisfying those two constraints given the position of the first shell:

$$x_1 = x(i_{begin}) \left(\frac{M_{ratio}}{D_{ratio}} \left(\frac{x(i_{core0})}{x(i_{begin})} \right)^3 + 1 \right)^{\frac{1}{3}}.$$

One can then define the index of the superior shell of the overdensity in the old halo radial hierarchy as that of the shell immediately under the radius x_1:

$$\left.\begin{array}{c} x(i) \leq x_1 \\ x(i+1) > x_1 \end{array}\right\} \Rightarrow i_{end} = i$$

F.2.3 Mass profile parameters

To establish the gauβian overdensity distribution on top of the original halo, we have to add the two densities together. Moreover we want to increase the mass resolution over the range of the overdensity by subdividing the original shell distribution into smaller, lighter shells (see figure 5.14). Combining these constraints, it was simpler to model the original halo mass profile with second degree polynomial interpolations between the boundaries of each shell included within the two overdensity boundary shells. This is done for each shell by constraining the polynomial parameters from the original values of the halo. The densities at the edge of each original shell region and the mass of the original shell are evaluated and used to set up the third order linear system for the shell's polynomial coefficients. They are then used to calculate intermediate densities at new shells' subdivisions which are integrated to yield the new shells' masses.

Because the mass of one original halo shell, which represents the volume between radii x_b and x_e, is calculated according to

$$massShell = \int_{x_b}^{x_e} \rho x^2 dx,$$

the expressions for the densities at the edges, computed according to the convention from section 4.5.3, and for the mass reads, in the calculations adopted here where the density is a second degree polynomial,

$$\begin{aligned} \rho_{0b} &= \rho(x_b) = a_2 x_b^2 + a_1 x_b + a_0 \\ \rho_{0e} &= \rho(x_e) = a_2 x_e^2 + a_1 x_e + a_0 \\ massShell &= a_2 \frac{x_e^5 - x_b^5}{5} + a_1 \frac{x_e^4 - x_b^4}{4} + a_0 \frac{x_e^3 - x_b^3}{3} \end{aligned} .$$

This linear system was solved using the LU decomposition with partial pivoting and row interchanges routine DGESV from the open source package LAPACK. Thus we used the output computed coefficients so as to model the background density over the original halo shell as

$$\rho_{background\ halo}(x) = a_2 x^2 + a_1 x + a_0,$$

and the background original halo mass profile, only valid over that original halo shell defining the coefficients, as

$$iMass_{background\ halo}(x) = a_2 \frac{x^5}{5} + a_1 \frac{x^4}{4} + a_0 \frac{x^3}{3} + cst. \tag{F.1}$$

Then we model the overdensity by a gauβian of the form

$$\rho_{overdensity} = \rho_0 e^{-\frac{(X - X_c)^2}{\sigma^2}}, \tag{F.2}$$

with characteristics as follow: the gauβian is chosen to be centered on a radial barycentre of its boundaries

$$x_c = w.x_1 + (1 - w)x(i_{begin}),$$

(we chose to keep the free weight $w = \frac{1}{2}$ in the simulations) with the radial range spanned by the overdensity

$$Y_0 = x_1 - x(i_{begin}).$$

Its radial dispersion is defined as

$$\sigma = \frac{qY_0}{n_1} \tag{F.3}$$

where q is the minimal weight, or fractional radial distance to the edge of the overdensity, defined as

$$q = \inf(w, 1 - w), \tag{F.4}$$

so that n_1 represents the smaller integer number of dispersion length separating the peak density at x_c and one of the edges of the radial span of the overdensity. From the mass of the gauβian overdensity defined, for the added perturbation part, in Eq.(F.2):

$$\delta M_{OD} = \int_{x(i_{begin})}^{x(i_{end})} \rho_0 e^{-\frac{(X - X_c)^2}{\sigma^2}} X^2 dX \simeq \int_{-\infty}^{+\infty} \rho_0 e^{-\frac{(X - X_c)^2}{\sigma^2}} X^2 dX,$$

the prescribed total mass of the overdensity allows the peak central density to be defined. That mass can be calculated using the prescribed mass ratio on one hand, and combining the overdensity region's original halo mass with the mass of the gauβian overdensity on the other hand, yielding an expression for the peak density:

$$M_{OD} = M_{old\ halo} + \delta M_{OD} = M_{ratio} iM(i_{core0}),$$

with the background mass measured on the final mass distribution before laying the overdensity

$$M_{old\ halo} = iM(I_{end}) - iM(I_{begin} - 1),$$

(recall that for shells which have not fallen into the core, the Lagrangian index is equal to the radial ordering) and the perturbation mass approximated by the infinite gauβian integral

$$\delta M_{OD} \simeq \rho_0 \sigma \int_{\mathbb{R}} e^{-x^2} (\sigma x + x_c)^2 \, dx = \rho_0 \sigma \sqrt{\pi} \left(\frac{\sigma^2}{2} + x_c^2 \right).$$

The density peak is then chosen as

$$\rho_0 = \frac{M_{ratio} iM(i_{core0}) - M_{old\ halo}}{\sigma \sqrt{\pi} \left(\frac{\sigma^2}{2} + x_c^2 \right)}.$$

Of course since we are interested in adding to the halo mass over the range of the overdensity region, a negative ρ_0 just means that the interplay between M_{ratio} and D_{ratio} led to a negative overdensity "added" mass, which will have to be rejected and a new set of parameters established.

The approximation made in the mass calculation is explicited by a change of variables

$$\delta M_{OD} = \rho_0 \sigma \int_{-wY_0/\sigma}^{(1-w)Y_0/\sigma} e^{-x^2} (\sigma x + x_c)^2 dx \simeq \rho_0 \sigma \int_{\mathbb{R}} e^{-x^2} (\sigma x + x_c)^2 \, dx.$$

Writing $f(X) = e^{-x^2}$ and using the definitions of Eqs.(F.4) and (F.3), the approximation made corresponds to keeping the edges of the gauβian as flat as possible:

$$\left| f' \left(q \frac{Y_0}{\sigma} \right) \right| = \left| -2xe^{-x^2} \Big|_{x = q\frac{Y_0}{\sigma}} \right| \ll 1 \Leftrightarrow 2.n_1 e^{-n_1^2} \ll 1. \tag{F.5}$$

It is ensured in the definition of the value of n_1. This value is constrained by the choice of a number k_1 such that $k_1 \gg 1$, so that the condition of Eq.(F.5) are satisfied for values of n_1 larger or equal to the choice we make:

$$n_1 = \sup \left\{ n | \frac{e^{n^2}}{n} < 2.k_1 \right\} + 1.$$

F.3 Overdensity mass profile

Using the previously defined parameters, one can calculate the new mass profile over the overdensity range in radius. An increase of the arrays size will implement the planned increase of mass definition of the overdensity region.

At first, the temporary storage variables are recorded for Lagrangian indices up to i_{begin}-1. Then the x-grid is subdivided over the range of the overdensity laying region (from i_{begin} to i_{end}).

The total number of extra shells is divided according to a radial range weighting between each old halo shells (the width of shells over the total overdensity radial width gives the fraction of shells allotted to them): the number of new shell spanning old halo shell 'i' is given by

$$n_i = int\left(\frac{x(i) - x(i_{begin}-1)}{x(i_{end}) - x(i_{begin}-1)}.N_{extra}\right) - \sum_{j=1}^{i-1} n_j.$$

Equal spacing is established between each extra shell within a given old halo shell. The new indices for the refined grid shells are noted with upper cases and calculated from the old indices as follow

$$I = i_{begin} - 1 + \sum_{j=i_{begin}}^{i-1} (n_j + 1) + k \qquad k \in |[1; n_i + 1]|.$$

From i_{begin}-1, the radial distribution of new shells follows:

$$X(i_{begin} - 1 + \sum_{j=i_{begin}}^{i-1} (n_j + 1) + k) = x(i-1) + \frac{x(i) - x(i-1)}{n_i + 1}.k \qquad k \in |[1; n_i + 1]|,$$

where the distinction made between old and new shell is reflected in the use of lower and upper cases respectively. Similarly for the distribution of velocities for new shells:

$$Y(i_{begin} - 1 + \sum_{j=i_{begin}}^{i-1} (n_j + 1) + k) = y(i-1) + \frac{y(i) - y(i-1)}{n_i + 1}.k \qquad k \in |[1; n_i + 1]|.$$

For the masses, we add on the gauβian overdensity mass to the polynomial-modeled background from Eq.(F.1)

$$Mass(I) = \delta M_{OD}(X(I)) + iMass_{background\ halo}(X(I)) - iMass_{background\ halo}(X(I-1)),$$

where the overdensity mass is calculated using a simple adaptive trapeze integration scheme: each new shell is subdivided evenly for the integration with a subdivision number

increased from 0 until the relative mass difference between the total overdensity added mass and its theoretical gauβian evaluation is negligible, in the sense that this relative mass difference is less than $1/k_1$. Thus, an optimal number of subdivision n_{sub} yields the overdensity mass for shell 'I'

$$\delta M_{OD}(X(I)) = \sum_{j=1}^{n_{sub}}$$

$$\frac{\left(x_{sub_j} - x_{sub_{j-1}}\right)}{2}\left[\left(\rho_0 e^{-\frac{(x_{sub_j}-x_c)^2}{\sigma^2}} x_{sub_j}^2\right) + \left(\rho_0 e^{-\frac{(x_{sub_{j-1}}-x_c)^2}{\sigma^2}} x_{sub_{j-1}}^2\right)\right],$$

where the subdivisions are defined by

$$x_{sub_j} = X(I-1) + \frac{X(I) - X(I-1)}{n_{sub}}.j.$$

To keep track of the overdensity in the new system we will just need to record the new beginning and ending shells' indices:

$$I_{begin} = i_{begin};\ I_{end} = i_{end} + \sum_{i=i_{begin}}^{i_{end}} n_i (= N_{extra})$$

(the last equality may not be true in practice).

For the rest of the halo, the transfer from old to new indices is straightforward:

$$\begin{aligned} X(I_{end}+i) &= x(i_{end}+i) \\ Y(I_{end}+i) &= y(i_{end}+i) \\ Mass(I_{end}+i) &= mass(i_{end}+i) \end{aligned} \quad .$$

We will resume using lower cases for the indices now that the extended halo with overdensity is established.

F.4 Accretion of the surrounding halo by the overdensity

We use the Lagrangian index for treating the overdensity separately as being contained between I_{begin} and I_{end} in Lagrangian space. The evolution of the overdensity leads to a redefinition of the edge indices.

The innermost shell is redefined starting from the original innermost shell in Lagrangian order. In Lagrangian order it is restricted to the range below the original innermost shell. Following the Lagrange Liouville stream winding towards the centre of the halo, the procedure then searches for the last radial density caustic, characterised by a vertical tangent to the phase space sheet. The new innermost shell is then defined as that just below that last radial density caustic, this time in the decreasing radius order.

The outermost shell is defined in the same way symmetrically: above the original outermost shell in Lagrangian order, and following the Lagrange Liouville stream winding towards the outermost shells of the halo. The procedure again searches for the outermost radial density caustic, characterised in the same manner as for the innermost caustic.The new outermost shell is then defined as that just above that last radial density caustic, this time in the increasing radius order. These constructive definitions of the edges of the evolved overdensity are summarised in figure 5.15.

Appendix G

Initial conditions of a collapse central mass

The set up of initial conditions for a central collapsed mass resembles closely that of the smoothed central density cusp, but admits crucial variations. In this case the central outer limit of the region initially collapsed into the black hole is set by r_{min}. The density contrast, or power law, proportionality constant is chosen so that the mass term that corresponds to the primordial density contrast is proportional to A and the scale dependence is expressed in units of r_{min} ($\frac{\delta M}{M_0} \propto A\left(\frac{r}{r_{min}}\right)^{-\epsilon}$). Thus this proportionality constant reads

$$d_0 = A.\left(\frac{r_{min}^{-\epsilon}}{3-\epsilon}\right)^{-1}.$$

G.1 Cosmological halo

G.1.1 Initial density profile

In this case, the notation for the density profile is given as

$$\rho = \rho_0(1 + d_0.r^{-\epsilon})\ r \geq r_{min}.$$

Inside of the limit radius, the density is 0, except for the singularity in the centre. In practice, we used the first shell of the halo placed at X=Y=0 to represent the collapsed mass. The second shell being placed at r_{min}.

G.1.2 Initial mass profile

If one remains outside the central region, the cumulative mass inside a given radius can be calculated as

$$iM = \int_0^r \rho r^2 dr = \rho_0 r^3 (\frac{1}{3} + \frac{d_0 r^{-\epsilon}}{3-\epsilon}) + \delta M_\bullet \qquad r \geq r_{min},$$

where $\delta M_\bullet$ is the extra mass in the black hole compared with the simple collapse of the power law density profile onto the central mass. For radii inside that central region, the mass is constant and given by

$$iM = centralMass = m_\bullet = \rho_0 r_{min}^3 (\frac{1}{3} + A) + \delta M_\bullet.$$

Apart from the black hole perturbation, the mass profile is of the same form as the one which leads to the inversion Eq.(4.18) except that iM in that equation has to be replaced by $iM - \delta M_\bullet$ and the $\Delta(r)$ function admits the new expression

$$\Delta(r) = \frac{d_0 r^{-\epsilon}}{3-\epsilon},$$

leading to the new inversion formula

$$r \simeq \left(\frac{3.iM_{halo}}{\rho_0}\right)^{\frac{1}{3}} (1 - \Delta(\left(\frac{3.iM_{halo}}{\rho_0}\right)^{\frac{1}{3}})), \tag{G.1}$$

where

$$iM_{halo} = iM - \delta M_\bullet = iM - centralMass + \rho_0 r_{min}^3 (\frac{1}{3} + A)^2)).$$

G.1.3 Shells initial masses and phase space position

Following similar methods as section 4.5.1, we will model the density distribution by Eq.(4.3) with the central shell representing the singularity in density. The continuous halo can again be implemented in three different ways. The cosmological shells still follow a Hubble flow:

$$y(i) = \frac{2}{3} x(i).$$

Then same distinction between various methods is applied from the need to use the inversion method of Eq.(G.1) and the need for an initial shell placement in the constitution of the mass profile.

Constant shell initial density

This method is also motivated by its resemblance to the cosmological concept of density fluctuation of a constant density background. We start here from central point mass and constant density equal to the background.The central mass is set as

$$mass(1) = m_1 = m_\bullet = centralMass$$

with its location defined at the origin and being stable by its position and velocity according to

$$x(1) = 0; y(1) = 0.$$

Then for the halo shells, we set the initial constant spacing with

$$x_i = r_{min} + \frac{(r_{max} - r_{min})}{n-1}(i-1).$$

The masses of the shells are filled according to a constant density: for $i \geq 2$,

$$mass(i) = m_i = \rho_0 \frac{\left((x_i)^3 - (x_{i-1})^3\right)}{3}$$

with x_{i-1}=r_{min} for i=2.

Finally, we shift the shell positions according to Eq.(G.1) to reproduce the density profile of the expected halo. The characteristics of this method are discussed in its smoothed density counterpart section (4.5.1).

Constant shell initial spacing

As for the previous smooth density set up, this method doesn't require mass inversion. The first shell represents the black hole in the same fashion as stated previously, in the constant shell initial density sub-paragraph. The rest of the shells are computed similarly as for the smoothed density, starting at r_{min} instead of 0: constant spacing for the shells yields for $i \geq 2$

$$x(i) = x_i = r_{min} + \frac{(r_{max} - r_{min})}{n-1}(i-1).$$

We again include the central point mass as our first shell:

$$mass(1) = m_1 = m_\bullet = centralMass.$$

Note the first shell, the central mass, is sitting still in the centre of the halo:

$$x(1) = 0; y(1) = 0.$$

The masses are then set to follow the expected density profile:

$$mass(i) = m_i = \rho_0 \left[\frac{\left((x_i)^3 - (x_{i-1})^3\right)}{3} + d_0 \frac{\left((x_i)^{3-\epsilon} - (x_{i-1})^{3-\epsilon}\right)}{3-\epsilon} \right]$$

with x_{i-1}=r_{min} for i=2.

Constant shell mass

This time, the inversion of the mass profile is needed, but the expression for the masses is trivial: again, the first shell is our central point mass, then all other shells have same mass, as required

$$mass(1) = m_1 = m_\bullet = centralMass$$

$$x(1) = 0; y(1) = 0$$

$$mass(i) = m_i \equiv smass$$

Then the positions of the shells are computed according to the approximation of Eq.(G.1).

G.2 Non-cosmological test of the dynamics

Once more, to allow for the possibility of a test using Henriksen & Widrow's results, given a special central mass so that $\delta M_\bullet = 0$, the black hole configuration was allowed for a pure power law initial density and 0 initial velocities.

G.2.1 Initial density profile

Using the same terms definitions as previously, the density profile then reads

$$\rho = \rho_0 d_0 . r^{-\epsilon} \; r \geq r_{min}.$$

For the density inside r_{min}, it is null everywhere except for the singular centre, holding the black hole mass.

G.2.2 Initial mass profile

Following the given density profile,

$$iM = \int_0^r \rho r^2 dr = \rho_0 r^3 (\frac{d_0 r^{-\epsilon}}{3-\epsilon}) + \delta M_\bullet \qquad r \geq r_{min},$$

whereas when the mass is measured inside r_{min},

$$iM = centralMass = m_* = \rho_0 r_{min}^3 A + \delta M_*.$$

Because of the use of constant shell spacing to create the initial shells, though possible in an exact fashion, we won't need to invert the mass profile.

G.2.3 Shells initial masses and phase space position

The first shell is still our central point mass:

$$mass(1) = m_1 = m_* = centralMass$$

$$x(1) = 0; y(1) = 0,$$

and we assume no flow

$$y(i) = 0.$$

Constant shell spacing

This is again the simplest choice of implementation. Shells are distributed evenly along the radial axis, starting from r_{min}:

$$x(i) = x_i = r_{min} + \frac{(r_{max} - r_{min})}{n-1}(i-1)$$

the masses then follow in order to form the prescribed density profile:

$$mass(i) = m_i = \rho_0 d_0 \frac{\left((x_i)^{3-\epsilon} - (x_{i-1})^{3-\epsilon}\right)}{3-\epsilon}$$

with x_{i-1}=r_{min} for i=2.

G.3 Density definition by shells and their positions

Because of the special status of the first central point mass shell, the definitions are slightly altered compared with the smoothed central density case.Moreover, the handling of the halo is simplified by considering that the innermost shell's inside boundary shifts immediately from r_{min} to 0 as soon as the halo is evolved. Otherwise a complex account of the evolution of this inside boundary would have been necessary, which was not in the scope of this test configuration.

G.3.1 Density contrast with background

The definition for the mass taken into account for the calculation of the density around shell "i", smoothing over a number *smooth* of shells, is now (E(n) still being the integer part of n):

$$MASS_i = \sum_{i=b_{inf}=\max(i+E(smooth/2)-smooth+1,2)}^{b_{sup}=\min(i+E(smooth/2),n)} m_i.$$

The definition of the volume of those shells is also altered ($t_{now} = 0$ corresponds to the initial time, the only one for which the region between 0 and r_{min} is considered empty):

$$VOLUME_i = x^3_{b_{sup}} - \left\{ \begin{array}{cc} x_{b_{inf}-1} & if\ b_{inf} \neq 2 \\ r^3_{min} & if\ b_{inf} = 2\ and\ t_{now} = 0 \\ 0 & otherwise \end{array} \right\}.$$

Again, the density contrast reads:

$$\frac{\delta\rho}{\rho_0}(i) = \frac{MASS_i}{\frac{\rho_0}{3}(VOLUME_i)} - 1.$$

G.3.2 Relative density without background

In the non-cosmological case, the relative density to an equivalent Einstein-de Sitter background is using the previous definitions of mass and volume to get:

$$\frac{\rho}{\rho_0}(i) = \frac{MASS_i}{\frac{\rho_0}{3}(VOLUME_i)}.$$

Appendix H

Real numbers and units(?)

Assuming the mapping of our model to the DM halo of the Milky Way, we can take approximates values to fit our halo at the end of the self-similar phase and the beginning of the virialised phase (at a self-similar time noted T_e).

H.1 Real numbers from the Milky Way

We recall (e.g. from Wilkinson & Evans 1999 [98], and from Binney & Merrifield 1998 [108], figure 10.36 for the estimate of the velocity dispersion) Milky Way approximate values for the halo, the values used in astronomy for the units of various quantities and we use standard units for the values of fundamental constants:

$$\begin{gathered} M_{MW} \simeq 2.10^{12} M_{\odot} \\ R_{MW} \simeq 200kpc \\ \sigma_V = \sqrt{\langle v^2 \rangle} \simeq 200km.s^{-1} \\ G = 6.67 \cdot 10^{-11} m^3 kg^{-1} s^{-2} \\ c \simeq 3.10^8 m.s^{-2} \\ 1M_{\odot} = 1.99 \cdot 10^{30} kg \\ 1pc = 3.086 \cdot 10^{16} m \end{gathered} .$$

The value of R_{MW} should be compared with, for instance, our distance to the Andromeda galaxy, which is located at about 700kpc from us. A typical black hole at the centre of a generic halo could range over $M_{\bullet} \simeq 10^8 - 10^9 M_{\odot}$. Even though there is no real evidence for the Milky Way to contain a central black hole of mass larger than $10^6 M_{\odot}$, we are more interested in generic and qualitative behaviours of the SSIM with a black hole. Because of the assumptions made in the model, masses, densities, lengths and times are measured in modified units. Masses are measured in units of $G.U_m$ because, in the dynamical equations (e.g Eq.(3.62)), gravity is set with G=1. Densities are measured in units of

$4\pi G.U_m.U_{Le}^{-3}$, where U_{Le} is the unit of length adopted in the simulation at the time of density measurement, because of our definition of the background de Sitter density (Eq.(3.64)). Lengths are measured in units of $U_X = U_r e^{-\delta T}$, which shows how it depends on time, the self-similar time being unitless, and derives directly from the rescaling of length in self-similar variables (Eq.(3.26)). Finally, non-self-similar time is measured in units of the initial time, which is set to 1 in the simulations. It can be taken as the epoch of recombination (around $3 \times 10^5 years$) to stand for the end of the dark matter fluctuation linear growth phase, also called Zel'Dovich approximation era. On another hand, velocity units are setting a natural time unit when combined with length units.

H.2 Units from the simulations

In what follows, units of a given measurement, say *Measurement*, are represented by the corresponding unit symbol , say $U_{Measurement}$. For mass, radial length and radial velocity units, we have adopted the convention that units within the simulations are represented by their name in lower case and their expression within the framework of the Milky Way-type dark halo will be in upper case: masses in the simulations are in U_m and in the real scales are in U_M (or U_{Gm} and U_{GM} when considering gravitating mass). Radial lengths are expressed in units U_r in the simulations and U_R respectively, and radial velocities are in units of U_{v_r} in simulations whereas they are in U_V in MKS units. The model at virialisation (at $T = T_e$) can be defined in terms of its total mass, its radial velocity dispersion (thanks to discussions and help from J.Stil [109]) and its maximum radius, as well as the respective translations between simulation units and real units for radii and radial velocities. Its total mass sets the mass resolution, or mass of one shell in the constant mass framework, here given for 10 000 shells. Thus its values from simulations are given by

$$
\begin{aligned}
Gm_{halo} &= 200 U_{Gm} \\
Gm_{1shell} &= 2.10^{-2} U_{Gm} \\
\sigma_Y = \sqrt{\langle Y^2 \rangle} &= 1.27.10^{-1} U_Y \\
v_r = Y e^{\nu T} &= Y e^{(\delta - \alpha)T} \\
X_{max} &= 3.10^{-2} U_X \\
r &= X e^{\delta T} U_r
\end{aligned}
$$

The presence of G in the mass expressions comes from the fact that G is taken to be 1 for the calculations, but is still present, for instance in the definition of the gravitational acceleration. We will suppress it eventually in the last expressions involving simulated mass. From there on, one can determine mass units, length units and velocity units, keeping in mind that the latter two, because of rescaling will depend on the self-similarity

class as well.

H.3 Determination of Dimensional units

H.3.1 Mass scales and resolutions

The mass scale is straightforward to compute (we use capitals for real units and lower cases for simulation units, the simulation units being set to 1 according to the point of reference taken)

$$\frac{Gm_{halo}}{U_{Gm}} = 200 = \frac{GM_{MW}}{U_{GM}} = \frac{M_{MW}}{U_M} \Rightarrow$$
$$U_M = M_{MW}\frac{U_{Gm}}{GM_{sim}} = \frac{M_{MW}}{200} = 10^{10}M_{\odot} \ ,$$

and the mass resolution is then

$$M_{1shell} = m_{1shell}U_M = 2.10^8 M_{\odot},$$

which is similar to the typical mass of a dwarf galaxy, thought to be the elementary merging bricks for galaxy formation.

Using the upper range of the central black hole masses ($M_\bullet = 10^9 M_\odot$) we can find that for the simulation one can use the value of initial central black hole mass according to

$$\frac{M_{MW}}{M_\bullet} = 2.10^3 = \frac{m_{halo}}{m_\bullet} \Leftrightarrow m_\bullet = 10^{-1}.$$

H.3.2 Length scales

The length units are set by the real radius at the virialisation, but the real units correspond to non scaled radius (we use the same upper case/lower case conventions and the simulation unit real radius of 1). It can be computed similarly to the mass unit, but keeping in mind the different scalings

$$\frac{R_{MW}}{U_R} = \frac{r_{max}}{U_r} = \frac{X_{max}e^{\delta T_e}}{U_r} \Rightarrow$$
$$U_R = \frac{R_{MW}}{X_{max}e^{\delta T_e}}U_r = \frac{R_{MW}}{X_{max}}e^{-\delta T_e} = \frac{2}{3}10^4 e^{-\delta T_e}.kpc \ ,$$

the time T_e of virialisation, which is almost exactly the end of the self similar phase, depending also on the self-similar class.

H.3.3 Velocity scales

The velocity unit springs out of the velocity dispersion:

$$\frac{\sigma_V}{U_V} = \frac{\sigma_{v_r}}{U_{v_r}} = \frac{\sigma_Y e^{(\delta-\alpha)T_e}}{U_{v_r}} \Rightarrow$$
$$U_V = \frac{\sigma_V}{\sigma_Y e^{(\delta-\alpha)T_e}}U_{v_r} = \frac{\sigma_V}{\sigma_Y}e^{(\alpha-\delta)T_e} = \frac{2}{127}10^5 e^{(\alpha-\delta)T_e} km.s^{-1} \ .$$
$$\simeq 1.57 \times 10^3 e^{(\alpha-\delta)T_e} km.s^{-1}$$

H.3.4 Time scale

If we use the natural time units from the combination of velocity units with length units, its expression is then

$$U_T = \frac{U_R}{U_V} \simeq 1.31 \times 10^{17} e^{-\alpha T_\epsilon}.s \simeq 4.14 \times 10^9 e^{-\alpha T_\epsilon}.yrs \simeq 4.14 e^{-\alpha T_\epsilon} Gyrs,$$

and the formation time of the system, from primordial fluctuation to the end of the accretion phase can be computed as

$$\Delta t = U_T e^{\alpha T_\epsilon} = 4.14 \times 10^9.yrs \simeq 4.14 Gyrs,$$

which is fixed by the choice of velocity dispersion and radius of the Milky Way halo and is consistent with and of order of the age of the universe.

H.4 The scaled Schwarzschild radius

H.4.1 General expression

The Schwarzschild radius can then be derived, using the upper case notation for its real mass and the lower case for the simulation's black hole mass, and from those units following its definition in terms of the black hole mass and in terms of the simulation's value as

$$\begin{aligned} R_{Sch} &= \frac{2GM_\bullet}{c^2} = \frac{2G\frac{(Gm_\bullet)}{U_{Gm}}U_M}{c^2} \\ &= \frac{r_{Sch}}{U_r}U_R = \frac{X_{Sch}e^{\delta T}}{1}U_R \end{aligned}.$$

Now G and c are expressed in MKS units in the previous equality and the U_R and U_M units are in parsecs and $M_\odot$, so the conversion yields

$$\begin{aligned} \frac{X_{Sch}}{U_X} &= \frac{2G}{c^2}\frac{1M_\odot(kg)}{1pc(m)}\frac{(Gm_\bullet)}{U_{Gm}}\frac{U_M}{U_R}e^{-\delta T} \\ &= 9.6 \cdot 10^{-4}\frac{e^{-\delta T}}{U_R}m_\bullet = \frac{X_{Sch}}{1} \end{aligned},$$

which reads for the expression found for U_R

$$X_{Sch} = \frac{3G}{c^2}\frac{1M_\odot(kg)}{1pc(m)}\frac{U_M}{10^7 pc}e^{-\delta(T-T_\epsilon(\delta))}m_\bullet = 1.4 \cdot 10^{-10}e^{-\delta(T-T_\epsilon(\delta))}m_\bullet. \quad \text{(H.1)}$$

Conversely, in real units the Schwarzschild radius reads

$$R_{Sch} = X_{Sch}e^{\delta T}U_R = \frac{2G}{c^2}\frac{1M_\odot(kg)}{1pc(m)}U_M m_\bullet = 9.6 \cdot 10^{-1}m_\bullet pc. \quad \text{(H.2)}$$

H.4.2 Time evolution

For a self-similar growth of the mass (recall that self-similar mass scales like $e^{(3\delta-2\alpha)T}$), this scaled radius is not constant but changes like

$$X_{Sch} \propto e^{2(\delta-\alpha)T}$$

for any self-similar class but for $\frac{\delta}{\alpha} = 1$.

H.5 Scales and self-similarity class

H.5.1 Length and velocity scales

In the main emblematic cases studied, recall that when the initial density profile goes like $\rho \propto r^{-\epsilon}$, the self-similarity class, with α chosen to be 1, is $\delta = \frac{2}{3}(1 + \frac{1}{\epsilon})$ and previous simulations teach us that $T_e(\epsilon = \frac{3}{2}) \simeq 10$ whereas $T_e(\epsilon = \frac{5}{2}) \simeq 15$. In those cases, the length and velocity units read

$$\begin{array}{lll} \epsilon = \frac{3}{2} \Rightarrow \delta = \frac{10}{9} & U_R \simeq 100pc & U_V \simeq 518\, km.s^{-1} \\ \epsilon = \frac{5}{2} \Rightarrow \delta = \frac{14}{15} & U_R \simeq 5.5pc & U_V \simeq 4\,281\, km.s^{-1} \end{array}$$

Of the two cases presented here only the shallow case ($\epsilon = \frac{3}{2}$) is consistent with a galactic halo typical velocity (the maximum available Y value being of order 0.3 in the shallow case, implying velocities of order 150 km/s), the steep case exhibiting values which are more compatible with clusters' dark haloes (with Ys of 0.6, the velocities reach 2500 km/s).

H.5.2 Scaled and real Schwarzschild radius

The scaled Schwarzschild radius becomes, at the beginning of the growth phase

$$X_{Sch}(T=0) = 1.4 \cdot 10^{-10} e^{\delta T_e(\delta)} m_\bullet.$$

so the Schwarzschild radius then reads, in real units and then in scaled units:

$$R_{Sch_{initial}} = 9.6 \cdot 10^{-1} m_{\bullet_{initial}} pc$$

$$\begin{array}{ll} \epsilon = \frac{3}{2} \Rightarrow \delta = \frac{10}{9} & X_{Sch_{initial}} = 9.4 \cdot 10^{-6} m_{\bullet_{initial}} \\ \epsilon = \frac{5}{2} \Rightarrow \delta = \frac{14}{15} & X_{Sch_{initial}} = 1.6 \cdot 10^{-4} m_{\bullet_{initial}} \end{array}$$

It becomes at the end of the infall phase, because of the length scaling,

$$X_{Sch}(T = T_e(\delta)) = 1.4 \cdot 10^{-10} m_\bullet e^{\delta \cdot 0} pc,$$

so it then reads, in real units and then in scaled units:

$$R_{Sch_{final}} = 9.6 \cdot 10^{-1} m_{\bullet_{final}} pc$$
$$X_{Sch_{final}} = 1.4 \cdot 10^{-10} m_{\bullet_{final}}.$$

H.5.3 Minimising the time evolution of X_{Sch}

The latter value for the scaled Schwarzschild radius is the same as the initial value only for $m_\bullet \propto e^{\delta T}$, that is growing self-similarly, and with $\frac{\delta}{\alpha} = 1$. For this reason, instead of the the $\epsilon = \frac{3}{2}$ and $\frac{5}{2}$ cases used as typical cases otherwise, this study focused on values of the initial density contrast indices around 2 (namely $\epsilon = 1.9$ and 2.1). This is so because these values lead to self-similarity classes as close to the conditions for which the self-similar growth of the black hole mass becomes stationary in scaled radius. The corresponding self-similar mass evolution (growth), with self-similar time, is then given by $\mu = 3\delta - 2 = \frac{2}{\epsilon}$ in the frame where we have set $\alpha = 1$:

$$\begin{array}{ll} \epsilon = 1.9 & \mu \simeq 1.05 \\ \epsilon = 2.1 & \mu \simeq 0.95 \end{array}$$

If the mass of the black hole grows according to self-similarity ($m_\bullet \propto e^{\mu T}$) the length rescaling in X_{Sch} will translate into an evolution with time following $X_{Sch} \propto e^{2(\delta-1)T}$ characterised by the exponent index $2(\delta-1) = \frac{2}{3}\left(\frac{2}{\epsilon} - 1\right)$, so that the expected behaviour of the scaled Schwarzschild radius if the mass of the black hole grows self-similarly will be

$$\begin{array}{ll} \epsilon = 1.9 & 2(\delta - 1) \simeq +0.035 \\ \epsilon = 2.1 & 2(\delta - 1) \simeq -0.032 \end{array} \qquad \text{(H.3)}$$

which offer very little evolution compared to the expected noise in mass evolution of the black hole.

H.6 Angular momentum evaluation with real units

In order to render the PLAM commensurable, characteristic rotational velocities and the Peebles' rotation parameter will be evaluated for our model in this section.

Because of spherical symmetry, the SSIM cannot evolve angular momentum assigned to its particles. In our simulations, the form of the angular momentum profile was obtained from Dimensional and similarity arguments. But the amplitude of the profile was limited according to visible effects on the system while maintaining a central core. In order to evaluate the physical meaning of those amplitudes, the next two section will devote themselves to evaluating a rotational velocity characteristic of the profile using physical units. The last section will compute the corresponding Peebles' λ_P parameters.

H.6.1 Characteristic rotational velocity

From a given initial angular momentum profile $j^2(r)$, the corresponding rotation profile can be obtained via

$$v_\perp^2 = \frac{j^2}{r^2}.$$

In the interesting case of the 'power law' profile, the initial form of the mass profile dictates that of the angular momentum, thus of the rotation profile, in scaled variables (note that since we place ourselves at T=0, X=r and all self-similar quantities are equal to their unscaled ones):

$$v_\perp^2 = \frac{j^2}{X^2} = J^2\rho_0\left(\frac{1}{3} + \frac{\lambda}{3-\epsilon}X^{-\epsilon}\right)X^2,$$

with $\lambda = A(1-B)r_{min}^{\epsilon}$ giving the amplitude of the primordial density fluctuation. In our simulations, was taken $A = \frac{1}{2}$, $B = \frac{5\epsilon}{3(\epsilon+2)}$ in order to reproduce the inner mass of a power law with our smoothed inner cusp, $\rho_0 = \frac{2}{3}$ for an Einstein-de Sitter background and $r_{min} = 0.5$. For the shallow and steep case studied with the presence of angular momentum, the values of $\epsilon = \frac{3}{2}$ and $\epsilon = \frac{5}{2}$ for the initial density profile and $J^2 = 10^{-3}$ and $J^2 = 9.10^{-3}$ for the angular momentum profile amplitude were respectively chosen.

The characteristic rotational velocity for the rotation profile was then defined by taking the average over the bound particles, i.e. those which should end up inside the constituted system. This conditions leads to the definition of a maximum radius, at a given value of J^2, labeled X_{max}, over which the average is taken:

$$\langle v_\perp^2\rangle = \frac{\int_0^{X_{max}} v_\perp^2 dX}{\int_0^{X_{max}} dX} = J^2\rho_0\left(\frac{1}{3^2} + \frac{\lambda}{(3-\epsilon)^2}X_{max}^{-\epsilon}\right)X_{max}^2. \tag{H.4}$$

With the proper rescaling, this is equivalent to taking

$$\langle v_\perp^2\rangle = \frac{3^{\frac{2}{\epsilon}-1}}{(3-\epsilon)^{\frac{2}{\epsilon}}}v_\perp^2\left(\left(1-\frac{\epsilon}{3}\right)^{\frac{1}{\epsilon}}X_{max}\right).$$

Evaluation of X_{max}

The Einstein-de Sitter universe is marginally bound, thus taking a perturbation on it yields a distribution that is bound everywhere:

$$E = \frac{H^2X^2}{2} - \frac{M}{X} = X^2\left(\frac{2}{9} - \rho_0\left(\frac{1}{3} + \frac{\lambda}{3-\epsilon}X^{-\epsilon}\right)\right)$$

is always negative, using the model's values of $H = \frac{2}{3}$, and $\rho_0 = \frac{2}{3}$, because $\frac{2}{9\rho_0} - \frac{2}{3} = 0 < \frac{\lambda}{3-\epsilon}X^{-\epsilon}$ is always verified ($\lambda > 0, \epsilon < 3$) for any X. Adding the angular momentum,

the situation yields a value for X_{max}. Indeed the effect of j is to make shells less bound by increasing their kinetic energies with rotation. Finding the shells that remain bound proceeds from evaluating the inequality

$$E = \frac{2}{9}X^2 - \frac{M}{X} + \frac{j^2}{2X^2} = \frac{2}{9}X^2 - (1 - \frac{J^2}{2})\frac{M}{X}$$
$$= X^2\left(\frac{2}{9} - \left(1 - \frac{J^2}{2}\right)\rho_0\left(\frac{1}{3} + \frac{\lambda}{3-\epsilon}X^{-\epsilon}\right)\right) < 0 \ .$$

In the previous string of equalities, the first step comes from recognising the form of the 'power law' angular momentum profile. The solution yields the range of bound particles according to

$$X < \left(\frac{\frac{2}{9(1-\frac{J^2}{2})\rho_0} - \frac{1}{3}}{\frac{\lambda}{3-\epsilon}}\right)^{-\frac{1}{\epsilon}} = r_{min}\left(\frac{2-J^2}{(2+\epsilon)J^2}\right)^{\frac{1}{\epsilon}} = X_{max}. \qquad \text{(H.5)}$$

From this expression can be seen that X_{max} tend to infinity when $J^2 = 0$, which is the usual Einstein-de Sitter case, and $X_{max} \underset{J^2 \to 2}{\longrightarrow} 0$.

Evaluation of the characteristic rotation velocity

From Eqs.(H.4) and (H.5), one can obtain the expression

$$\langle v_\perp^2 \rangle = \frac{J^2}{6}\left(\frac{1}{9} + \frac{J^2}{3(3-\epsilon)(2-J^2)}\right)\left(\frac{2-J^2}{(2+\epsilon)J^2}\right)^{\frac{2}{\epsilon}}. \qquad \text{(H.6)}$$

Thus the characteristic rotation velocity in scaled variables which represents the amount of angular momentum present in a given model is given by

$$V_\perp = \sqrt{\langle v_\perp^2 \rangle} = \sqrt{\frac{J^2}{6}\left(\frac{1}{9} + \frac{J^2}{3(3-\epsilon)(2-J^2)}\right)}\left(\frac{2-J^2}{(2+\epsilon)J^2}\right)^{\frac{1}{\epsilon}}.$$

H.6.2 Physical characteristic rotational velocity

In order to compare the characteristic rotation of a model with more real evaluations on haloes, one has to translate the units into real ones. This is done following appendix H.3:

$$V_{\perp real} = V_\perp U_V = V_\perp \frac{2}{127} 10^5 e^{(1-\delta)T_e},$$

with T_e being the self-similar time at the end of the self-similar phase (10 in the shallow case used here, 15 in the steep one) and δ still representing the self-similar class. With the

values used in our simulations, the characteristic rotational velocities are for the shallow and steep cases respectively

$$V_{\perp real}(\epsilon = 1.5) \simeq 154 km.s^{-1}$$
$$V_{\perp real}(\epsilon = 2.5) \simeq 266 km.s^{-1} \ ,$$

which are quite reasonable.

H.6.3 Peebles' rotational support parameter (to be appendix I, G, H, or ...)

In the description of turbulence in cosmological structures, a parameter can be defined that characterises the rotational support of a given system (see Peebles 1993 [114]): if we estimate the ratio of centrifugal acceleration from the system's characteristic rotational velocity to its characteristic gravitational acceleration, we can define the rotational parameter as

$$\lambda_P^2 = \frac{a_\phi}{a_g} = \frac{\frac{v_\phi^2}{r}}{\frac{GM}{r^2}} = \frac{rv_\phi^2}{GM} = \frac{\frac{M^2 r^2 v_\phi^2}{M^2 r} \frac{GM^2}{r}}{GM} = \frac{L^2 E}{G^2 M^5}, \tag{H.7}$$

where we have used the total mass of the system M, its angular momentum L and its total energy E. In the light of previous calculations, we can link the angular momentum L to the specific angular momentum used in the model by computing the characteristic specific angular momentum of the system:$L = M \langle j^2 \rangle$. The total energy can be defined using the radius of the system X_{core} at the end of the self-similar phase T_e :

$$E = \frac{GM^2}{X_{core} e^{\delta T_e}}.$$

Putting those definitions together with the fact that the mass of the system is given by the initial mass at the last binding radius X_{max} (see section H.6.1), one can rewrite Eq.(H.7) into

$$\lambda_P^2 = \frac{M^2 \langle j^2 \rangle GM^2}{G^2 M^5 X_{core} e^{\delta T_e}} = \frac{\langle j^2 \rangle}{GM X_{core} e^{\delta T_e}}.$$

In the previous expression, our model gives the various quantities in model units, so to get the real value for the parameter we need to transfer into real units.

Expression of the model's rotation parameter

We first evaluate the operative expression of the parameter λ_P^2 in terms of the expressions given in the problem: the mass of the system and the characteristic angular momentum.

Mass of the system The expression for the mass of the system comes from the mass of the initially bound system:

$$M = M(X_{max}) = \rho_0 \left(\frac{1}{3} + \frac{\lambda}{(3-\epsilon)} X_{max}^{-\epsilon} \right) X_{max}^3.$$

The expression for the last bound radius have been computed previously (section H.5), so combining it with the expression for $\lambda = A(1-B)r_{min}^{\epsilon}$ in the mass (and A=0.5) yields

$$\begin{aligned} M &= \rho_0 \left(\tfrac{1}{3} + \tfrac{2A}{3(2+\epsilon)} \tfrac{(2+\epsilon)J^2}{2-J^2} \right) r_{min}^3 \left(\tfrac{2-J^2}{(2+\epsilon)J^2} \right)^{\frac{3}{\epsilon}} . \\ &= \rho_0 \left(1 + \tfrac{J^2}{(2-J^2)} \right) \tfrac{r_{min}^3}{3} \left(\tfrac{2-J^2}{(2+\epsilon)J^2} \right)^{\frac{3}{\epsilon}} \end{aligned}$$

Characteristic angular momentum In parallel with Eq.(H.4), the characteristic angular momentum can be defined initially by

$$\langle j^2 \rangle = \frac{\int_0^{X_{max}} j^2 dX}{\int_0^{X_{max}} dX} = J^2 \rho_0 \left(\frac{1}{15} + \frac{\lambda}{(3-\epsilon)(5-\epsilon)} X_{max}^{-\epsilon} \right) X_{max}^4, \tag{H.8}$$

which is equivalent to taking

$$\langle j^2 \rangle = \frac{5^{\frac{4}{\epsilon}-1}}{(5-\epsilon)^{\frac{4}{\epsilon}}} j^2 \left(\left(1 - \frac{\epsilon}{5} \right)^{\frac{1}{\epsilon}} X_{max} \right).$$

The expression of $\langle j^2 \rangle$ can then be rewritten in the same way as for the mass into

$$\begin{aligned} \langle j^2 \rangle &= J^2 \rho_0 \left(\tfrac{1}{15} + \tfrac{2A}{3(2+\epsilon)(5-\epsilon)} \tfrac{(2+\epsilon)J^2}{2-J^2} \right) r_{min}^4 \left(\tfrac{2-J^2}{(2+\epsilon)J^2} \right)^{\frac{4}{\epsilon}} . \\ &= \tfrac{J^2 \rho_0}{5} \left(1 + \tfrac{J^2}{(2-J^2)(1-\frac{\epsilon}{5})} \right) \tfrac{r_{min}^4}{3} \left(\tfrac{2-J^2}{(2+\epsilon)J^2} \right)^{\frac{4}{\epsilon}} \end{aligned}$$

Rotation parameter Thus the rotation parameter can be expressed in terms of the problem's quantities so that

$$\lambda_P^2 = \frac{J^2 \left(1 + \frac{J^2}{(2-J^2)(1-\frac{\epsilon}{5})} \right) r_{min} \left(\frac{2-J^2}{(2+\epsilon)J^2} \right)^{\frac{1}{\epsilon}}}{5G \left(1 + \frac{J^2}{(2-J^2)} \right) X_{core} e^{\delta T_c}}. \tag{H.9}$$

Real units

The model's masses are always expressed in unscaled units, therefore the masses in mks units can be written

$$M_{real} = MU_M.(1 M_\odot)$$

(see appendix ??) whereas if the angular momentum is also expressed in unscaled units, the conversion to real ones requires to transit through scaled angular momentum before getting to real mks units

$$\begin{aligned} j^2_{real} &= j^2_{ss} U_R^2 U_V^2 (1kpc)^2 (1km.s^{-1})^2 \\ &= j^2 e^{-2(2\delta-1)T} e^{2\delta T} U_R^2 e^{2(\delta-1)T} U_V^2 (1kpc)^2 (1km.s^{-1})^2 \\ &= j^2 U_R^2 U_V^2 (1kpc)^2 (1km.s^{-1})^2 \end{aligned} .$$

The need for mks units comes from the use of G in the expressions. Again the angular momentum is taken at the end of the infall phase, so $T = T_e$. Eventually the radius is made real with

$$r_{core} = X_{core} e^{\delta T_e} U_R (1kpc).$$

Thus the rotation parameter should be corrected for real units by

$$\lambda^2_{P_{real}} = \frac{\langle j^2 \rangle U_R^2 U_V^2 (1kpc)^2 (1km.s^{-1})^2}{GMU_M.(1M_\odot) X_{core} e^{\delta T_e} U_R (1kpc)} = \frac{\langle j^2 \rangle e^{-\delta T_e} U_R U_V^2 (1kpc)(1km.s^{-1})^2}{GMU_M.(1M_\odot) X_{core}}.$$

Thus the real rotation parameter can be obtained with

$$\begin{aligned} \lambda^2_{P_{real}} &= \frac{\langle j^2 \rangle e^{-\delta T_e} \frac{2}{3} 10^4 e^{-\delta T_e} \left(\frac{2}{127} 10^5 e^{(1-\delta)T_e}\right)^2 (3.086 \times 10^{19} m)(10^3 m.s^{-1})^2}{6.67 \times 10^{-11} m^3 kg^{-1} s^{-2} M 10^{10}.(1.99 \times 10^{30} kg) X_{core}} \\ &= \frac{\langle j^2 \rangle}{M X_{core}} \frac{e^{2(1-2\delta)T_e} \frac{2}{3} \left(\frac{2}{127}\right)^2 3.086 \times 10^{39}}{6.67 \times 1.99 \times 10^{29}} \\ &= \frac{\langle j^2 \rangle}{M X_{core}} e^{2(1-2\delta)T_e} \frac{2}{3} \left(\frac{2}{127}\right)^2 \frac{3.086 \times 10^{10}}{6.67 \times 1.99} \end{aligned} . \quad \text{(H.10)}$$

Real rotation parameter expression and values

General expression The general expression yielded for the rotation parameter as a function of initial density contrast index ϵ, the corresponding similarity class δ and time of the end of infall T_e as well as the angular momentum parameter J^2 can be obtained from Eqs.(H.9) and (H.10) into the form

$$\begin{aligned} \lambda^2_P &= \frac{J^2 \left(1 + \frac{J^2}{(2-J^2)(1-\frac{\epsilon}{5})}\right) r_{min} \left(\frac{2-J^2}{(2+\epsilon)J^2}\right)^{\frac{1}{\epsilon}} 2^3 \times 3.086}{5 \left(1 + \frac{J^2}{(2-J^2)}\right) X_{core} 3 \times 127^2 \times 6.67 \times 1.99 \times 10^{-10} e^{-2(1-2\delta)T_e}} \\ &= \frac{J^2 \left(1 + \frac{J^2}{(2-J^2)(1-\frac{\epsilon}{5})}\right) \left(\frac{2-J^2}{(2+\epsilon)J^2}\right)^{\frac{1}{\epsilon}}}{\left(1 + \frac{J^2}{(2-J^2)}\right) e^{-2(1-2\delta)T_e}} 1.28 \times 10^6 \end{aligned} .$$

The previous expression enables us to compute the values for each case considered.

Shallow case In the shallow case, where we took $\epsilon = \frac{3}{2}$, the corresponding values for the similarity class, the end time of infall and the angular momentum parameter are respectively $\delta = \frac{10}{9}$, $T_e = 10$ and $J^2 = 10^{-3}$. The corresponding calculation for the rotation parameter yields

$$\lambda_P^2 \simeq 2.14 \times 10^{-6} \Rightarrow \lambda_P \simeq 0.0015.$$

Steep case In the steep case we took $\epsilon = \frac{5}{2}$, and the corresponding $\delta = \frac{14}{15}$, $T_e = 15$ and $J^2 = 9 \times 10^{-3}$. The rotation parameter then becomes

$$\lambda_P^2 \simeq 2.81 \times 10^{-7} \Rightarrow \lambda_P \simeq 0.00053.$$

Bibliography

Quand j'ai un peu d'argent,
j'achète des livres,
et s'il m'en reste un peu
j'achète de la nourriture et des
vêtements.

Erasme

[1] Sancisi, R., & van Albada, T.S., in *Dark Matter in the Universe* eds. J. Kormendy & G. Knapp (Reidel, Dordrecht, 1987), p. 67, in Kolb, E.W., & Turner, M.S., *The Early Universe* (Addison-Wesley, Redwood, Calif. 1990), p. 18

[2] Bertola, F., & Capaccioli, M., 1975, Ap.J., **200**, *439*

[3] Carlberg, R.G. *et al.*, 1999, Ap.J., **516**, *552*

[4] Songaila, A., Cowie, L., Hogan, C., & Rugers, M., 1994, Nature, **368**, *599*

[5] Holder, G.P., & Carlstrom, J.E., Proc. of *Microwave Foreground*, ed. A. de Oliveira-Costa, ASP Conference Series 181 (1999) 199 ,(astro-ph/99904220)

[6] van Waerbeke, L., *et al.*, 2000, A&A, **358**, *30*

[7] Faber,S.M., & Gallagher, J.S., 1979, Ann. Rev. Astron. & Ap., **17**, *135*

[8] Peebles, P.J.E., 1980, *Physical Cosmology*, eds R. Balian, J. Audouze & D.N. Schramm (Amsterdam:North Holland), p. 213

[9] Schramm, D.N., & Turner, M., 1998, Rev. Mod. Phys., **70**, *303*

[10] EROS Collaboration, Aubourg, E. *et al.*, 1993, Nature, **365**, *623*

[11] Ivanov, P., Naselsky, P., & Novikov, I., 1994, Phys. Rev. D**50**, *7173*

[12] The Kamiokande Collaboration, Hirata, K.S. *et al.*, Phys. Lett. B**205**, *416*

[13] Peccei, R., & Quinn, H.R., 1977, Phys. Rev. Lett., **38**, *1440*

[14] Bahcall, N.A., Ostriker, J.P., Perlmutter, S., & Steinhardt, P.J., 1999, Science, **284**, *1481*

[15] Lineweaver, C.H., & Barbosa, D., 1998, Ap.J., **495**, *624*

[16] Lineweaver, C.H., & Barbosa, D., 1998, A&A, **329**, *799*

[17] Tegmark, M., 1999, Ap.J., **514**, *L69*

[18] Bergström, L., 2000, Rept. Prog. Phys., **63**, *793,* (hep-ph/0002126)

[19] Shandarin, S.F., & Zel'Dovich, Ya. B., 1989, Rev.Mod.Phys., **61**, *185*

[20] Sugiyama, N.,Proc. of *Workshop on Dark Matter and the Structure of the Universe*, ed. M. Sasaki (1989) 182

[21] Peebles, P.J.E.,1980, *The Large Scale Structure of the Universe* (Princeton: Princeton University Press).

[22] Bardeen, J.M., Bond, J.R., Kaiser, N., & Szalay, A.S., 1986, Ap.J.,**304**, *15* (BBKS)

[23] Doroshkevich, A.G., 1970, Astrophysica, **6**, *320*

[24] Doroshkevich, A.G., & Shandarin, S.F., 1978, Soviet Astron., **22**, *653*

[25] Bond, J.R., Cole S., Efstathiou, G., & Kaiser, N., 1991, Ap.J., **379**, *440* (BCEK)

[26] Bond, J.R., & Myers, S.T., 1996, Ap.J.S., **103**, *1 / 41 / 63*

[27] Press, W.H., & Schechter, P., 1974, Ap.J., **187**, *425* (PS)

[28] Lacey, C., & Cole S., 1993, M.N.R.A.S., **262**, *627*

[29] Shapiro, P.R., Iliev, I.T., & Raga, A.C., 1999, M.N.R.A.S., **307**, *203*

[30] Gunn, J.E., & Gott, J.R., 1972, Ap.J., **176**, *1*

[31] Kravtsov, A.V., Klypin, A.A., Bullock, J.S., & Primack, J.R., 1998, Ap.J., **502**, *48*

[32] Navarro, J.F., Frenk C. S., & White S.D.M., 1996, Ap.J., **462**, *563* (NFW)

[33] Syer, D., & White, S.D.M., 1998, M.N.R.A.S., **293**, *337*

[34] Lynden-Bell D.,1967, M.N.R.A.S., **136**, *101*

[35] Fillmore, J.A., & Goldreich, P., 1984, Ap.J., **281**, *1*

[36] Bertschinger, E., 1985, Ap.J.S., **58**, *39*

[37] Hoffman, Y., & Shaham, J., 1985,Ap.J., **297**, *16* (HS85)

[38] Hoffman, Y., 1985,Ap.J., **328**, *489*

[39] Moutarde, F., Alimi, J.-M., Bouchet, F.R., & Pellat, R., 1995, Ap.J., **441**, *10*

[40] Henriksen, R.N., Proc. of *Ecole des Houches*, Scale invariance and Beyond, eds. B., Dubrulle, F., Garner, & D., Sornette (Berlin: Springer, 1997) 63

[41] Henriksen, R.N., & Widrow, L.M., 1997, Phys.Rev.Lett., **78**, *3426* (HW97)

[42] Henriksen, R.N., & Widrow, L.M., 1999, M.N.R.A.S., **302**, *321* (HW99)

[43] Carter, B., & Henriksen, R.N., J.M.P.S., 1991, **32**, *2580* (CH91)

[44] Henriksen, R.N., & Widrow, L.M., 1995, M.N.R.A.S., **276**, *679* (HW95)

[45] Subramanian, K., Cen, R., & Ostriker, J.P., 2000, Ap.J.,**538**, *528*,(1999a, astro-ph/9909279)

[46] Subramanian, K., 2000, Ap.J.,**538**, *517*,(1999b, astro-ph/9909280)

[47] Ryden, B.S., & Gunn, J.E., 1987, Ap.J., **318**, *15*

[48] del Popolo, A., Gambera, M., Recami, E., & Spedicato, E., 2000, A&A, **353**, *427*

[49] Avila-Reese, V.,Firmani, C., Klypin, A., & Kravtsov, A.V., 1999, M.N.R.A.S., **310**, *527*

[50] Lokas, E.L., 2000, M.N.R.A.S., **311**, *423*

[51] Sikivie, P., Tkachev, I.I.,& Wang, Y., 1997, Phys.Rev.D, **56**, *1863*

[52] White, S.D.M., & Zaritsky, D., 1992, Ap.J., **394**, *1*

[53] Ryden, B.S., 1993, Ap.J., **418**, *4*

[54] Teyssier, R., Chièze, J.P., & Alimi, J.-M., 1997, Ap.J., **480**, *36*

[55] Tormen, G., Bouchet, F.R., & White, S.D.M., 1997, M.N.R.A.S., **286**, *865*

[56] de Vaucouleurs, G., 1948, Ann. d'Astrophys., **11**, *247*

[57] van Albada, T.S., 1982, M.N.R.A.S., **201**, *939*

[58] Bertin, G., & Stiavelli, M., 1984, A&A, **137**, *26*

[59] Stiavelli, M., & Bertin, G., 1985, M.N.R.A.S., **217**, *735*

[60] Merritt, D.,Tremaine, S., & Johnstone, D., 1989, M.N.R.A.S., **236**, *829* (MTJ)

[61] Aguilar, L.A., & Merritt, D., 1990, Ap.J., **354**, *33*

[62] Jaffe, W., 1983, M.N.R.A.S., **202**, *995*

[63] Hernquist, L., 1990, Ap.J., **356**, *359*

[64] Moore, B., Ghigna, S., Governato, F., Lake, G., Quinn, T., & Stadel, J., Proc. of *12th Potsdam Cosmology Workshop, Large Scale Structures: Tracks and Traces* (Potsdam), eds. V. Mueller, S. Gottloeber, J.P. Muecket, & J. Wambsganss, World Scientific (1998) 37 and Proc. of *Galactic Halos* (U.C. Santa-Cruz), ed. D. Zaritsky, ASP Conference Series 136 (1998a) 426, (astro-ph/99711259)

[65] Moore, B., Governato, F., Quinn, T., Stadel, J., & Lake, G., 1998b, Ap.J., **499**, *5*

[66] Huss, A., Jain, B., & Steinmetz, M., 1999a, Ap.J., **517**, *64*

[67] Huss, A., Jain, B., & Steinmetz, M., 1999b, M.N.R.A.S., **308**, *1011*

[68] Kull, A., 1999, Ap.J.L., **516**, *L5*

[69] Jing, Y.P., 2000, Ap.J., **535**, *30*

[70] Jing, Y.P., & Suto, Y., 2000, Ap.J.L., **529**, *L69*

[71] Moore, B., Quinn, T., Governato, F., Stadel, J., & Lake, G., 1999, M.N.R.A.S., **310**, *1147*

[72] Ghigna, S., Moore, B., Governato, F., Lake, G., Quinn, T., & Stadel, J., 2000, Ap.J., **544**, *616*,(1999, astro-ph/9910166)

[73] Tittley, E.R., & Couchman, H.M.P., 2000, M.N.R.A.S., **315**, *834*

[74] Voglis, N., 1994, M.N.R.A.S., **267**, *379*

[75] Stil, J., 1999, Doctoral Thesis, Leiden Observatory

[76] Moore, B., 1994, Nature, **370**, *629*

[77] Sellwood, J.A., 2000, Ap.J.L., **540**, *L1*,(astro-ph/0004352)

[78] Walker, M.A., 1999, M.N.R.A.S., **308**, *551*

[79] Flores, R.A., & Primack, J.R.,1994, Ap.J.L., **427**, *L1*

[80] van den Bosch, F.C., Robertson, B.E., Dalcanton, J.J., & de Blok, W.J.G., 2000, A.J., **119**, *1579*

[81] Nusser, A., & Sheth, R., 1999, M.N.R.A.S., **303**, *685*

[82] Peebles, P.J.E., 1972, Gen.Re.Grav., **3**, *63*

[83] Young, P., 1980, Ap.J., **242**, *1232*

[84] Quinlan, G.D., Hernquist, L., & Sigurdsson, S., 1995Ap.J., **440**, *554*

[85] Nakano, T., & Makino, M., 1999, Ap.J.L., **525**, *L77*

[86] Henriksen, R.N., & Le Delliou, M., 2001, submitted to M.N.R.A.S.

[87] Binney, J., & Tremaine, S., 1987, *Galactic Dynamics* (Princeton: Princeton University Press).

[88] Spergel, D.N., & Hernquist, L., 1992, Ap.J.L., **397**, *L75*

[89] Natarajan, P., Hjorth, J., & van Kampen, E., 1997, M.N.R.A.S., **286**, *329*

[90] Stiavelli, M., & Bertin, G., 1987, M.N.R.A.S., **229**, *61*

[91] Fujiwara, T., 1983, P.A.S.J., **35**, *547*

[92] Misner, C.W., Thorne, K.S., & Wheeler, J.A., 1973, *Gravitation* (New York: W.H.Freeman & Co).

[93] d'Inverno, R., 1992, *Introducing Einstein's Relativity* (Oxford: Clarendon Press).

[94] Henriksen, R.N., 1989, M.N.R.A.S., **240**, *917*

[95] Henriksen, R.N., private communications on radial spherical symmetric CH91 formalism applied to the CBE-Poisson system

[96] Henriksen, R.N., private communication on Cartesian coordinates, CH91 formalism.

[97] Henriksen, R.N., private communications on self-similarity index determinations for radial orbits and for spherical-symmetric angular momentum

[98] Wilkinson, M.I., & Evans, N.W., 1999, M.N.R.A.S., **310**, *654*

[99] Rasio, F.A., Shapiro, S.L., & Teukolsky, S.A., 1989, Ap.J., **344**, *146*

[100] Merrall, T.E.C., private communication

[101] Hanyu, C., & Habe, A., 2000, submitted to Ap.J., astro-ph/0011004

[102] Merrall, T.E.C.,private communication from PhD Thesis in progress, Queen's University, Kingston, Canada

[103] Sikivie, P. & Ipser, J.R., 1992, Phys. Lett. B, **291**, *288*

[104] Hoffman, Y., Shlosman, I., & Shahiv, G., 1979, M.N.R.A.S., **189**, *737*

[105] Longair, M.S.,,1998, *Galaxy Formation* (Berlin: Springer-Verlag)

[106] Henriksen, R.N., private communications on self-similar coarse-graining of the CBE in radial spherical symmetry

[107] Caroll, B.W., & Ostlie, D.A., 1996, *An introduction to modern astrophysics* (Reading, Massachusetts: Addison-Wesley Publishing Co)p661

[108] Binney, J., & Merrifield, M., 1998, *Galactic Astronomy* (Princeton: Princeton University Press)p677

[109] Stil, J., private communications on the calculation of the SSIM's velocity dispersion for significant real halo comparison

[110] Knebe, A. Kravtsov, A.V., Gottlöber, S., &Klypin, A.A., 2000, M.N.R.A.S., **317**, *630*

[111] Leeuwin, F., & Athanassoula, E., 2000, M.N.R.A.S., **317**, *79*

[112] Henriksen, R.N., & Le Delliou, M., 2001, in preparation for M.N.R.A.S.

[113] Bullock, J.S., Dekel, A., Kolatt, T.S., Kravtsov, A.V., Klypin, A.A., Porciani, C., & Primack, J.R., 2000, submitted to Ap.J., astro-ph/0011001

[114] Peebles, P.J.E., 1993, *Principles of Physical Cosmology*, (Princeton: Princeton University Press)

[115] Henriksen, R.N., private notes on Poisson's equation and an inner cups radius